

Advanced Gas Turbine

DOE/NASA 0168-10

NASA CR - 179484

EDR 12344

AGT

Technology Project

(NASA-CR-179484) ADVANCED GAS TURBINE (AGT)
TECHNOLOGY PROJECT Final Annual Report,
1985 (General Motors Corp.) 160 p CSCL 21A

1985 Annual Report

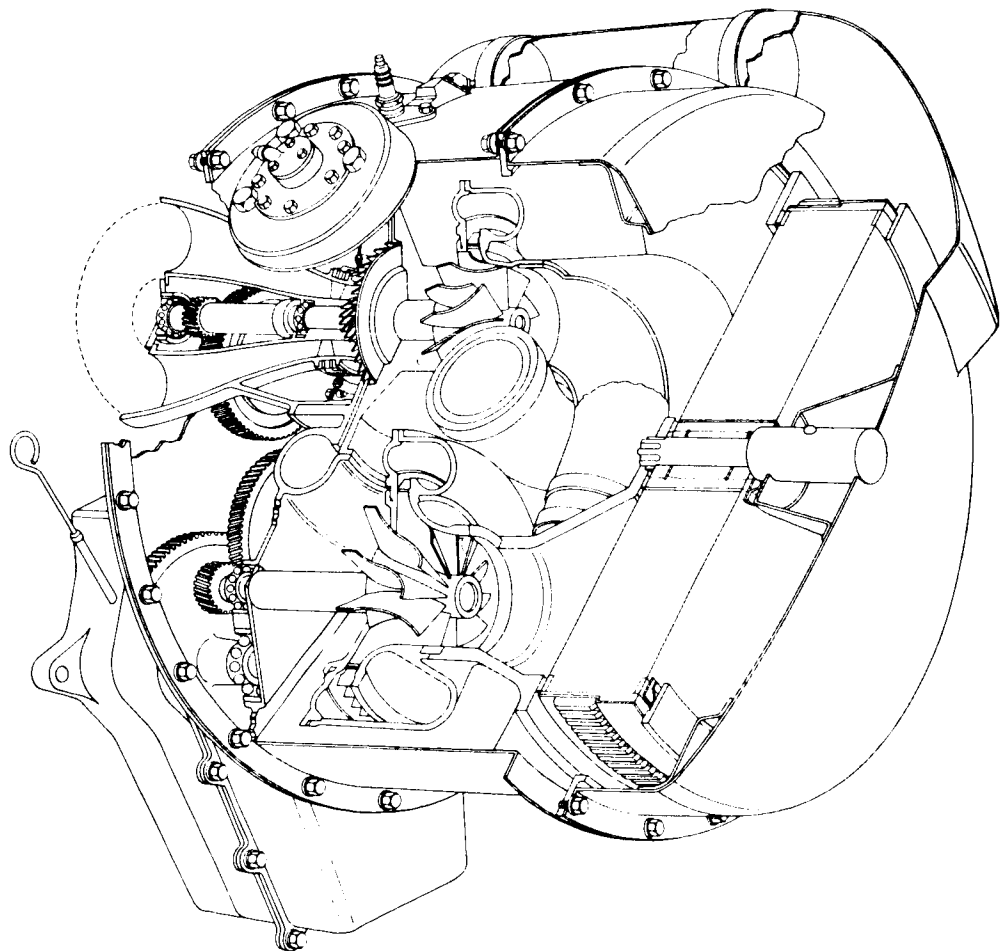
N87-11995

Allison
GAS TURBINE DIVISION
General Motors Corporation
P.O. Box 420
Indianapolis, Indiana 46206-0420

Unclas
G3/37 44920

1 September 1986

FINAL



Prepared for
National Aeronautics
and Space Administration
Lewis Research Center
Cleveland, Ohio 44135
Contract DEN 3-168

For U.S. Department of Energy
Conservation and Renewable Energy
Office of Transportation Systems

NOTICE

This report was prepared to document work sponsored by the United States Government. Neither the United States nor its agent, the United States Department of Energy, nor any Federal employees, nor any of their contractors, subcontractors, or their employees makes any warranty, express or implied, or assumes any legal liability or responsibility for the accuracy, completeness, or usefulness of any information, apparatus, product, or process disclosed, or represents that its use would not infringe privately owned rights.

DOE/NASA 0168-10
NASA CR - 179484

EDR 12344

Advanced Gas Turbine AGT Technology Project

1985 Annual Report

Allison Gas Turbine Division
General Motors Corporation
Indianapolis, Indiana 46206-0420

1 September 1986

**Prepared for
NATIONAL AERONAUTICS AND SPACE ADMINISTRATION
Lewis Research Center
Under Contract DEN 3-168**

**for
U.S. Department of Energy
Conservation and Renewable Energy
Office of Transportation Systems**

FOREWORD

This report presents a technical summary of the Allison Gas Turbine project to develop an automotive gas turbine power-train system under NASA Contract DEN 3-168 (Department of Energy funding). The report covers the 1985 calendar year.

The basic objective of this project is to develop the technology base for an advanced automotive gas turbine that, when installed in a Pontiac A6000 class vehicle of 1360 kg (3000 lbm) inertia weight, will achieve a fuel economy of 18 km/l (42.5 mpg), meet or exceed the Federal emission requirements, and have alternate fuel capability.

Several General Motors Divisions and other companies are major contributors to this effort. They are

as follows: Allison Gas Turbine Division—prime contractor and team leader, overall power-train and controls responsibility; Pontiac Motor Division—vehicle and cost studies; Delco Remy Division—starter/boost motor; Corning Glass Works—regenerator; Sohio Engineered Materials Co (formerly Carborundum); and GTE Laboratories—ceramics.

The Allison Program Manager for the AGT 100 is H. E. (Gene) Helms; design effort is directed by Leonard Lindgren; materials effort is directed by Dr. Peter Heitman; and project effort is directed by Philip J. Haley. The NASA AGT 100 Project Manager is Paul T. Kerwin.

TABLE OF CONTENTS

Section	Title	Page
	Forward	i
	Summary	1
	Introduction	2
I	Vehicle System Development*	
II	Engine Development	7
	2.1 Reference Power-Train Design*	
	2.2 Experimental Engine	7
	2.2.1 Fabrication	7
	2.2.2 Experimental Engine Testing	7
	2.2.3 Performance Analysis	18
III	Compressor Development	22
	3.1 Compressor Aerodynamic Development	22
	3.1.1 Double Splitter Impeller Test	22
	3.1.2 Comprehensive Data Analysis	23
	3.1.3 Planned Rig Modifications and New Impeller Design	33
	3.2 Compressor Rig Mechanical Development*	
	3.3 Compressor Mechanical Development	39
	3.3.1 Modified Type 1A Impeller (Cut Back Blades)	39
	3.3.2 Steel Compressor Shroud	39
IV	Gasifier Turbine Development	46
	4.1 Gasifier Turbine Aerodynamic Development	46
	4.2 Gasifier Turbine Mechanical Development	47
	4.2.1 Vibration/Balance Activity	47
	4.2.2 Summary of Engine Builds and Test Experience	51
	4.3 Ceramic Gasifier Turbine Design	52
	4.3.1 SiC Gasifier Turbine Engine Test and Postfailure Investigation, S/N 2, BU12	52
	4.3.2 Silicon Nitride Gasifier Turbine	55
	4.3.3 Ceramic Gasifier Turbine Design—Static Components	56
V	Power Turbine Development	70
	5.1 Power Turbine Aerodynamic Analysis*	
	5.2 Power Turbine Mechanical Development*	
	5.3 Ceramic Power Turbine Design	70
	5.3.1 Ceramic Power Turbine Rotor Design	70
	5.3.2 Ceramic Power Turbine Design—Static Components	70
VI	Combustor Development	77
	6.1 Test Facility	77
	6.2 Test Results	77

*No activity this period

TABLE OF CONTENTS (CONT)

Section	Title	Page
	6.2.1 Combustor Liner Pressure Loss	77
	6.2.2 Combustor Proof Testing	80
	6.2.3 Alternate Fuel Demonstration	80
VII	Regenerator Development	84
	7.1 Design and Material Development	84
	7.1.1 Regenerator Seal Tests	84
	7.1.2 Regenerator Disk	85
	7.2 Rig Development Testing	87
VIII	Secondary Systems	93
	8.1 Gearbox	93
	8.1.1 Power Transfer Clutch	93
	8.1.2 Oil Pump and Regulating Valve	94
	8.2 Bearings and Shaft Seals	94
	8.2.1 Bearings*	
	8.2.2 Shaft (Carbon) Seals	94
IX	Materials Development	96
	9.1 Thermal Barrier Development	96
	9.1.1 Material Qualification	96
	9.1.2 Process Development	96
	9.1.3 Advanced Material Development	97
	9.2 Silicon Carbide Component Development	98
	9.2.1 Gasifier Turbine Rotor	98
	9.2.2 Gasifier Turbine Scroll Assembly	109
	9.2.3 Turbine Scroll Static Components Thermal Simulation Rig	120
	9.2.4 Power Turbine Rotor	121
	9.2.5 Power Turbine Scroll Assembly Development	124
	9.3 Silicon Nitride Component Development	126
	9.3.1 Gasifier Rotor	126
	9.3.2 Gasifier Turbine Scroll Assembly Development	135
	9.3.3 Power Turbine Rotor	135
	9.3.4 Power Turbine Scroll Assembly Development	138
	9.4 Fiber Reinforced Glass Ceramics	139
X	Controls Development	145
	10.1 Improved Fuel System*	
	10.2 Software Changes to Support Engine Testing	145
XI	Transmission Development*	
XII	Supportive Manufacturing, Cost, and Marketability	146
	12.1 Manufacturing Feasibility	146
	12.2 Cost Analysis*	
	Appendix	147

*No activity this period

LIST OF ILLUSTRATIONS

Figure	Title	Page
1	AGT 100 program plan	3
2	AGT 100 engine in Pontiac A6000	3
3	AGT 100 advanced gas turbine engine	3
4	Cross section of AGT 100 gas turbine engine	4
5	Design fuel economy goal for a 1364 kg (3000 lbm) automobile powered by AGT 100 gas turbine	5
6	Design goal of vehicle wide-open-throttle performance	5
7	AGT 100 ceramic components	6
8	Cumulative burning test hours of AGT 100 experimental engine	8
9	AGT 100 leakage system	8
10	AGT 100 gasifier turbine backplate air leakage sources	8
11	AGT 100 backface leakage test configuration	9
12	Turbine backface leak test	10
13	Schematic of leak detection flow path	10
14	Leakage as determined by orifice measurements	11
15	Typical vibration and whip during test of engine S/N 1 BU13	13
16	Ceramic gasifier scroll test cycle	14
17	Apparent failure incident indication as depicted by data trace during test of ceramic rotor, S/N 2 BU12 engine test data	15
18	Typical data trace depicting test of Kyocera ceramic part	17
19	AGT 100 engine cross-section showing locations of motion instrumentation	17
20	AGT 100 engine S/N 2 BU14 ceramic gasifier scroll test cycle	19
21	Comparison of original type 1A and double-splitter reduced blade friction compressor impellers	22
22	Meridional flow path comparison of different compressor blade shapes	23
23	Overall compressor performance for CX-53 BU6 and CX-53 BU3 rigs	24
24	CX-53 BU6 compressor clearance measurements as a function of corrected speed	25
25	Effect of clearance and inlet guide vane reset on compressor performance	25
26	AGT 100/CX-40 compressor rig	27
27	AGT 100/CX-53 compressor rig	28
28	CX-40 BU5 rig compressor rig	29
29	CX-40 BU3 compressor performance	30
30	CX-40 BU3, BU5 impeller blade normal thickness distribution	31
31	CX-40 BU5 compressor performance	32
32	CX-40 rig compressor performance along operating line (10% minimum surge margin)	33
33	CX-53 BU2 engine compressor performance	34
34	CX-53 BU2 engine compressor performance	35
35	Compressor operating line performance	36
36	CX-40 BU3, and BU5 and CX-53 BU2, BU3, and BU6 compressor flow range comparison	37
37	CX-53 rig compressor performance along operating line (10% minimum surge margin)	38
38	AGT 100 compressor impeller pressure recovery	38
39	Impeller pressure recovery, $N\sqrt{\theta} = 100\%$, near surge	38
40	AGT 100 compressor impeller inlet axial velocity ratios	38
41	CX-53 rig performance along operating line (10% minimum surge margin)	39
42	AGT 100 compressor	41
43	Steel insert in aluminum front cover of CX-53 compressor rig	42
44	AGT 100 compressor design point efficiency predictions	42
45	AGT 100 compressor impeller design evolution	42
46	AGT 100 compressor arbitrary blade study—leading edge	43
47	Impeller inlet blade angle distribution for arbitrary blade study	43

LIST OF ILLUSTRATIONS (CONT)

Figure	Title	Page
48	Impeller leading edge sweep concept	43
49	Leading edge sweep performance	43
50	AGT 100 compressor flow size as a function of total-to- static compressor efficiency	44
51	Steel shroud insert design	44
52	Comparison of steel and aluminum compressor shroud isotherms at max power, 100% N1, steady state condition	45
53	Loss analysis results based on gasifier turbine rig data	46
54	Rig layout of cambered vane set	47
55	Gasifier turbine rig configuration	47
56	Gasifier engine section	48
57	Gasifier assembly balance fixture	50
58	Condition of the ceramic rotor assembly after engine testing	52
59	Ceramic rotor airfoil natural frequencies	53
60	Ceramic rotor inducer blade dynamic fracture test	53
61	Probabilistic assessment of dynamic fracture test results	54
62	Foreign object damage rig used to investigate potential impact damage to the ceramic gasifier rotor	54
63	Airfoil damage resulting from FOD impact, SiC gasifier turbine	55
64	Bench test FOD rig preliminary results using a gasifier rotor made from SiC material (zero initial velocity on balls)	55
65	Modified inducer blade thickness	56
66	Campbell diagram, redesigned (thickened) inducer region airfoil, SiC gasifier rotor	56
67	Silicon nitride rotor attachment designs	57
68	Calculated gasifier rotor assembly modes-brazed rotor/shaft attachment	58
69	Calculated gasifier rotor assembly modes-interference configuration	58
70	Calculated maximum principal stress for interference fit configuration Si_3N_4 rotor at 100% speed and 1080°C (1976°F) TIT	58
71	Equivalent stresses, Inco 907 shaft at 100% speed and 1080°C (1976°F) TIT for interference fit attachment	59
72	Calculated temperatures for the Kyocera braze joining of Si_3N_4 rotor and metal shaft at 100% speed and 1288°C (2350°F) TIT	59
73	Thermal analysis of Si_3N_4 rotor/metal shaft at 100% speed and 1080°C (1976°F) TIT for the interference fit configuration	60
74	Frequency-speed interference diagram gasifier turbine-silicon nitride, drawing airfoil thickness	60
75	Calculated mode shape, third and fourth mode, Si_3N_4 material rotor	61
76	Gasifier turbine scroll assembly finite element model geometry	61
77	Radial thermal growth of gasifier turbine Si_3N_4 outer backplate and SiC scroll	63
78	Radial thermal growth of gasifier turbine SiC outerbackplate and SiC scroll	64
79	Radial thermal growth of gasifier turbine Si_3N_4 outer backplate and Si_3N_4 scroll	66
80	Crack indications in αSiC gasifier turbine outer backplate after engine test	67
81	Origin of failure in αSiC gasifier turbine outer backplate	67
82	Modification of gasifier turbine outer backplate to reduce local tensile hoop stress	68
83	Allison alternate gasifier turbine scroll design and Kyocera alternate scroll design	68
84	Kyocera alternate design silicon nitride gasifier turbine scroll construction	69
85	Kyocera alternate design silicon nitride gasifier turbine scroll assembly	69
86	Gasifier turbine heat shield installation	69
87	Redesigned (thicker) inducer region airfoil, ceramic power turbine rotor	70
88	Campbell diagram, silicon nitride (SN 220M) material thickened airfoil	70
89	Comparison of original design SiC power turbine scroll and Kyocera alternate design Si_3N_4 power turbine scroll	72

LIST OF ILLUSTRATIONS (CONT)

Figure	Title	Page
90	Kyocera alternate design silicon nitride power turbine scroll body casting	73
91	Power turbine heat shield installation	73
92	Power turbine scroll assembly finite element model	73
93	Steady-state (RPD condition) operating temperatures for SiC ceramics power turbine scroll assembly	74
94	Max principal stress in SiC ceramic power turbine scroll assembly—steady-state (RPD) conditions	74
95	Deflected shape plot for SiC ceramic power turbine scroll assembly operating at RPD conditions	75
96	Probability of survival of SiC ceramic power turbine scroll assembly components as a function of time during start-up cycle	75
97	SiC power turbine component temperatures at 70 sec into transient start-up cycle	75
98	Max principal stress in SiC ceramic power turbine scroll assembly components 70 sec into transient start-up cycle	76
99	Deflected shape plot for SiC ceramic power turbine scroll assembly at 70 sec into transient start-up cycle	76
100	AGT 100 combustor pressure loss calibration, Rig 54, BU19, Series A	78
101	AGT 100 combustor pressure loss calibration	79
102	AGT 100 combustor pressure loss calibration comparison of BU16 (old) and BU19 (new) data .	81
103	AGT 100 methanol fuel combustion	82
104	Comparison of CO-NO _x emissions from methanol and diesel (jet) fuel combustion	83
105	Regenerator seal showing displacement of rim segment and worn corner	84
106	Power curve regression of radial modulus of rupture (MOR) on axial position	85
107	Comparison of tangential (Y _t) and radial (Y _r) modulus of rupture	86
108	Radial tensile stress versus coefficient of thermal expansion	88
109	Radial compressor stress versus coefficient of thermal expansion	89
110	Tangential tensile stress versus coefficient of thermal expansion	90
111	Tangential compression stress versus coefficient of thermal expansion	91
112	Coefficients of thermal expansion versus temperature	92
113	Speed, clutch pressure, and turbine inlet temperature as a function of time during power transfer clutch engagement	93
114	Speed, clutch pressure, and turbine inlet temperature as a function of time during power transfer clutch disengagement	94
115	Thermal expansion of various zircon batches as compared to silicon carbide	96
116	Shrinkage correlation with specific surface area	97
117	Typical defect in fired microstructure	97
118	Granule interiors at three water contents	98
119	Cumulative probability of failure as a function of spin speed, Group 8 (1985) SiC gasifier rotors	109
120	Rotor SiC/metal shaft attachment	112
121	SiC scroll body following 1925°F proof test	114
122	Corning composite ceramic inner backplate following 1925°F proof test	114
123	Corning composite ceramic inner backplate laminate configurations	115
124	Crack indications in αSiC gasifier turbine outer backplate	116
125	Origin of failure in αSiC gasifier turbine outer backplate	117
126	Location of crack origins in gasifier turbine αSiC outer backplate	117
127	Loads imposed on gasifier turbine scroll assembly during engine test	118
128	Modification of gasifier turbine outer backplate	119
129	AGT 100 scroll test thermal shock rig: Rig 54, BU4 Series A, start nozzle operation	121
130	AGT 100 scroll test thermal shock rig: Rig 54, BU4 Series A, start nozzle operation	122
131	AGT 100 scroll test thermal shock rig: Rig 54, BU4, start nozzle operation	123

LIST OF ILLUSTRATIONS (CONT)

Figure	Title	Page
132	AGT 100 scroll test thermal shock rig: Rig 54, BU4, start nozzle operation	124
133	AGT 100 scroll test thermal shock rig: Rig 54, BU4 Series A, main nozzle operation	125
134	AGT 100 scroll test thermal shock rig: Rig 54, BU4 Series A, main nozzle operation	125
135	Initial failure, airfoil release at root (4:00 position) at 54,800 rpm, siliconized gasifier rotor, S/N 1-11	127
136	Initial failure, airfoil release at root (2:00 position) at 48,100 rpm, siliconized gasifier rotor, S/N 8-11	128
137	Kyocera slip-cast SN220M sintered Si ₃ N ₄ gasifier turbine rotor	128
138	Fracture surface of Kyocera Si ₃ N ₄ rotor brazed to Inco 907 shaft (0004-8). Origins are located at large	130
139	Cross section of Kyocera Si ₃ N ₄ rotor 0004-8 showing nonuniform braze thickness. Note direct contact at fracture origin (bottom picture)	131
140	Fracture surface of Kyocera Si ₃ N ₄ rotor 0004-3 broken in load test (36.54 MPa (5300 lb/in. ²). Origin is located at large black arrow	132
141	Cross section of Kyocera Si ₃ N ₄ rotor 0004-3 showing nonuniform braze thickness. Note direct contact at fracture origin (B)	133
142	Si ₃ N ₄ rotor shaft/compressor shaft joining schemes. (a) brazed joint (configuration 1), (b) interference fit joint (configuration 2)	134
143	Calculated gasifier rotor assembly modes (configuration 1)—tiebolt stiffening load included	135
144	Calculated gasifier rotor assembly modes (configuration 2)—tiebolt stiffening load included	136
145	Contour plot of calculated maximum principal stress for interference fit (configuration 2), Si ₃ N ₄ rotor at 100% speed and 1976°F turbine inlet temperature (TIT)	137
146	Contour plot of equivalent stress, Inco 907 shaft at 100% speed and 1976°F turbine inlet temperature (TIT) for interference fit attachment	137
147	Contour plot of calculated temperatures for the Kyocera braze joining of Si ₃ N ₄ turbine and metal shaft (configuration 1) at 100% speed and 1288°C (2350°F) TIT	138
148	Thermal analysis of Si ₃ N ₄ rotor and metal shaft at 1080°C (1976°F) TIT and 100% speed for the interference fit (configuration 2)	139
149	Frequency-speed interference diagram gasifier turbine-silicon nitride (at speed and temperature), drawing airfoil thickness	140
150	Calculated mode shape, third and fourth mode, Si ₃ N ₄ material rotor	141
151	GTE silicon nitride material (PY-6) gasifier rotor featuring radially pullable airfoils	141
152	Corning ceramic composite gasifier turbine inner backplate laminate configurations	142
153	Linear deflection as a function of load, Corning LAS III—flat preform composite ceramic inner backplate	143
154	Linear deflection as a function of load, Corning BMAS-III—flat preform composite ceramic inner backplate	143
155	Linear deflection as a function of load, Corning BMAS-III—stepped preform composite ceramic inner backplate	144

LIST OF TABLES

Table	Title	Page
I	AGT 100 project and design objectives	2
II	Aerodynamic component rigs—status at end of 1985	4
III	AGT 100 engine carbon dioxide tracer concentrations	11
IV	Carbon dioxide test results—80/70 point	12
V	Helium test data and results	12
VI	Ceramic parts	14
VII	AGT 100 maximum power engine performance and EPA combined cycle fuel economy	20
VIII	AGT 100 engine component characteristics	21
IX	AGT 100 configurations	26
X	Jet/wake flow model data reduction	40
XI	Ceramic material properties	62
XII	Probabilities of survival for gasifier turbine scroll assembly components fabricated from silicon carbide (RPD conditions)—POS	62
XIII	Comparison of probability of survival for Si ₃ N ₄ and αSiC gasifier turbine outer backplates at RPD operating conditions (when assembled with αSiC scroll and αSiC inner backplate)	63
XIV	Probabilities of survival for components of silicon nitride gasifier turbine scroll assembly (RPD conditions)	65
XV	Probability of survival and maximum principal stress for ceramic power turbine	74
XVI	Comparison of data for radial and tangential permeation rates	87
XVII	Strength data for lots 3 and 4	97
XVIII	Process development, gasifier turbines	99
XIX	Inspection evaluation, gasifier turbines (1985 program)	102
XX	HIP process rotors (all processed at 137 MPa 20 X 10 ³ lb/in ² in an Argon atmosphere)	110
XXI	Status of engine candidate gasifier rotor assemblies	110
XXII	Detail components in the first tested SiC gasifier turbine scroll assembly	113
XXIII	Detail components of second engine tested ceramic gasifier turbine scroll assembly (engine D-2 BU14)	115
XXIV	Evaluation, siliconized (KX02) gasifier rotors	126
XXV	Siliconized rotor program	126
XXVI	Disposition Kyocera slip-cast SN220M gasifier turbine rotors	129
XXVII	Spin test results for Kyocera SN220M Si ₃ N ₄ rotors	129
XXVIII	Strength characteristics of Kyocera SN250 Si ₃ N ₄	134
XXIX	Summary of purchase orders issued for silicon nitride gasifier turbine static components	136
XXX	Summary of purchase orders issued for silicon nitride power turbine static components .	142

SUMMARY

AGT 100 activities during the past year were highlighted by extensive engine testing, ceramic component fabrication and evaluation, component performance rig testing, and analytical studies. Although significant technical challenges remain, all areas experienced progress.

Significant accomplishments accrued in the engine testing activity. Ten experimental assemblies (builds) were evaluated using the two engines. 1985 accumulated operating time was 120 hr of burning and 170 hr total. Total cumulative engine operating time to date is 395 hr.

Engine testing verified the effectiveness of most design modifications and continued to be free of major failures. Both engines have been limited to about 84% gasifier speed due to case vibration and/or shaft displacement (whip). Build number 13 of engine S/N 1 used flow mechanical and trace gas techniques to conclude that the primary source of engine working fluid leakage occurs through the regenerator seals. Power transfer clutch operation was successfully tested in build 14 of S/N 1 and was used for over two hr in the slipping mode with significant speed differentials in build 13 of S/N 2, resulting in no wear. Build 16 of S/N 1 was the initial test of a Kyocera Si_3N_4 ceramic gasifier rotor; this rotor was successfully running at year's end.

Six transient start nozzle cycles were successfully executed in two engine builds (S/N 2 BU9 and 10) on an αSiC gasifier scroll assembly. An outer backplate crack was addressed by a design change. Build 11 of S/N 2, aimed at dynamics investigation, was aborted due to a power turbine seizure caused by improper seating of a scroll locating shim. The second αSiC gasifier rotor engine test (build 12 of S/N 2) resulted in blade tip failures, as had the first such test in 1984. These occurred at 899°C (1650°F) and 60% speed. Foreign object damage or blade vibration is suspected.

Build 13 of engine S/N 2 was instrumented to examine engine vibration and rotor whip. Preliminary results indicate rotor unbalance as the problem source. This build was also the first definitive use of the pilotless combustor igniter. After testing to high temperatures in the scroll rig, the previously engine-tested αSiC scroll assembly was incorporated in engine S/N 2, build 14 and tested at 80% airflow, 1066°C (1950°F). Testing continued at year's end.

Thus, in 1985, silicon carbide scroll assemblies and silicon nitride rotors were added to the list of ceramic components successfully engine-tested. The ceramic combustor assembly, regenerator disk, bulkhead, turbine vanes, piston rings, and couplings are continuing to operate satisfactorily in the engine.

Component development activity included rig testing of the compressor, combustor, and regenerator. A compressor rig test was run to examine performance changes arising from reducing surface friction. A compressor shroud design change to reduce heat recirculation back to the inlet was executed. A new compressor impeller design was initiated, with target efficiency greater than 80%, based on an extensive data review. Combustor activities include qualification of ceramic parts for engine use and alternate fuel testing (methanol). A new design was initiated to eliminate fuel tube coking on DF-2 at very high burner inlet temperatures. Hot regenerator rig testing on new vendor purchased in-board seals has resulted in the initiation of a quality control program with that seal vendor. A seal rim preload test was successfully conducted to evaluate GM patented features to minimize seal distortion. The effects of temperature fluctuations on radial strength were determined for a regenerator matrix. Material strength was also determined for an advanced regenerator matrix material.

Ceramic component activity continues to focus on the development of state-of-the-art material strength characteristics in full-scale engine hardware. Injection-molded sintered αSiC and slip-cast Si_3N_4 gasifier turbine rotors were delivered from Sohio/Carborundum and Kyocera, respectively, and underwent analysis, spin tests, and engine testing, as noted. SiC gasifier scrolls were supplied by Sohio (a and siliconized) and by Norton (siliconized). Power turbine scroll detail design drawings were released. 1986 plans include gasifier and power turbine rotors and scrolls from both Sohio and Kyocera, plus gasifier rotors from GTE.

Fiber reinforced glass-ceramic composite turbine (inner) backplates were fabricated by Corning Glass Works. The BMAS-III stepped-platform material performed well in engine testing. Backplates of MAS material were delivered but have not been engine-tested.

INTRODUCTION

This is one of a series of annual reports documenting work performed on an Advanced Gas Turbine (AGT) Technology Development Project for automotive applications. The work is being conducted by Allison Gas Turbine Division of General Motors Corporation under NASA/DOE contract DEN 3-168.

The objectives of the project, as highlighted in Table I, are to develop an experimental power-train system that demonstrates the following: (1) the potential of a combined cycle fuel economy of 18.1 km/l (42.5 mpg) using diesel fuel No. 2 in a 1986 automobile of 1364 kg (3000 lbm) weight class on a 15°C (59°F) day, (2) emission levels less than 1986 federal standards, and (3) the ability to use a variety of fuels. It is intended that the technology demonstrated through this project will assist the automotive industry in making a go/no-go decision regarding the production engineering development of gas turbine power trains.

In meeting the project objectives, the engine will be designed to accomplish the following, also outlined in Table I: (1) achieve reliability and life comparable to conventional 1986 vehicular power plants, (2) achieve initial and life-cycle power-train costs competitive with those for 1986 power trains, (3) demonstrate vehicle acceleration suitable for safety and maneuverability, and (4) meet 1986 federal vehicle noise and safety standards.

transmission, and electronic control system installed in a 1985 Pontiac Phoenix passenger car. However, Government funding constraints after the first year resulted in a reduction of the program scope.

Activities eliminated included fabrication and testing of the transmission and vehicle. The electronic control scope was narrowed from that of controlling the engine, transmission, and vehicle to controlling an engine on a dynamometer. Figure 1 depicts the activity areas and schedule for the revised project.

The AGT 100 design was originally matched to the Pontiac Phoenix X-body car. A front-wheel-drive car, it was one of the General Motors advanced passenger cars, emphasizing efficiency of space and weight to combine comfort and function with high fuel economy. The AGT 100 will also fit into the Pontiac A6000, as shown in Figure 2. This is an A-body car that is slightly larger and is the latest GM front-wheel design with potential to replace the X-body car in the Pontiac future marketing of cars. The Fiero, a Pontiac mid-engine personal car, might also be powered by the AGT 100 engine.

The AGT 100, shown in Figures 3 and 4, is a two-shaft, regenerative gas turbine engine. In all respects, this engine design is tailored for high-volume application to fuel-efficient passenger cars. Its two-shaft configuration allows (1) the use of conventional transmissions, manual or automatic, and (2) turbine tip speeds (approximately 503 m/s [1650 ft/sec]) commensurate with available ceramic material properties (strength and variability). Single-shaft configurations were rejected by Allison because of the corresponding requirement for a continuously variable transmission and for approximately 40% higher turbine rotor ceramic material strength (for equal reliability). Careful attention was given to component arrangement for both vehicle installation and management of potentially high heat losses. All hot-section components are grouped together, bounded on one end by the regenerator, on the other end by the gearbox, and enclosed by a well-insulated cylindrical case. High turbine inlet temperature is possible through the use of ceramic hot-section parts. This, coupled with high aerodynamic component efficiencies, produces low fuel consumption and a 50% improvement in composite miles per gallon (30% energy efficiency improvement) over current spark-ignition engine technology.

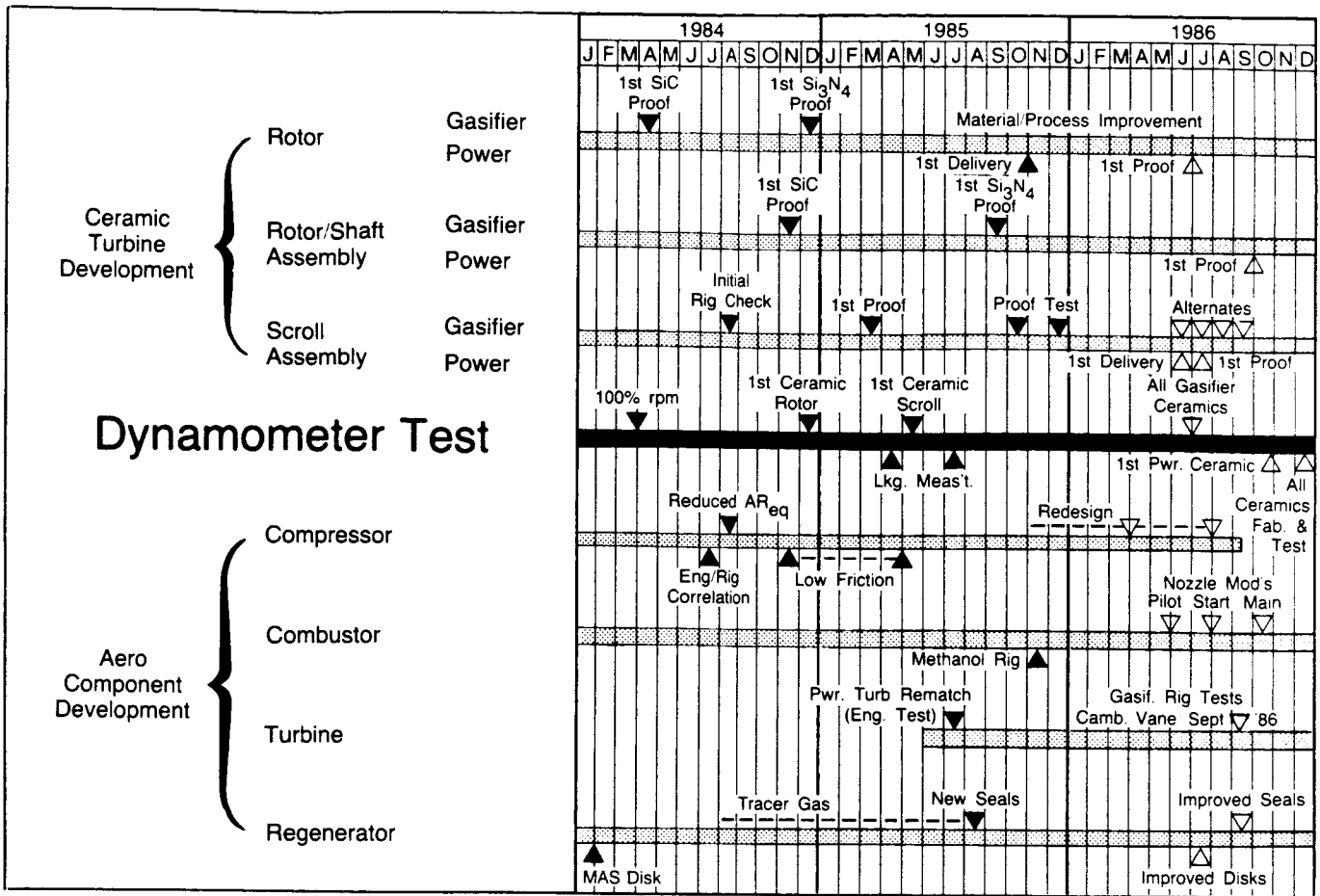
Table I.

AGT 100 project and design objectives.

<u>Project objectives</u>	<u>System design objectives</u>
18.1 km/l (42.5 mpg) in 1986 automobile	Comparable reliability and life
Meet 1986 emission standards	Competitive initial and life-cycle costs
Alternate fuels capability	Competitive accelerations Meet noise/safety standards

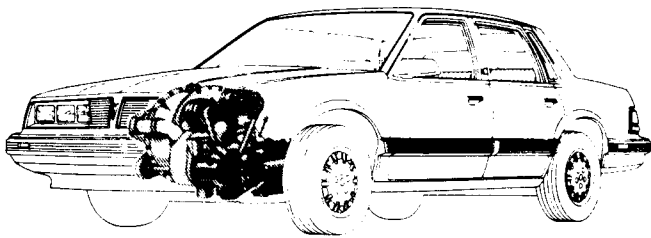
Initially, the project scope included the fabrication and chassis dynamometer testing of the engine,

ORIGINAL PAGE IS
OF POOR QUALITY



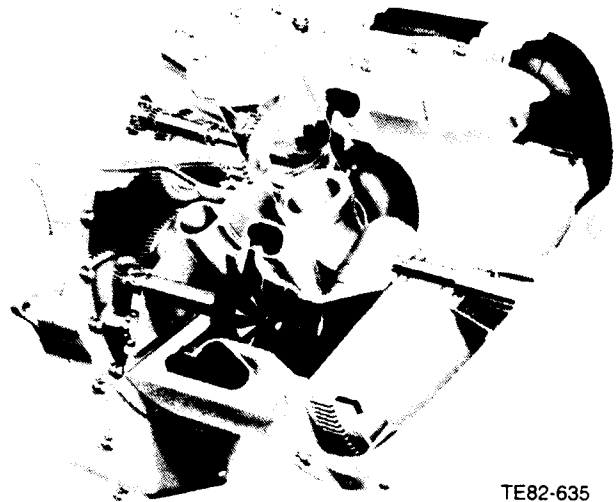
TE86-3010

Figure 1. AGT 100 program plan.



TE85-5461

Figure 2. AGT 100 engine in Pontiac A6000.



TE82-635

Figure 3. AGT 100 advanced gas turbine engine.

Most important is that the AGT 100 uses existing technologies for shafts, bearings, cases, control system, accessories, etc, and thereby provides a reliable test device for evaluating ceramic aerodynamic components.

Design goals of fuel economy and vehicle performance are shown in Figures 5 and 6. The fuel economy design goal is 18.1 km/l (42.5 mpg) for a compo-

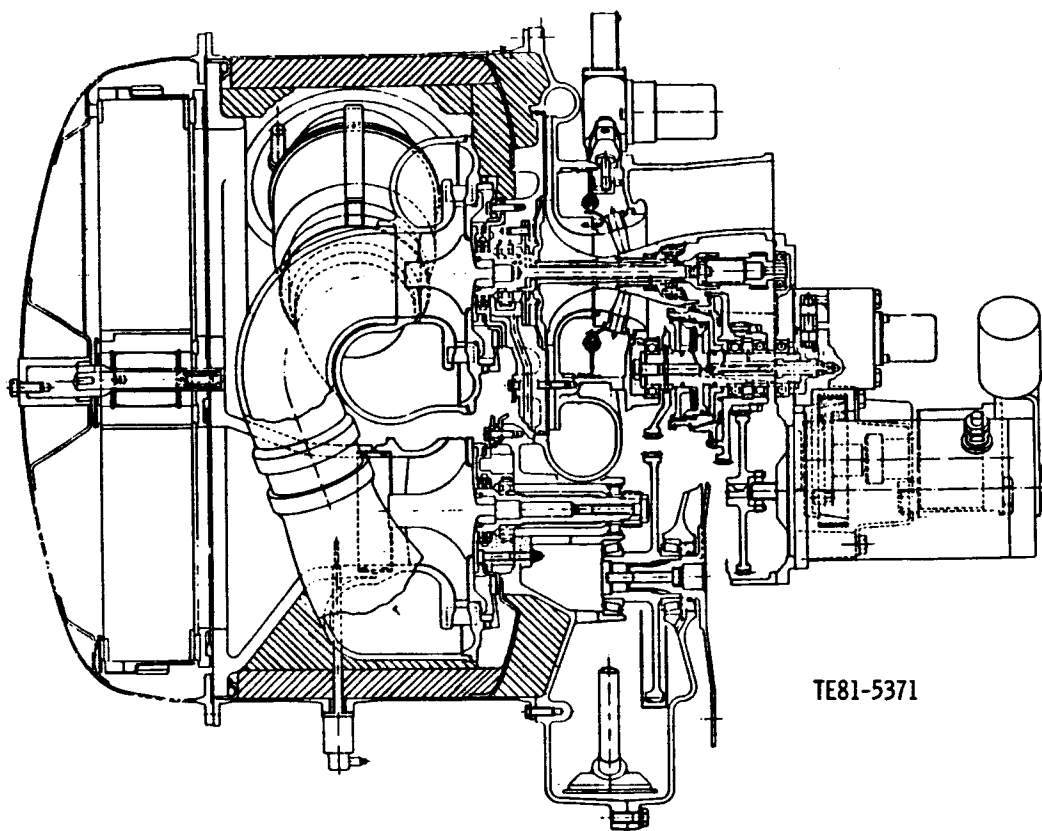


Figure 4. Cross section of AGT 100 gas turbine engine.

site driving cycle comprising a 55-45% mix of urban and highway cycles. Peak road-load fuel economy is over 25.5 km/l (60 mpg) at approximately 56 km/h (35 mph). Average driving cycle velocity is 43 km/h (27 mph). Figure 6 shows the velocity versus time relationship following a wide-open throttle acceleration from stop. The gas-turbine-powered vehicle is faster at all except the very early elapsed times.

The main development challenges in the program are in building small, high-performance gas turbine components and developing ceramic components for the required high engine cycle temperatures that are price competitive and capable of being produced in an automotive production environment. The AGT 100 ceramic components are shown in Figure 7.

Because of the small-size engine (0.35 kg/s [0.76 lbm/sec] airflow), extensive rig testing, outlined in Table II, is being performed in component development. A major ceramic component development program is being pursued, and the ultimate success of the engine depends on the success of this activity.

Table II.

Aerodynamic component rigs—status at end of 1985.

<u>Component</u>	<u>Builds</u>	<u>Hours</u>
Compressor	12	468
Combustor		
Development Rig	22	198
Scroll Rig	5	9
Turbines		
Gasifier	2	204
Power	1	26
Interturbine duct	3	239
Regenerator		
Cold side flow distribution	8	110
Hot side flow distribution	1	72
Seal leaf leakage	10	100
Hot simulator rig	84	577
Ceramic seal platform	10 units	57
		2060

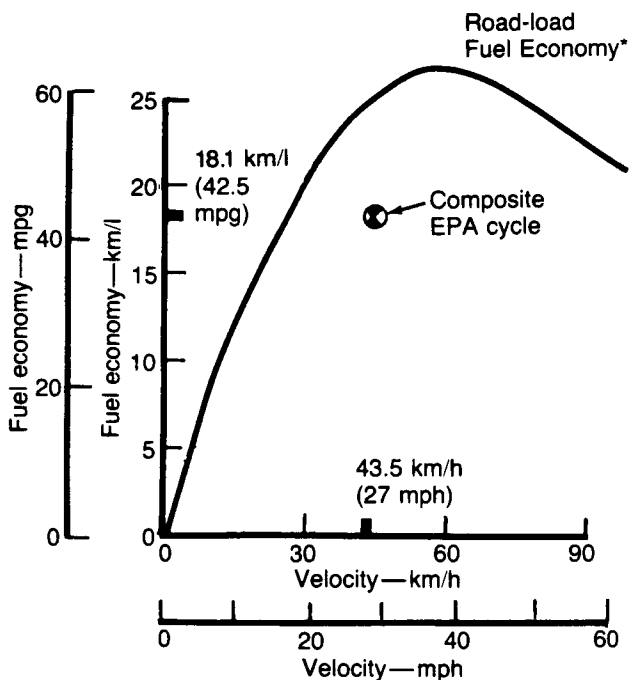
Mechanical development of the engine is being conducted in two essential phases. The first incorporates early available ceramic components with metal substitutes for those components requiring further development. This phase includes metal turbine rotors and engine operation at 1080°C (1976°F) turbine inlet temperature. The second phase includes engine demonstration of all ceramic component types at 1288°C (2350°F) turbine inlet temperature. The transition from the first to second phase will occur in steps as each new ceramic component becomes available.

A team concept is used in this project, with many of the team members being General Motors' divisions. Allison is the prime contractor and team leader with responsibility for the overall power train and controls. Pontiac Motor Division (PMD) has integrated vehicle design and cost analysis responsibility, and Delco Remy is responsible for the starter/boost system for the engine. The primary non-GM groups

on the team are Sohio Engineered Materials Company (formerly Carborundum), Corning Glass Works (CGW), and GTE Laboratories, Inc (GTE), who are involved in the ceramic effort.

This report is structured on a component basis (e.g., all work relating to the gasifier turbine rotor, including rig work and ceramic rotor development, is discussed as a part of the gasifier turbine section). Exceptions to this are functional areas that are not peculiar to any one major component: engine subsystems, cover structures, gearbox and power transfer, rotor bearings, shaft/seals, and secondary flow. Separate sections are presented for materials development and controls development.

Certain sections are omitted in this report because no effort was expended in those areas. These sections are identified in the Table of Contents to preserve continuity.



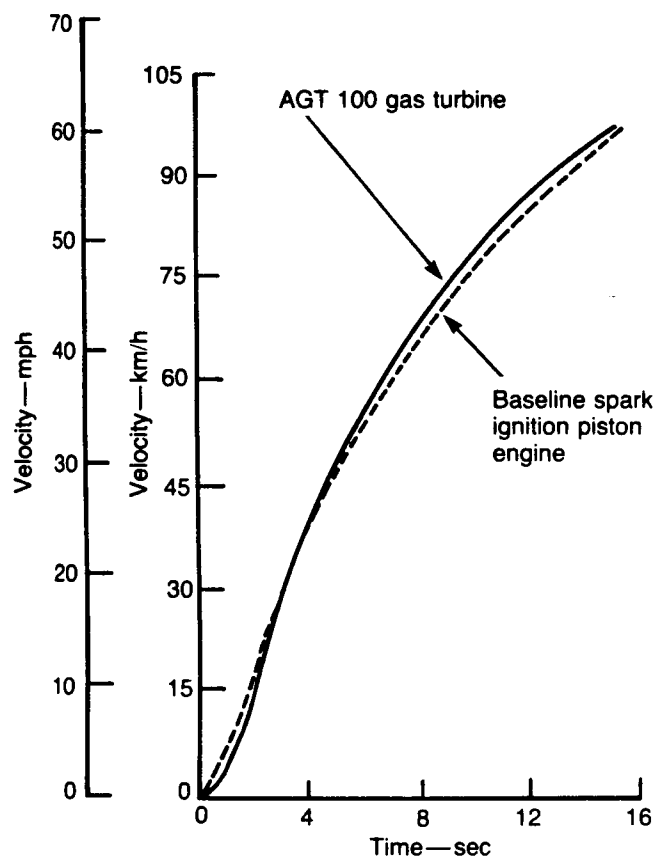
EPA Driving Cycle Fuel Economy*

	km/l	mpg
Urban	15.1	35.5
Highway	23.8	56.0
Composite**	18.1	42.5

*Based on diesel No. 2 fuel and 15°C (59°F) day

**55-45% mix

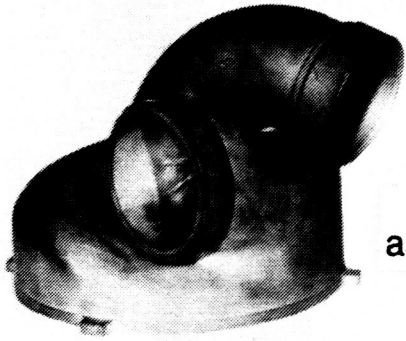
TE85-3025



TE85-3026

Figure 5. Design fuel economy goal for a 1364 kg (3000 lbm) automobile powered by AGT 100 gas turbine.

Figure 6. Design goal of vehicle wide-open throttle performance.



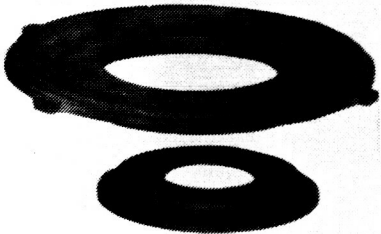
Scroll assembly



Turbine rotor

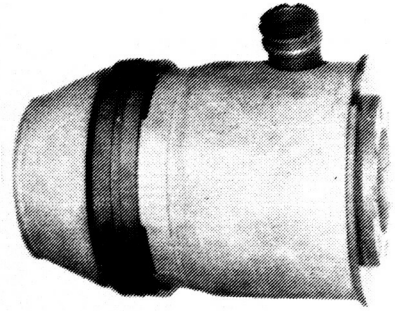


Turbine vanes

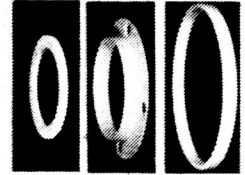


Scroll backplates

Combustor



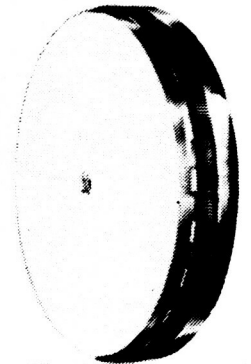
Seal



Thermal barriers



Regenerator seal platform and duct



Regenerator
TE82-5884

Figure 7. AGT 100 ceramic components.

ORIGINAL PAGE IS
OF POOR QUALITY

II. ENGINE DEVELOPMENT

2.2 EXPERIMENTAL ENGINE

2.2.1 Fabrication

No major metal engine part fabrication efforts were initiated during this period. The engine test program required the replacement of consumable and failed parts, parts rework for design modification, and fabrication of new parts to implement new designs.

Ceramic hardware procurement and development is a continuing effort. The largest 1985 procurement was obtained from Sohio and included rotors, vanes, and smaller quantities of scrolls, inner and outer backplates, combustor bodies, domes, dilution bands, and couplings. Kyocera supplied both bare and brazed rotors and shims. Other vendors included Norton, Corning, and Feldmuehle supplying scrolls, inner backplates, and shims, respectively.

During this reporting period work was released to fabricate ceramic power turbine scrolls and rotors. The only previous use of ceramic power turbine parts had been vanes and shims.

2.2.2 Experimental Engine Testing

During the previous reporting period, the engine test program had progressed through a total running time of 224 hr 31 minutes, including 156 hr 14 minutes of burn time.

The test program goal during the present reporting period continues to be the identification of engine-related mechanical and aerodynamic problems as well as engine component modifications necessary to improve engine operation, durability, and performance. An additional particular goal is to test ceramic components as they become available, gradually exposing them to the total engine environmental operating conditions.

During this reporting period a number of new ceramic parts were engine tested. Ceramic gasifier turbine rotors were tested in two different engine builds. Additionally, a ceramic gasifier turbine scroll with its associated ceramic parts (vanes and outer backplate) underwent testing in both the scroll rig and the engine.

During the current reporting period engine S/N 1 acquired an additional 123 hr 35 minutes (including 84 hr 05 minutes burning) of running time. Engine S/N 2 added 46 hr 53 minutes (including 35 hr 39 minutes of burning) of running time. Total running time accumulated in both engines at the end of this reporting period was 394 hr 59 minutes, 275 hr 58 minutes of which involved hot fire testing.

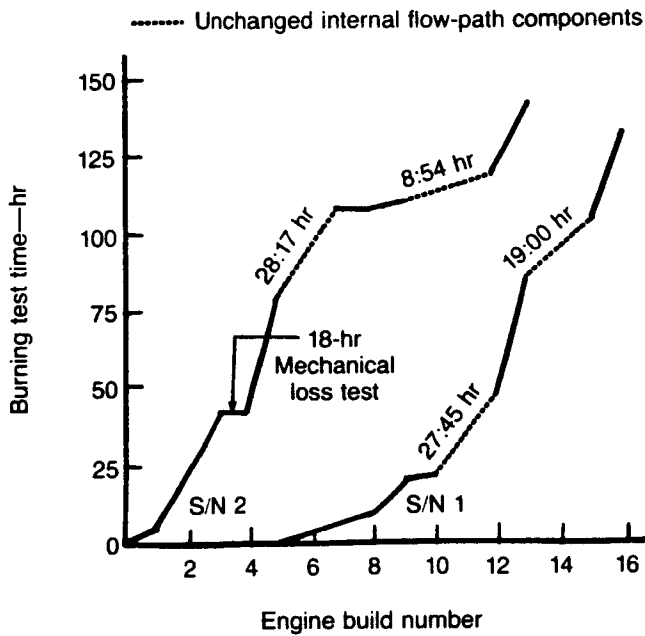
Figure 8 graphically displays the burning operating time, in a cumulative manner, for the two experimental engines.

Each build configuration and test accomplished in this reporting period is discussed chronologically in the following pages. Detailed discussion of the condition of component parts after test can be found in the report section discussing that component.

Engine S/N 1 BU13 and Test. There are several locations within the engine where working fluid leakage can occur. The sources of leakage, as schematically depicted in Figure 9, can involve flow paths to overboard, compressor discharge to gearbox, compressor discharge to turbine exhaust (regenerator seals), and burner inlet pressure to several points within the turbine flow path.

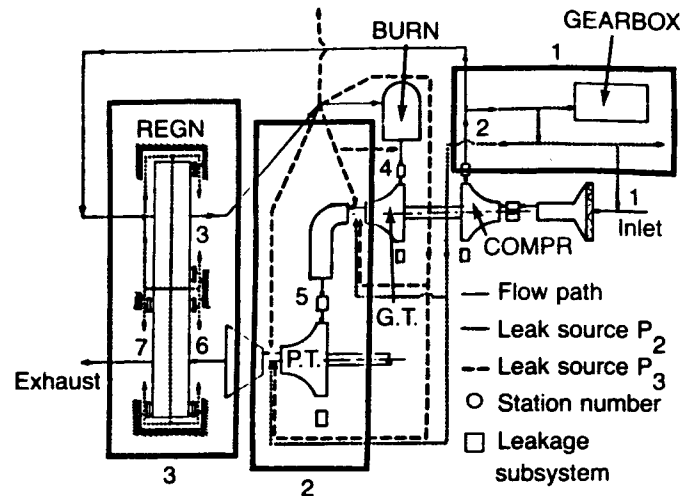
Consequently, a test program was initiated to investigate the magnitude of the working fluid leakage at each location. Two separate techniques were employed to investigate overboard leakage of the flow path. Prior to test operation, the engine inlet and exhaust lines are closed and the engine is externally pressurized to a low pressure level. Leakage at split-lines, instrumentation connections, and the gearbox vent are then checked and corrected if significant. Additionally, early in the test program a tracer powder was introduced into the engine airflow with the result that no significant external leakage was detected.

Leakage from the compressor discharge and burner inlet pressure airflow can occur at several places since the flow paths of both turbines (at which potential leakage can occur) are immersed in the burner inlet air cavity. The leakage test program was designed to address evaluation of many of these potential points of leakage and consisted of the following steps:



TE86-2470

Figure 8. Cumulative burning test hours of AGT 100 experimental engine.



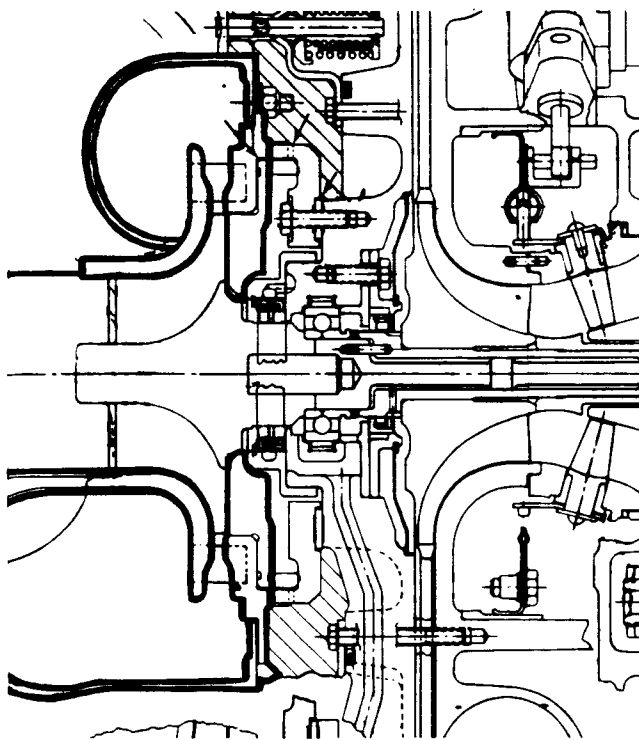
TE86-2472

Figure 9. AGT 100 leakage system.

1. turbine backface cavity cold bench test
2. turbine airflow rate calibration
3. hot engine run with tracer gas and flow calibrated turbines

The potential leakage points involving the turbine backface cavities are denoted in Figure 10. Leakage paths may exist at surfaces shown by the arrows at the gasifier turbine and at comparable locations at the power turbine. A test configuration was assembled using several engine parts with added inlet and outlet plugs at locations as depicted in Figure 11. Application of air pressure to the burner inlet cavity produced leakage that was individually measured by flow tubes at each turbine. The resultant leakage values are plotted in Figure 12 and compared to the leakage values used in the engine performance computation model. Both the power and gasifier turbine measured leakage rates determined from this cold test are lower than their predicted values used in the calculated engine performance model.

The second step in the leakage program involved flow calibration of the turbines. The flow calibration is used during engine testing to determine the actual flow at the turbines as compared with measured flow into the engine. A version of the engine configuration in which the regenerator and combustor were removed served as the test rig used for the flow calibration. Instrumentation normally present in the engine, i.e. temperature prior to the vane row and pressure taps at both the inlet and outlet to the vane row permitted the vane row to be calibrated as a nozzle orifice. The turbines were individually flowed while rotating to eliminate downstream asymmetric blockage. A separately measured flow was supplied from air pressure facilities for calibration purposes.



TE86-3011

Figure 10. AGT 100 gasifier turbine backplate air leakage sources.

The third step in the leakage test program involved hot testing in the engine using both the calibrated turbines and tracer gas. The leakage source and amount was determined by using an engine configuration in which air exiting the compressor was exhausted to the atmosphere and clean air was supplied to the regenerator. A schematic of this test setup is depicted in Figure 13. Airflow was measured at the following locations:

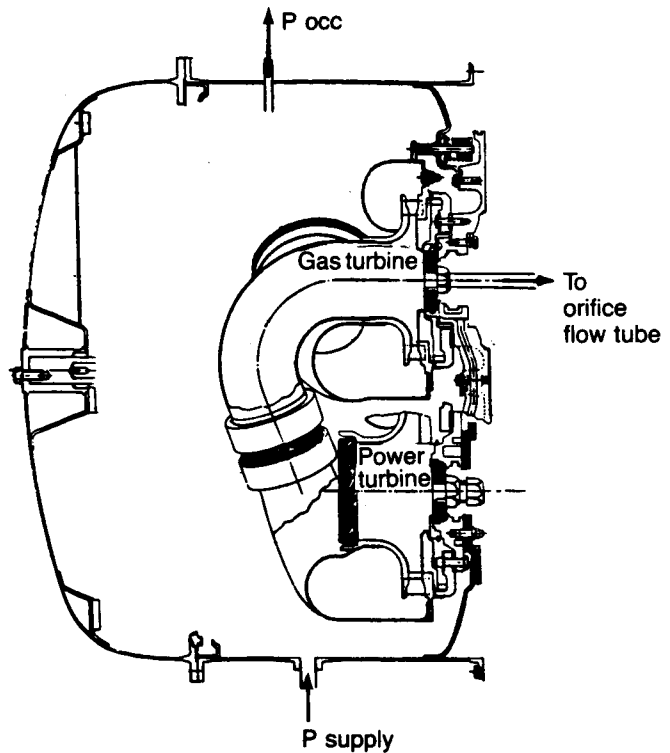
- compressor inlet
- compressor discharge
- regenerator inlet
- gasifier turbine nozzle (vane) row
- power turbine nozzle (vane) row

As a consequence flow leakage between stations in the same flow path could be determined.

In addition, CO_2 (generated in the combustor) and helium (injected at the compressor inlet) were used as tracer gases. Sampling probes allowed CO_2 concentrations to be measured at combustor discharge and engine exhaust. The CO_2 dilution determined from these two measurements is a measure of leakage flow into the flow path downstream of the combustor. Similarly, the injection of helium into the compressor permitted the measurement of He concentration at the compressor discharge (exhaust) and in the turbine exhaust. These measurements were used to determine the amount of air leakage from the compressor into the turbine flow paths.

The test engine configuration used for the airflow orifice and He tracer gas measurements included a flow splitter, which replaced the air tube leading from the compressor to the regenerator. Compressor air, as stated, was dumped overboard after measurement and test facility air supplied through a pressure regulator replaced the compressor air and fed directly to the regenerator.

Engine leakage (orifice airflow) testing was performed in the speed range of 40% to 80% of full speed of the gasifier shaft. Leakage was determined from the orifice flow pressure measurements made at the compressor inlet, compressor discharge, regenerator inlet, gasifier turbine, and power turbine. The results of these airflow measurements are presented in Figure 14. Leakage between the compressor inlet and compressor outlet was determined to be nearly negligible. Similarly, the measured leakage between the turbines is inconsequential. However, leakage between the compressor and gasifier turbine was found to be excessive, particularly at speeds below 65%. This leakage was primarily through the regenerator seals. At teardown, measurements showed the hot seal to be substantially warped. A design modification has been identified; refer to the regenerator section for details.



P_{occ} = Pressure, outer combustor case, virtually equal to pressure within the combustion case

TE86-2471

Figure 11. AGT 100 backface leakage test configuration.

In addition to leakage calculation by direct airflow measurements, two separate tests were performed to calculate leakage using tracer gases. The first test used CO_2 as the tracer gas. Additional CO_2 gas was injected into the combustor in a normal engine to raise the concentration level at the combustor exit to approximately 10%. CO_2 concentration was then measured at the combustor exit, power turbine exit, and engine exhaust. The second test used helium as the tracer gas. The first method inferred the amount of air leaking into a flow path containing carbon dioxide from the point-to-point dilution of carbon dioxide. The second method made use of the parallel flow paths separated by one or more seals. One flow path was seeded with helium, and the other was monitored for helium. The amount of helium detected in the unseeded flow path is nearly proportional to the leakage at the seals.

The regenerator rig was used to develop the seeding and sampling procedures for both helium and carbon dioxide prior to engine testing. Samples were introduced into evacuated gas cylinders for later evaluation with a mass spectrometer for the helium

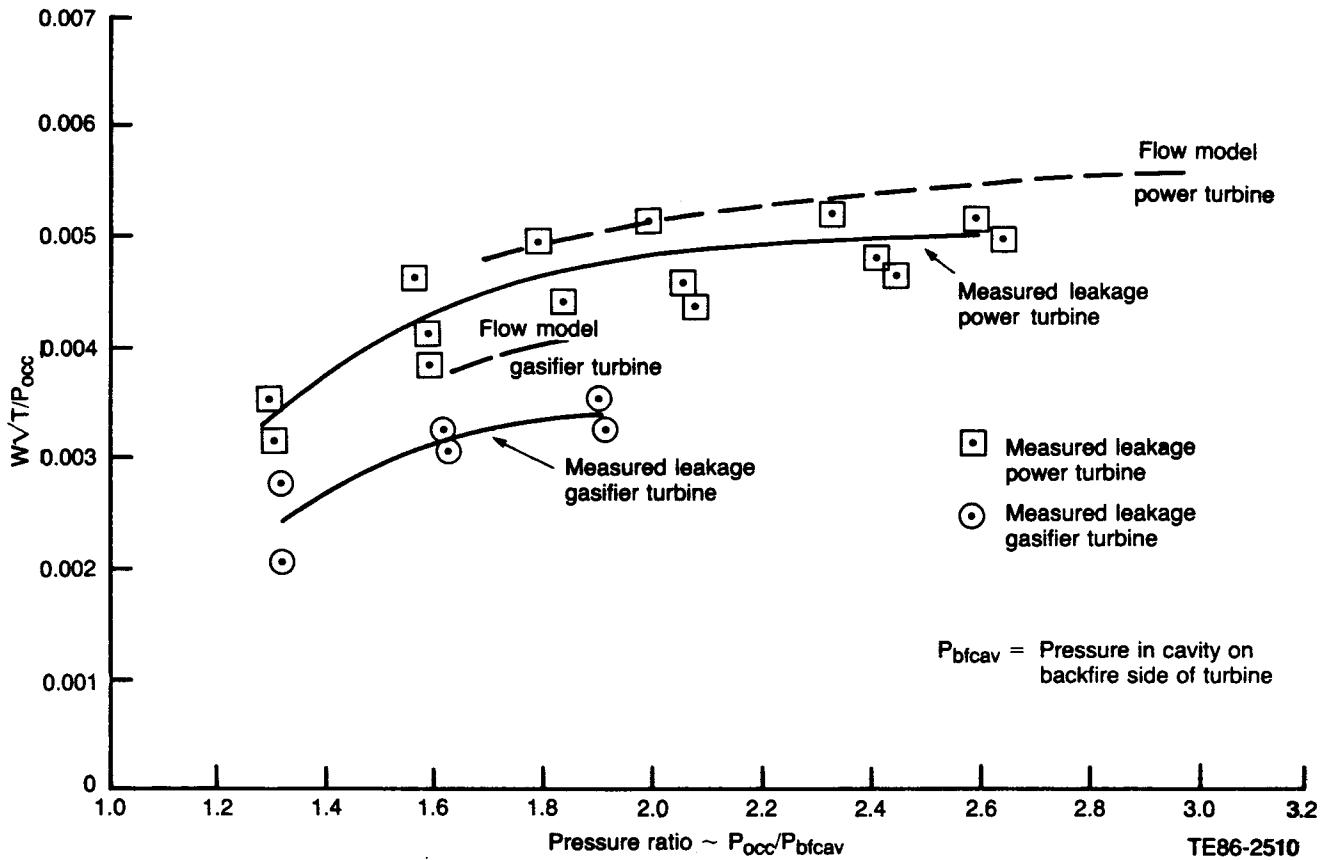


Figure 12. Turbine backface leak test.

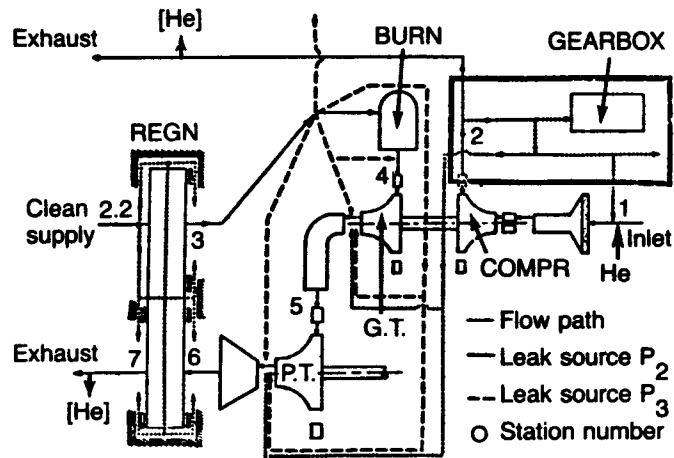


Figure 13. Schematic of leak detection flow path.

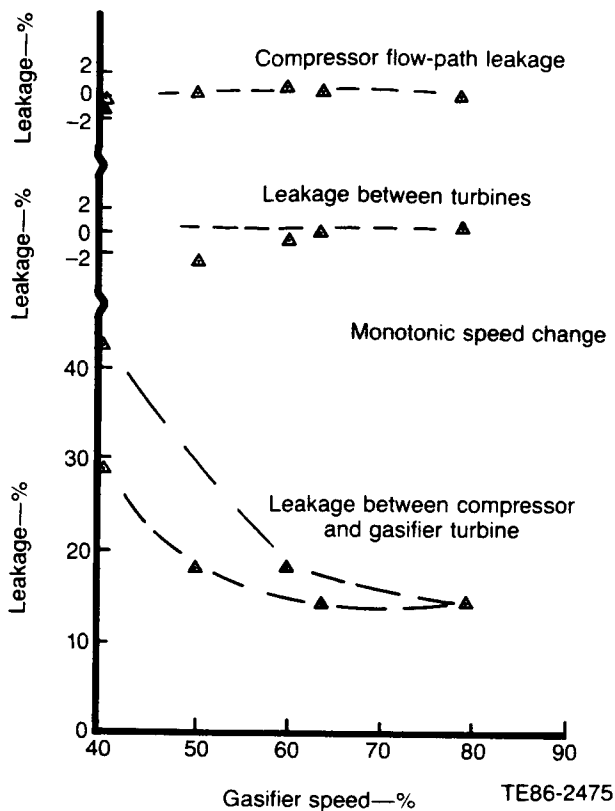


Figure 14. Leakage as determined by orifice measurements.

tests. The carbon dioxide levels varied from point-to-point and were measured on-line sequentially using a nondispersive infrared analyzer typically employed for emissions characterization. Seeding with both gases was tested by using manifolded pressurized cylinders of pure helium and carbon dioxide with flow controlled by pressure regulators.

The regenerator rig also provided a suitable system for verifying the carbon dioxide technique since the rig directly measures the leakage of a relatively large amount of air into a gas path with an elevated CO₂ level due to combustion. Development efforts for the carbon dioxide technique were begun on the regenerator rig in 1984 and continued through 1985. The regenerator rig results indicated a carbon dioxide dilution effect could indeed be measured, but the quantitative results were not always in agreement with direct leakage measurements, nor were they systematically related.

The first engine test attempted to quantify regenerator seal leakage and leakage at the turbine scroll and shaft seals. Valuable operational experience with the carbon dioxide measurement was gained in the engine tests, but the actual leakage numbers were suspect.

The gas sampling points, stations 4, 6, and 7 depicted in Figure 13, that were used for the carbon dioxide tracing tests, segregate the following leak paths:

- Station 4-6
 - gasifier turbine scroll splitline
 - gasifier turbine face seal
 - gasifier turbine shaft seal
 - gasifier turbine ceramic scroll spacer
 - gasifier turbine thermal isolator
 - interturbine duct piston rings
 - power turbine scroll splitline
 - power turbine face seal
 - power turbine shaft seal
 - power turbine ceramic scroll spacer
 - power turbine thermal isolator
 - one power turbine exhaust piston ring
- Station 6-7
 - one power turbine exhaust piston ring
 - regenerator seals

Carbon dioxide baseline data were obtained for two engine operating points, nominally 80/70 and 70/50 (%N₁/%N₂). At both operating points, data were taken with carbon dioxide seeding at the combustor to amplify the dilution effect. The concentration data are tabulated in Table III. These data showed increases in CO₂ concentration that are unrealistic for the system, and the data that were consistent showed a much smaller dilution effect than expected. The leakage results for the 80/70 operating point, reported in Table IV, reflect the inconsistencies in the raw data.

The data were reduced using a program that solves the combustion equation to determine the complete gas composition at station 4, the combustor outlet, and then calculates the leakage between stations 4 and 6 and 6 and 7 in terms of gasifier turbine inlet flow. The leakage equations were derived from the steady-state flow species conservation and continuity equations applied to the AGT 100 engine flow

Table III.

AGT 100 engine carbon dioxide tracer concentrations.

	Carbon dioxide volume concentration—%		
	Station 4	Station 6	Station 7
80/70 point			
Baseline	1.655	1.636	1.735
Seeded	11.41	12.00	11.94
Seeded	11.41	10.86	10.70
70/50 point			
Baseline	—	1.307	1.399
Seeded	10.54	10.49	10.21

Table IV.
Carbon dioxide test results—80/70 point.

	<u>Leakage—% gasifier turbine flow</u>		
	<u>Baseline</u>	<u>Seeded</u>	
Station 4-7 (total)	-4.6	-4.14	6.14
Station 4-6 (turbines)	1.15	-4.63	4.71
Station 6-7 (regenerator)	-5.75	0.49	1.43

path. The equations are applicable only for stable systems, and the inconsistent results are believed to be caused by unsteady conditions. The gases were sampled and analyzed from the three stations consecutively, possibly subject to a bias from drifting burner outlet temperature or unsteady seeding.

As a result of this experience, a differential non-dispersive infrared analyzer was purchased for future measurements. This instrument senses the difference in concentration between two sample streams rather than the absolute concentration level in one stream. The instrument removes the bias due to drifting conditions.

Helium was employed as the tracer gas for subsequent tests. These tests again used the split flow path engine configuration. The engine inlet was seeded with helium, and the flow was exhausted downstream of the compressor. Clean flow was supplied to the turbines through the regenerator inlet. Any helium measured in the exhaust had to leak from the inlet seeded flow path through the turbine shaft seals. Gases from stations 2 and 7, the compressor and exhaust outlet respectively, were sampled into evacuated gas cylinders and analyzed after the test using a mass spectrometer. The sample cylinders were presumed to contain sufficient gas to provide a reasonable time average of data. Data were obtained for two operating points, nominally 80/70 and 65/50 (%N1/%N2).

The major components of the engine gases sampled were determined to be helium, water, nitrogen, oxygen, and carbon dioxide. Mass spectrometer data for each of these were reduced to determine the overall composition at each station. The station 7 analysis was compared with the composition indicated for the engine exhaust based on conventional (Reference ARP 1256A) emissions measurements. The differences were relatively small.

The data were then reduced to leakage mass fractions using an equation derived from steady flow

species conservation and continuity equations. The averaged mass spectrometer data and resulting leakages are given in Table V. The accuracy of the measurements was estimated to be ± 12 -15% of inlet flow, and can probably be improved for future tests.

The Flow Systems Group estimated the turbine shaft seal backface leakage totaled 0.42% of the engine inlet flow, based on engine measured pressures and clearances for BU13. The agreement between these two independent leakage measures is good. The AGT 100 engine tracer gas measurements have demonstrated the potential of the helium leakage measurement technique for engines where parallel flow paths can be established.

A vibration investigation was also initiated on this configuration after vibration limits were reached in the plane of the compressor inlet at 84% of the maximum gasifier speed. The gasifier whip level at this speed was also relatively high. Three accels were performed from 60% to 84% gasifier speed. Vibration and whip data were recorded on magnetic tape for real-time analysis. The accels were performed with oil temperatures of 48°C (120°F) and 111°C (232°F) as well as power turbine speeds of 25% and 70%. A plot of one of these accels is shown in Figure 15. These variations had little effect on vibration levels.

Testing of engine S/N 1 was terminated after the engine was automatically shutdown due to an exhaust gas overtemperature. Data indicated that the regenerator disk had stopped rotating. Upon disassembly, it was found that the ring gear had separated from the disk due to overheating of the silicone interface material. The overheating was attributed to an incorrect reverse installation of the disk/ring gear assembly in the regenerator cover.

The gasifier rotor and bearing support assembly was removed from the engine and the rotor was check balanced while still installed in the support. Imbalance was determined to be 2.5 times the blueprint limit at the turbine bearing. Without disassembling the rotor, balance cuts were made on the tur-

Table V.
Helium test data and results.

	<u>Helium mole fraction</u>		<u>Turbine shaft seal leakage—% inlet flow</u>
	<u>Station 1</u>	<u>Station 7</u>	
	80/70 point	0.0872	0.000512
65/50 point	0.1244	0.000847	0.49

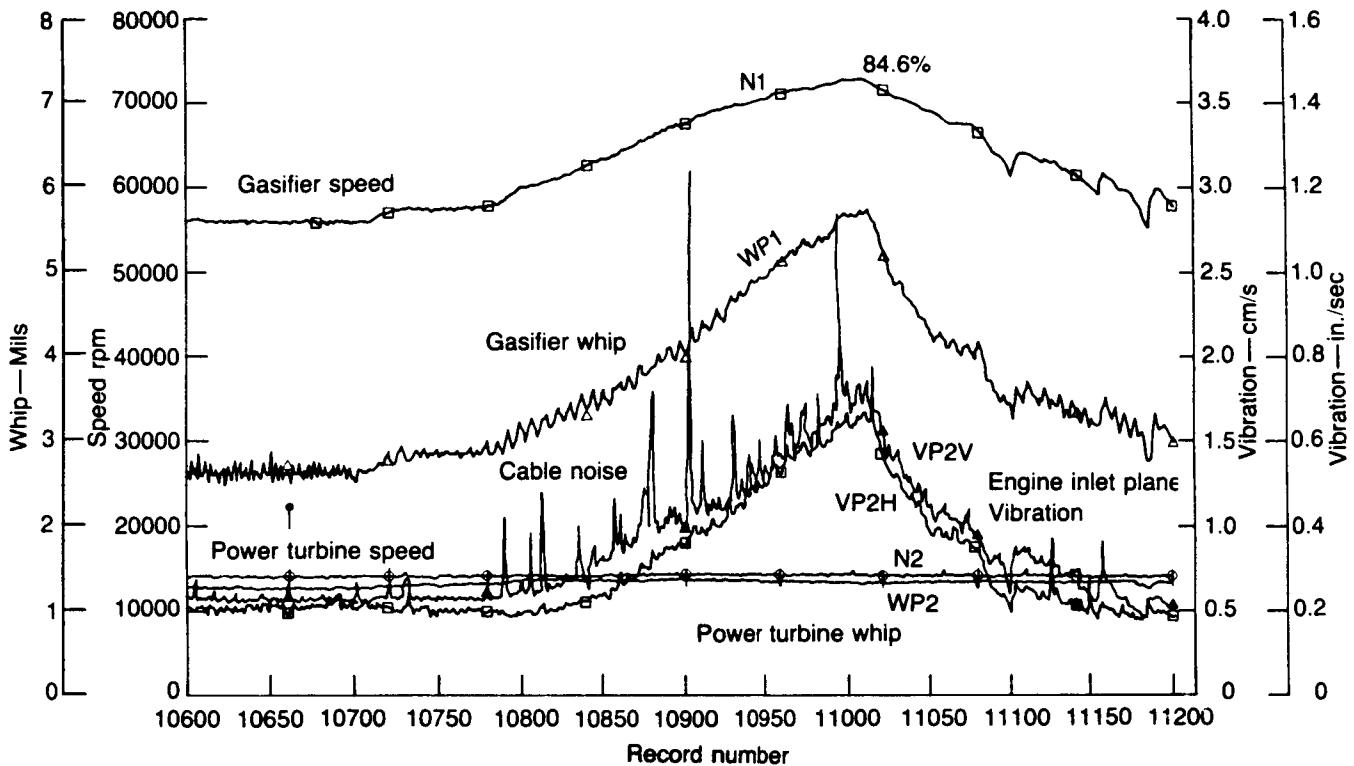


Figure 15. Typical vibration and whip during test of engine S/N 1 BU13.

TE86-2476

bine and impeller to bring the rotor to a near-perfect balance for the next engine build.

During the testing reported, S/N 1 engine accumulated 2 hr 28 minutes of burning time and an additional 2 hr 38 minutes of motoring. Total time on this engine following BU13 stood at 100 hr 23 minutes.

Engine S/N 2 BU9, BU10, and Test. S/N 2 engine BU9 was assembled to test a gasifier turbine ceramic scroll package. This ceramic scroll test was the first in an engine environment. The ceramic parts assembled into the engine are shown in Table VI.

All of the static structure intended to be ceramic and associated with the gasifier turbine was included in the engine assembly. All of these parts, except the last two listed, were included in the package that had been proof tested in the thermal shock scroll rig.

The engine test run was planned to consist of one start-stop cycle followed by inspection and then continued testing for five more cycles. The attendant thermal cycle was intended to expose the ceramic parts to a moderate level of temperature as the first step in the test series using temperatures of increasing severity.

The first engine test cycle is recorded in Figure 16. The burner inlet temperature, turbine inlet temperature, and gasifier speed are presented as a function of time for the complete start-stop cycle. The maximum temperature attained was about 943°C (1730°F.)

At the conclusion of this first cycle, the engine was removed from the stand for a limited teardown inspection of the ceramic parts. No problems were observed with this limited teardown.

The engine was then reassembled as BU10 and tested to increase the number of start-stop cycles to six. These thermal cycles were similar to the first one.

Complete teardown inspection revealed all of the parts to be unaffected by the test with the exception of the outer backplate. This part developed a crack running radially through a locating slot. An analysis of this test result is in section 9.2.2. The analysis identified the necessity for redesign and modification of both the outer backplate and the coupling between the gasifier and power turbine scrolls.

Engine S/N 2 BU11. Following the ceramic scroll test, the S/N 2 engine was reassembled (BU11) with

Table VI.
Ceramic parts.

Gasifier turbine scroll	α SiC	Sohio
Gasifier turbine outer backplate	α SiC	Sohio
Gasifier turbine inner backplate	BMAS II	Corning
Gasifier turbine vanes (18)	α SiC	Sohio
Gasifier turbine scroll shim	Zirconia	Feldmuehle
Interturbine coupling piston rings (2)	Refel SiC	Pure carbon
Dilution band (combustor)	α SiC	Sohio
Combustor body	α SiC	Sohio
Pilot flame holder tube	α SiC	Sohio
Interturbine coupling	Refel SiC	Pure carbon
Power turbine exhaust piston ring	Refel SiC	Pure carbon

a metal gasifier turbine scroll assembly. A test was initiated to investigate whip and vibration levels throughout the speed range. This engine build incorporated a gasifier assembly for which imbalance had been checked in the final assembled condition and was known to be within print limits. In all prior builds the assembly procedure did not ensure that final assembly was within specified balance limits.

During the initial test run of BU11 the power turbine shaft seized while rotating at 20% speed. A review of data indicated that excess pressure existed behind the power turbine inner backplate that in turn produced unbalanced pressure loads allowing the backplate to move into the turbine wheel. A rub pattern observed following teardown of the engine confirmed that this analysis was correct. Improper seating of the scroll locating shim was judged to be the cause. No significant damage was sustained.

Engine S/N 2 BU12 and Test. Engine S/N D-2 BU12 was configured with the second Sohio ceramic gasifier rotor to be tested in an engine. The goal of this build was to expose the ceramic rotor to a combustor lightoff followed by a thermal cycle designed to test the rotor to 60% N1 and 898°C (1650°F) turbine inlet temperature (TIT). The thermal cycle consisted

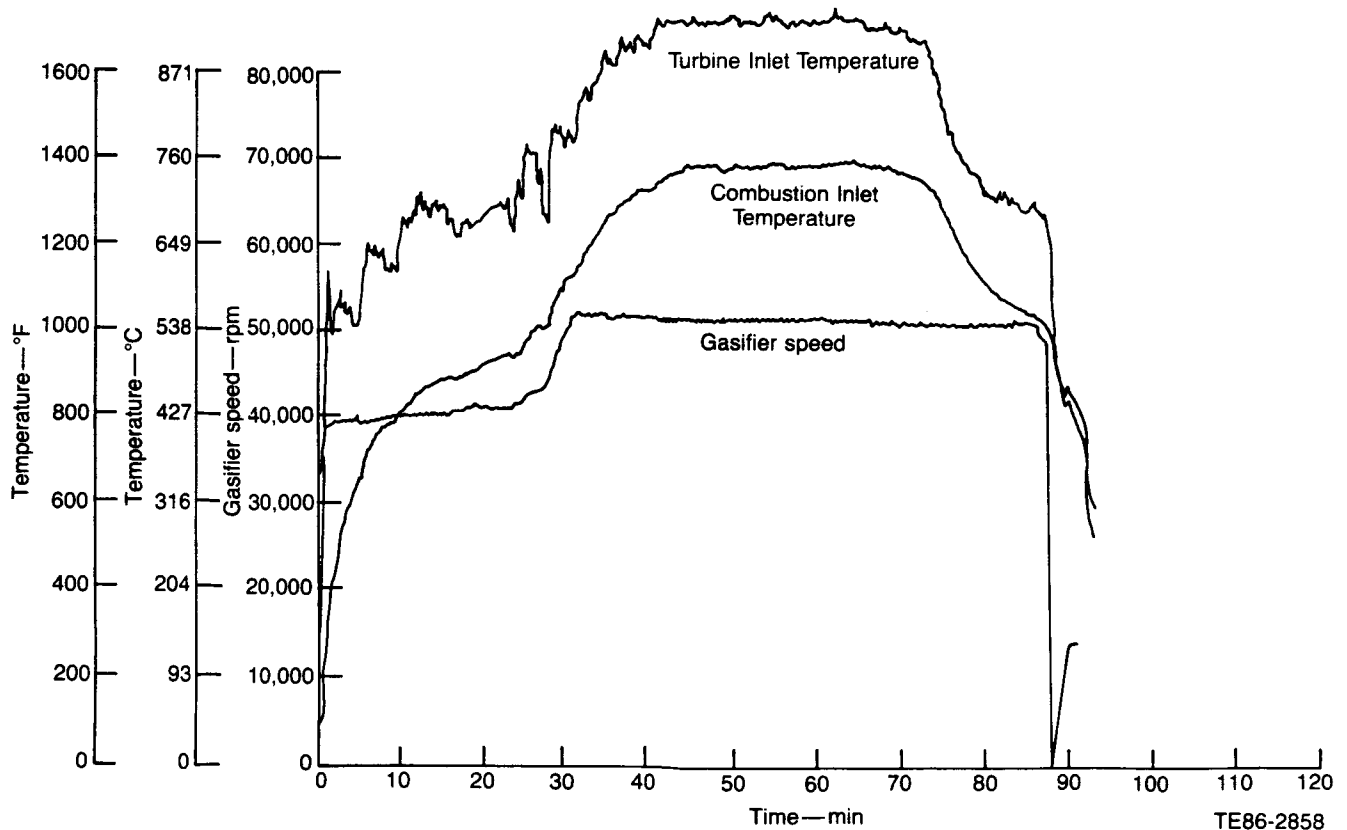


Figure 16. Ceramic gasifier scroll test cycle.

of the following:

- a cold motoring to 45% N1
- a soft lightoff controlling the TIT to 537°C-676°C (1000°F-1250°F)
- an increase in speed to 60% N1
- an increase in temperature to 898°C (1650°F)
- a 20-minute dwell period at 898°C (1650°F)
- a decrease in temperature to 648°C (1200°F)
- shutdown and inspection

The entire cycle was to last approximately 1 hr 30 minutes.

The cold motoring was completed without problems. A normal lightoff was performed but was shortly followed by an increase in gasifier shaft whip and a decrease in gasifier speed. This is illustrated in Figure 17. The temperature increase was due to the engine control box adding fuel to compensate for the drop in speed. Since the change in gasifier whip was small and the hydraulic starter torque appeared to be about the same throughout the run (implying no turbine damage), the rest of the test was completed. After a cool down period the engine was borescoped and the ceramic turbine inducer vane tips appeared to be missing. The engine was then disassembled and the inducer vane tips were confirmed as missing. The incident following the lightoff is believed to be indicative of the failure. The total test time during this

build was 1 hr 28 minutes burning and 12 minutes motoring. The total test time for this engine following this build was 118 hr 11 minutes burning and 46 hr 45 minutes motoring.

Engine S/N 1 BU14, BU15, and Test. S/N 1 BU13 engine was rebuilt as BU14 using a normal flow path configuration and a rebalanced gasifier rotor. This metal scroll and turbine buildup was for a functional test with special interest in engine vibration and power transfer clutch operation. Engine oil was changed at this time from Dexron II to MIL-L-23699.

A gasifier speed scan resulted in vibration limits again limiting speed to 84% N1. All vibration and whip levels were very similar to those recorded on the previous build.

Power transfer clutch testing consisted of a total of eight separate engagements, all of which were completed successfully. All engagements were performed at a gasifier speed of 60% N1. Four engagements were performed with the power turbine speed at 57% N2 and four more with the power turbine speed at 63% N2. Also, four of the engagements were made with the dynamometer controlling the power turbine in speed control and four with the dynamometer in load control.

Numerous combustor flameouts were encountered during testing along with erratic BVG move-

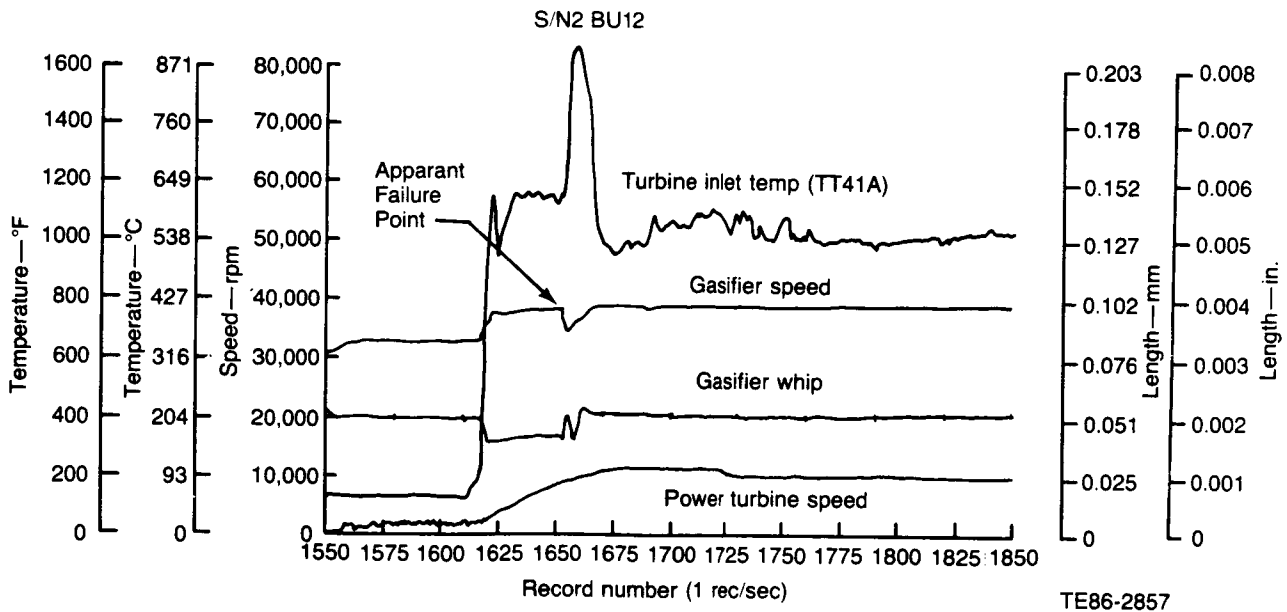


Figure 17. Apparent failure incident indication as depicted by data trace during test of ceramic rotor, S/N 2 BU12 engine test data.

ment. A flow check of the fuel metering valve controls revealed that the valve was flowing excess fuel, as compared to preset calibration, for a given voltage input. The presence of an engine speed sensor caused a reduction in voltage input to the valve thus reducing the fuel flow rate to that required to maintain the desired engine rpm. The consequence of this error in fuel flow as a function of valve input voltage was an incorrect calculation of the fuel/air ratio. The electronic control that computes the fuel/air ratio to the engine infers fuel flow rate through the valve from the current flowing to the metering valve controls. An incorrect fuel/air ratio calculation results, in turn, in an incorrect burner variable geometry (BVG) setting. Dialing in positive BVG bias allowed acceptable engine operation until the valve metering control was repaired.

Test hours accumulated by S/N 1 engine during this report period were 52 hr 46 minutes burning and 10 hr 17 minutes motoring. Total time on this engine now stands at 163 hr 59 minutes.

The engine was removed from the test stand to correct an oil leak and returned as BU15. After five minutes of further engine operation at 60% N1 speed, an incident of high vibration and high bearing temperature occurred. Engine teardown revealed a failure of the No. 1 position carbon seal. Only a small portion of the carbon from the two rings remained in the seal housing. The remaining carbon was broken in several pieces and badly oxidized. Failure of this seal allowed hot air to enter the bearing cavity causing the ball separator of the No. 1 turbine bearing to expand and rub the outer race. The carbon seal had accumulated a total running time of 55 hr 19 minutes when it failed. Higher temperature seals have been ordered.

Engine S/N 1 BU16 and Test. The first test of a Kyocera Si_3N_4 ceramic gasifier turbine rotor was designated for BU16 of engine S/N 1. The goal of this test was to expose the rotor to a combustor lightoff followed by a mild thermal cycle. Subsequent tests would involve thermal cycles of increasing severity.

The initial thermal cycle exposed the rotor to an inlet temperature of 898°C (1650°F) at 60% speed (51,750 rpm). A borescope inspection confirmed that the rotor was intact. Four more cycles were performed with cycle parameter changes as follows:

- Cycle No. 2—60% N1 speed, 898°C (1650°F) TIT (repeat of cycle No. 1)
- Cycle No. 3—70% N1 speed, 898°C (1650°F) TIT
- Cycle No. 4—70% N1 speed, 1079°C (1975°F) TIT (start nozzle)
- Cycle No. 5—70% N1 speed, 1079°C (1975°F) TIT (main nozzle)

Figure 18 shows a trace of the cycle No. 5 gasifier turbine inlet temperature and speed.

Approximately 20 hr of additional durability testing were performed on the rotor at 60% N1 speed and 1065°C (1950°F) TIT.

Test speed was increased to 70% N1 but was limited to this level because of an apparent high pressure in the power turbine backplate cavity. It was discovered on teardown, however, that the instrumentation lines had been mislabeled and the actual pressure was, in fact, normal.

Gasifier shaft whip reached a level of 5 mils at 70% N1 and 1079°C (1975°F) TIT. With a whip limit of 7 mils, it is believed that whip levels would have precluded all but a modest increase in speed during these tests.

Test hours accumulated by S/N 1 engine during this report period were 28 hr 51 minutes burning and 2 hr 38 minutes motoring. Total time on this engine now stands at 195 hr 28 minutes.

Engine S/N 2 BU13 and Test. Several instances of high engine vibration and gasifier rotor shaft whip have occurred during engine testing. Most of these instances have been at 83% to 88% of the maximum gasifier speed range. The characteristic of vibration as a function of speed has usually indicated a rotor unbalance to be responsible, although measured imbalance has usually been to specified limits or better as assembled.

Suspect causes of the vibration response include the casing mode, torsional coupling of the gear train lowering a rotor mode into the operating speed range, bottoming of the compressor bearing squeeze film damper thereby lowering the first bending mode of the rotor system to near 75,000 rpm, and finally, lack of rotor assembly balance. To investigate these possible causes an instrumented engine test was proposed. Instrumentation to monitor squeeze film deflection, case motion, rotor torsional response, coupling shaft whip, and shaft rotation/whip phasing were added to engine S/N 2 BU13.

The location of the extensive instrumentation used is presented in Figure 19. At location A a whip pickup was used to determine the squeeze film motion. Vibration pickups were mounted inside the case at locations B, C, and E to monitor the response of the support structure. An axial vibration pickup was located at F. Two whip pickups, 90 deg apart circumferentially, were also located at position C to measure coupling shaft response. A whip pickup was placed at D with a mark on the shaft to determine phase timing of the shaft. Torsional motion of the shaft was also determined with a pickup at E monitoring gear tooth passage.

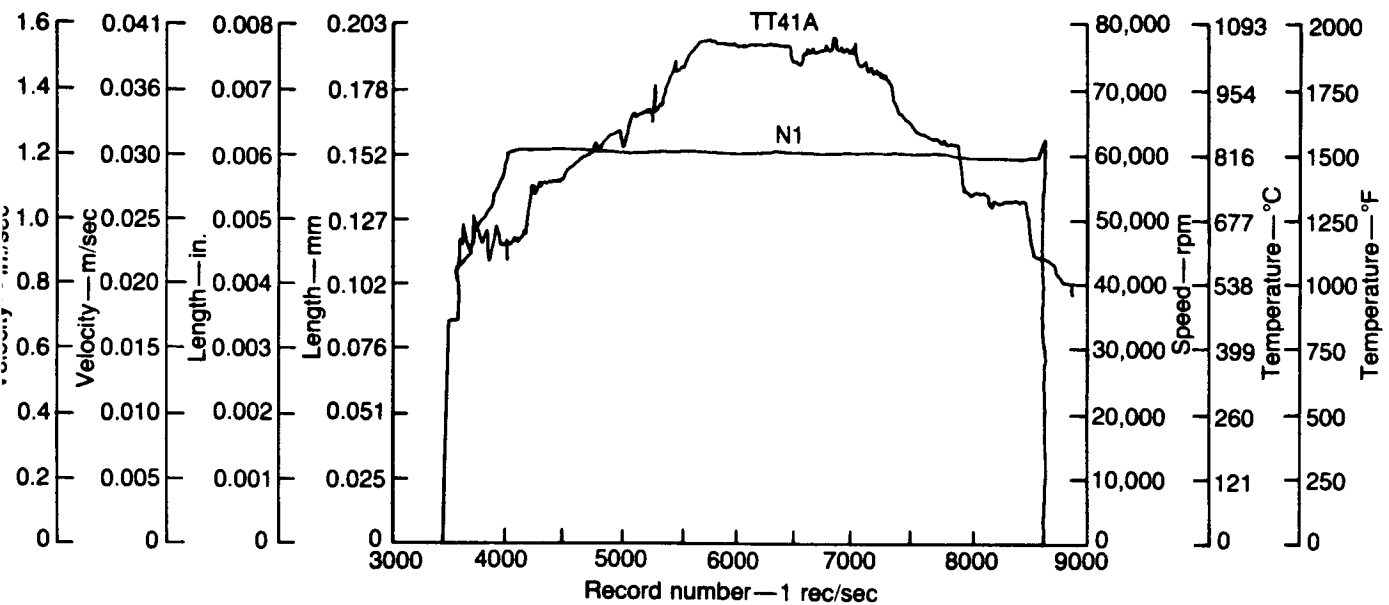
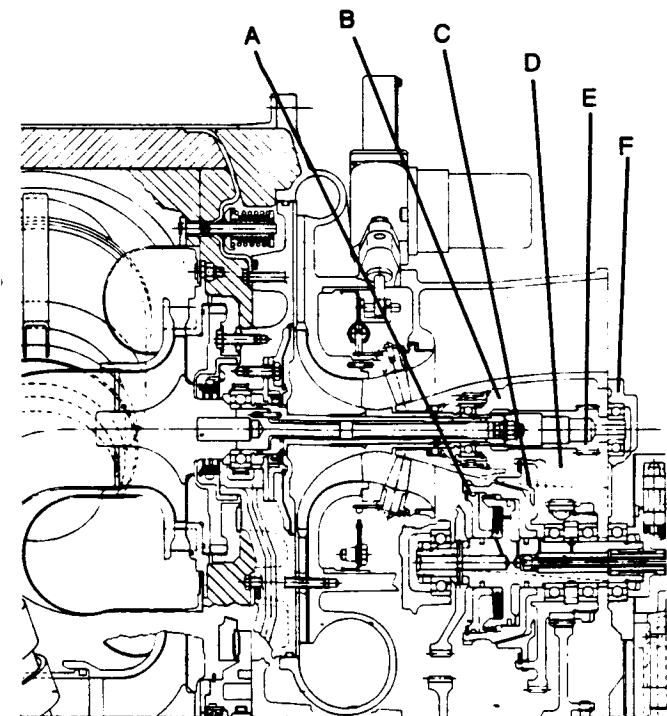


Figure 18. Typical data trace depicting test of Kyocera ceramic part.

TE86-2859



TE86-3012

Figure 19. AGT 100 engine cross-section showing locations of motion instrumentation.

Testing was completed in late November and included the following engine operating conditions. Slow accelerations and decelerations of the gasifier rotor were performed at constant power turbine rotor speeds of 15,000 and 45,000 rpm. Two oil temperatures of 48°C (120°F) and 40°C (230°F) were used during this transient running to determine damper oil viscosity effects on response. Temperature transients in TIT from 704°C (1300°F) to 982°C (1800°F) for gasifier speeds of 60%, 70%, and 85% of the maximum gasifier speed were also obtained to ascertain rotor response as a function of temperature. During engine operation all instrumentation response was monitored and recorded on tape for data reduction purposes.

Data reduction analysis was begun in December. Preliminary results of the data evaluation indicate that there is no casing mode participation as well as no torsional coupling of the system. Lack of significant phase change in the high response speed range also implies that a rotor mode is not being encountered. The squeeze film damper response is low until about 85% rpm and then increases rapidly in amplitude to the limit speed of 89% rpm. At this point the damper is not bottomed, based on the waveform of the response, and is operational although actual amplitudes are not known because of calibration problems. At the high response rotor speeds, the frequency of response for all pickups is synchronous.

Based upon these test results the response is considered indicative of rotor unbalance and is not significantly amplified by rotor or case modal participation. This unbalance is thought to be associated with a force couple introduced due to the close proximity of the turbine and compressor correction planes used in the low speed balance procedure and/or due to inherent bowing of the rotor system. Further analysis using rotor dynamics modeling, balance tests, and rotor measurements will be made to investigate corrective methods to lower the force coupling. An iterative three plane balance procedure employing the front compressor tie bolt location will be explored as a method of reducing the force couple. To determine what effect the spline interface and coupling shaft have on this response, and for possible trim balancing on the engine as required, modifications to the gearbox case will be made to allow an access plate so that indexing of the coupling shaft can be accomplished with minimum difficulty. The capability of performing a high speed balance of the rotor system will also be pursued with outside consultants.

In summary, the test program on this engine build included the first engine testing of the pilotless combustor configuration and additional testing of the power transfer clutch. The pilotless combustor configuration in principle replaces the pilot fuel nozzle arrangement with two centerbody located spark igniters. The original pilot fuel system is ignited by a single spark located at the pilot nozzle within the flame tube. For this test the pilot system was disconnected. Engine starts, using start nozzle flow, were successful with the new centerbody spark igniters over a start speed range from 25% to 38% gasifier speed. Subsequently, lean blowout data, using main nozzle flow, were obtained to determine if the presence of the centerbody spark ignition could be used to extend the main nozzle lean blowout limits at low burner inlet temperatures. As expected, the small amount of energy produced by the centerbody spark igniters proved to be insufficient to extend these lean blowout limits. The pilotless combustor remained in the engine for subsequent test programs during this build as its start characteristics are excellent.

The power transfer clutch was exercised during this engine test program. Clutch engagements and disengagements were made with the gasifier shaft initially rotating at 60% speed and the power turbine shaft rotating at various speeds from near synchronous down to 40%. All test results were routinely smooth and no problems were encountered.

Engine S/N 2 BU14. The primary purpose of this engine build was to increase test time of the gasifier ceramic scroll, turbine vanes, and inner backplate that had been previously tested in engine S/N 2 BU9

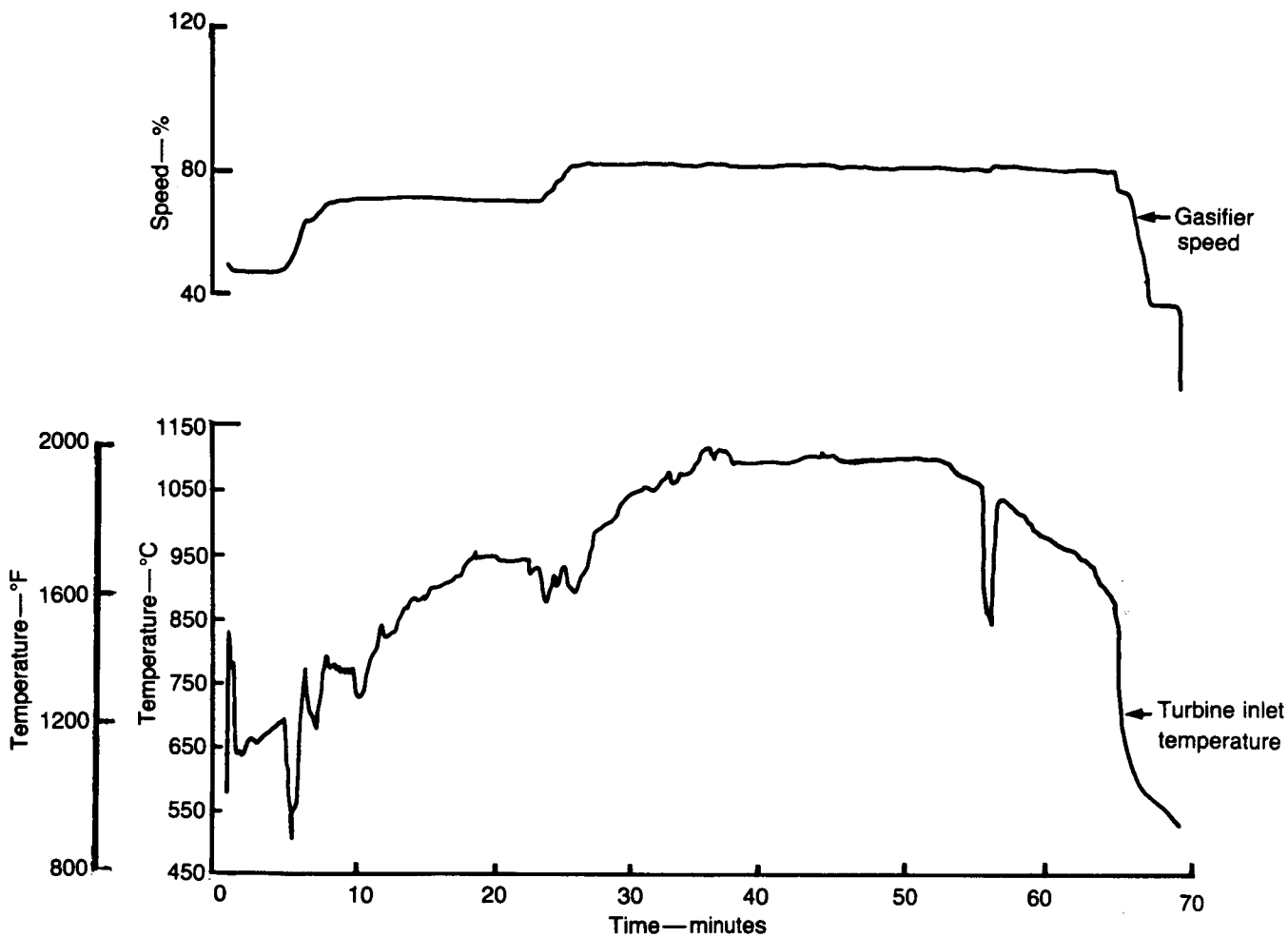
and BU10. That testing, six cycles of engine operation to 60% speed and 926°C (1700°F), resulted in a crack in the outer backplate of that package. The outer backplate was redesigned and this new design along with the original scroll, vanes, and inner backplate were bench tested in the scroll thermal shock rig to conditions of 80% engine speed and 1065°C (1950°F). These parts were then installed in engine S/N 2 BU14.

Two cycles of a planned six cycle test had been successfully completed by the end of the current reporting period. A typical cycle, as run, is shown in Figure 20. The temperature transients occurring at the 6th and 56th minute in the test cycle were unplanned excursions. These transients are caused by fuel flow variation due to inadvertent application of starter-motor torque. This torque is often used as an aid in controlling the engine speed. If starter torque is applied too rapidly during turbine inlet temperature changes at constant rpm, speed control sensors can cause a corresponding reduction in fuel flow and, hence, turbine inlet temperature. When the starter torque application rate is reduced, the fuel flow rate and the turbine inlet temperature recover to the desired values. Application of starter torque is generally controlled by the operator and, although the observed temperature transients are rare, they do sometimes occur. Analysis of the temperature transients in Figure 20, however, indicates that the rate of thermal cycling is less than that experienced at light-off or shutdown. Further, more severe thermal cycling has been experienced in the scroll rig with no observed subsequent damage to the ceramic scroll assembly. Thus, while the temperature transients are a potential source of thermal shock and are undesirable, no ceramic rotor or scroll assembly damage has been directly contributed to such excursions. Engine operational procedures and controls are constantly being revised to eliminate undesirable events such as those described above.

2.2.3 Performance Analysis

Performance analysis of the AGT 100 engine involved the initial development of a mathematical computer model containing component performance matching that accurately represented engine test performance obtained from engine D1 buildup 11. The program included a heat transfer model based on extensive analysis of the engine test results and a regenerator seal leakage model with characteristics substantiated by gasifier turbine flow calibration obtained from engine D1 buildup 13 hardware.

The computer model was subsequently updated to reflect demonstrated component performance and operational engine build clearances to be able to es-



TE86-2478

Figure 20. AGT100 engine S/N2 BU14 ceramic gasifier scroll test cycle.

estimate current engine performance. The model was recently updated to reflect projected (December 1986) component performance and engine build clearances to permit estimation of end of program engine performance.

Table VII presents the maximum power engine performance and Environmental Protection Agency (EPA) combined cycle fuel economy estimates for the current engine and projected end of program engine

configurations. The reference power-train design (RPD) engine is included for reference. Table VIII details the component characteristics for the current and projected end of program engine configurations. The two engine configurations projected for the end of program represent two different levels of component characteristics and improved quality as defined in Table VIII.

Table VII.

AGT 100 maximum power engine performance and EPA combined cycle fuel economy.

	<u>Current</u>	<u>End of program (December 1986)</u>	<u>RPD</u>	
<u>Engine</u>				
Turbine inlet temperature (TIT)—°C (°F)	1080 (1976)	1204 (2200)	1204 (2200)	1287 (2350)
Maximum power—kW (HP)	31.3 (42.1)	49.2 (66.0)	54.5 (73.2)	74.5 (100)
Specific fuel consumption (SFC)—mg/W.hr (lb/hp.hr)	369 (0.607)	299 (0.492)	259 (0.427)	197 (0.325)
<u>Components</u>				
Compressor, W_a —Kg/sec (lb/sec)	0.312 (0.687)	0.347 (0.766)	0.338 (0.745)	0.345 (0.760)
R_c	4.35	4.89	4.5	4.5
η —%	75.1	77.6	80.1	82.8
Gasifier turbine, η —%	78.4	78.3	81.5	84.6
Power turbine, η —%	85.4	86.4	86.4	86.7
Regenerator, η —%	91.3	91.0	91.0	94.7
Leakage—%	5.2	5.0	4.4	5.2
<u>Parasitic losses</u>				
Engine leakage—%	4.6	4.4	4.2	2.5
Cycle, ΔP —%	14.5	19.0	16.5	14.1
Mechanical loss—kW (HP)	7.4 (10.0)	7.7 (10.3)	7.8 (10.4)	5.8 (7.8)
Heat rejection—W(Btu/min)	10,761 (612)	8633 (491)	5785 (329)	1670 (95)
<u>Fuel economy, DF2</u>				
EPA combined cycle— km/l (mile/gal)	8.3 (19.5)	10.1 (23.7)	11.6 (27.3)	18.1 (42.5)

Table VIII.

AGT 100 engine component characteristics.

	<u>Current</u>	<u>End of program (December 1986)</u>	
TIT—°C (°F)	1080 (1976)	1204 (2200)	1204 (2200)
Compressor	Type 1A	Type 1A and steel shroud	New design
Gasifier turbine	Metal	Ceramic	Ceramic
Vanes	as designed	as designed	Cambered design
Axial clearance—mm (in.)	1.321 (0.052)	0.940 (0.038)	0.965 (0.038)
Radial clearance—mm (in.)	0.406 (0.016)	0.330 (0.013)	0.330 (0.013)
Power turbine	Metal	Ceramic	Ceramic
Axial clearance—mm (in.)	1.24 (0.049)	0.965 (0.037)	0.940 (0.037)
Radial clearance—mm (in.)	0.457 (0.018)	0.381 (0.015)	0.381 (0.015)
Regenerator			
Leakage			
Part power	Rising ⁽¹⁾	Flat ⁽²⁾	Flat ⁽²⁾ -0.5%
Temperature limit—°C (°F)	982 (1800) (not reached)	982 (1800)	982 (1800)
Engine leakage			
Shaft seal clearance—mm (in.)	0.051 (0.002)	0.0406 (0.0016)	0.0406 (0.0016)
Heat rejection	(3)	(4)	(5)

(1) D1 BU13 characteristic based on D1 BU13 gas generator turbine flow calibration

(2) Best rig demonstrated characteristic

(3) D1 BU11 insulation quality

(4) (3) + compressor scroll to gearbox insulation, improved T₃ plenum insulation fit, gas generator and power turbine heat shields

(5) (4) + improved T₃ plenum insulation quality, isolated oil drain tubes, T₃ plenum to combustor coolant insulation.

III. COMPRESSOR DEVELOPMENT

3.1 COMPRESSOR AERODYNAMIC DEVELOPMENT

In the current reporting period, compressor development activities were dedicated to testing a double splitter Type 1A impeller and to comprehensively reviewing the aerodynamic data accumulated on both rigs (CX-40 and CX-53) involved in developing the AGT 100 compressor. As a result, the CX-53 rig has been modified to limit the heat recirculation through the shroud. A new impeller design has been initiated to obtain higher compressor efficiency.

3.1.1 Double Splitter Impeller Test

CX-53 rig test build 6 (BU6) was performed during the early portion of 1985. This test was an attempt to determine the trade-off between increased impeller blade loading and blade surface friction reduction. The double splitter impeller was a reworked Type-1A impeller originally tested in 1984 (CX-53 BU3). The Type 1A impeller demonstrated a measurable gain in high speed efficiency compared to the original engine impeller. The detailed performance maps of the

Type 1A impeller, obtained during rig testing, were presented in last year's annual report. Although the gain was considerable it was short of the design goal and the impeller modification was judged insufficient to justify replacement costs of the original impeller in both of the engines. Consequently, the Type 1A impeller was used as the test piece to make the double splitter impeller. The rework involved cutting the original Type 1A splitters to 60% of the meridional distance while every other full length blade was cut back to the original splitter location of 30% of the meridional distance. Both sets of splitter leading edges were blended to reduce the abrupt change in blade thickness blockage produced by the modifications. This yielded an impeller with eight full blades, eight primary splitters, and 16 secondary splitters. A photograph (Figure 21) of the original and the double splitter impellers illustrates the rework performed. The Type-1A impeller incorporated identical blade shape but reduced blade thickness as compared to previous AGT 100 impellers. Previous rig tests (CX-40 BU5) incorporating both reduced blade thickness and exit height (reducing diffusion) indicate that these modifications improve performance. The impeller flow paths (Figure 22) depict the narrowed exit blade height and the double splitter locations.

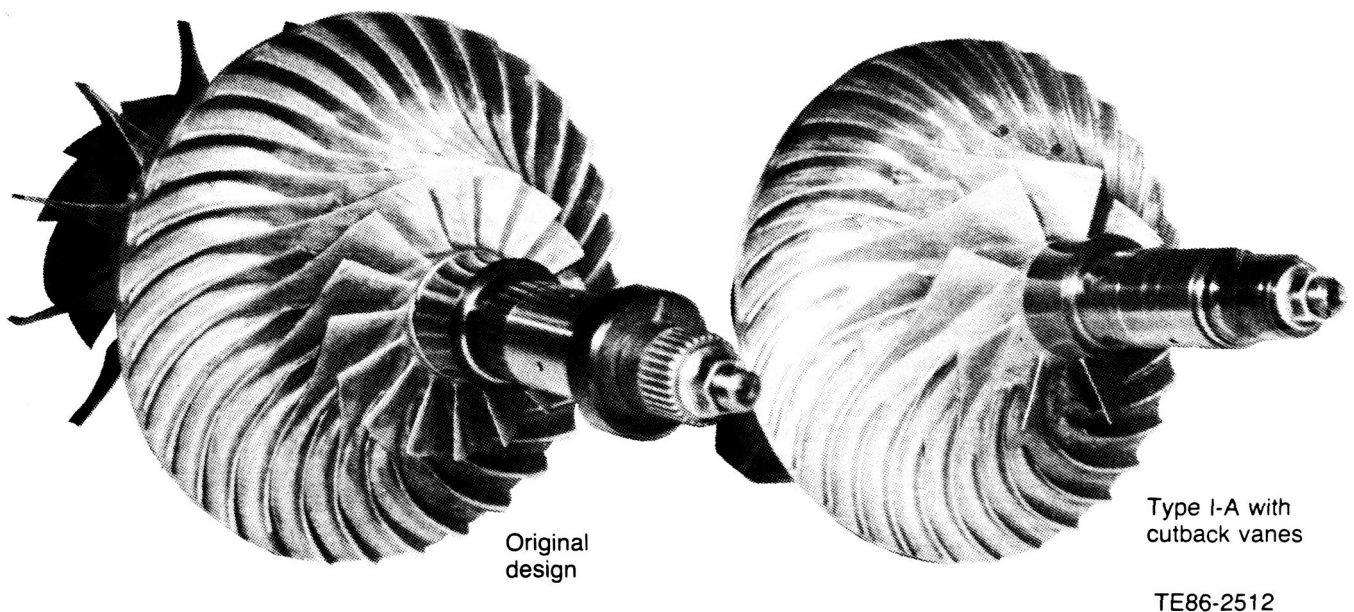


Figure 21. Comparison of original type 1A and double-splitter reduced blade friction compressor impellers.

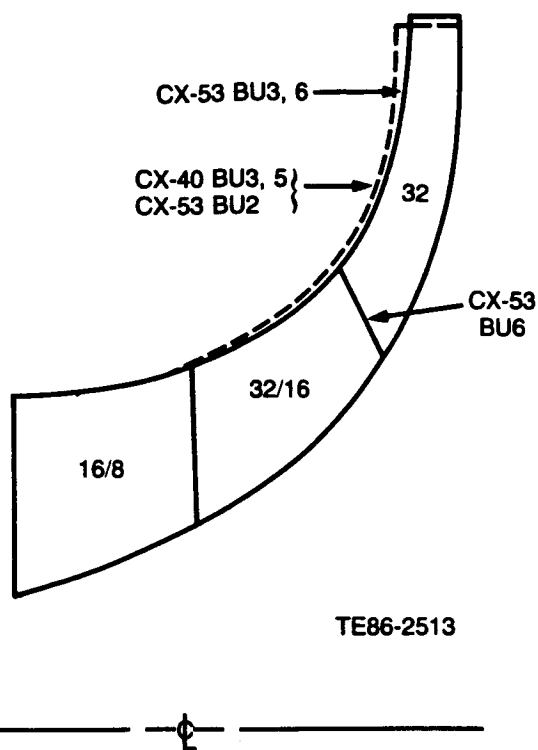


Figure 22. Meridional flow path comparison of different compressor blade shapes.

The performance of the double splitter impeller (BU6) is compared to that of the Type-1A impeller (BU3) in Figure 23. Although the high speed (100%) flow capacity of the modified impeller increased by 3.5%, its efficiency levels as compared to the Type-1A were reduced at all speeds. The modified impeller's peak efficiencies, for example, were lower than BU3's (Type-1A) by 2 to 1.5% at 50 to 100% speed. The aerodynamic increase in losses incurred by increased blade loading, through reduction of the blade solidity, is greater than the reduction in loss through lower surface friction. An analysis of the internal pressure measurements (described later) confirmed this conclusion.

CX-53 BU6 was also the first test of the AGT 100 compressor to use dynamic clearance probes. The probes, a special miniature design, operated flawlessly with a high degree of accuracy. This was confirmed by post-test rub patterns. The readings from these probes are presented in Figure 24. Data depicted in the figure indicate a 0.010 cm (0.004 in.) discrepancy between the two tip probes at design speed. This is indicative of the impeller cocking at high speeds. The two probes measuring the knee clearance were in agreement, indicating that clear-

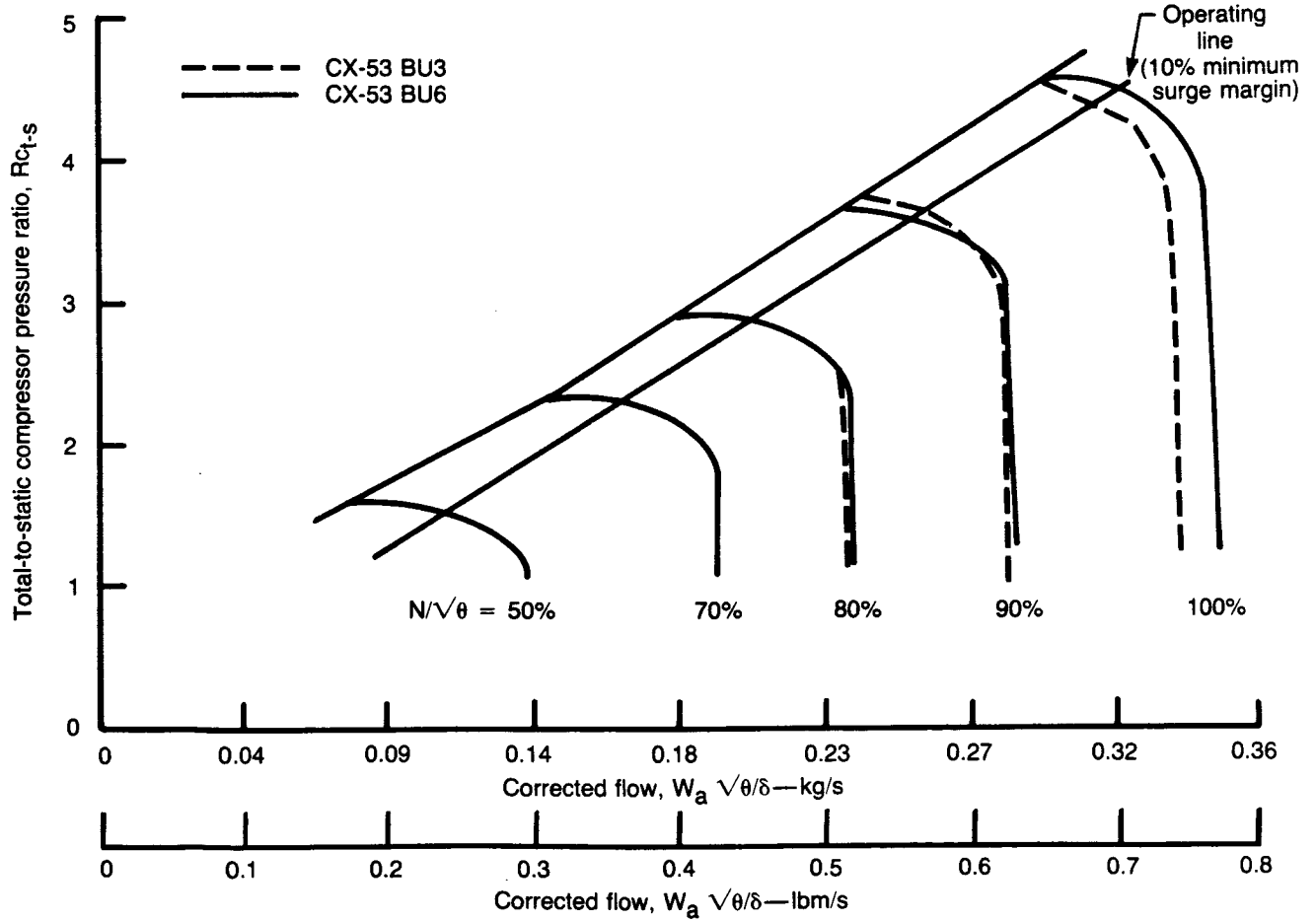
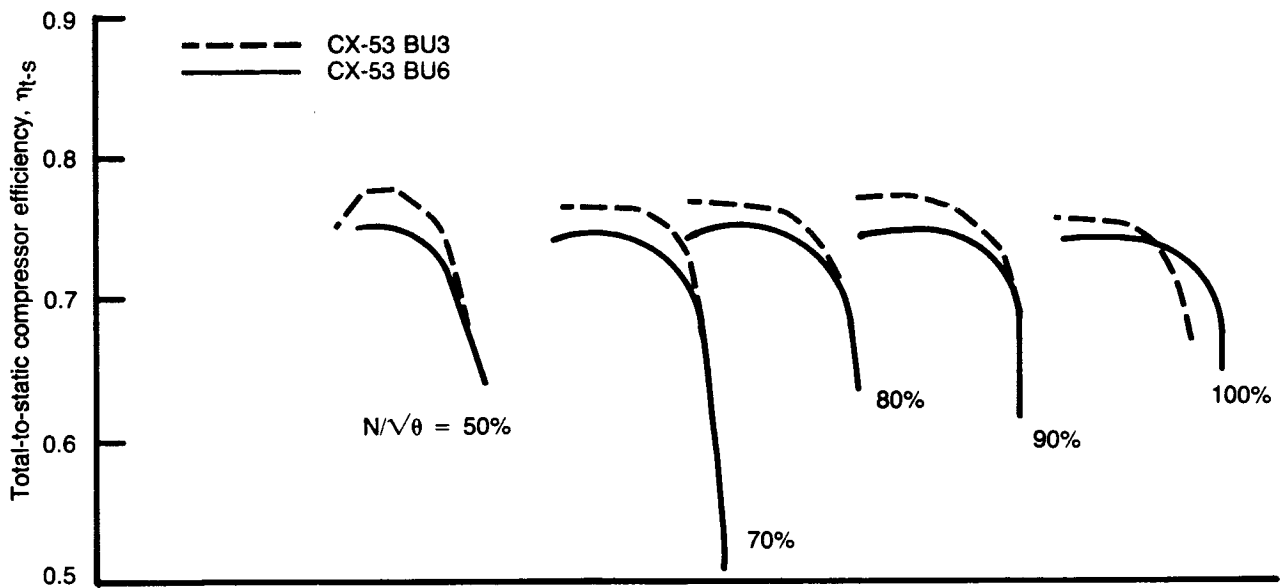
ance discrepancies in the knee region are less dependent on speed than clearances at the impeller tip. The probes do, however, indicate that the knee clearance is about 0.015 to 0.018 cm (0.006 to 0.007 in.); the exact amount of clearance depends on loading, especially at high speeds. The knee clearance data indicates an increase in clearance (approximately 0.0089 cm [0.0035 in.]) upon loading from choke to surge at design speed.

The modified compressor was also tested to investigate the effects of clearance and variable inlet guide vane (IGV) settings. The compressor was first retested at 0 deg IGV angle and at 50%, 70%, and 80% corrected speeds after closing the cold build clearance by 0.010 cm (0.004 in.). This test was limited to 80% corrected speed to prevent hardware damage caused by expected rub at higher speeds. The IGVs were closed to 40 deg and the lower three speed lines retested. The results of both reducing clearance and prewhirl as compared to the baseline operating characteristics of the impeller are presented in Figure 25. The results indicate a substantial improvement in test performance, 2% at both 50% and 70% corrected speed and 1.3% at 80% corrected speed, respectively, above the baseline impeller, as a result of both reduced clearance and prewhirl. The effects of the clearances measured on CX-53 BU6 on stage performance are discussed in detail in a later section.

In summary, the testing of CX-53 build 6 proved beneficial in determining the trade-off of impeller blade loading and friction, in proving the viability of the miniature clearance prober, and in demonstrating the importance of clearance and IGV setting angle on performance. Even on the small size of the AGT 100 compressor, reducing friction at the cost of blade loading results in a significant loss in compressor efficiency (1.5% to 2%).

3.1.2 Comprehensive Data Analysis

A comprehensive analysis of all compressor data obtained on the AGT 100 compressor rig was undertaken during the last reporting period. The goal of this effort was to determine the modifications/re-design required to improve the compressor performance. The analysis concentrated on the data obtained when the rigs were considered to be in a steady-state heat transfer operating condition. Both early (CX-40) and later (engine hardware, CX-53) rig data were reanalyzed. Although the rigs were thermally stabilized, steady-state heat recirculation substantially affects compressor performance. Recommendations resulting from this study, discussed in the following section, are to isolate the impeller from



NOTE: All lines are a result of data points

TE86-2515

Figure 23. Overall compressor performance for CX-53 BU6 and CX-53 BU3 rigs.

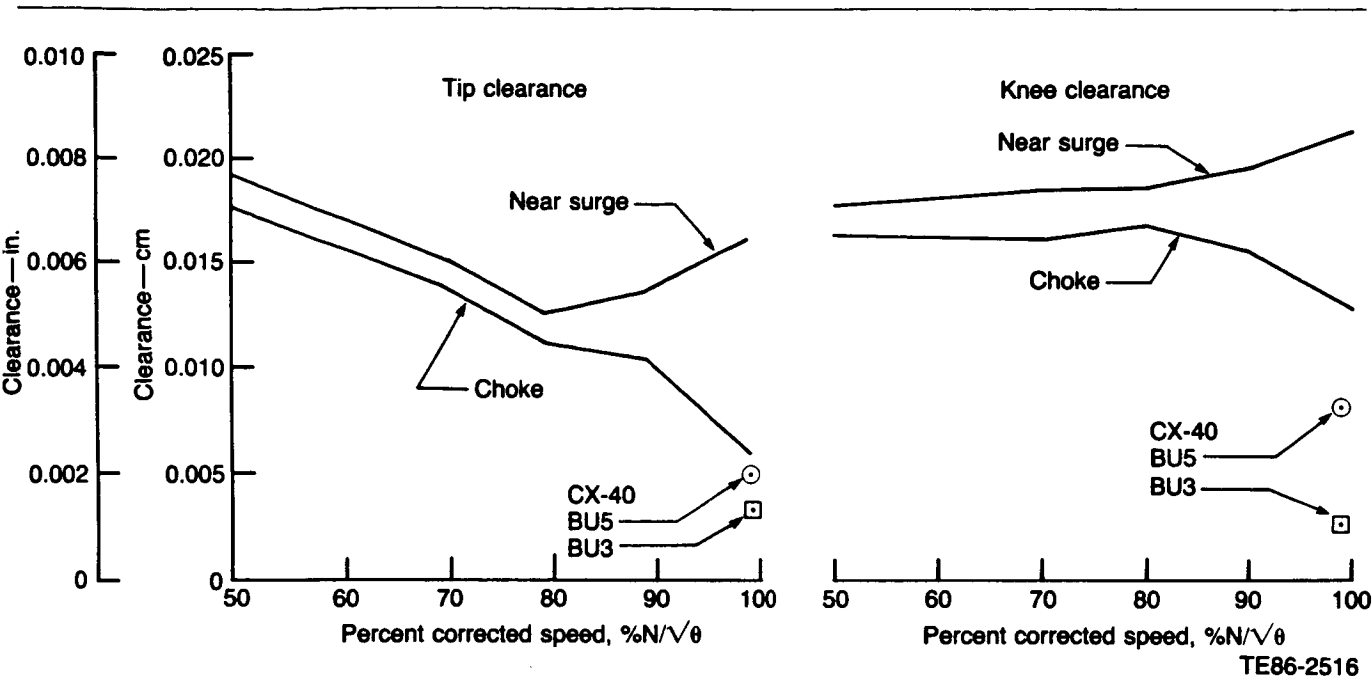
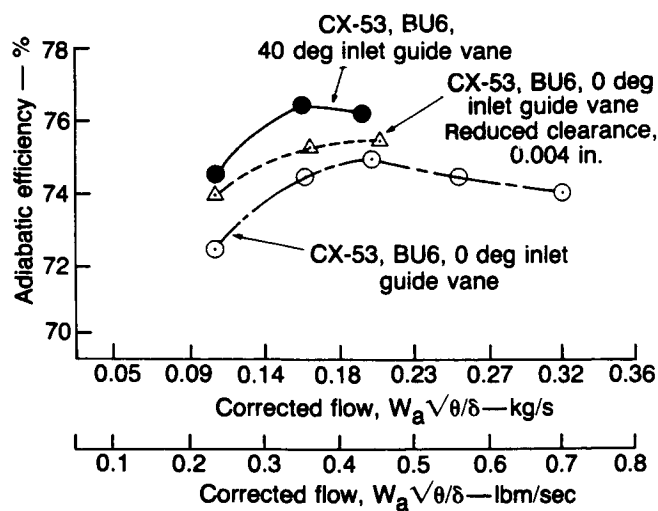


Figure 24. CX-53 BU6 compressor clearance measurements as a function of corrected speed.



TE86-2914

Figure 25. Effect of clearance and inlet guide vane reset on compressor performance.

Data History. Five builds of the CX-40 rig and six builds of the CX-53 rig have been used for compressor testing. The most important of these are builds 3 and 5 of the CX-40 rig and builds 2, 3, and 6 of the CX-53 rig. These builds encompass all of the major configurations tested. Some of the important differences of these compressor rig builds are presented in Table IX. Although the CX-40 rig was tested with two different inlet configurations (an earlier bifurcated inlet and the present engine inlet), only the data with the present engine inlet were studied. It has been determined that both inlets performed identically, this was also reconfirmed during this reanalysis of pertinent data. CX-40 BU5 employed thinner impeller blades and narrower diffuser vane heights than those in CX-40 BU3. These modifications were made to unchoke the impeller at design speed and to achieve the necessary surge margin for stable operation throughout the engine's operating envelope. CX-53 BU2 incorporated the present engine compressor configuration, which differs from CX-40 BU3 only in inducer blade thickness. The set of data obtained in these tests permits a very close comparison of the operating characteristics of the two different rigs. CX-53 BU3 tested an impeller having a considerably smaller exit width while CX-53 BU6 used the same impeller with blading removed to simulate a double splitter design. Both of these builds were attempts to obtain test data that would guide the redesign of a new, more efficient compressor. The narrowed exit width impeller (Type-

heat recirculation from the diffuser and to redesign the impeller using new design concepts that address the small size of this compressor. Both of these recommendations will be pursued during the next reporting period.

Table IX.
AGT 100 configurations.

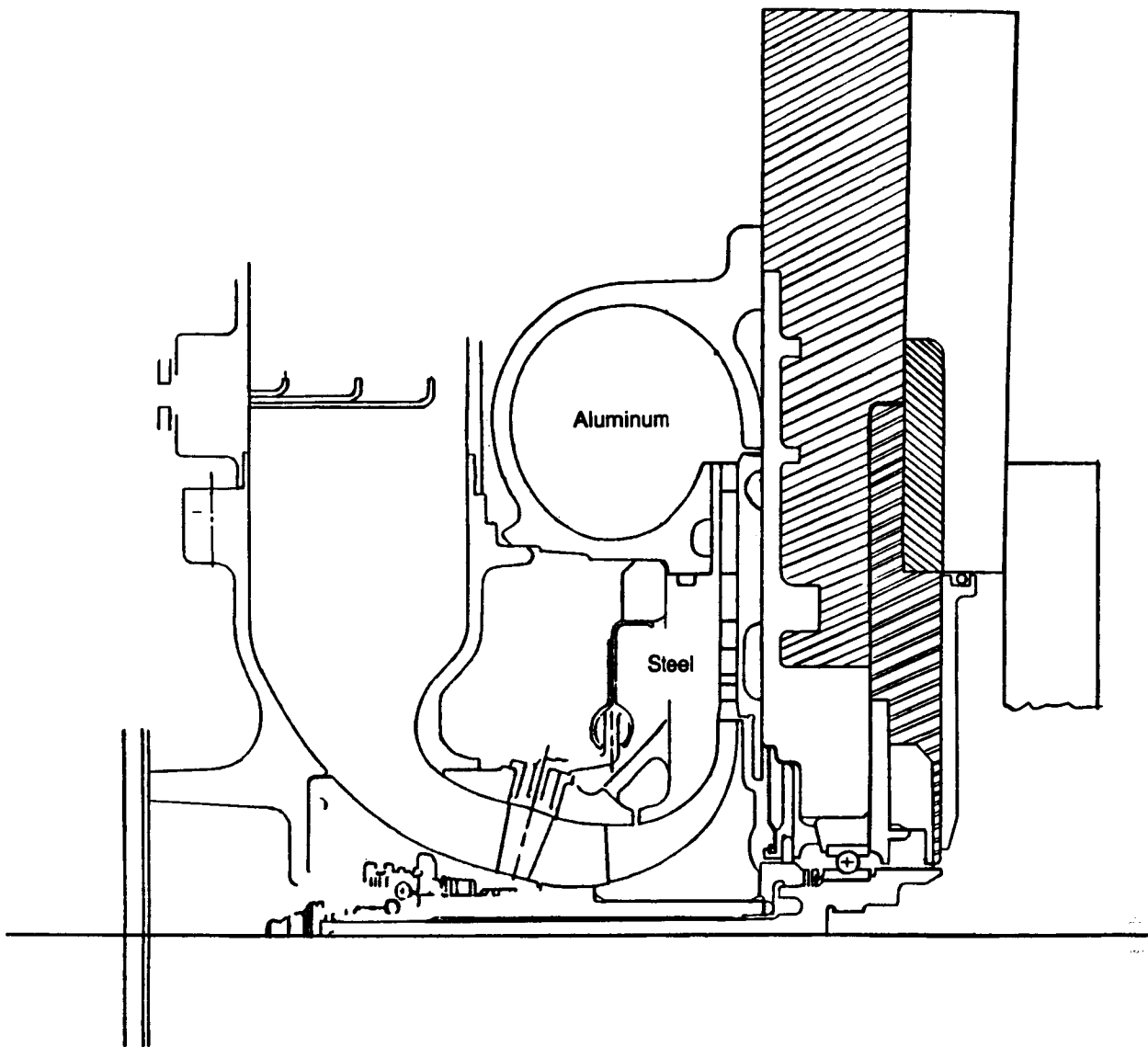
<u>Rig/build</u>	<u>CX40/BU3</u>	<u>CX40/BU5</u>	<u>CX53/BU2</u>	<u>CX53/BU3</u>	<u>CX53/BU6</u>
Inlet	Eng	Eng	Eng	Eng	Eng
Shroud	Steel	Steel	Aluminum	Aluminum	Aluminum
Impeller	Original	Thinned	Engine	Narr ext	DbI split
No. blades	16/32	16/32	16/32	16/32	8/16/32
Rt 2	2.365	2.365	2.365	2.410	2.410
B 2	0.218	0.218	0.218	0.1681	0.1681
Diffuser	Wedge	Wedge	Wedge	Wedge	Wedge
No. vanes	21	21	21	21	21
R3/R2	1.08	1.08	1.08	1.084	1.084
B4	0.1868	0.1681	0.1868	0.1681	0.1681
W4	0.170	0.170	0.170	0.1870	0.1870
That area	0.6669	0.6001	0.6669	0.6601	0.6601
Area ratio	4.04	4.04	4.04	3.682	3.682
Scroll	Tang-ext	Tang-ext	Ax-ext	Ax-ext	Ax-ext

1A) also has an increased exit diameter to regain the flow lost by narrowing the exit. As a consequence, it was necessary to employ a new diffuser design for CX-53 builds 3 and 6.

Rig History. Compressor tests, as performed on the two rigs, indicated a considerable difference in compressor performance. The two rigs (Figures 26 and 27) differ substantially in the rear bearing arrangement and in the front cover—impeller shroud housing configuration. Test problems with the first rig (CX-40) led to a decision to construct the second rig (CX-53). The CX-40 rig was very difficult to thermally stabilize because of the large steel rear support and the close proximity of the rear bearing to the aerodynamic flow path. This close proximity produced heat transfer from the rig to the rear bearing oil. As a result, the rig operated in a highly nonadiabatic condition leading to low compressor exit temperature measurements that prevented the accurate prediction of compressor efficiencies. For the most part, these design deficiencies were corrected for those builds included in this data reanalysis. These corrections were achieved by reworking the rear bearing support, reducing the steel support thickness, and supplanting with insulation. In addition, the rear bearing oil was heated to minimize heat transfer. However, the oil could not be heated to a temperature equal to that of the compressor discharge air at speeds equal to or exceeding 90%. Compressor ef-

ficiencies measured at these speeds were optimistic by approximately 0.5% (Figure 28). Another reason to build a new rig was due to discrepancies in the CX-40 and engine measured airflows. Engine measured airflows were consistently less (approximately 10%) than those measured in CX-40 BU3 (the engine configuration rig) using the same impeller. This remained true even when the impellers for the engine were thinned in the inducer region (CX-40 BU5). A new rig (CX-53) was designed and built to correct the remaining thermal problems in the rear bearing support area and to use as much engine hardware as possible. In fact, all parts but the rear bearing support are engine hardware. Additionally, the CX-53 rig was designed to adjust the cold clearances (static) with a simple adjusting calibrated screw mechanism. This feature allows simple and fast determination of the clearance effects that are important with small compressors.

Individual Build Data Analysis, CX-40 BU3 and 5. CX-40 BU3 performance (Figure 29) indicates too little surge margin relative to the engine operating line. Although design flow was achieved, these results also indicated an impeller inducer choking problem. The large decrease in efficiency at design speed and the flow speed lapse rate at the high flow rate range of the map are also indicative of choked flow. Impeller measurements revealed the blade thickness to be greater than design, therefore creating the choking



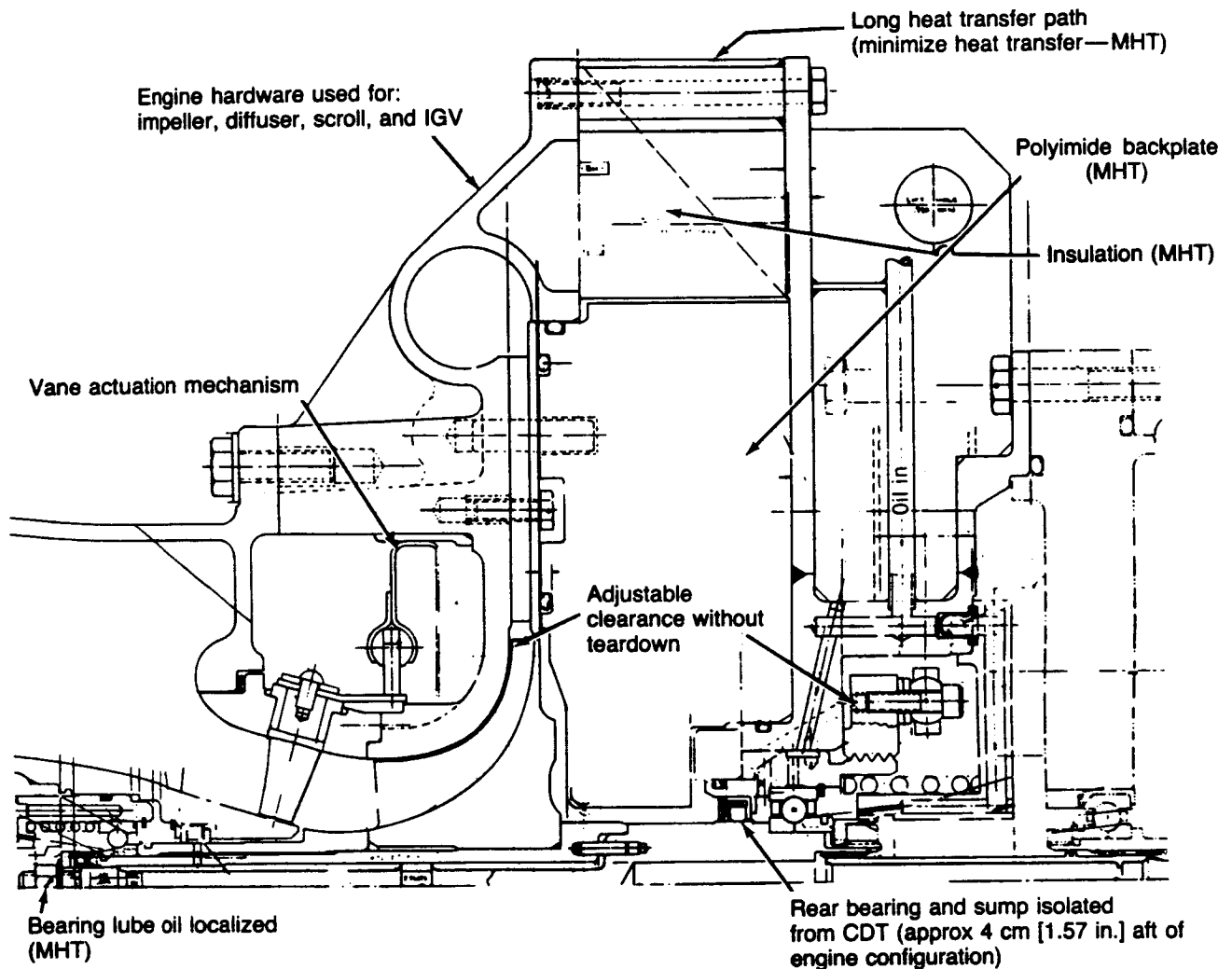
TE86-2910

Figure 26 AGT 100/CX-40 compressor rig.

condition. The blade thickness was thinned for CX-40 BU5, as depicted in Figure 30. The diffuser throat area was reduced by 10% (reduced vane height) since thinning the blades would have produced an overflow condition at the design speed. This reduction in diffuser throat area would also be beneficial by increasing the surge margin.

CX-40 BU5 performance (Figure 31) indicates that the desired surge margin was achieved, however, the design speed airflow was above the design value. The efficiency and flow lapse rates also indicate that the choking problem of BU3 was eliminated.

The operating line efficiencies for BU3 (Figure 32), adjusted to 10% minimum surge margin, have a design speed efficiency of 75.1%. By comparison, the design speed efficiency for BU5, shown in the same figure, is 77.1%. Although the high speed efficiency of BU5 is greater than BU3, the part speed performance of BU3 is considerably superior. This result is probably due to the inherent increase in blade loading, diffusion, and sensitivity to incidence with the thinner blades of BU5.



TE84-478A

Figure 27. AGT 100/CX-53 compressor rig.

CX-53 BU2, 3, and 6. The rig performance of the engine compressor (CX-53 BU2) exhibited entirely different characteristics than that obtained using a similar compressor on the earlier rig. The compressor map obtained from BU2 (Figures 33 and 34) indicates that the airflow, pressure ratio, and efficiencies are greatly reduced. However, the rig performance data matched engine results, accomplishing one objective for building the new rig. A comparison of CX-40 BU3 and CX-53 BU2 (two very similar compressor configurations) is presented in Figure 35. The airflow of CX-53 BU2 at design speed is approximately 15% less than the airflow of the compressor in CX-40 BU3.

Similarly, CX-53 BU2 compressor efficiency is about 3% lower than CX-40 BU2. The reduced airflow of the engine compressor cannot be a choking problem because the impeller inducer blades of the engine compressor are thinner than the compressor in CX-40 BU2 (the only significant difference between the two) and the airflow is less at all speeds. Further, the flow range (choke-surge) at any given speed is greater for the CX-53 rig (Figure 36), which is another indication that the two rigs operate quite differently.

CX-53 BU3 (Type 1A) and 6 (double-splitter) incorporated revisions to the impeller design to improve

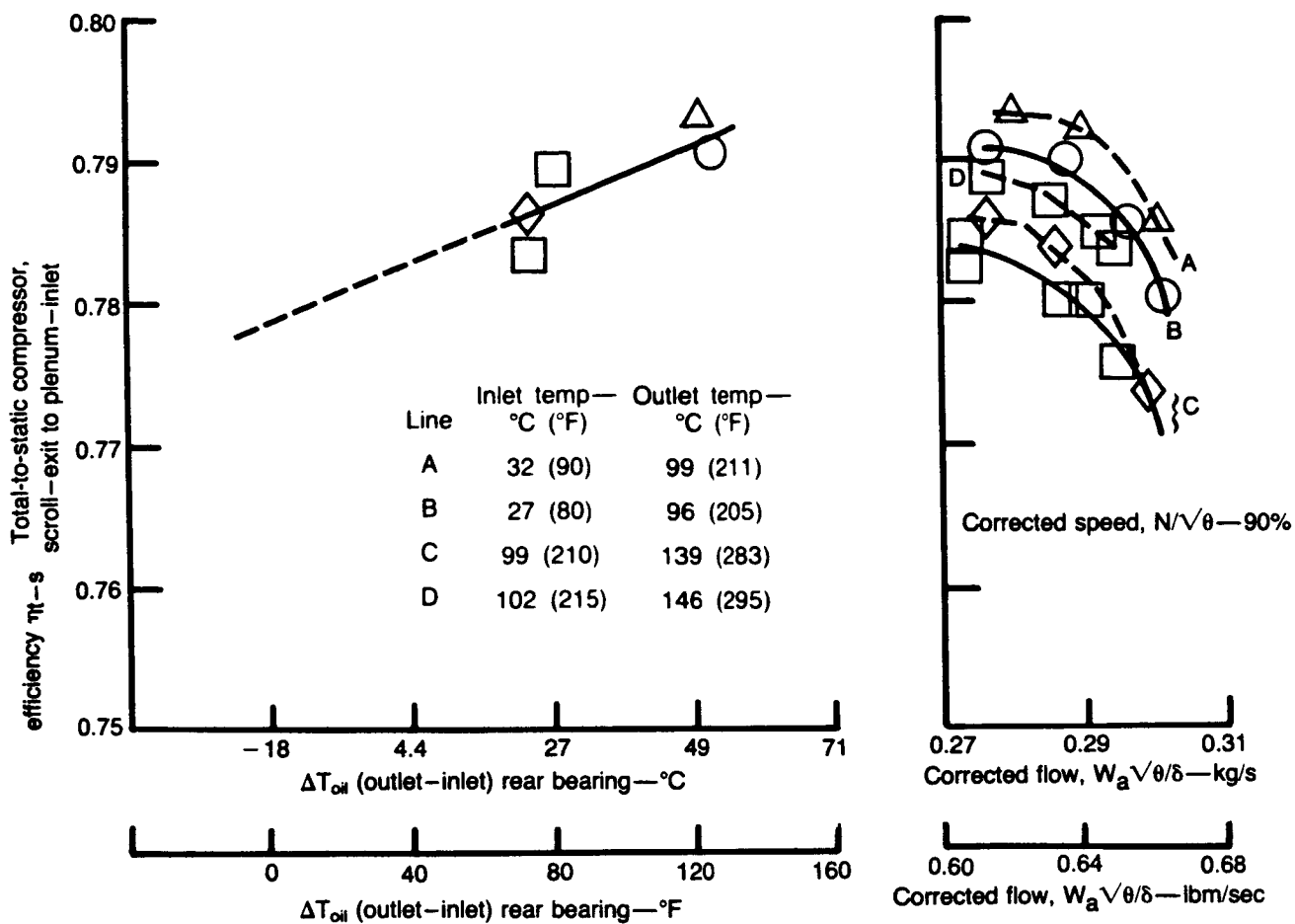
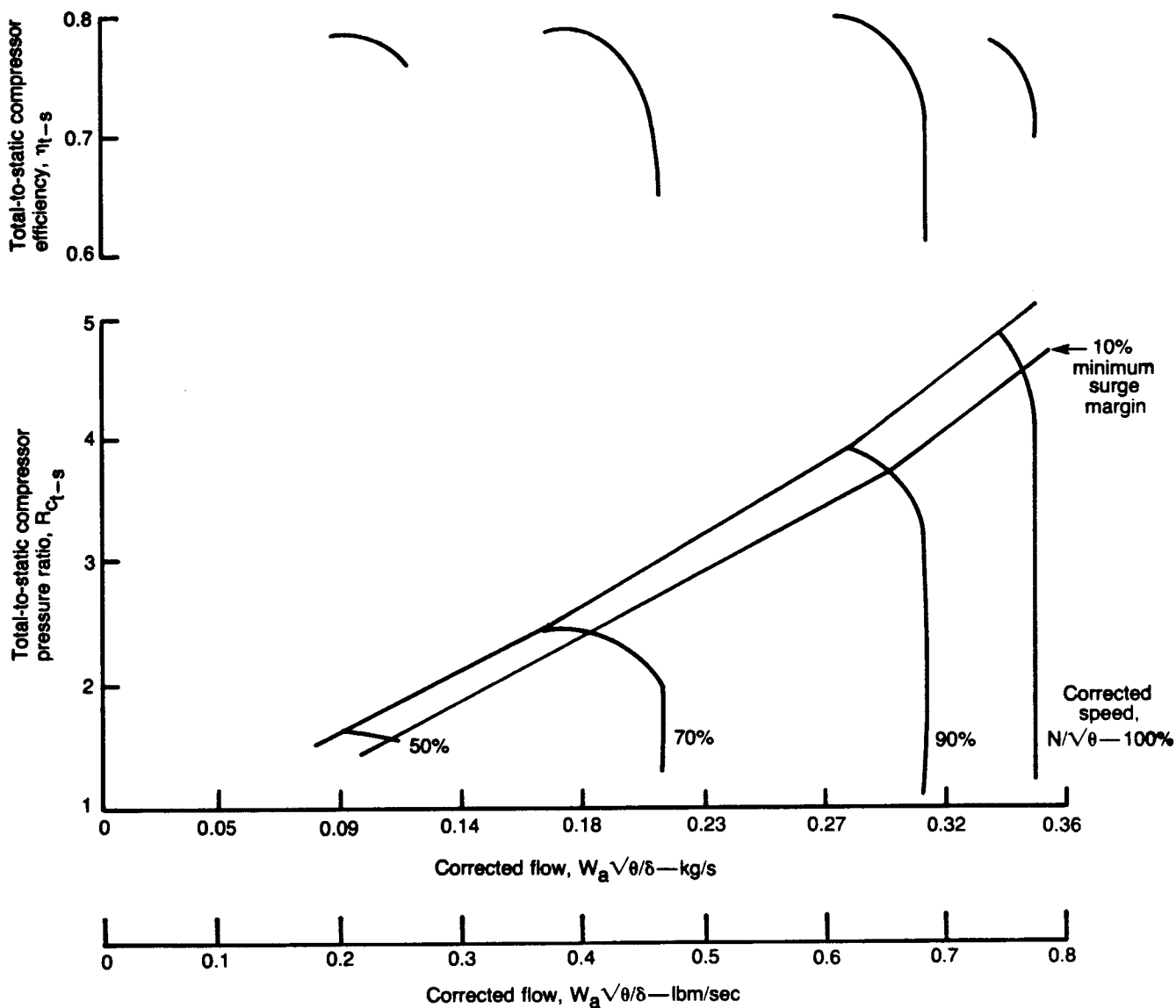


Figure 28. CX-40 BU5 rig compressor rig.

performance. BU3 used the same basic impeller as all other builds, with the exit width narrowed considerably—25% (refer to Figure 22). BU6 used the same impeller as BU3 reworked to the double splitter configuration described earlier. The operating line efficiencies of BU3 and 6 are presented in Figure 37. The exit width reduction of BU3 improved the efficiency significantly in the high speed region (3% at design speed) while also increasing airflow and pressure ratio. However, its performance is short of the design goal. BU6, in contrast, lost efficiency at all speeds, as compared to BU3, indicating a poor trade-off between increased impeller blade loading and reduced surface friction.

All rig builds, except CX-53 BU2, were instrumented with impeller shroud static pressures, diffuser inlet and exit static and total pressures, and diffuser passage pressures and temperatures. These measurements are invaluable in understanding the performance differences between the two rigs.

The impeller static pressure recovery and the impeller inlet velocity profile were two parameters primarily used in the analysis of the data obtained from the impeller shroud instrumentation. As defined in Figure 38, the impeller pressure recovery parameter is similar to a diffuser-like recovery factor in which the measured static pressure is ratioed to the local total relative pressure. The impeller pressure recovery term calculated in this form is a measure of the shroud diffusion and does not include any pressure rise due to changes in wheel speed. This recovery term is calculated at each of the shroud static pressure measurement locations with respect to the inlet shroud flow conditions. Allison has found this parameter to be extremely useful in analyzing effects due to impeller choking, inducer stall, clearance changes (and sensitivity to such change), impeller internal stall, and impeller flow recirculation or back-flow. The difference between the inlet shroud static and plenum total pressures in combination with the



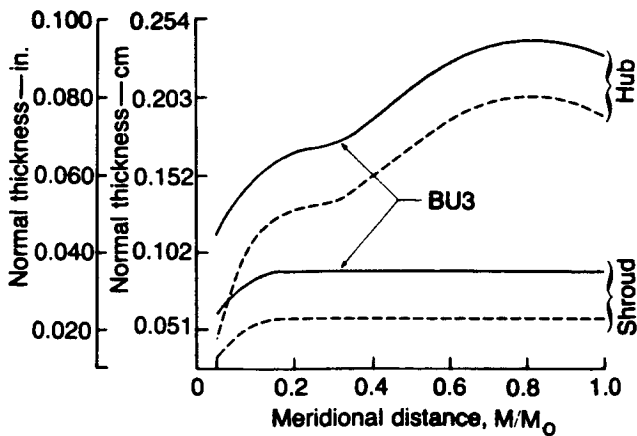
TE86-2912

Figure 29. CX-40 BU3 compressor performance.

one-dimensional continuity equation was used to calculate the shroud velocity and the average inlet velocity. These velocities are ratioed, denoted as the inlet velocity ratio, and plotted as a function of flow and speed. The character of the resulting plot is an indication of shroud-hub inlet flow shifts that result from inducer stall and impeller flow recirculation.

The impeller pressure recovery term, calculated near surge conditions at design speed, is presented as a function of meridional distance in Figure 39. Data from all of the instrumented builds as well as those of another Allison compressor (with much larger flow,

the IGT 404) were used in the construction of the figure. The IGT 404 compressor is very efficient and is characterized by a pressure ratio of 4:1, an overall total to static efficiency of 83% at design speed, and a 10% surge margin. CX-40 BU5 pressure recoveries are similar to the 404 data indicating strong diffusion throughout the impeller. CX-40 BU3 pressure recoveries are significantly depressed by comparison, which confirms the impeller choke condition first determined from performance map data analysis. The CX-40 BU3 also exhibits strong diffusion, much like



TE86-2913

Figure 30. CX-40 BU3, BU5 impeller blade normal thickness distribution.

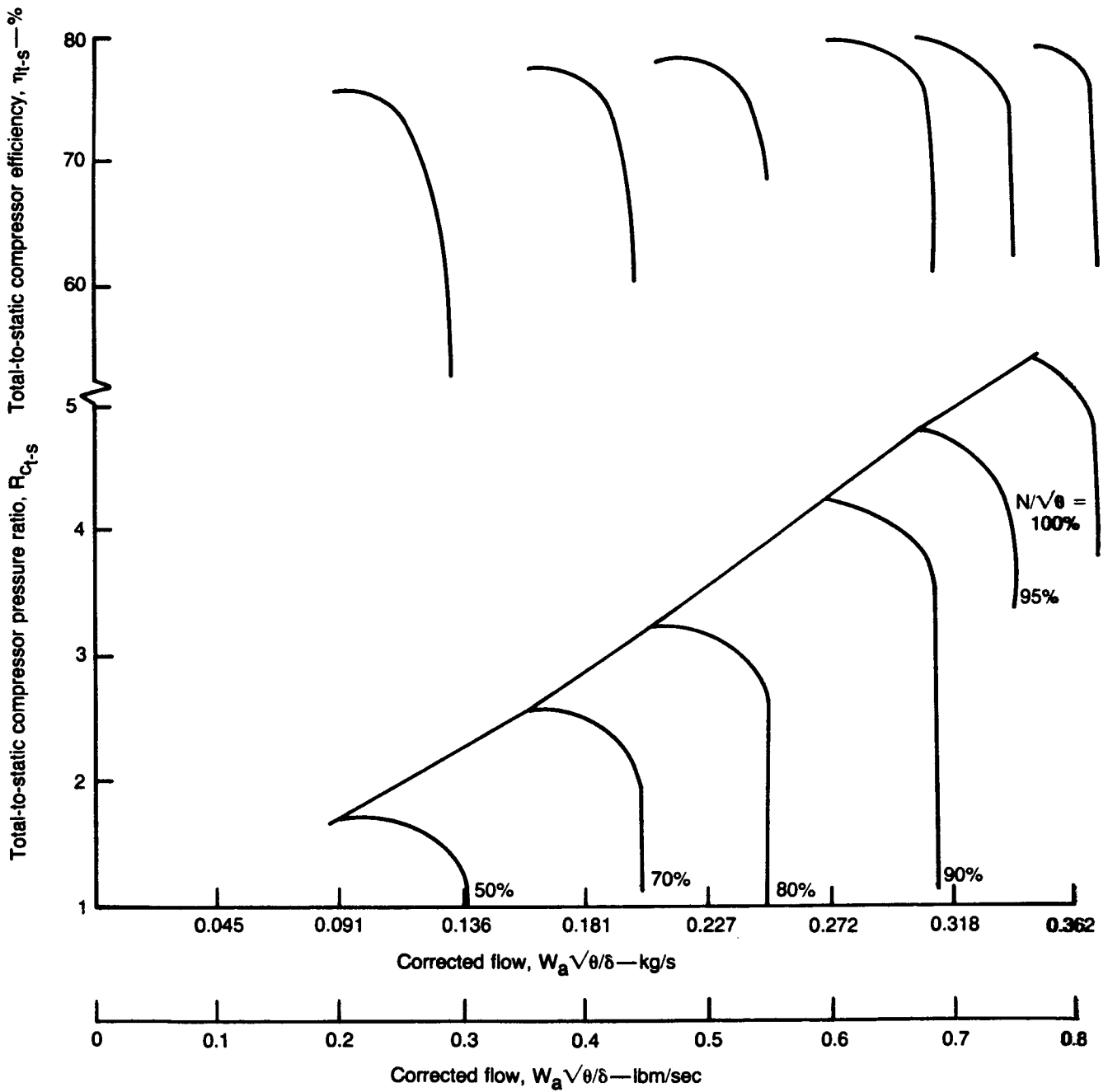
BU5. CX-53 BU3 and 6 (the latter is not shown in the figure), however, indicate that completely different characteristics are occurring in the compressor. There appears to be little diffusion over the entire impeller, which effectively creates high impeller exit blockage and high aerodynamic losses leading to low overall compressor efficiency. The higher pressure recovery at the impeller inlet of the CX-53 builds is due to the lower flow and is an indication that inducer stalling due to incidence is not a problem and is not the cause of the reduced flow rate observed during both engine and CX-53 rig builds and the engine compressor are a result of reduced work and high aerodynamic losses to the diffuser throat (within the impeller). Impeller flow recirculation creates impeller pressure recoveries very similar to the observed data, but recirculation generally occurs at low speeds as a result of high inducer incidences, leading to gross inducer stall. High impeller to shroud clearances also result in depressed impeller pressure recoveries, but the decrease in magnitude is much less than the differences observed between CX-40 and CX-53 rig test data. Also, clearance testing performed on the CX-53 rig and clearance measurements obtained on CX-53 BU6 indicate that the differences between the rigs cannot be totally explained by clearance phenomena. Thus, no conventional aerodynamic explanation can explain the observed differences in impeller pressure recoveries between CX-40 and CX-53 rig test data.

The impeller inlet velocity ratios presented in Figure 40 indicate huge differences in test results obtained from the two rigs. Generally, impellers with no inlet swirl have an impeller inlet velocity ratio

between 1.1 and 1.2 at design speed. This ratio decreases at lower speeds to approximately 0.9-1.0 as the inducer begins to stall as flow shifts toward the hub. At even lower speeds, the velocity ratios drop even lower to 0.0-0.9 as flow recirculation appears. The CX-40 data as presented in Figure 40 follow this description, but the CX-53 data are totally foreign in nature. CX-53 rig data indicate low velocity ratios exist over the entire operating regime; this is generally associated with large flow shifts toward the hub. This flow shift could be a result of impeller flow recirculation, but is considered unlikely due to the favorable incidences at the higher speeds. Further, if flow recirculation is present in the CX-53 rig data and is used to explain rig data, why recirculation was not present in CX-40 testing is questionable.

Impeller to shroud clearances were varied on CX-53 BU2 and 6 with the effects on operating line performance shown in Figure 41. When clearances were opened, 0.013 cm (0.005 in.) from nominal as in BU2, as much as a 2% loss in efficiency occurred. However, when nominal clearances were reduced, 0.010 cm (0.004 in.) as in BU6, a gain in efficiency of approximately 1% was obtained. High speeds were avoided with reduced clearance to eliminate heavy rub. Running clearances were measured at two circumferential locations near the impeller knee and tip exit. These measurements, described in Figure 24, indicate that the clearances were not, in general, unreasonably large. There was a considerable difference detected in clearance between choke and surge conditions at high speeds that caused some variation in airflow along the choked portion of the speed lines. However, this result was not observed in the CX-40 rig test speed line data, leading to the conclusion that the clearances did not change during CX-40 rig testing. The measured knee clearances obtained during CX-53 rig testing were running somewhat greater than desired and were approximately 0.013 cm (0.005 in.) larger than CX-40 test run conditions. The clearance differences between CX-40 and CX-53 could account for approximately 1% of the observed efficiency difference between the rigs. This corresponds with the previous conclusion from impeller static pressure recoveries; that is, the clearance effects do not, and cannot, account for all of the performance differences observed in the test data obtained from CX-40 and CX-53 rig testing.

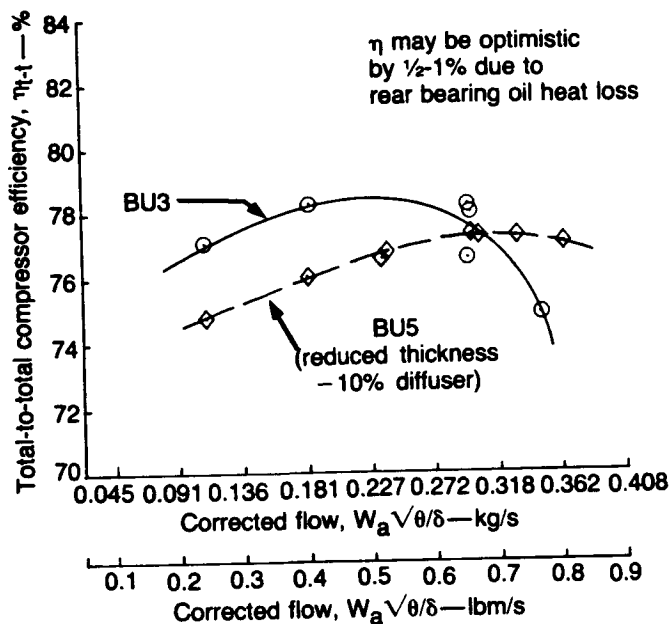
Summary of Test Data Analysis. Summary and results from the data reduction obtained through the use of Allison's stage design and analysis calculation (based on Creare's jet/wake flow model) are pre-



NOTE: All lines are a result of data points

TE86-2921

Figure 31. CX-40 BU5 compressor performance.



TE86-2922

Figure 32. CX-40 rig compressor performance along operating line (10% minimum surge margin).

sented in Table X. An examination of the information presented in the table reveals that not only is the impeller's performance less efficient during CX-53 rig testing, but the high impeller exit blockage is feeding into the diffuser, creating high diffuser exit blockages and reducing the diffuser's static pressure recovery. The analysis also reveals that impeller slip factors for the CX-53 rig test data are well below those obtained during CX-40 rig testing and totally beyond Allison's experience. However, the CX-40 impeller slip factor data are within Allison's experience, with values of 0.87 for BU5 and values for BU3 only slightly reduced because of inducer choking. The reduced slip factors measured during the CX-53 rig testing are an additional indication that there is a basic problem with the CX-53 rig and engine configuration, which translates into poor impeller performance.

A comparison of heat transfer characteristics of the two rigs shows some rather large differences. The metal temperatures in the inlet guide vane region for similar data points at 90% speed are significantly different, as seen in Figure 42. CX-53 rig test metal tem-

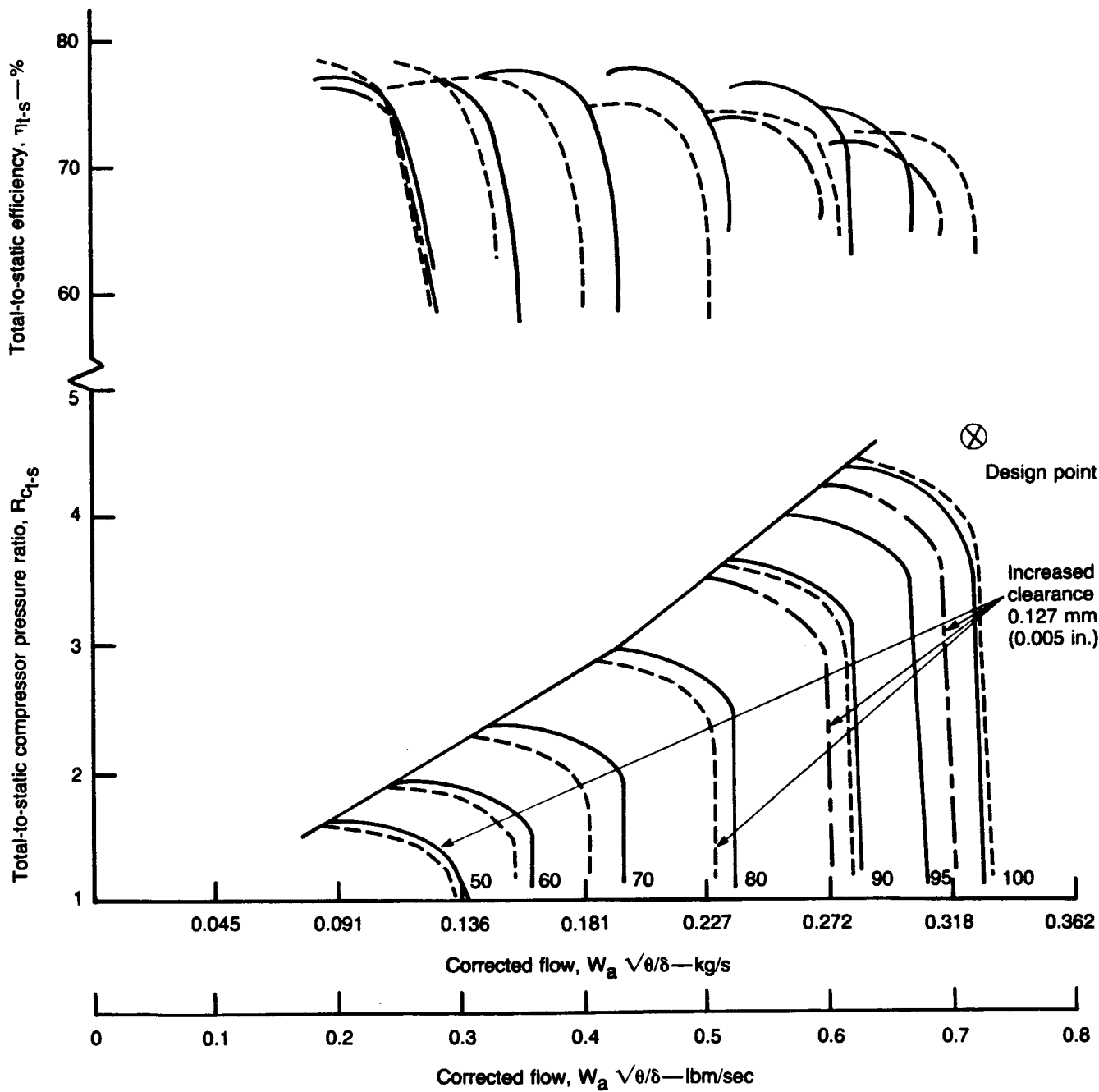
peratures are considerably larger than those observed in CX-40 rig testing, indicating increased heat recirculation. Additionally, the measured difference between the diffuser passage temperature and the compressor discharge temperature in the CX-53 rig (also presented in Figure 42) reveals that with the addition of insulation the heat loss from the rig was reduced to nearly zero, but a large difference between the two temperatures is still present. This again is indicative of a significant amount of heat recirculation from the compressor exit to the inlet in the CX-53 rig. It is reasonable to assume that the thick aluminum shroud housing used on the CX-53, as opposed to the steel shroud on the CX-40, is the cause for this additional heat recirculation.

It was concluded that, in the absence of any logical and identifiable aerodynamic differences between the two rigs, the increased shroud heat recirculation of the CX-53 rig is reducing the impeller pressure recovery resulting in poor impeller and overall compressor efficiency measurements. Analysis of the data indicates no real compressor design deficiencies. For example, efficiency improvement attempts resulted in a 3% gain at high speeds when the impeller exit width was narrowed (BU3 Type 1A) while an approximate 2% loss at all speeds occurred when the solidity of the impeller was reduced (BU6, double-splitter). Additionally, measured impeller to shroud clearances and the resultant effects of clearance on efficiency indicate that the clearance can be reduced enough to gain approximately 1% in efficiency. These are all predictable results. As a consequence, it is concluded that it is the existence of a serious heat recirculation problem in both the CX-53 rig and the engine hardware that results in the observed poor compressor performance.

3.1.3 Planned Rig Modifications and New Impeller Design

This subsection presents a discussion of the planned rig modification and provides information on the impeller design.

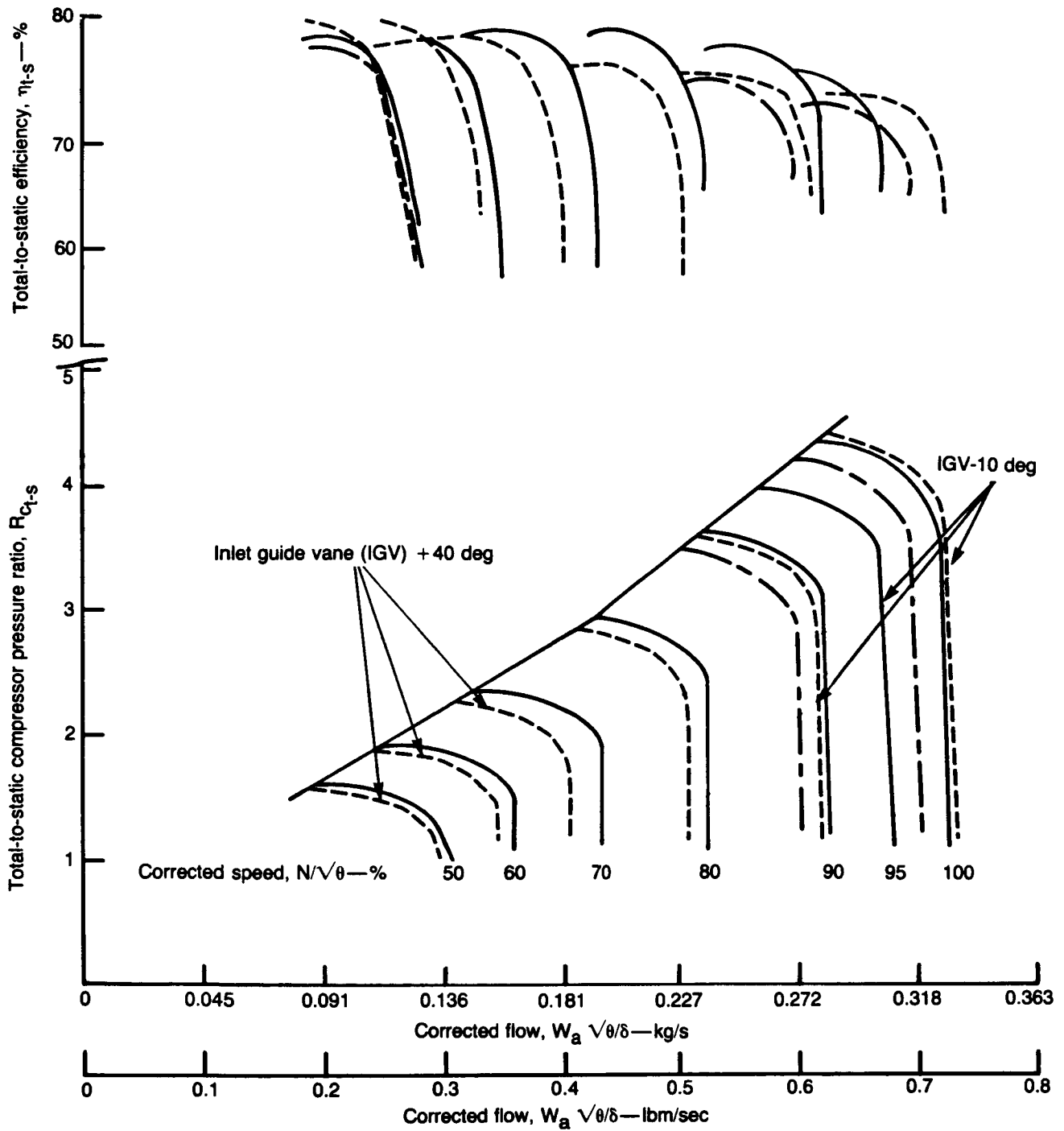
Rig Modifications to Reduce Heat Recirculation. The analysis revealed the need for rig and engine modification to minimize heat recirculation to not only regain the performance levels of the CX-40 rig, but to increase the AGT 100's performance with a new compressor design. A rig redesign was accomplished in 1985 that replaced the aluminum impeller shroud and diffuser front plate with a thin steel shroud and diffuser front plate insert into the large aluminum casting. The aluminum casting also includes the compressor discharge scroll and the inner gear case. The reduced thermal conductivity of steel and the thinned cross section should reduce the heat recirculation to



NOTE: All lines are a result of data points

TE86-2923

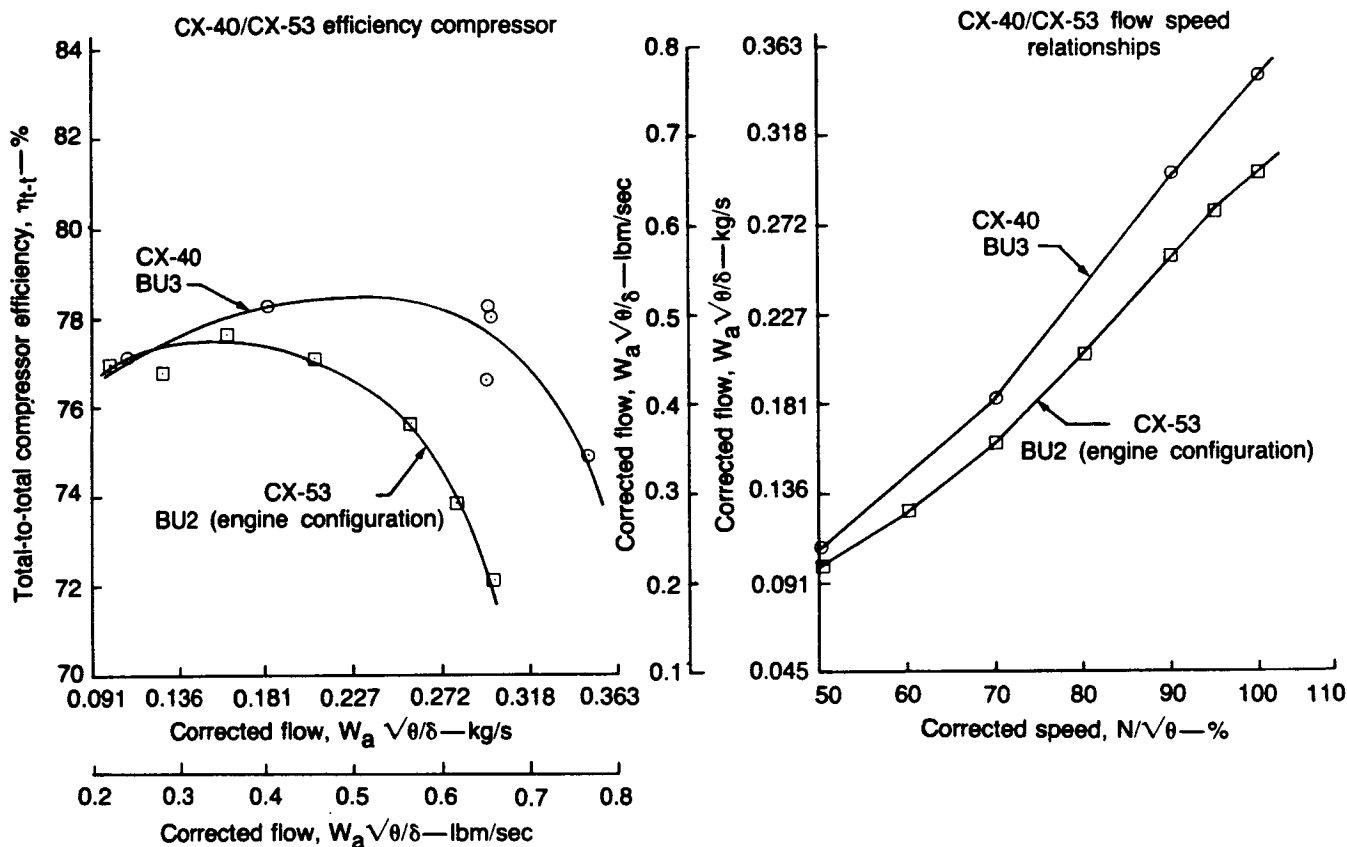
Figure 33. CX-53 BU2 engine compressor performance.



NOTE: All lines are a result of data points

TE86-2924

Figure 34. CX-53 BU2 engine compressor performance.



TE86-2925

Figure 35. Compressor operating line performance.

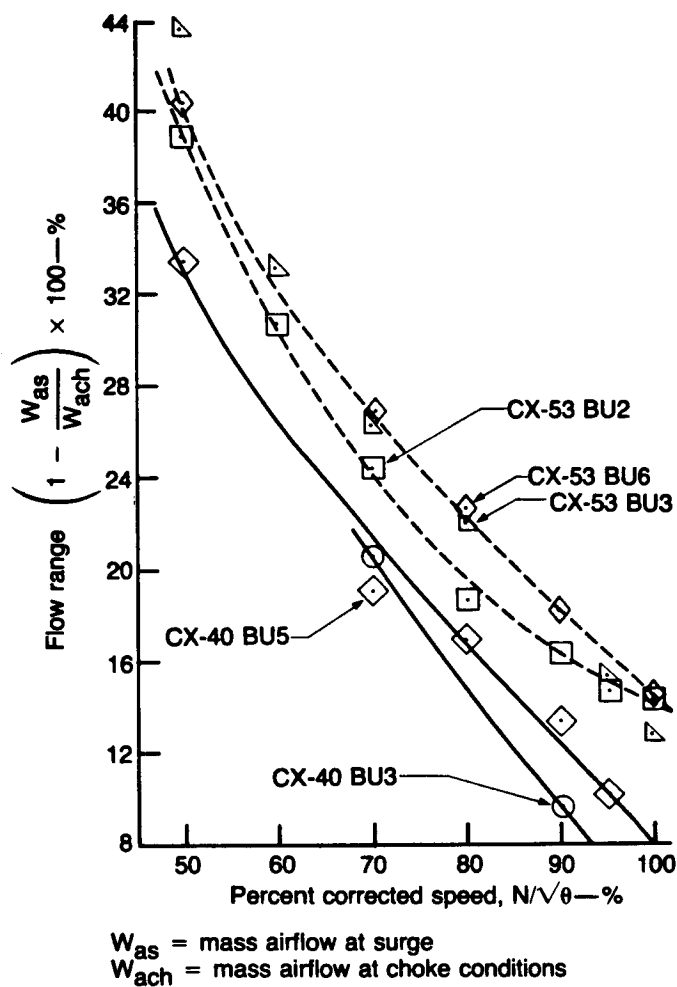
the levels measured during CX-40 rig testing. This rework, depicted in Figure 43, is in progress. Rig testing is scheduled to begin in the May-June 1986 time frame.

The planned rig testing includes the impeller configuration that has had to date the most positive impact on performance, i.e., the narrowed exit width Type-1A used in the CX-53 BU3 test. A second Type 1A impeller has been machined. Additionally, the shroud will be recontoured, if necessary, to ensure the proper impeller-shroud match.

Compressor Potential Performance Gain Estimates.

The performance potential of the AGT 100 compressor in a rig or engine free of adverse heat transfer effects has been estimated. The performance improvements are expected through increased airflow and efficiency. The airflow is expected to increase to the design level (or possibly more) because the impeller's inducer blade thickness is the same as the impeller tested in CX-40 BU5, which exceeded the design

airflow value. Impeller work and efficiency are expected to increase due to the reduced heat recirculation. A near-term achievable efficiency of 79% can be estimated by using either CX-40 BU5 test data or CX-53 BU2 and 3 test data as the starting point (Figure 44). Starting from CX-40 BU5 test data, the 79% efficiency goal can be achieved by adding the performance improvements due to narrowing the impeller exit width as observed between CX-53 BU2 and 3 test data. The entire effect (3% potential gain) has not been included due to possible magnification resulting from the heat recirculation of the CX-53 rig. Also, Allison experience with other centrifugal compressors does not indicate that this large of an effect should be expected. Seventy-nine percent efficiency can also be achieved by using CX-53 BU2 test data as a base, adding the efficiency advantage of BU3 (narrowed exit width), including the efficiency difference be-



TE86-2926

Figure 36. CX-40 BU3 and BU5, and CX-53 BU2, BU3, and BU6 compressor flow range comparison.

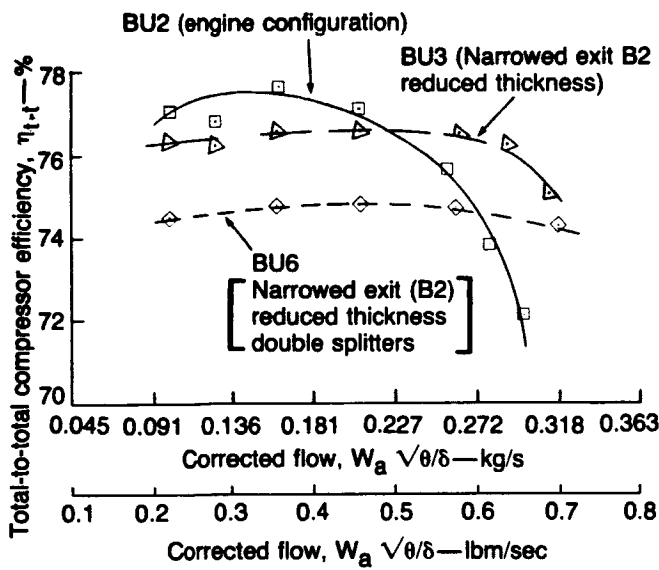
tween CX-40 BU3 and CX-53 BU2 (due to the rig heat transfer effects), and including efficiency improvements due to decreased clearances (as determined during CX-53 rig testing).

New Impeller Design and Estimated Compressor Efficiency. The recommended impeller redesign would employ another degree of freedom on blading shape to better control blade loading, choke flow characteristics, and inducer incidences. The present AGT 100 impeller is constructed with the blade meanline defined along the hub and shroud, and the blade meanline between the hub and shroud connected linearly at even meridional distances (normals) at the hub and shroud. The blade thickness is applied linearly about the normals in the meridional plane.

The recommended new blading would describe both blade surfaces along separate linear lines (Figure 45). This results in more control of the blade thickness and blade angles between the hub and shroud, while maintaining the linear surfaces necessary for numerically controlled machining of developmental hardware. The increased control of the thickness and blade angles results in a blade leading edge shape similar to that shown in Figure 46. The redesign also incorporates a significant reduction in blade thickness in the midspan region. A leading edge blade angle distribution that could be realized from the new blading technique is presented in Figure 47. As depicted, these changes lead to decreased inducer incidences while increasing the impeller's flow capacity. This results in an efficiency increase across the entire operational impeller speed range while enhancing part speed stability. The impeller redesign will also incorporate impeller leading edge sweep, which reduces inducer shock losses while enhancing the new blading concept (Figure 48). Allison has tested the effect of leading edge sweep with two different impellers designed for the same operating conditions. One of the impellers had a radial leading edge design, while the other incorporated a swept leading edge. The test results shown in Figure 49 indicate a significant increase in flow range between choke and surge for the swept leading edge impeller, resulting in broader efficiency characteristics. The lower choke flow of the swept leading edge design is believed to be a result of a hub condition not inherent to leading edge sweep and it will not exist in the new AGT 100 impeller design. The impeller redesign will incorporate the advantages resulting from the narrow exit width design of the CX-53 BU3 test impeller. Thus, the new impeller design will combine new blading techniques with those design criteria already identified through rig and engine testing that resulted in improved compressor performance.

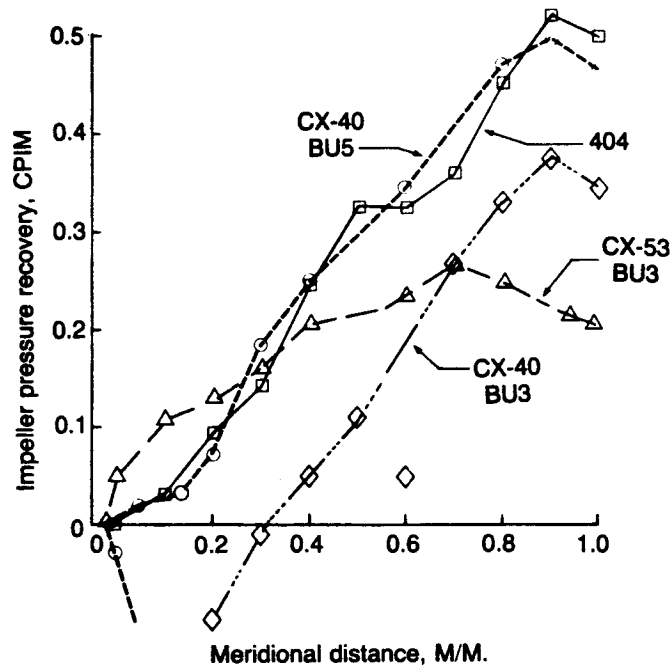
The design was initiated in 1985 with an expected completion in the April-May 1986 time frame. Testing of the new design is planned for the fall of 1986.

The efficiency estimation for the new design (refer to Figure 44) uses the 79% near-term goal with 1.5% added as a result of the proposed new blade design to attain an estimated efficiency of 80.5%. This estimated gain is somewhat difficult to verify because no analytical model exists to yield insight into this design and, therefore, the gain in efficiency is based on a combination of experience and intuition regarding the advantages of the incidence and swept leading edge. To place this performance gain in perspective, previous and planned AGT 100 compressor efficiencies are compared to the efficiencies of several existing Allison compressors in Figure 50. As the compari-



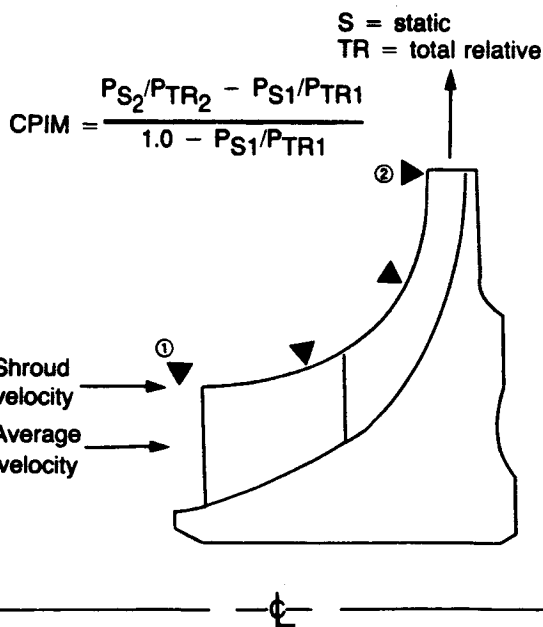
TE86-2927

Figure 37. CX-53 rig compressor performance along operating line (10% minimum surge margin).



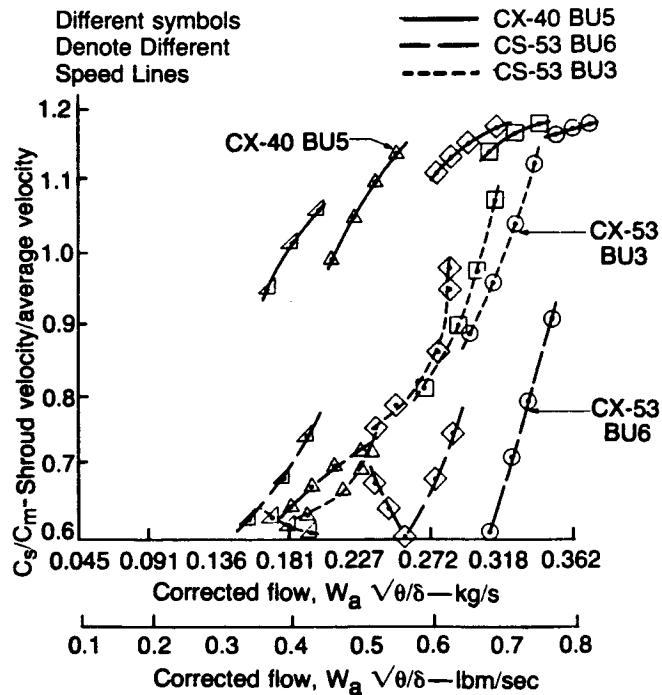
TE86-2929

Figure 39. Impeller pressure recovery, $N/\sqrt{\theta} = 100\%$, near surge.



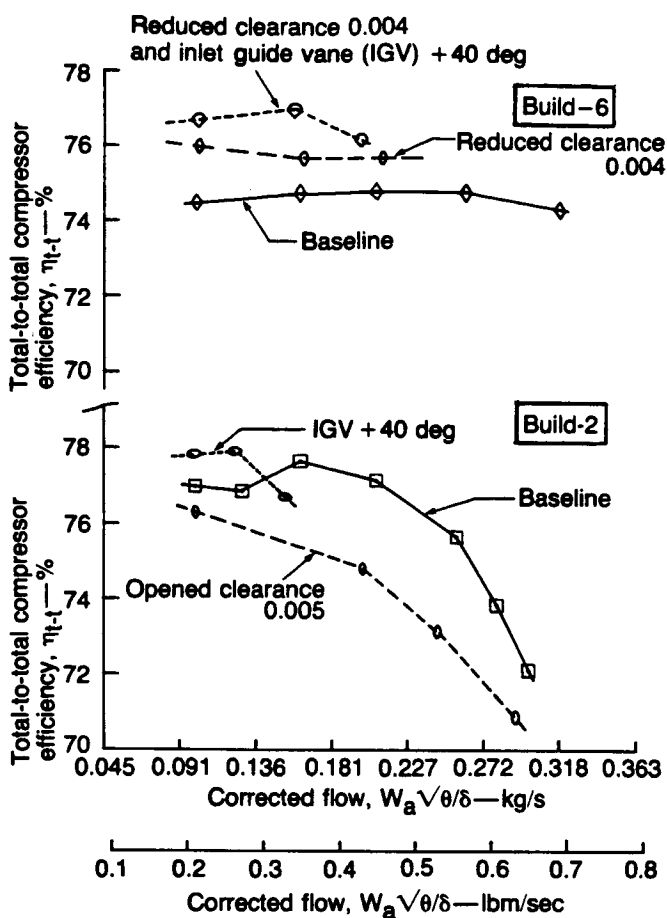
TE86-2928

Figure 38. AGT 100 compressor impeller pressure recovery.



TE86-2920

Figure 40. AGT 100 compressor impeller inlet axial velocity ratios.



TE86-2890

Figure 41. CX-53 rig performance along operating line (10% minimum surge margin).

son indicates, an efficiency in the 80% region is an ambitious but reasonable goal.

3.3 COMPRESSOR MECHANICAL DEVELOPMENT

Compressor mechanical development activity this period included modification and rig testing of a Type-1A impeller, the replacement of an aluminum compressor shroud with a reduced thermally conductive steel shroud, and the continuation of a gasifier assembly balance effort. The latter effort, which involves both the compressor and gasifier turbine, is reported in subsection 4.2, Gasifier Turbine Mechanical Development.

3.3.1 Modified Type 1A Impeller (Cut Back Blades)

In an effort to improve the performance of the Type-1A impeller, modifications were made to reduce the number of full length blades and to introduce a set of secondary splitter blades. Initial testing of the modified Type-1A impeller on the compressor rig was limited to 80% speed due to excessive vibration (this work is described in the 1984 annual report). Following improvements to the impeller assembly, the modified Type-1A impeller was successfully tested to 100% speed early in this reporting period. These tests permitted the necessary data to be obtained for assessment of the modified impeller performance characteristics (refer to section 3.1).

3.3.2 Steel Compressor Shroud

Compressor performance has been below program goals for all of the impeller designs tested to date in the engine and on the current compressor rig. The current AGT 100 compressor rig (CX-53) is designed to closely simulate the engine by using engine hardware for the compressor rotating and stationary components. This includes the shroud, diffuser wall, and scroll, which are all integral parts of the large aluminum casting that also forms part of the gearbox. The upstream mating components, including the aluminum IGV support assembly, are also common between the engine and compressor rig.

Conduction of heat from the relatively hot impeller exit, diffuser, and scroll regions into the cooler IGV support and impeller shroud regions appears to be adversely affecting compressor performance. This performance degradation is believed to occur through the addition of excessive heat to the inlet air before and during the compression process. This phenomenon may also be introducing adverse boundary layer effects. Performance is expected to improve after replacing the shroud and IGV support assembly with a lower thermal conductivity material (stainless steel), thereby decreasing heat transfer to the inlet air before and during compression. This expectation is supported by analytical analysis and actual test data obtained from an earlier AGT 100 compressor rig (CX40). This rig's shroud was fabricated from steel.

Thus, in order to improve compressor performance, the aluminum shroud and IGV support assembly are being replaced with stainless steel. The existing aluminum shroud is being machined out of an existing inner gear case assembly and replaced with stainless steel. A stainless steel IGV support assembly is also being manufactured. These stainless steel parts have a thermal conductivity approximately on an

Table X.

Jet/wake flow model data reduction.

	<u>CX40/BU5</u>	<u>CX40/BU3</u>	<u>CX53/BU3</u>	<u>CX53/BU6</u>
Rdg	1349	1065	647	757
$W_a \sqrt{\Theta/\delta}$	0.805	0.769	0.6871	0.684
R_{C_t-tD} —diffuser exit	5.211	4.624	4.524	4.664
η_{C_t-tDS}	0.7881	0.758	0.774	0.764
N/Θ	86,120	86,216	86,232	86,217
SM—surge margin	10%	10%	10%	10%
C_S/C_M —impeller inlet vel. ratio (shroud/avg)	1.18	1.15	0.961	0.610
AREQ—impeller equivalent area ratio	2.43	2.54	2.41	2.39
CPIM—imp. pressure recovery	0.455	0.294	0.195	0.177
BIMP—imp. exit blockage	0.662	0.695	0.617	0.644
SF—slip factor	0.862	0.823	0.787	0.808
η_{imp} —eff. of imp	0.875	0.841	0.842	0.845
$CP_{2*.4}$ —imp. to dif. throat pressure rec.	0.120	0.124	0.219	0.242
COEF—imp. to dif. friction coef.	0.0152	0.0124	0.0098	0.0184
η_{t-t4} —dif. inlet eff.	0.823	0.804	0.811	0.786
M4—dif. throat Mach #	0.798	0.777	0.681	0.633
$CP_{4.5}$ —dif. press. recovery	0.741	0.698	0.634	0.667
BLK-5—dif. exit blockage	0.338	0.325	0.429	0.459
η_{t-s5} —tot.-static eff. dif. exit	0.768	0.740	0.747	0.736
$\eta_{O/A}$ —overall eff.	0.773	0.744	0.751	0.742

NOTE: dif.—diffuser
imp.—impeller
eff.—efficiency

order of magnitude less than that of aluminum and will be configured to the Type-1A compressor design.

Testing of the steel shrouded Type-1A compressor will initially be performed on the CX-53 compressor rig. Engine testing of the steel shroud will follow the rig test. The modified hardware has been designed to be compatible with the compressor rig and the engine.

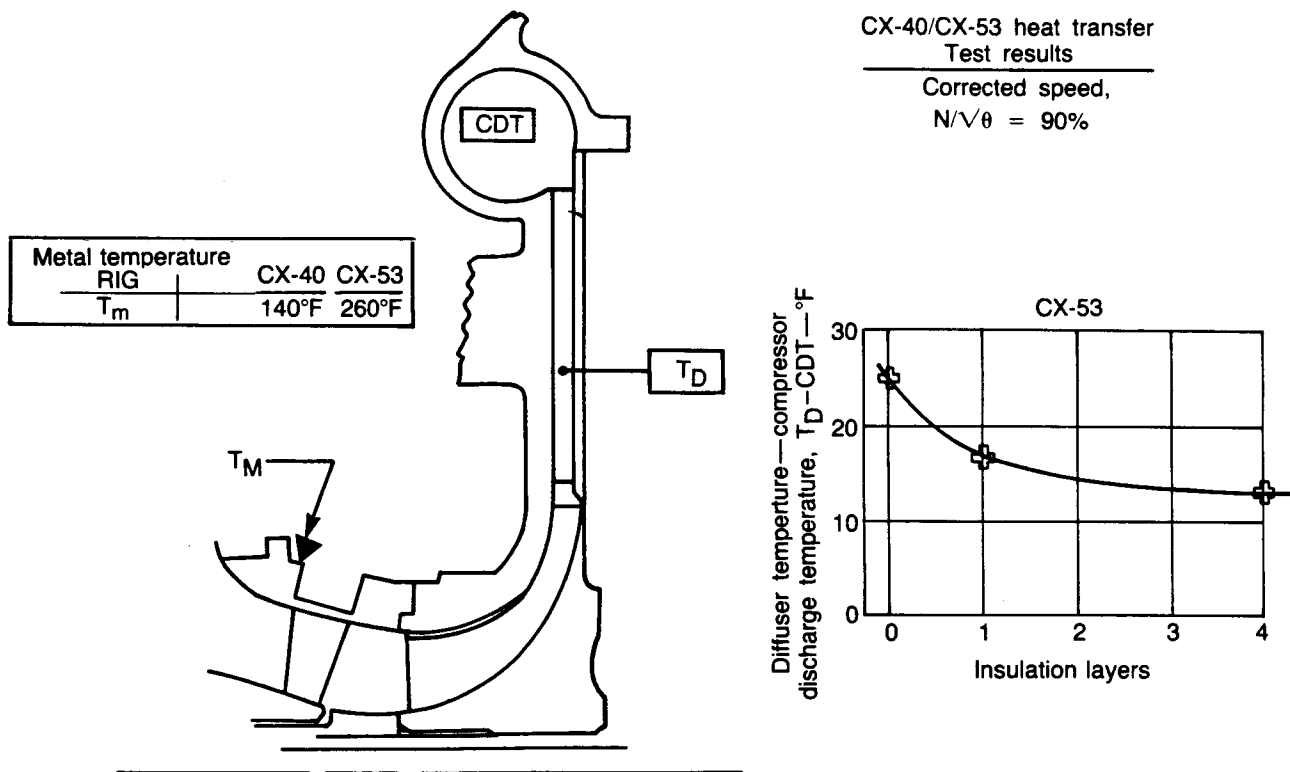
The steel shrouded compressor design is depicted in Figure 51. Provision for maintaining the location of the shroud relative to the impeller as the parts reach operating temperature has been incorporated in the design. This redesign requires a substantial diametral press fit of 0.41-0.43 mm (0.016-0.017 in.) at the pilot diameter at room temperature. A heat transfer analysis of the steel shrouded assembly indicates

that a slight interference fit will still be maintained at the higher steady-state operating temperatures. The heat transfer analysis also predicts that the steel shroud will operate at increasingly cooler temperatures, compared to the aluminum shroud, in a direction forward from the impeller exit region toward the inlet region, Figure 52. The temperature difference is predicted to approach 38°C (100°F) at the outer wall near the IGVs and at the impeller inlet region when operating at steady state, 100% N1 speed, and maximum power conditions.

The steel shroud extends outward along the diffuser wall. This design incorporates additional thermal resistance and prevents an undesirable boundary layer trip at the interface between the aluminum housing and the steel shroud.

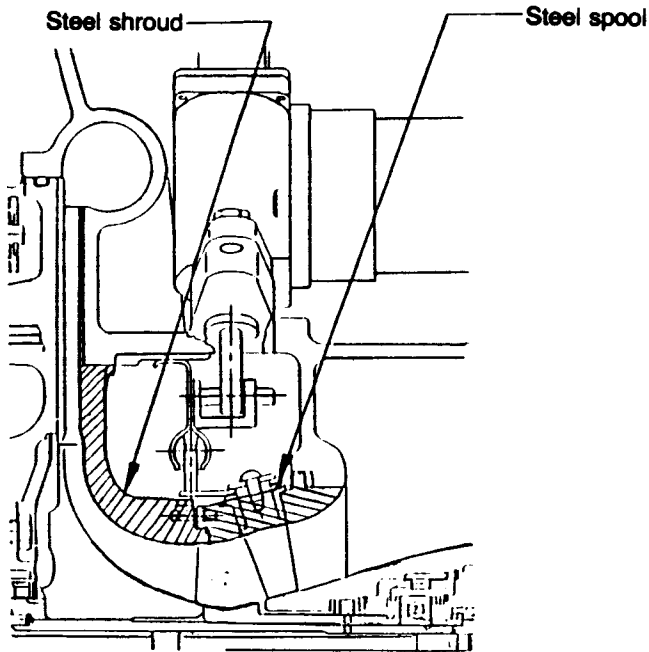
At the end of this reporting period, the design and heat transfer analysis of the steel shroud have been completed and the inner gear case assembly has been reworked to accept the steel shroud. The steel shroud and the steel IGV support assembly have been fabricated and the steel shroud has been successfully installed in the reworked inner gear case.

Final machining of the steel shroud flow path and pilot features, and the IGV support assembly flow path, as well as instrumentation of the new parts for compressor rig testing, are yet to be accomplished. These efforts will be completed during the next reporting period.



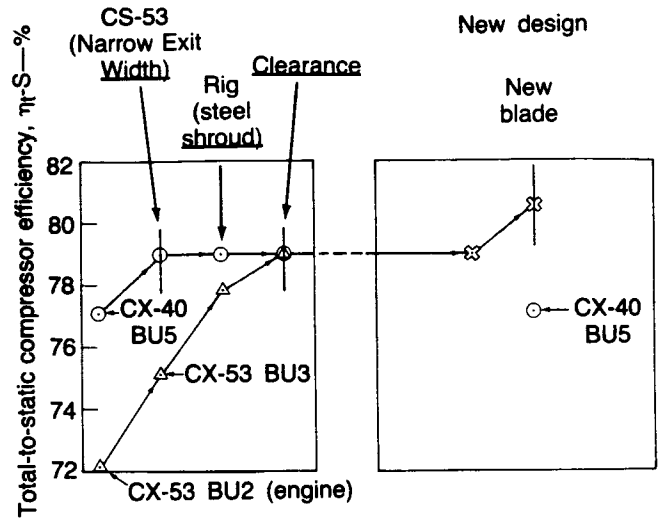
TE86-2892

Figure 42. AGT 100 compressor.



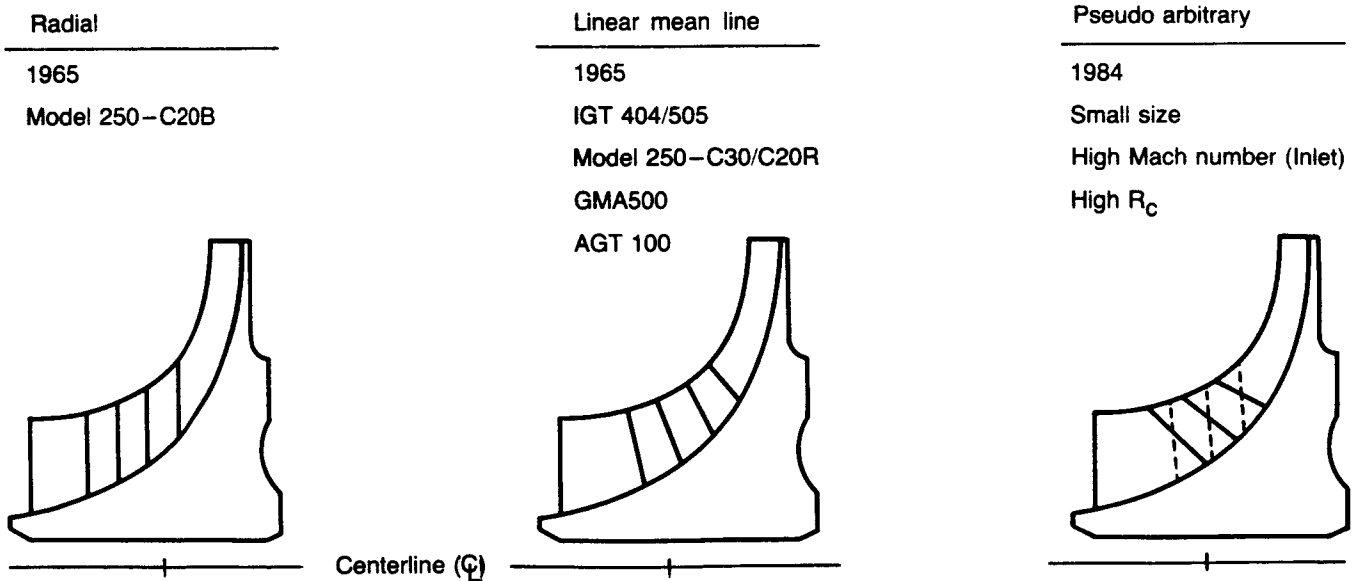
TE86-2891

Figure 43. Steel insert in aluminum front cover of CX-53 compressor rig.



TE86-2893

Figure 44. AGT 100 compressor design point efficiency predictions.



TE86-2894

Figure 45. AGT 100 compressor impeller design evolution.

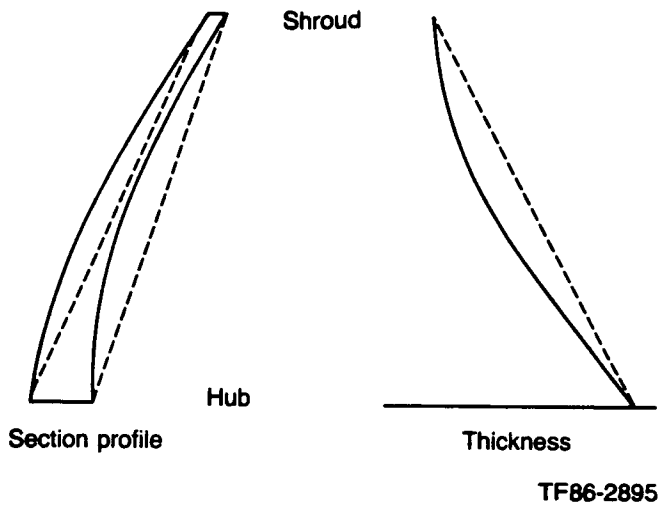


Figure 46. AGT 100 compressor arbitrary blade study—leading edge.

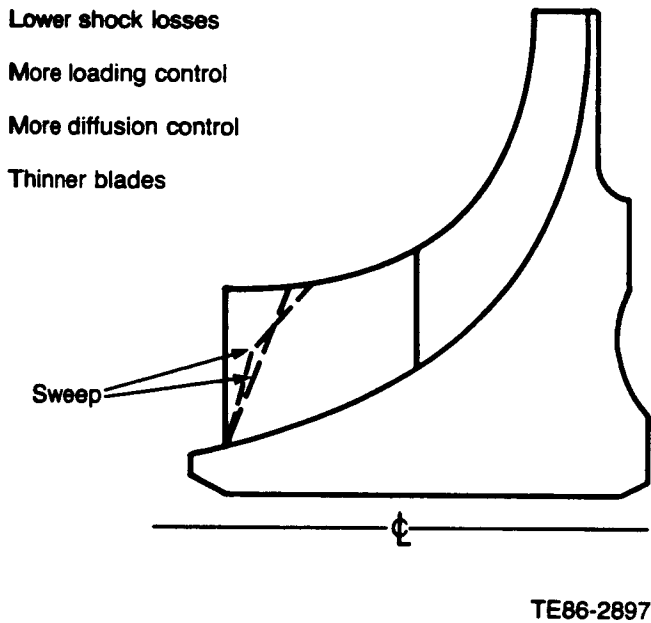


Figure 48. Impeller leading edge sweep concept.

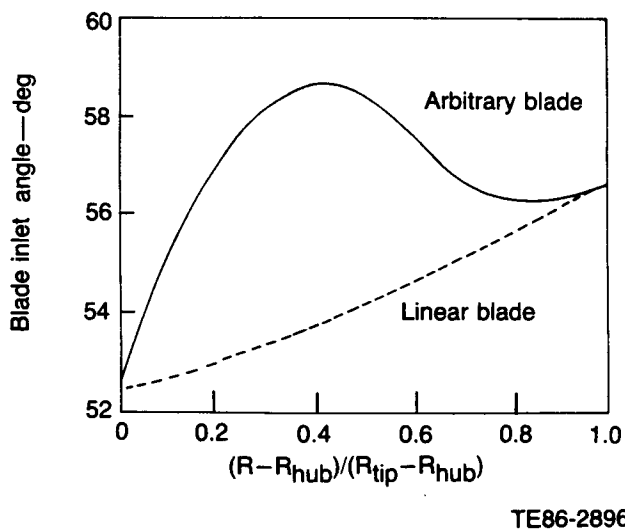


Figure 47. Impeller inlet blade angle distribution for arbitrary blade study.

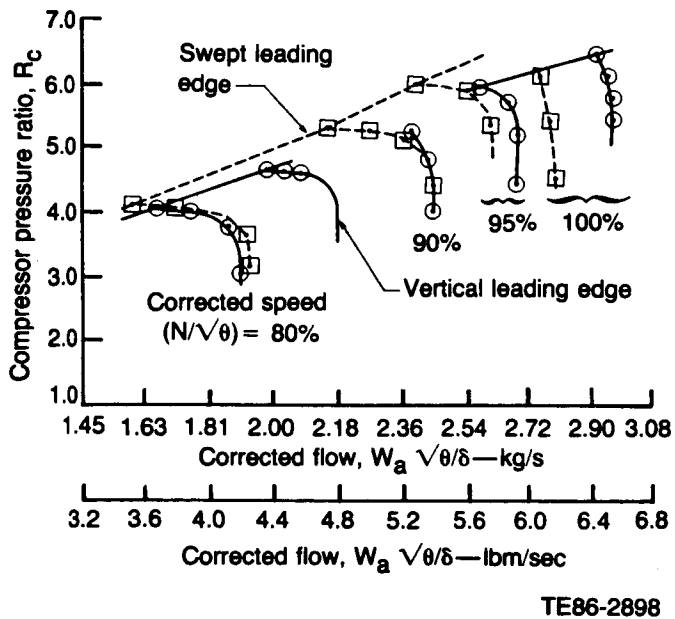
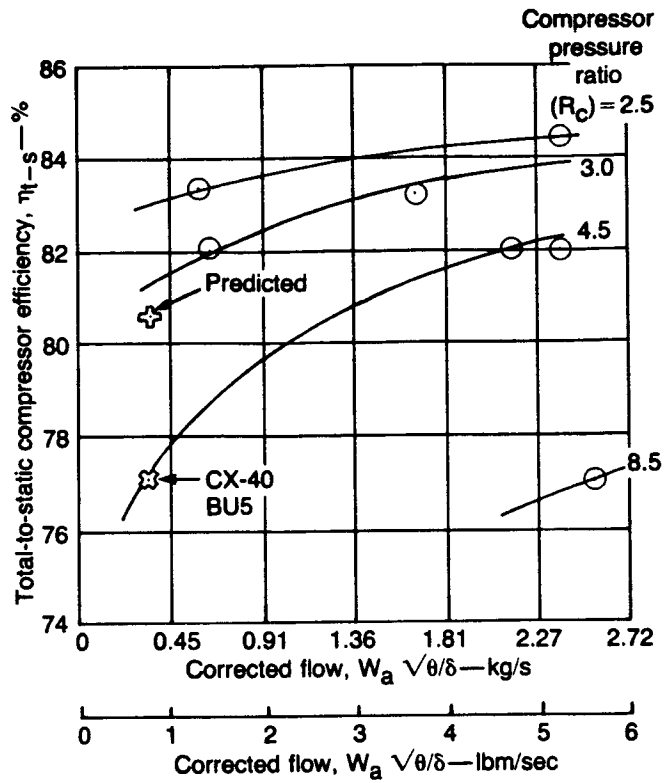
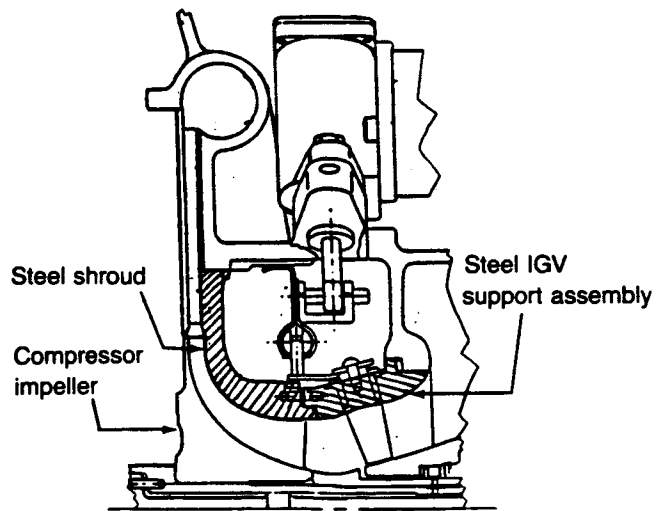


Figure 49. Leading edge sweep performance.



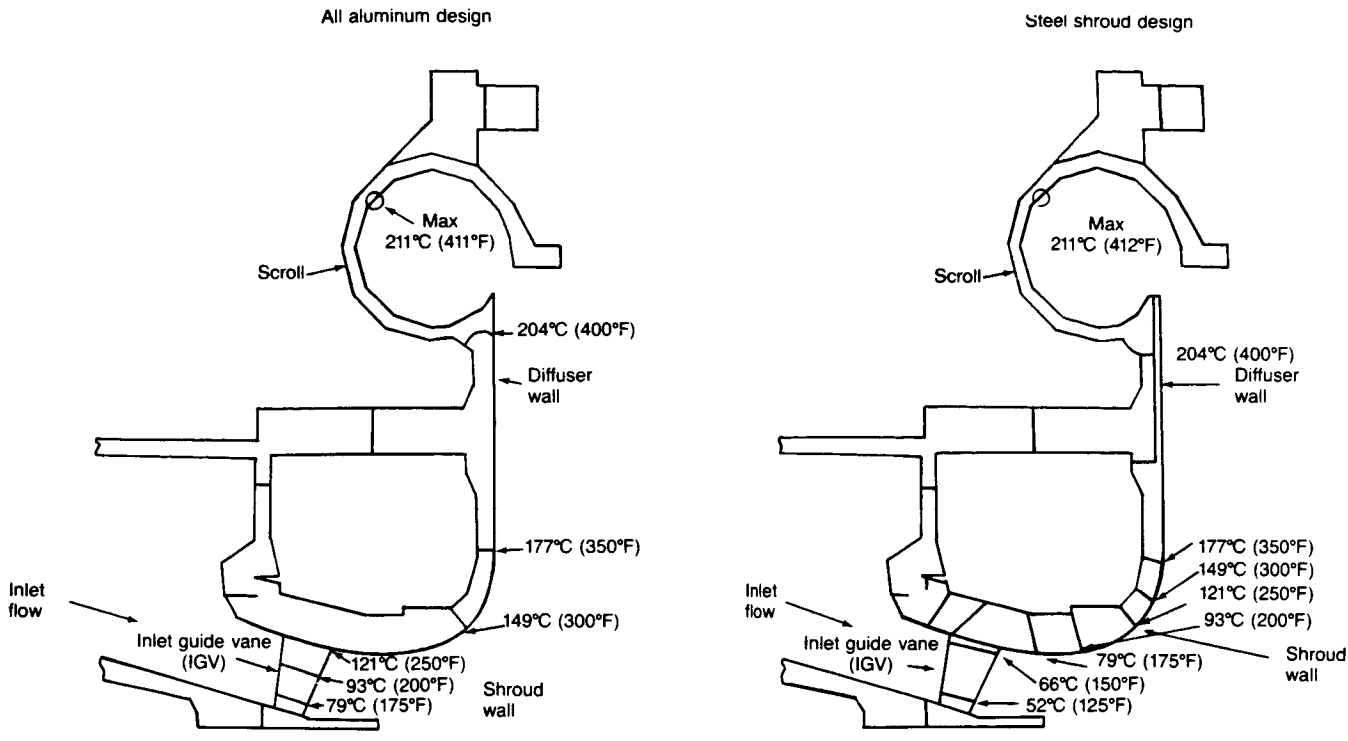
TE86-2899

Figure 50. AGT 100 compressor flow size as a function of total-to-static compressor efficiency.



TE86-2491

Figure 51. Steel shroud insert design.



TE86-2842

Figure 52. Comparison of steel and aluminum compressor shroud isotherms at max power, 100% N1, steady-state condition.

IV. GASIFIER TURBINE DEVELOPMENT

4.1 GASIFIER TURBINE AERODYNAMIC DEVELOPMENT

Gasifier turbine aerodynamic development during this reporting period included performance improvements through redesign of the vanes and characterization of performance sensitivity to various vane and rotor running clearances.

Results from previous rig testing, as presented in Figure 53, identified the gasifier turbine vane as a high (relative to design) efficiency loss element. As a result of a comparison of the gasifier turbine vane design with the more efficient power turbine vane

design two items have been identified that have the potential for improving the gasifier turbine performance. These two design changes involve a reduction in trailing edge blockage from 10.8% to 7.3% and a reduction of downstream turning (suction surface camber downstream of the throat) from 10 deg to 0 deg. These two objectives are being accomplished by using an existing cambered vane configuration (see Figure 54) from an existing turbocompound engine radial turbine. Modified turbine rig hardware is being fabricated to accept these vanes as the turbine size is coincidentally nearly identical to that of the AGT 100.

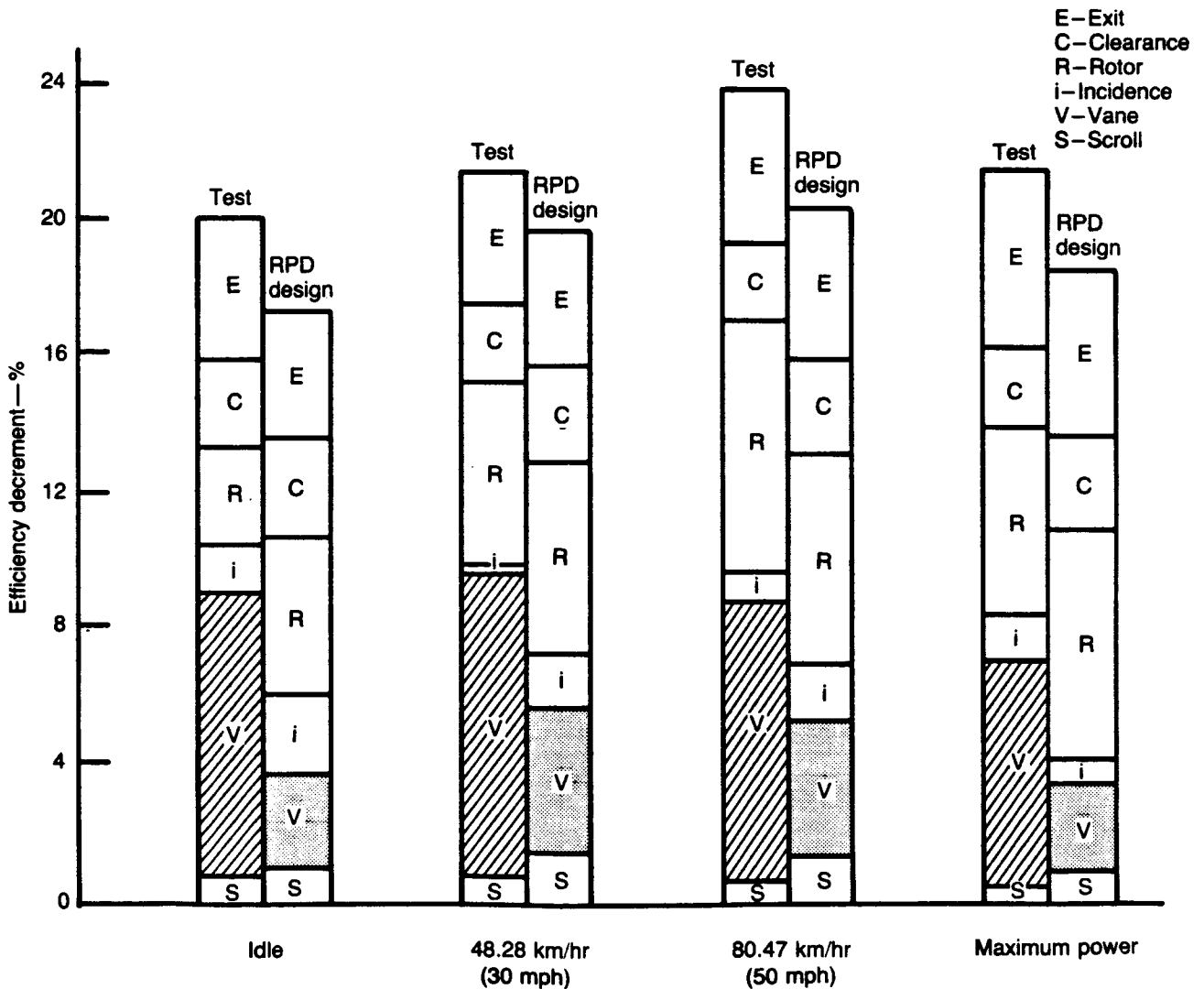


Figure 53. Loss analysis results based on gasifier turbine rig data.

TE86-2492

The planned test series will also experimentally characterize the sensitivity of performance to running clearance; a design parameter particularly important for ceramic turbine design. These tests are designed to examine three critical areas: (1) vane slot clearance, (2) rotor axial clearance, and (3) rotor radial clearance, as depicted in Figure 55. Vane slot leakage testing will be initially investigated with clearances similar to those in previous rig testing. Further testing will investigate the effects of both increased and sealed clearances. Axial rotor clearance performance sensitivity tests will be conducted using increased clearances obtained by shimming. Radial rotor clearance effects will be tested with normal axial clearances but with a trimmed shroud.

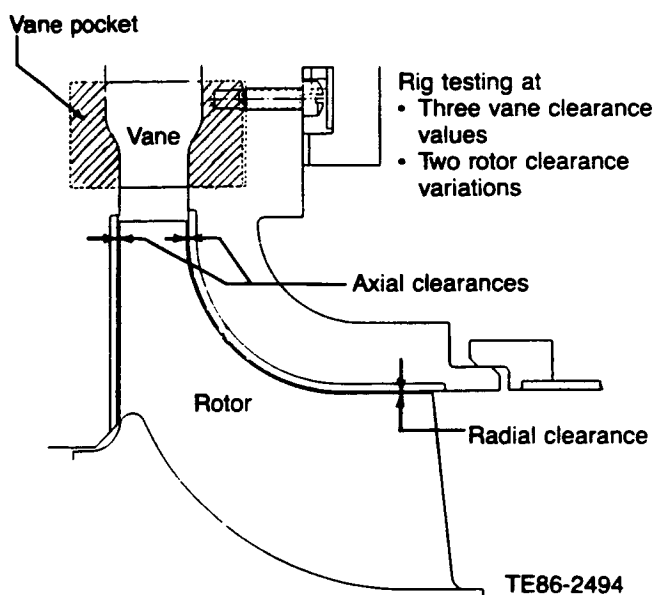


Figure 55. Gasifier turbine rig configuration.

4.2 GASIFIER TURBINE MECHANICAL DEVELOPMENT

Gasifier turbine mechanical development during this reporting period concentrated on vibration/balance activities.

4.2.1 Vibration/Balance Activity

Overview. As described in the 1984 annual report consistent achievement of 100% gasifier speed (N1) from build to build has not been possible. While two engine builds have successfully run to 100% N1 (S/N-1, BU8, and BU11), other engine builds have encountered speed limitations due to excessive vibration and/or gasifier shaft whip. Several studies (both analytical and experimental) have been undertaken to eliminate this undesirable gasifier behavior. As gasifier assembly balance is considered to be of critical

importance, changes have been made to improve the balance procedure of the gasifier engine section, which is depicted in Figure 56. Additionally, balance fixture equipment has been modified, and a new balance machine with increased capacity has been procured.

A significant balance milestone was attained during this reporting period, namely the amount of gasifier assembly rigid body dynamic imbalance, as installed in the engine prior to test, can now be determined. This was accomplished through the use of the new balance procedure, the modified balance fixture, and the new balance machine. As a result, it is now possible to obtain and verify rotor imbalances well within print allowable limits (.085 gm-in.) for gasifier assemblies as final assembled for engine test. One gasifier assembly (S/N 1, BU14) was successfully rigid body balanced to the capabilities of the balance machine by making small final balance corrections in the accessible blade channels. (The main balance correction planes are inaccessible when the gasifier assembly is final assembled in the bearing support). Unfortunately, this level of rigid body balance improvement had little or no effect on vibration and/or whip limits and engine testing is still limited to speeds below 100% N1.

In an effort to gain additional insight into the nature of the vibration and whip, one of the test engines (S/N 2, BU13) was equipped with additional instrumentation to measure squeeze film deflection, case motion, rotor rotational response, coupling

Cambered airfoils designed and tested in turbocompound turbine reset for proper flow capacity

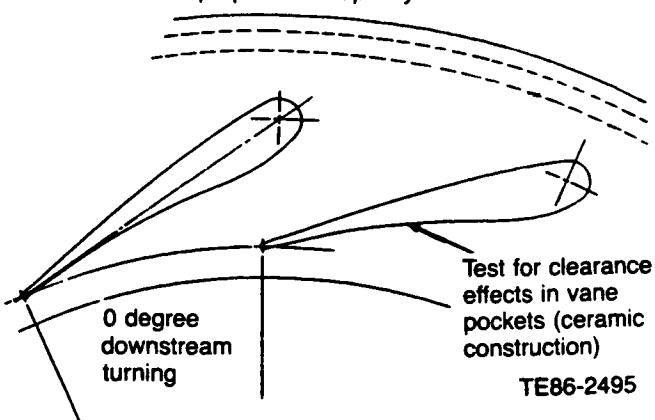


Figure 54. Rig layout of cambered vane set.

shaft whip, and shaft rotation/whip phasing. An engine test with this additional instrumentation was performed near the end of the reporting period. The analysis resulting from this test indicates that the vibration levels encountered are primarily due to rotor imbalance and are not significantly amplified by rotor or case resonance.

As the gasifier assembly balance was determined to be well within limits as a rigid body before engine testing, it is apparent that this type of balance of the gasifier assembly is not sufficient to eliminate vibration/whip problems. Thus, new techniques relative to balancing will be explored during the next reporting period. These include the effect of the gasifier pinion shaft on the gasifier assembly balance, the determination of a method to balance the assembly while minimizing internal force couples, and the

feasibility of performing a high speed balance. The first technique addresses the potential imbalance that may arise because the gasifier pinion shaft is balanced only as a detail part, not with the gasifier assembly as a whole unit. The latter two techniques are intended to correct vibration/whip problems that may arise because the gasifier assembly is not perfectly rigid and may be deflecting at high speeds due to internal force couples that cannot be detected by rigid body low speed balancing. The gasifier assembly bow produced can in turn produce additional imbalance. For example, at 100% N1 (86,256 rpm) an internal force couple of only 0.1 gram-in. resulting from an imbalance in any plane produces a corresponding unbalanced force of 21 kg (47 lb) in that plane; thus, significant forces can be developed by relatively small imbalances. The current balance procedure is not capable of removing such internal imbalances but

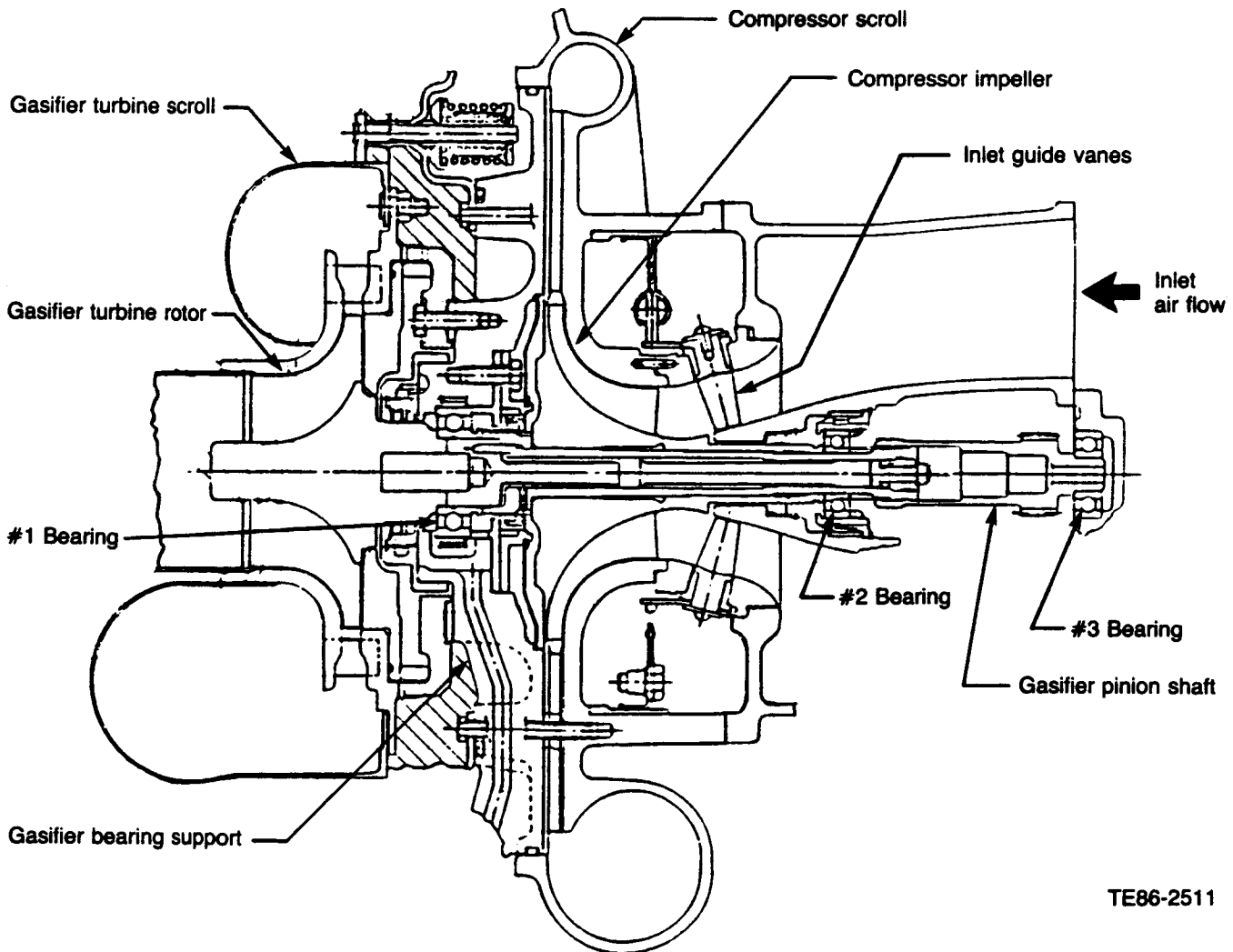


Figure 56. Gasifier engine section.

TE86-2511

only ensures that they cancel in such a way that the net reaction at the bearings is zero. Because of the fixed and localized nature of the balance correction planes, the distributed nature of the source imbalance, and the inability of any balance machine to identify the source of the unbalance, internal force couples will almost always be present with a low speed balance. Thus, the latter two techniques will be considered for minimizing or counteracting the undesirable effects of such force couples.

BALCO Consultation and Balance Study Results. As previously reported, Allison enlisted The Balancing Company, Inc (BALCO) to study the gasifier assembly balance procedures. BALCO specializes in balancing rotors and was requested to recommend methods for ensuring adequate balance during engine testing.

Allison supplied BALCO with a gasifier assembly for use in its balance investigation. Balco's activity included balance repeatability studies and assessment of the feasibility of balancing the assembly on engine bearings. This activity included balance studies when disassembling and reassembling the gasifier, tightening and loosening the tiebolt nut, changing tiebolt nuts, axially shocking the assembly with a hammer, rotating the impeller relative to the turbine, rotating the bearing races, and varying the balancing speed with the gasifier unit assembled with the entire No. 1 engine bearing.

The results of the repeatability studies were consistent with Allison's balance studies and practice. Balance repeatability was determined to be within the allowable balance limit (.085 gm-in.) at each bearing plane for the disassembly/reassembly sequence using a given set of hardware. Balance repeatability is considered to be important because of the present requirement of disassembling the rotor after balancing for subsequent installation in the engine bearing support. A large change in balance was detected when the No. 1 engine bearing replaced the No. 1 dummy bearing. This balance change was not unexpected and has led to the investigation of alternate balancing methods that eliminate the use of the dummy races in the balancing procedure.

BALCO also indicated that the present gasifier mechanical design appeared sound with regard to balance and that the permitted amount of imbalance was reasonable; however, they recommend elimination of disassembly after balancing. An extensive redesign of the gasifier support structure would be required to accommodate such a change. Thus, initial balancing of the gasifier assembly will normally require disassembly of the gasifier section and removal from the bearing support due to the magnitude of imbalance typically present and the corresponding

necessity to gain access to the balance correction planes. However, after initial balancing and reassembly in the bearing support, additional minor balance corrections will be made without further disassembly by removing small amounts of mass from the accessible impeller and turbine rotor flow paths.

Other BALCO balance study conclusions are as follows:

- axial shock of the assembly produced small changes in balance but was not effective in seating the components
- balance changed significantly with tiebolt nut torque but was generally repeatable when fully torqued
- balance changes produced by exchanging tiebolt nuts were essentially insignificant when fully torqued, indicating that balance changes with torque were not due to individual nut anomalies
- rotation of the No. 1 engine bearing inner race 180 deg produced balance changes on the order of twice the balance limit at the No. 1 bearing plane, indicating that even high quality engine bearings must maintain their position relative to the other components subsequent to balancing
- balance continued to change significantly when the entire No. 1 engine bearing was used until stabilization occurred above approximately 1800 rpm, indicating that there is a minimum acceptable speed required for balancing on the entire ball bearing when no axial load is applied

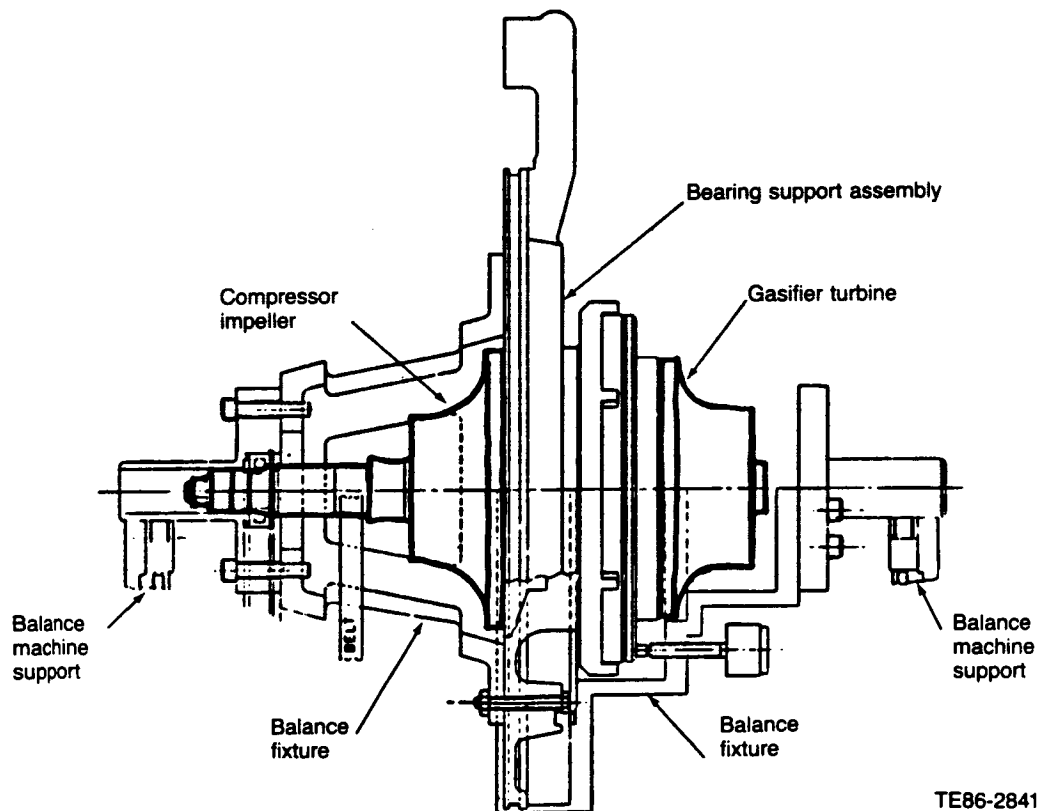
Balance Procedure Changes. The procedure used to balance the AGT 100 gasifier assembly has undergone continual evolution, becoming increasingly more sophisticated with time. Early builds balanced the two major detail assemblies (impeller assembly and gas turbine rotor assembly) about their detail axes, built the gasifier assembly on dummy bearing races, balanced it, and then reassembled the gasifier assembly with engine bearings in the engine. Imbalance introduced by a change in the rotational axes caused by variations between the dummy bearings and engine bearings, or build nonrepeatability effects, was left uncorrected. Additionally, the imbalanced state of the gasifier assembly as installed in the engine was unchecked and unknown. Despite this early, nonrigorous balance technique, two engine builds successfully ran to 100% N1, S/N 1, BU8 and BU11. However, a number of other builds that used this identical procedure were not successful in attaining full gasifier speed. Engine S/N 1, BU11 was also the first build incorporating a squeeze film damper (SFD) in place of spring bar isolators at the No. 2 bearing location. However, subsequent builds of both test engines using the SFD have been limited to speeds below 100% N1.

A balance fixture was designed to allow the gasifier assembly imbalance to be checked while assembled for engine test. The balance fixture supports the gasifier assembly as installed in the engine bearing support structure and is placed on the balance machine to check the gasifier assembly imbalance. The gasifier assembly, as it appears in the balance fixture, is depicted in Figure 57. Initial usage of the balance fixture was not successful; indicated imbalances varied greatly with rotational speed. Modifications were subsequently made to the balance fixture to permit it to completely support the gasifier assembly at both ends, and a new balance machine with greater rotor weight and combined weight and speed capacity was procured. These modifications and additions successfully allow the balance fixture to be used to recheck the balance of the gasifier assemblies as assembled on engine test build and teardown. The balance fixture was used extensively during this reporting period.

The balance procedure was extensively revised during this period to eliminate the dummy bearings

from the balance procedure and to balance the gasifier assembly as assembled for engine test. These balance procedural changes now incorporate the balance fixture as a key part of the balance process. The balance procedure consists of the following steps:

1. The impeller assembly and gas turbine rotor assembly are individually balanced as detail parts upon initial usage.
2. The impeller/turbine orientation requiring the least amount of balance correction is selected.
3. The gasifier assembly, assembled in the bearing support and balance fixture, is temporarily corrected with balance weights.
4. The gasifier assembly is disassembled for access to the balance correction planes. Corrections determined in step 3 are performed.
5. The gasifier assembly is reassembled in the bearing support and balance fixture for a final check balance. Small corrections are made in the blade channels if required.



TE86-2841

Figure 57. Gasifier assembly balance fixture.

The new balance procedure is very successful in producing gasifier assemblies that possess a high degree of rigid body dynamic balance about their actual engine test rotational axes.

4.2.2 Summary of Engine Builds and Test Experience

Engine S/N 1, BU13. This was the first AGT 100 engine build to successfully employ the balance fixture to verify the imbalance of a gasifier assembly of an as-assembled build ready for engine test. (The modified balance fixture had been successfully used on S/N 2, BU8 to check balance the as-assembled gasifier assembly prior to engine test. However, this build was the first to incorporate a ceramic rotor, and testing was not planned to exceed 60% N1. Thus, balance requirements were less stringent and no rigorous balance program was conducted on BU8 to achieve minimal imbalance). The new balance procedure was employed twice during BU13 to balance the rotor assembly to an acceptable level. The first balance procedure reduced the imbalance at the No. 1 bearing from 23 to 4 times the print limit. The imbalance at the No. 1 bearing is usually greater than the imbalance at the No. 2 bearing since most of the rotor mass is supported by the No. 1 bearing. The second balance procedure successfully reduced the imbalance at the No. 1 bearing to approximately the allowable limit; final imbalance at the No. 2 bearing was less than 0.33 times the limit.

Subsequent engine testing failed to obtain full speed as vibration limited the gasifier speed to 84% N1. A teardown check balance of the gasifier assembly in the balance fixture indicated that its imbalance had increased during engine testing to approximately two and one half times the allowed limit. However, all BU13 and teardown (TD) 13 balance activities were performed on the old balance machine as the new, larger capacity machine was not operational at the time. Thus, the accuracy of all check balance measurements are suspect due to the old balance machine limitations.

Engine S/N 2, BU9 through TD11. BU9 was the second AGT 100 engine build to successfully employ the new balance fixture and procedure. The initial employment of the balance procedure reduced the imbalance at the No. 1 bearing from four to two times the allowable limit. Additional balance corrections, performed by removing stock from the turbine flow path without disassembling the gasifier assembly, reduced the imbalance at the No. 1 bearing to just under the allowable limit. The final imbalance at the No. 2 bearing was less than half of the allowable limit.

No attempt was made to run at full gasifier speeds during BU9 and BU10 as the associated tests were

devoted to thermal cycle testing of a ceramic gasifier scroll package with speeds intentionally limited to 60% N1. The ceramic scroll package was replaced with metal components in BU11 to facilitate another attempt to attain full gasifier speed; the test was aborted due to a seized power turbine rotor. The gasifier assembly had not been disassembled since it was balanced for BU9. Subsequent check balance of the gasifier assembly on TD11 indicated that the imbalance magnitudes at the bearings were essentially the same as on BU9. Again, the accuracy of the BU9 and TD11 check balance measurements are suspect because the new, high capacity balance machine was not operational.

Engine S/N1, BU14 through TD15. The gasifier assembly from BU13 was rebalanced for BU14; disassembly was not necessary. Rebalancing to the allowable limit was accomplished by removing stock from the turbine rotor blade channel. After removal from the balance machine, a decision was made to improve the balance down to the machine limits, theoretically one-tenth that of the print limit. When the gasifier assembly was replaced on the balance machine, however, the indicated imbalance at the No. 1 bearing had increased by one-third. This unexpected increase in imbalance was determined to have resulted from several deficiencies built into the old balance machine. Variations in machine drive belt tension and pedestal height, and the process of removal/reinstallation of the gasifier assembly itself were found to have significant effects on the indicated imbalance. Suspected limitations of this low capacity balance machine were confirmed and it was removed from further use. The new balance machine with increased capacity was then available and placed in operation. The same BU14 gasifier assembly was used to conduct similar tests on the new machine. Indicated imbalances as determined by the new machine were virtually unaffected by any of the factors previously identified.

The gasifier assembly was rebalanced on the new machine without disassembly by removing additional stock from the turbine blade channel. Indicated imbalances near one-tenth the allowable limit were obtained. Subsequent engine testing, however, was again speed limited when vibration limits were exceeded near 84% N1. The gasifier assembly was not removed from the engine until TD15. A check balance could not be performed on TD15 because the No. 1 bearing was damaged as a result of a No. 1 seal failure.

Engine S/N 2, BU12. This build incorporated the second Sohio ceramic rotor to undergo engine testing. No rigorous balance procedure was conducted

to minimize imbalance since the test plan did not require the gasifier to exceed 60% N1.

Engine S/N 1, BU16. This build incorporated the first Kyocera silicon nitride ceramic rotor. The gasifier assembly was balanced using the new balance procedure and the new balance machine. The initial balance attempt reduced the imbalance at the No. 1 bearing from 12 to 1.4 times the allowable limit and from five to two-thirds the allowable limit at the No. 2 bearing. No additional balancing was attempted so as to avoid damage to the ceramic rotor, and, additionally, the test was planned to be conducted at reduced speed. Shaft whip measured 5 mils at 70% N1; it is expected that the 7-mil limit would have been exceeded before full speed was achieved. The speed was limited to 70% N1 because of measured high power turbine backplate pressure. This measurement was subsequently determined to be erroneous. A teardown check balance indicated that the No. 1 bearing imbalance had increased by a factor of three and the No. 2 bearing imbalance by a factor of two.

Engine S/N 2, BU13 and BU14. Special instrumentation was included in BU13 to study the gasifier assembly vibration/whip response during engine operation. The gasifier assembly was balanced to approximately 0.5 times the allowable limit at the No. 1 bearing and 0.35 times the allowable limit at the No. 2 bearing. Subsequent engine testing was limited to 90% N1 due to excessive vibration and whip. Data analysis was not completed during this reporting period, but initial indications are that the response is due to imbalance and not to resonance of the gasifier assembly or support structure. Additionally, the squeeze film damper at the No. 2 bearing does not appear to be bottoming.

The same gasifier assembly was used for BU14 without rebalancing as BU14 was a ceramic scroll package test in which high speeds were not required. BU14 engine testing was not completed during this period and a teardown check balance has not been performed.

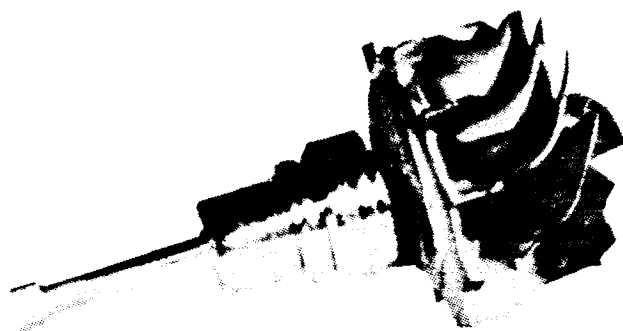
Engine S/N 1, BU17. This was the second engine build to incorporate the Kyocera silicon nitride ceramic gasifier rotor first run in S/N 1, BU16. Prior to installation in BU17, the gasifier assembly was rebalanced. By repeating the balance procedure and making small final corrections in the rotor blade channels, a near-perfect rigid body balance was achieved (the measured imbalance approached the limits of the balance machine's capabilities). The gasifier assembly in this state was installed in BU17, but engine testing was not initiated during this reporting period. Engine test plans include an attempt to achieve 100% N1.

4.3 CERAMIC GASIFIER TURBINE DESIGN

4.3.1 SiC Gasifier Turbine Engine Test and Postfailure Investigation, S/N 2, BU12

Rotor S/N FX34360 was installed in engine S/N 2, BU12 and ran for approximately one hr at idle conditions (also see section 2.2.2). Post-test teardown inspection revealed failed inducer blade tips as shown in Figure 58. However, the remainder of the rotor, including the exducer region of the airfoils, was intact. The rotor-shaft attachment was structurally sound and no damage downstream of the blade tips was observed.

Post-test investigation considered several phenomena in an attempt to identify the cause of the inducer tip failure. These included thermal shock, overspeed, airfoil rub, material strength/ flaw, foreign object damage (FOD), and vibration response to vane passage. It was concluded that FOD was the probable failure mode, vibration was a potential mode, and the other phenomena had only a remote probability of contributing to the failure.



VS85-893

Figure 58. Condition of the ceramic rotor assembly after engine testing.

The dynamic characteristics of the airfoil were both analytically and experimentally assessed through use of two-dimensional (2-D) and three-dimensional (3-D) finite element simulation and bench tests, respectively. The 2-D simulation successfully predicted the airfoil natural frequencies (substantiated by bench test), and the frequencies are presented as a function of rotor speed on an interference response diagram in Figure 59. This diagram identifies the particular rotor speeds at which the natural fre-

quencies of the rotor airfoil would be coincident with the periodic pulse resulting from the 18-vane passage. Examination of the engine test records identified the 31,000 to 38,000 rpm speeds as the likely range for fracture of the inducer tips. This was based on data for engine vibration, rotor whip, temperatures, and power. This speed range is identified in the figure as the event—the probable inducer tip fracture event. It is not coincident with inducer response to vane passage.

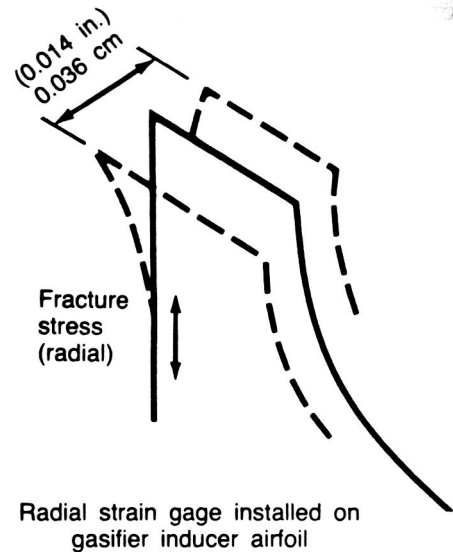
The nature of the response of the inducer airfoil at its resonant frequency was experimentally investigated. The objective of the tests was an assessment of the fracture stress and the corresponding analytic probability of survival for the measured fracture stress. Four airfoils were instrumented with radially oriented strain gages placed at the maximum stress location and then were excited at their natural frequencies. The excitation was increased until fracture occurred. The airfoils failed between 289.6 MPa (42.0×10^3 lb/in.²) and 326.1 MPa (47.3×10^3 lb/in.²) with a tip double amplitude of 0.356 mm (0.014 in.) (Figure 60).

Three-dimensional finite element models, as shown in Figure 61, were used to assess the probability of survival of the airfoil in the first mode for the observed tip deflection. The partial cube (3-D) inducer finite element model (FEM) was shown to accurately model the mode shape and frequency of the more complex full airfoil model. Mean probability of survival, calculated at ± 319.9 MPa (46.4×10^3 lb/in.²) (which corresponds with observed tip amplitude at fracture) would seem to indicate that inherent average rotor blade strength was only 71% of the material characteristic strength as determined from modulus

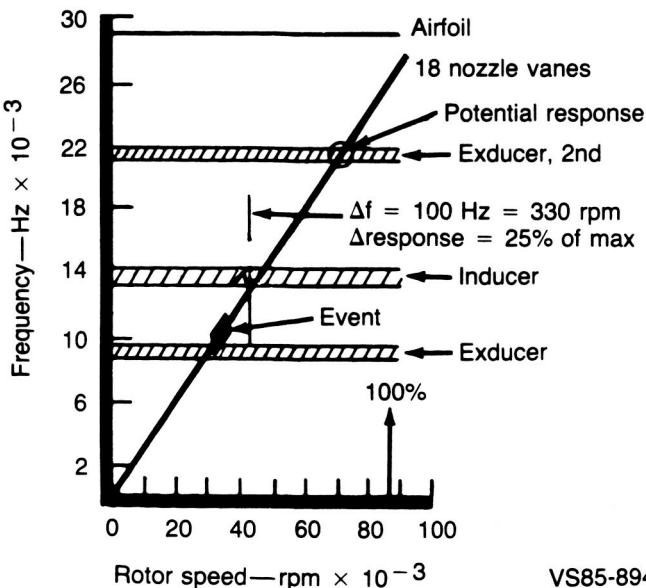
of rupture (MOR) test bars. The 71% MOR correlates with the rotor material strength deduced from spin burst characterization tests. It is unlikely that the ± 319.9 MPa (46.4×10^3 lb/in.²) level of inducer excitation was present in the engine at the failure event (see Figure 59); therefore FOD was concluded to be the probable failure mode.

FOD Failure Mode Investigation. A bench test investigation is being conducted to investigate the nature of impact failure of gasifier turbine inducer airfoils made from SiC material. A containment (coffin)

Dynamic fracture stress (4 airfoils)
first inducer mode
290–326 MPa ($42,000$ – $47,300$ lb/in.²)



VS85-895A

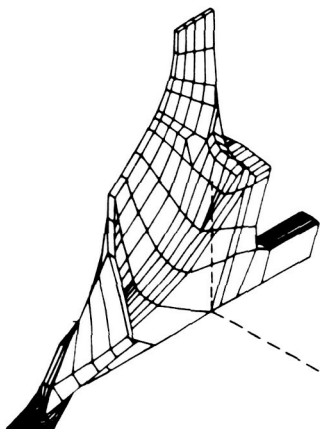


VS85-894

Figure 59. Ceramic rotor airfoil natural frequencies.

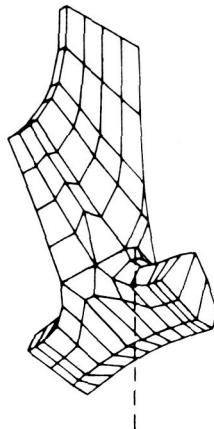
Figure 60. Ceramic rotor inducer blade dynamic fracture test.

Full cube
finite element model
(statics)



Elements = 514
Nodes = 2479
DOF* = 6160

Partial cube inducer
finite element model
(dynamics)



Elements = 60
Nodes = 523
DOF = 1347

*DOF = degrees of freedom

For an airfoil stress of ± 320 MPa ($\pm 46,400$ lb/in²) and the following MOR strengths the resulting probability of survival (POS) is:

Rotor Material Strength	POS
100% MOR	0.94
71% MOR	0.50

VS85-896A

Figure 61. Probabilistic assessment of dynamic fracture test results.

rig (Figure 62) has been developed for FOD testing. The purpose of these tests is to determine the relationship between rotor speeds and foreign object particle sizes that cause rotor failure upon impact.

The coffin rig is built with the axis of rotor rotation parallel to the base of the coffin. The rotor is bonded to an arbor and spin driven. The dropping mechanism is basically a trap door arrangement, actuated by a solenoid, allowing the particle to free fall without any initial velocity. FOD particles investigated include steel ball bearings and shot varying in size from 0.406 mm (0.016 in.) to 3.175 mm (0.125 in.) in diameter. A thick, wax ring encircles the rotor to catch the FOD particle as it is deflected from the inducer tips, as well as any resulting rotor debris. This technique reduces the probability of secondary impacts. The coffin rig is evacuated to less than 1 mm (0.039 in.) of mercury, absolute pressure, by a combination of two vacuum pumps.

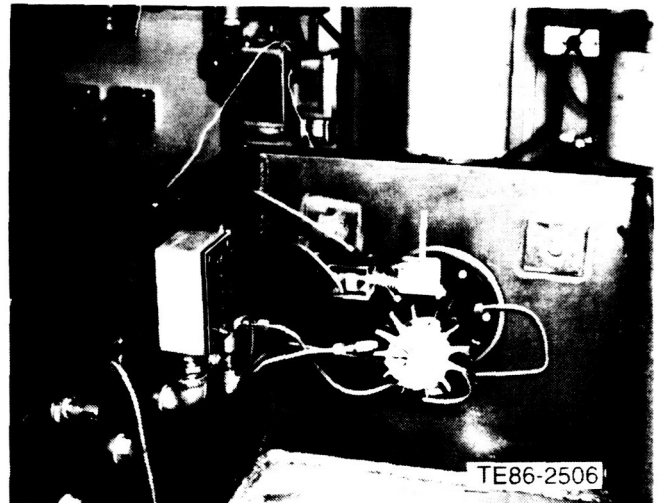


Figure 62. Foreign object damage rig used to investigate potential impact damage to the ceramic gasifier rotor.

Documented impact tests were performed primarily on four silicon carbide gasifier rotors previously proof-tested to between 94,000 and 95,000 rpm. These impact tests were conducted at rotor speeds varying between 35,000 to 90,000 rpm. Impacting particle size varied from 0.4699 mm (0.0185 in.) to 3.175 mm (0.125 in.) in diameter. An example of rotor damage sustained during testing is presented in Figure 63. A preliminary data curve representing the relationship between rotor speed, particle size, and the onset of rotor damage is presented in Figure 64. Testing will be continued during the next reporting period to further characterize the nature of impact failure and substantiate the preliminary data results.

Airfoil Vane Passage Response Investigation. As gasifier (SiC) inducer airfoil vibration is considered a potential failure mode a FOD-free test is planned to investigate airfoil response to potential vane excitation pulses. This is an experiment designed to observe the dynamic response of the inducer airfoils in a clean engine environment. The engine will be motored to approximately 50% N1 with no combustion and a fine screen installed over the scroll inlet to preclude particles from passing through the nozzle vanes and impacting the gasifier airfoils. The goal is to demonstrate a sufficient lack of airfoil response to vane excitation at rotor critical speeds coincident with the inducer first response mode. It is planned to conduct this test during the next reporting period. Testing will be conducted with nine and eighteen vanes installed in the scroll. With nine vanes, half the normal complement, the coincidence of inducer and vane passage frequency will be well above the operating speed range.

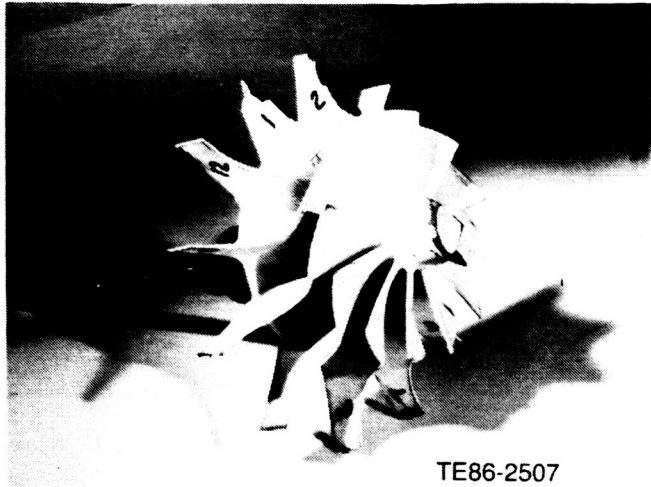


Figure 63. Airfoil damage resulting from FOD impact, SiC gasifier turbine.

Thickened Airfoil Design. The design of a thickened airfoil has been implemented for potential improvement in impact resistance. The design criteria were: (1) no increase in the airfoil stress levels and hence no change in the airfoil taper ratio and (2) no change in the flow controlling exducer throat area. The resulting thickness increase is graphically illustrated in Figure 65. In addition to the potential improvement in impact resistance (which will also be experimentally determined), the stiffened airfoil shifts the first inducer mode well above the operating range as shown in Figure 66. Processing of rotors incorporating this thicker airfoil is discussed in section 9.2.1.

4.3.2 Silicon Nitride Gasifier Turbine

Two attachment designs are being analyzed for joining the Si_3N_4 rotor to the metal (Inco 907) gasifier shaft, as illustrated in Figure 67. Both use an air gap to reduce heat flux from the gasifier rotor into the compressor shaft. One design uses a braze joint and the other an interference fit. Both designs are being analytically evaluated to assess the effects of rotor dynamics, heat transfer, and stress. The calculated rotor assembly resonant dynamic modes (and corresponding frequencies) for the brazed configurations and interference fit are presented in Figures 68 and 69, respectively. The first three modes shown consist of the two rigid body modes and the first bending mode. All modes are outside the engine operating speed range; the first bending mode is predicted to occur at 130% N1. This is considered a desirable and safe margin.

Stress analyses of the Si_3N_4 rotor and shaft attachment during this reporting period have been focused on the interference fit configuration. Calculated

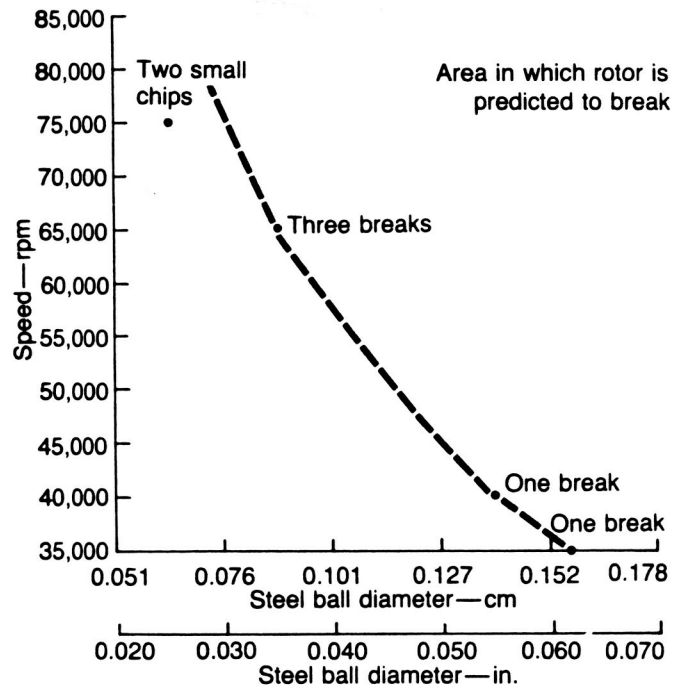
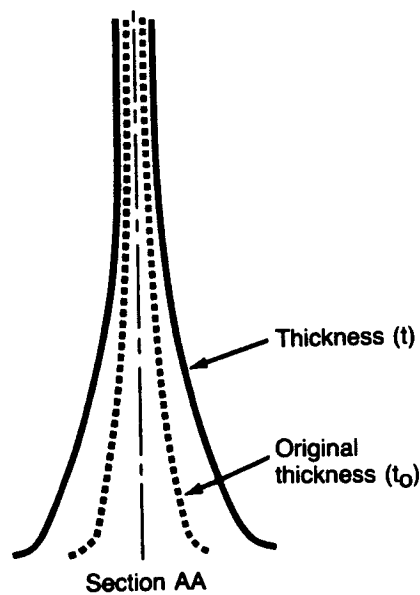
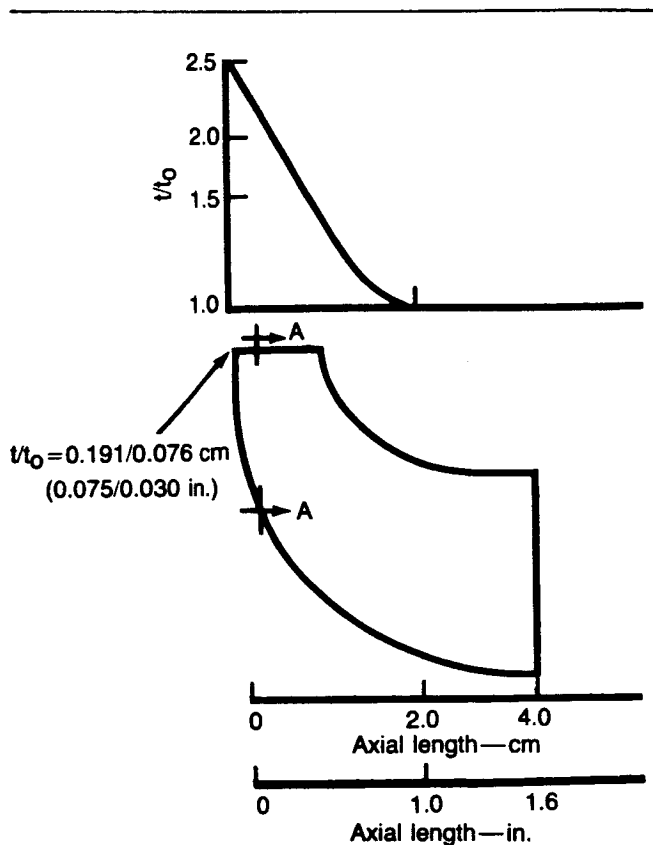


Figure 64. Bench test FOD rig preliminary results using a gasifier rotor made from SiC material (zero initial velocity on balls).

stresses for both the rotor and shaft at 100% speed, steady-state operation, and 1080°C (1976°F) turbine inlet temperature (TIT) are presented in Figures 70 and 71, respectively. The predicted stresses are well within acceptable levels.

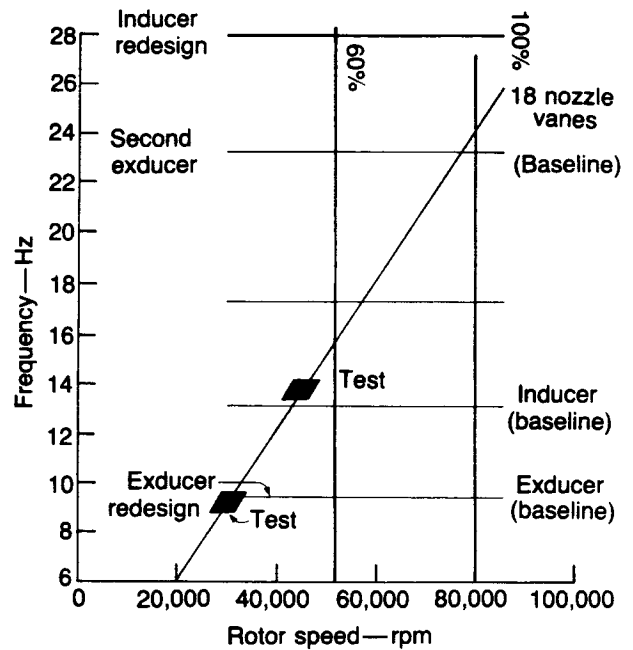
The Kyocera braze joint configuration is based on results of their turbocharger experience. The configuration features an air gap between the rotor and shaft to reduce heat flux into the shaft. Steady-state thermal analysis, Figure 72, at 100% speed and 1287°C (2350°F) TIT predicts the shaft temperature at the bearing location to be 210°C (410°F), approximately the same level as the SiC rotor system for the same operating conditions. The steady-state temperature distribution for the interference fit attachment configuration at 100% speed and 1080°C (1976°F) TIT is depicted in Figure 73.

Airfoil natural frequencies were calculated for the finished machined Si_3N_4 rotor, and the results are shown in Figure 74. The interference diagram compares the calculated frequencies with possible vane passage excitation throughout the rotor speed range. Potential resonant response of the third and fourth modes is possible within the engine operating range. The calculated mode shapes for these modes are presented in Figure 75.



VS85-897A

Figure 65. Modified inducer blade thickness.



Note: All test data from baseline turbine.

TE86-2509

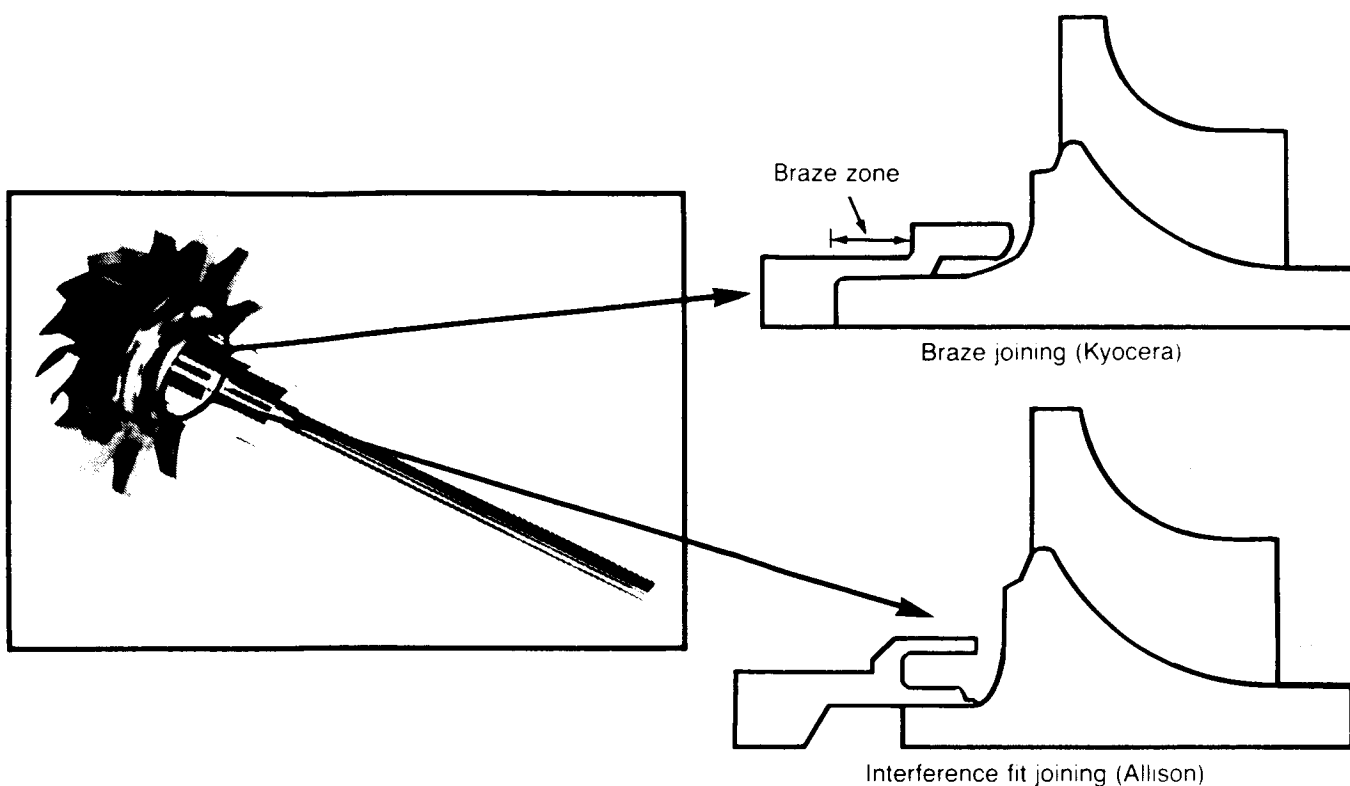
Figure 66. Campbell diagram, redesigned (thickened) inducer region airfoil, SiC gasifier rotor.

In preparation for engine testing, the rotor airfoil natural frequencies were also bench test measured. These data are also shown in Figure 74. The measured natural frequencies of the first inducer and exducer resonant conditions are higher than the calculated frequencies because the calculated frequencies were based on the specified airfoil thickness of 0.76 mm (0.029 in.) whereas the actual thickness was 1.0 mm (0.039 in.). Both the inducer and exducer region of the gasifier airfoil successfully passed through potential vane passage response during the numerous speed excursions of the rotor up to a maximum of 60,000 rpm during engine operation.

4.3.3 Ceramic Gasifier Turbine Design—Static Components

During this reporting period design activity efforts were focused on determining the operating characteristics of the gasifier turbine static components. This effort included the following:

- analysis
 - start-up transient and steady-state operation of an all silicon carbide scroll assembly
 - start-up transient and steady-state operation of a scroll assembly with a silicon nitride outer backplate substituted for a silicon carbide outer backplate
 - start-up transient and steady-state operation of an all silicon nitride scroll assembly
- design



VS85-898

Figure 67. Silicon nitride rotor attachment designs.

- investigation of the fracture of a silicon carbide outer backplate during engine testing and modifications to reduce local thermal and mechanical stresses
- configuration of a silicon nitride scroll assembly
- modification of the gasifier turbine heat shield and surrounding components to simplify installation within the engine
- comparison of the operating characteristics of a gasifier turbine scroll assembly with silicon carbide and silicon nitride outer backplate

A fracture of an α SiC gasifier turbine outer backplate during engine testing initiated an investigation to evaluate a Si_3N_4 outer backplate in combination with a successfully engine tested α SiC gasifier turbine scroll.

This investigation was conducted using FEM analysis of a two-dimensional axisymmetric model, Figure 76, of the gasifier turbine scroll assembly and adjoining metal engine structure. Heat transfer and stress analyses were performed at two different engine operating conditions to determine the operating characteristics of a Si_3N_4 outer backplate assembled with an α SiC scroll. The initial operating condition to

be analyzed was a transient start-up cycle. Temperature and stress data were calculated at 10-sec intervals for the first 100 sec of operation. The next operating point considered simulated steady-state operation at the RPD design condition (1287°C [2350°F] TIT). Duplicate analyses were conducted for an α SiC outer backplate (assembled with an α SiC scroll) to allow direct comparison of results. Selected Si_3N_4 and α SiC material properties used in the analyses are tabulated in Table XI.

The calculated probability of survival (POS) of the components of a scroll assembly in which all components were α SiC is presented in Table XII. The smallest POS for the overall assembly occurs at about 60 sec into the start-up cycle. The overall POS then improves to 0.997613 at RPD steady-state conditions.

When silicon nitride material is substituted for silicon carbide in the outer backplate (only) of the gasifier turbine the probability of survival for the outer backplate improves significantly during the start-up transient condition.

The POS of the outer backplate for the two materials during the start-up cycle and at RPD steady-state conditions is compared in Table XIII. The effect of

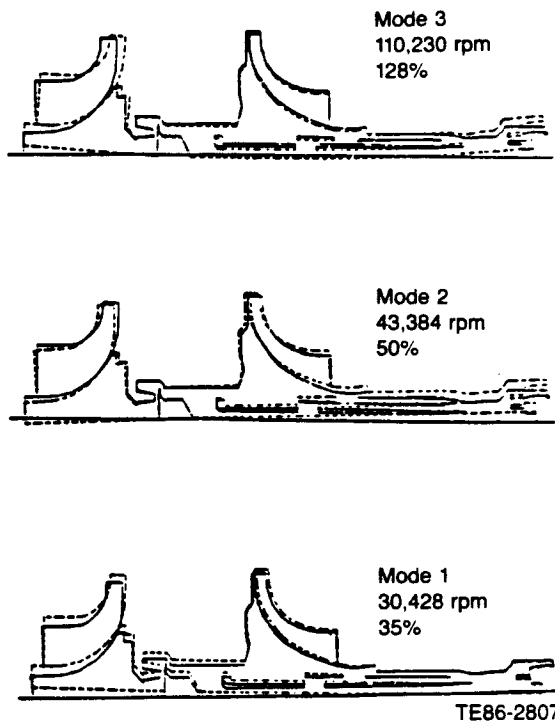


Figure 68. Calculated gasifier rotor assembly modes-brazed rotor/shaft attachment.

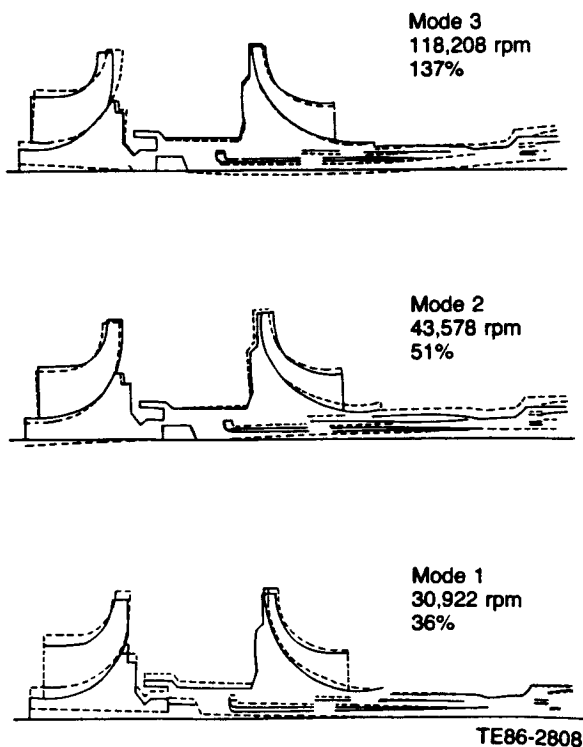


Figure 69. Calculated gasifier rotor assembly modes-interference configuration.

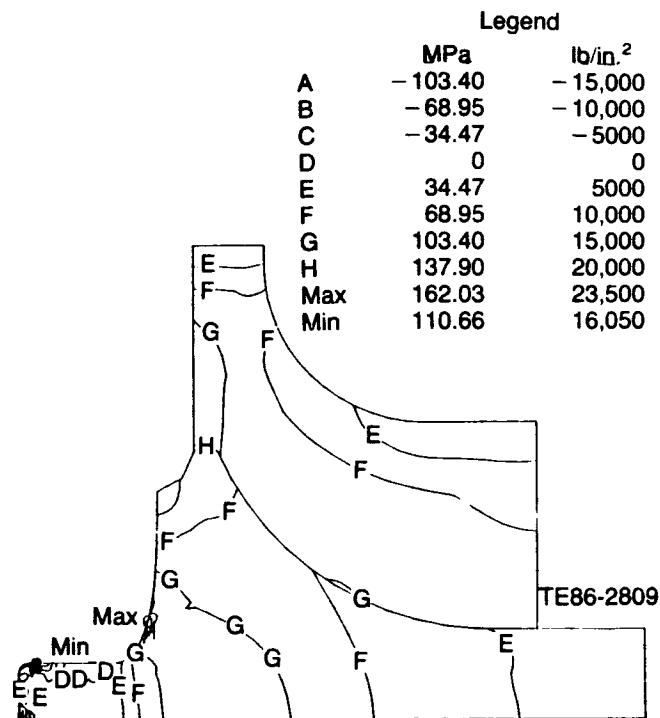


Figure 70. Calculated maximum principal stress for interference fit configuration Si_3N_4 rotor at 100% speed and 1080°C (1976°F) TIT.

the higher strength and Weibull modulus of Si_3N_4 is clearly evident.

The analysis also considered the effect of the lower coefficient of thermal expansion of the Si_3N_4 material when compared to αSiC (see Table XI). The reduced thermal expansion in the Si_3N_4 outer backplate as compared with that of the αSiC scroll results in a subsequent separation of the two parts at the outside pilot diameter as they heat. The separation of the two parts at the pilot diameter is greatest (0.127 to 0.152 mm [0.005 to 0.006 in.] radially) at the steady-state RPD operating condition. The radial thermal growth at the pilot diameters of the Si_3N_4 outer backplate and αSiC scroll during both transient and steady-state (RPD) operating condition are presented as a function of time in Figure 77. The αSiC scroll begins to thermally separate from the Si_3N_4 outer backplate at about 55 sec into the start-up cycle; this separation continues during the remainder of engine warm-up to the RPD operating condition. The close fit of the pilot diameters at the scroll/outer backplate interface is to maintain concentricity between the scroll shroud and the turbine rotor. Separation of the scroll from the outer backplate potentially allows the

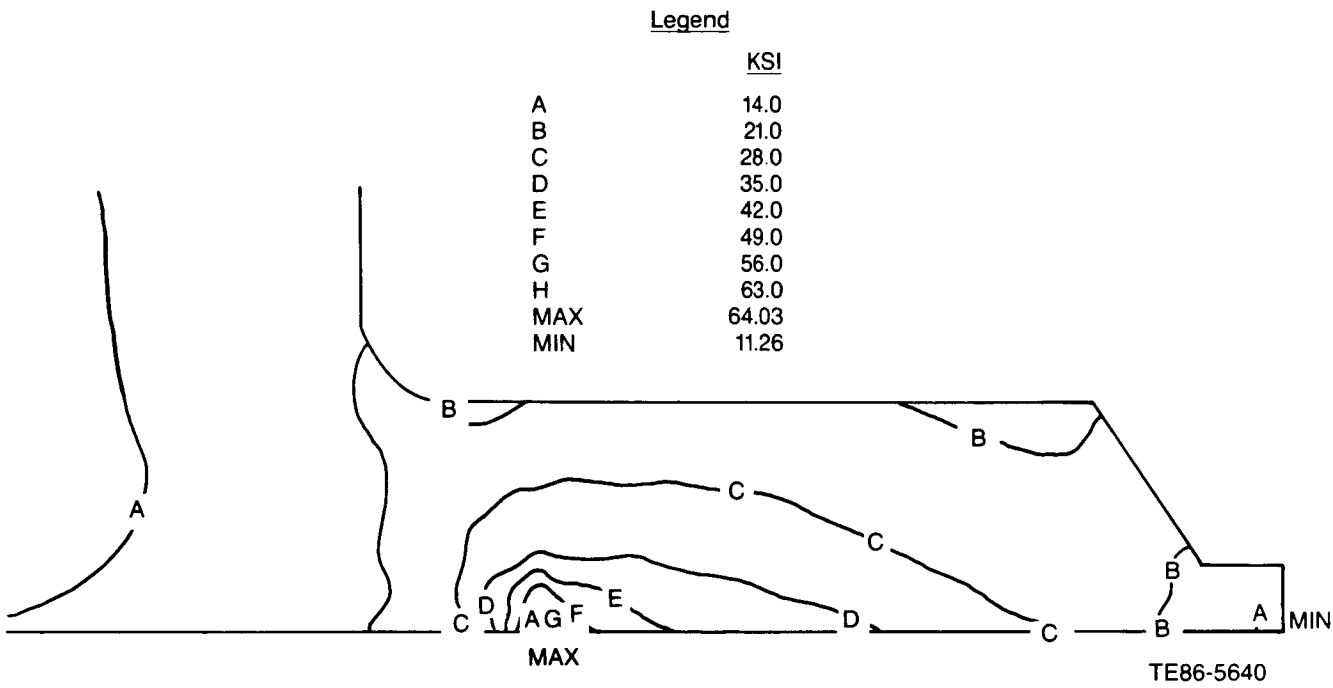


Figure 71. Equivalent stresses, Inco 907 shaft at 100% speed and 1080°C (1976°F) TIT for interference fit attachment.

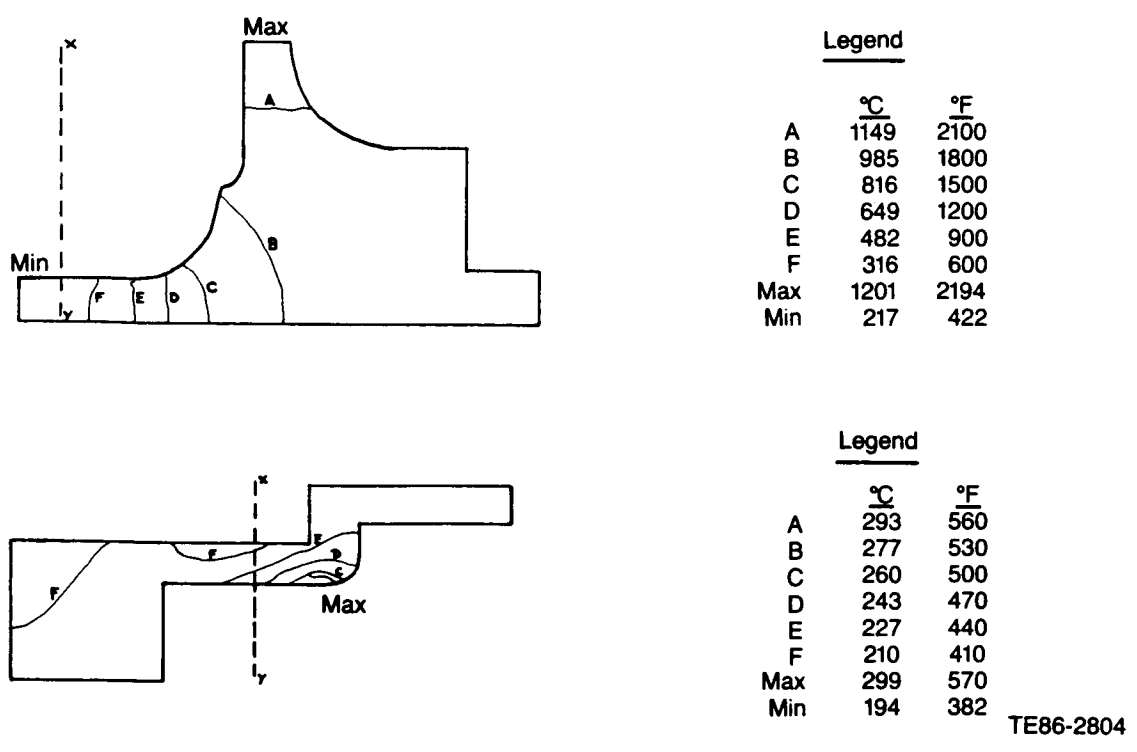
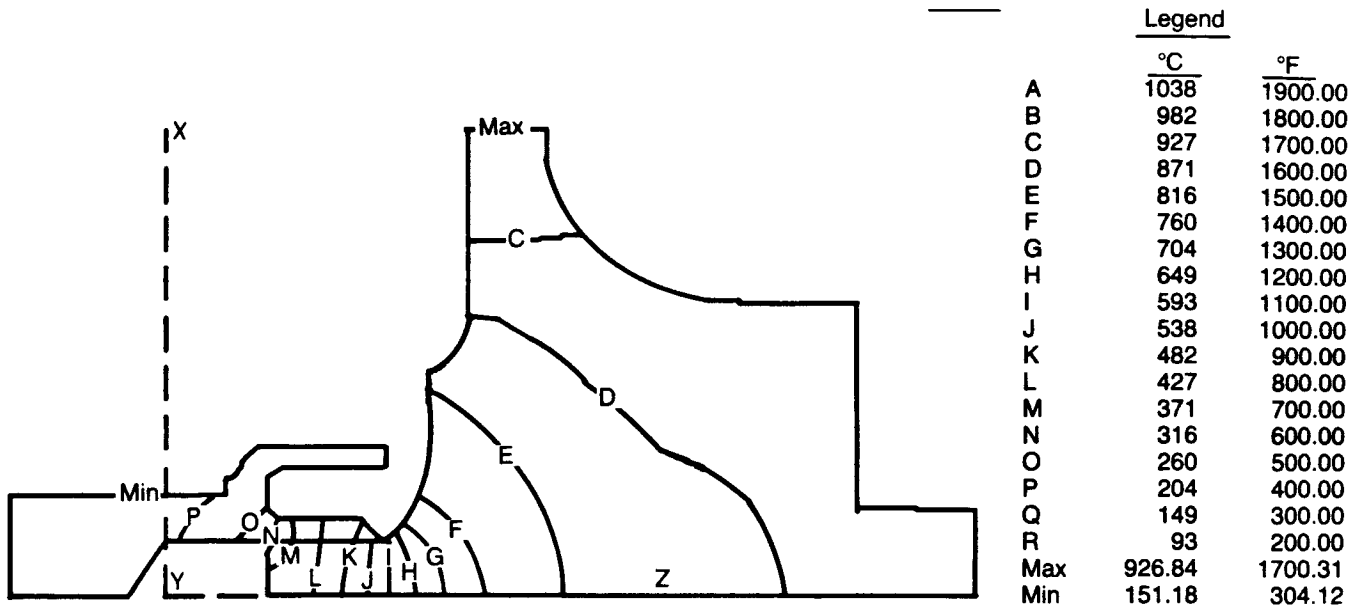


Figure 72. Calculated temperatures for the Kyocera braze joining of Si₃N₄ rotor and metal shaft at 100% speed and 1288°C (2350°F) TIT.



TE86-2805

Figure 73. Thermal analysis of Si_3N_4 rotor/metal shaft at 100% speed and 1080°C (1976°F) TIT for the interference fit configuration.

shroud to shift up to 0.127 mm (0.005 in.) radially with respect to the rotor. Thus, additional radial clearance would be required to prevent turbine rotor rub. However, additional turbine rotor operating clearance is undesirable because of its severe impact on turbine efficiency.

Separation of pilot diameters does not occur when an αSiC outer backplate is used with an αSiC scroll. In contrast, the αSiC outer backplate thermally grows into the scroll during the transient cycle and continues to maintain a close fit at the scroll/outer backplate interface; therefore, no additional turbine rotor clearance is required. The radial thermal growth of an αSiC outer backplate and αSiC scroll during both the transient and steady-state (RPD) operating conditions are presented as a function of time in Figure 78.

This investigation indicates that the use of a Si_3N_4 outer backplate in combination with an αSiC scroll is unacceptable because the critical scroll locating function at the outer backplate/scroll interface is not maintained. This condition is caused by the dissimilar thermal expansion coefficients of the two materials.

Gasifier Turbine Scroll Assembly Fabricated from Silicon Nitride. An analysis of a gasifier turbine scroll assembly fabricated totally from silicon nitride was then initiated to determine the probability of survival of the components and the deflected shapes of the entire assembly and its individual components during

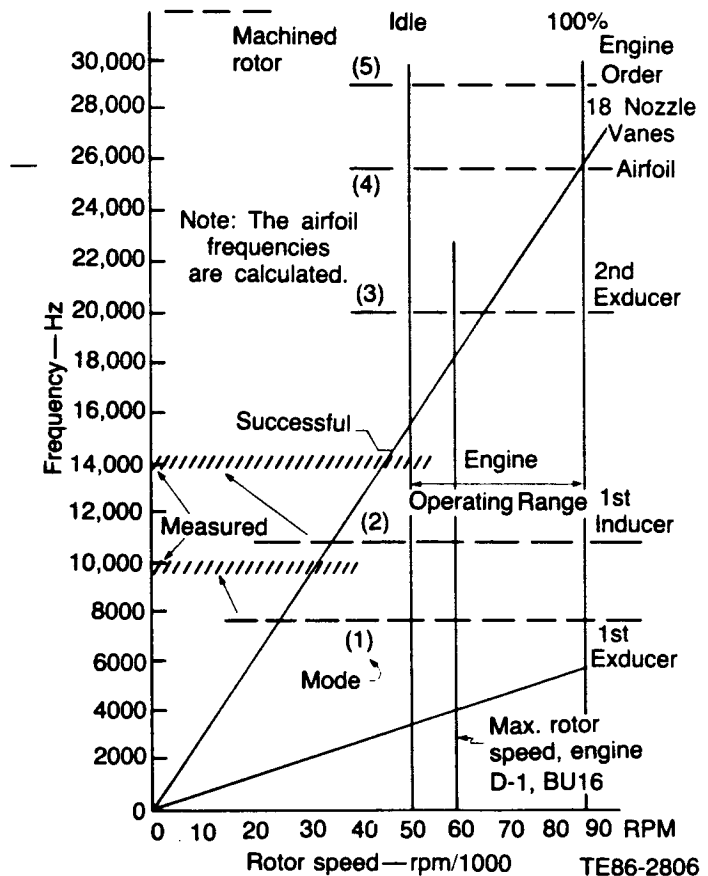
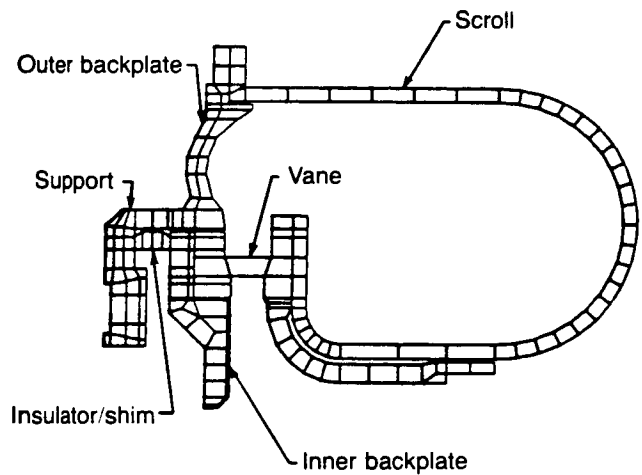
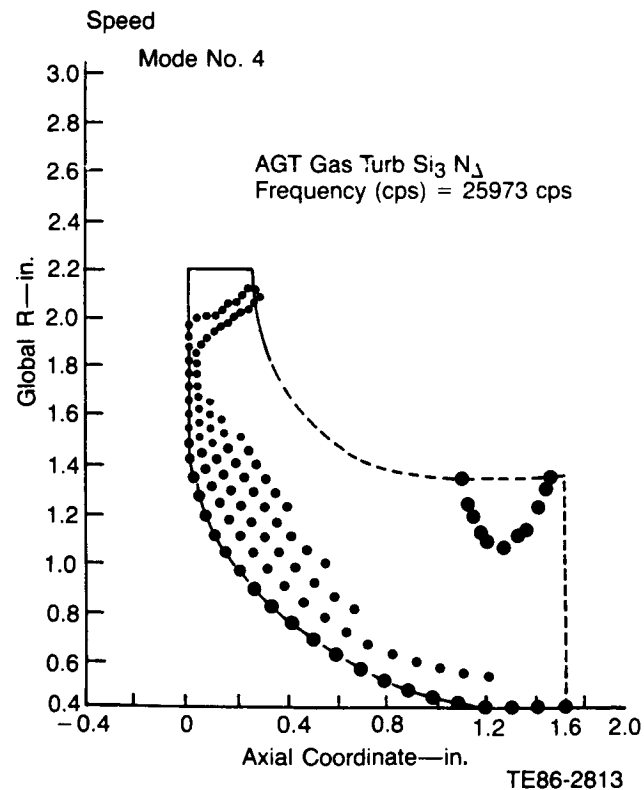
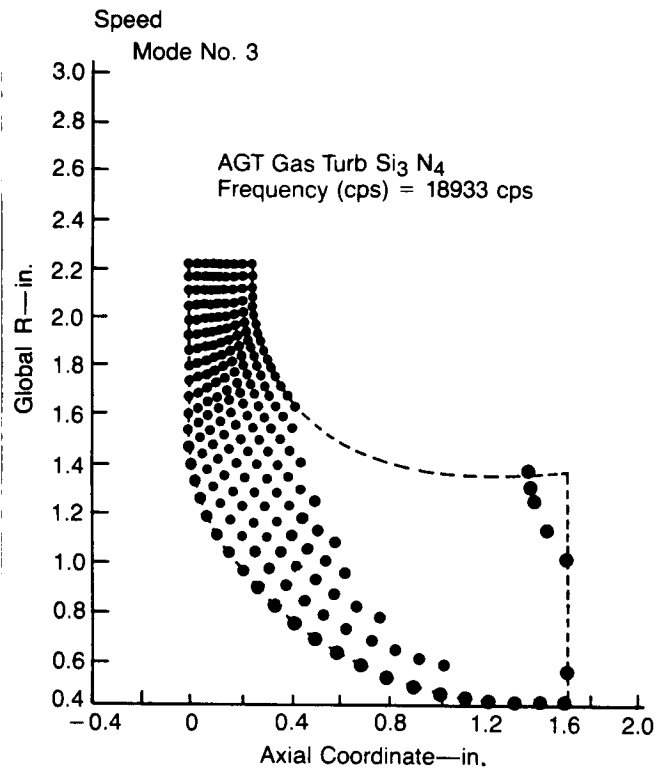


Figure 74. Frequency-speed interference diagram gasifier turbine-silicon nitride, drawing airfoil thickness.



TE86-2496

Figure 76. Gasifier turbine scroll assembly finite element model geometry.

engine operation. For purposes of comparison, the analysis was performed to simulate the same engine operating conditions (start-up transient and steady-state operation condition at the RPD condition, 1287°C (2350°F) turbine inlet temperature [TIT]) employed in the previous SiC analysis. The scroll assembly FEM used in the previous analysis (Figure 76) was also employed in this analysis. The silicon nitride material characteristics used in this analysis were those presented in Table XI.

The calculated probability of survival for the silicon nitride scroll assembly is very high during both start-up transient and steady-state (RPD) operation. Probabilities of survival for the individual components and overall assembly are shown in Table XIV. These probabilities of survival, based on fast fracture strength data, exceed the engine design goal of 0.999375 set for each failure site.

Figure 75. Calculated mode shape, third and fourth mode, Si_3N_4 material rotor.

Table XI.
Ceramic material properties.

	<u>Si₃N₄</u>	<u>αSiC</u>
Density	0.119	0.115
Young's modulus at 1200°C (2192°F), (lb/in. ² x 10 ⁻⁶)	26.3	55.5
Characteristic strength, lb/in. ² x 10 ³		
Surface at RT	98.2	48.7
Surface at 1200°C (2192°F)	86.3	48.7
Volume at room temperature	67.2	25.6
Volume at 1200°C (2192°F)	59.0	25.6
Weibull modulus		
Surface	15	8.7
Volume	15	8.4
Coefficient of thermal expansion, in./in.-°F	2.14 x 10 ⁻⁶	2.73 x 10 ⁻⁶
Poisson's ratio	0.27	0.17
Thermal conductivity Btu/hr-in.-°F at 1200°C (2192°F)	0.500	1.81

Table XII.
Probabilities of survival for gasifier turbine scroll assembly components fabricated from silicon carbide (RPD conditions)—POS.

<u>Time—sec</u>	<u>Scroll</u>	<u>Outer backplate</u>	<u>Inner backplate</u>	<u>Insulating shim (ZrO₂)</u>	<u>Overall assembly</u>
10	1.000000	1.000000	1.000000	1.000000	1.000000
20	0.999937	0.999977	0.999893	1.000000	0.999807
30	0.993139	0.997002	0.988332	1.000000	0.978608
40	0.979039	0.987951	0.960813	1.000000	0.929339
50	0.981865	0.972120	0.939065	1.000000	0.896329
60	0.988216	0.962730	0.928869	1.000000	0.883712
70	0.993379	0.964223	0.945664	1.000000	0.905794
80	0.996508	0.976624	0.969297	1.000000	0.943338
90	0.998487	0.986563	0.983974	1.000000	0.969284
100	0.999403	0.991104	0.989880	1.000000	0.980488
Steady-state	0.997801	0.999999	0.999813	1.000000	0.997613

Table XIII.
 Comparison of probability of survival for Si_3N_4 and αSiC gasifier turbine outer backplates at RPD operating conditions (when assembled with αSiC scroll and αSiC inner backplate).

Time—sec	POS	
	Si_3N_4	αSiC
10	1.000000	1.000000
20	1.000000	0.999977
30	0.999998	0.997002
40	0.999997	0.987951
50	0.999998	0.972120
60	0.999998	0.962730
70	0.999999	0.964223
80	0.999999	0.976629
90	0.999999	0.986563
100	0.999999	0.991104
Steady-state RPD condition	0.999999	0.999999

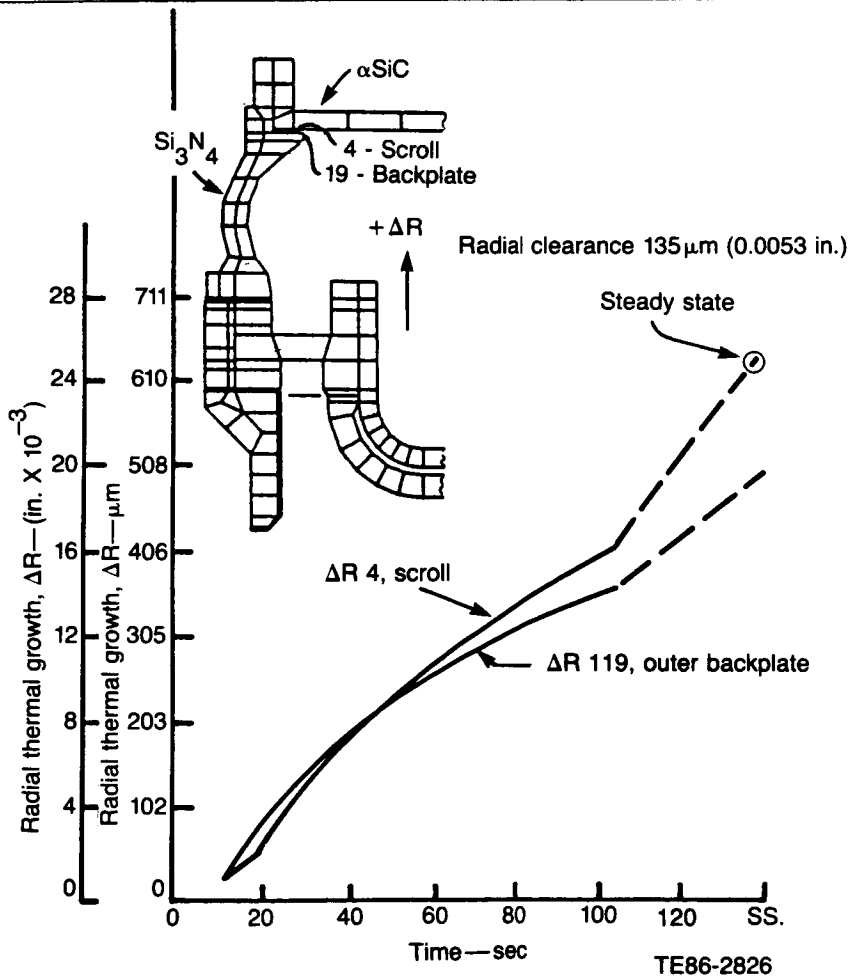
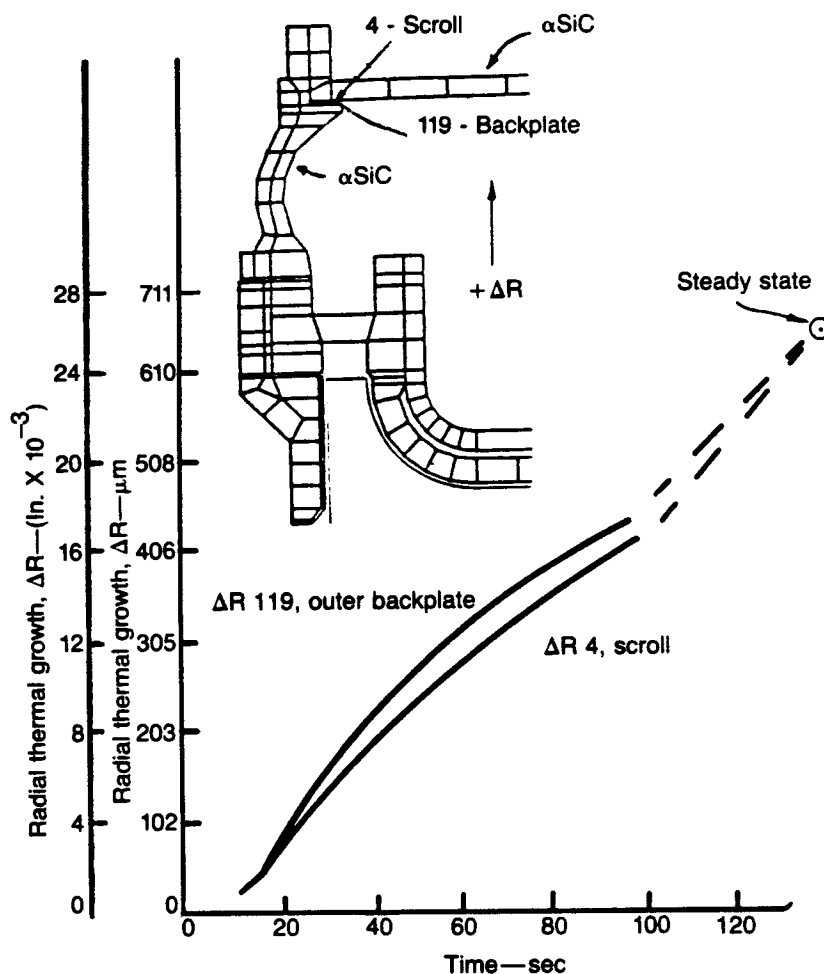


Figure 77. Radial thermal growth of gasifier turbine Si_3N_4 outer backplate and SiC scroll.



TE86-2827

Figure 78. Radial thermal growth of gasifier turbine SiC outer backplate and SiC scroll.

Calculated thermal/mechanical growth at the piloting diameter of the silicon nitride outer backplate and scroll body are presented in Figure 79. During both start-up and steady-state operation the outer backplate expands slightly more than the scroll, thereby maintaining the desired fit between the two components. Cold assembly clearance between the two parts is adjusted to obtain proper fit during operation.

Gasifier Turbine Outer Backplate Redesign. The first α SiC gasifier turbine outer backplate to be engine tested fractured during engine testing. This outer backplate had previously been successfully tested in the scroll thermal shock test rig. Two fractures occurred during subsequent engine testing and are both described in detail in subsection 9.2.2. One fracture

shown in both Figures 80 and 81, may have been caused by a thermal gradient in the part at the origin of the crack. The crack originated in a corner of one of six cross-key slots and propagated radially inward and outward as shown in Figure 80.

The design of the gasifier turbine outer backplate was subsequently modified, as shown in Figure 82, to reduce thermal stress in the region of the fracture origin. The continuous circumferential rim in which the six cross-key slots are cut was removed except at the actual position of the cross-key slots. This initial modification reduced the local thickness of the component by nearly a factor of two and resulted in a reduction of the tensile hoop stress in the region of the cross-key slots. The second modification reduced the stress concentration at the bottom of the cross-key slots by increasing the depth of the slots and

Table XIV.

Probabilities of survival for components of silicon nitride gasifier turbine scroll assembly (RPD conditions).

Time—sec	Scroll	Outer backplate	Inner backplate	Insulating shim (ZrO ₂)	Overall assembly
10	1.000000	1.000000	1.000000	1.000000	1.000000
20	0.999999	1.000000	1.000000	1.000000	0.999999
30	0.999999	0.999999	0.999998	1.000000	0.999997
40	0.999999	0.999999	0.999989	1.000000	0.999989
50	0.999999	0.999999	0.999998	1.000000	0.999985
60	0.999999	1.000000	0.999995	1.000000	0.999995
70	1.000000	1.000000	0.999999	1.000000	0.999999
80	1.000000	1.000000	0.999999	1.000000	0.999999
90	1.000000	1.000000	0.999999	1.000000	0.999999
100	1.000000	1.000000	0.999999	1.000000	0.999999
110	1.000000	1.000000	0.999999	1.000000	0.999999
120	1.000000	1.000000	0.999999	1.000000	0.999999
Steady-state	1.000000	1.000000	1.000000	1.000000	1.000000

machining a full radius at the bottom of the slot(s) in place of the initial sharp corners.

Design of Silicon Nitride Gasifier Turbine Static Components. The favorable probability of survival and satisfactory thermal growth characteristics of a silicon nitride gasifier turbine scroll assembly (scroll, vanes, and inner and outer backplates) have been demonstrated through analysis. The results of the analysis led to a decision to procure silicon nitride gasifier turbine static components; successful testing of a silicon nitride gasifier turbine rotor also favorably influenced this decision.

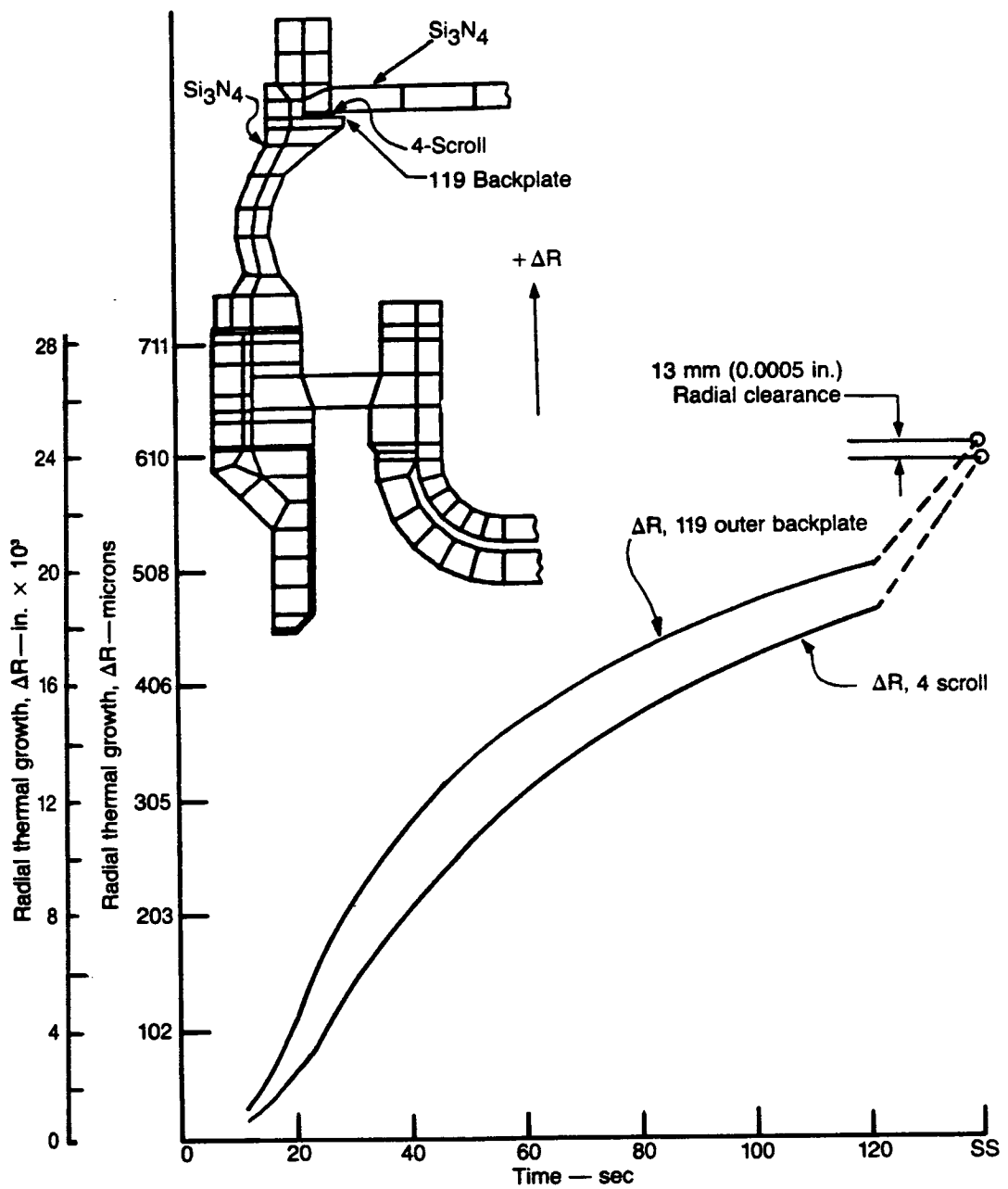
Allison prepared an alternate gasifier turbine scroll design during 1984. This design featured a separately fabricated inlet section and a revised scroll body casting configuration that improved mold release. This alternate scroll design was then analyzed to obtain transient and steady-state temperatures, stresses, and probability of survival (the results were reported in the 1984 Annual Report). The vendor (Kyocera) selected to supply silicon nitride gasifier turbine scrolls submitted a proposal to revise the alternate scroll design. The revision involved a new configuration in the region of the bonded joint between the scroll body and the shroud; this proposal was accepted.

The revised configuration and Allison's original alternate design concept are presented in Figure 83.

The separately fabricated inlet section bonded to the scroll body and a typical cross section of the Kyocera scroll body casting are shown in Figure 84. A cross section of the complete silicon nitride gasifier turbine scroll assembly, indicating the bonded joints between the scroll body, shroud, and outlet transition elbow is presented in Figure 85. Although construction differences are evident the original and vendor alternate scroll assemblies have similar scroll flow areas and the complete scroll assemblies (scroll body, shroud, exit, and inlet connection features) are interchangeable.

The silicon nitride inner and outer backplate configurations are also identical to the corresponding silicon carbide components. The silicon nitride outer backplate design incorporates the recent silicon carbide design modification as depicted in Figure 82.

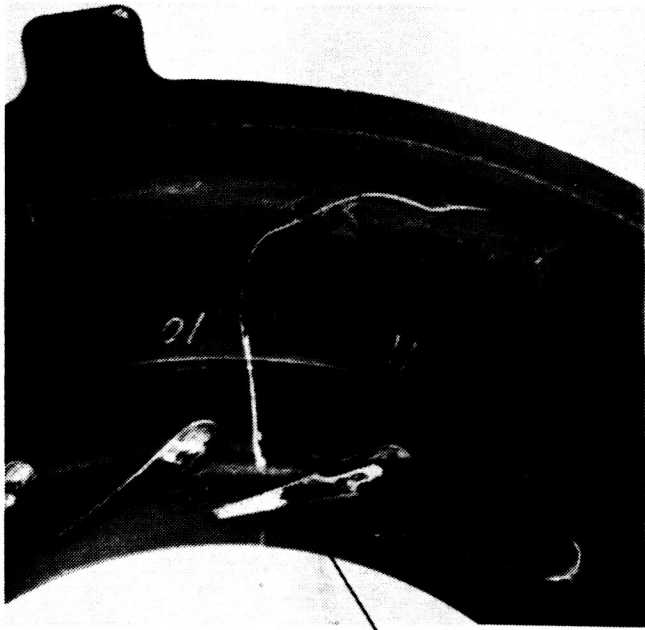
Gasifier Turbine Heat Shield Design. Gasifier turbine heat shields have recently been fabricated to be installed in the turbine assembly in an effort to reduce radiant heat transfer from the hot turbine inner backplate to the adjoining metal engine structure. The heat shield has been designed so that its installation is optional; installation (or omission) of the shield in the turbine assembly does not impact the dimensional stack of the engine. The heat shield may be used with either ceramic or metal turbine scroll assemblies. The heat shield, as it would appear if installed in the gasifier turbine, is shown in Figure 86.



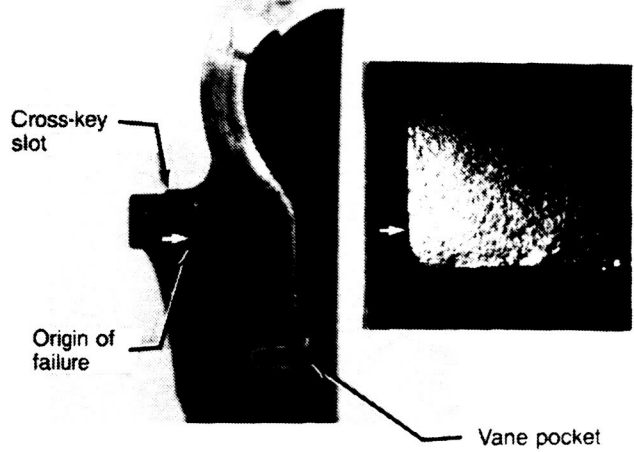
TE86-2828

Figure 79. Radial thermal growth of gasifier turbine Si₃N₄ outer backplate and Si₃N₄ scroll.

ORIGINAL PAGE IS
OF POOR QUALITY

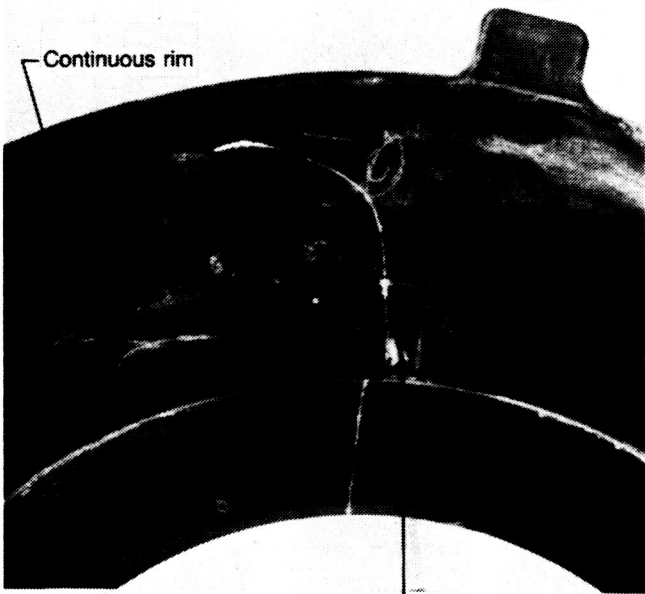


Vane pocket



TE86-2840

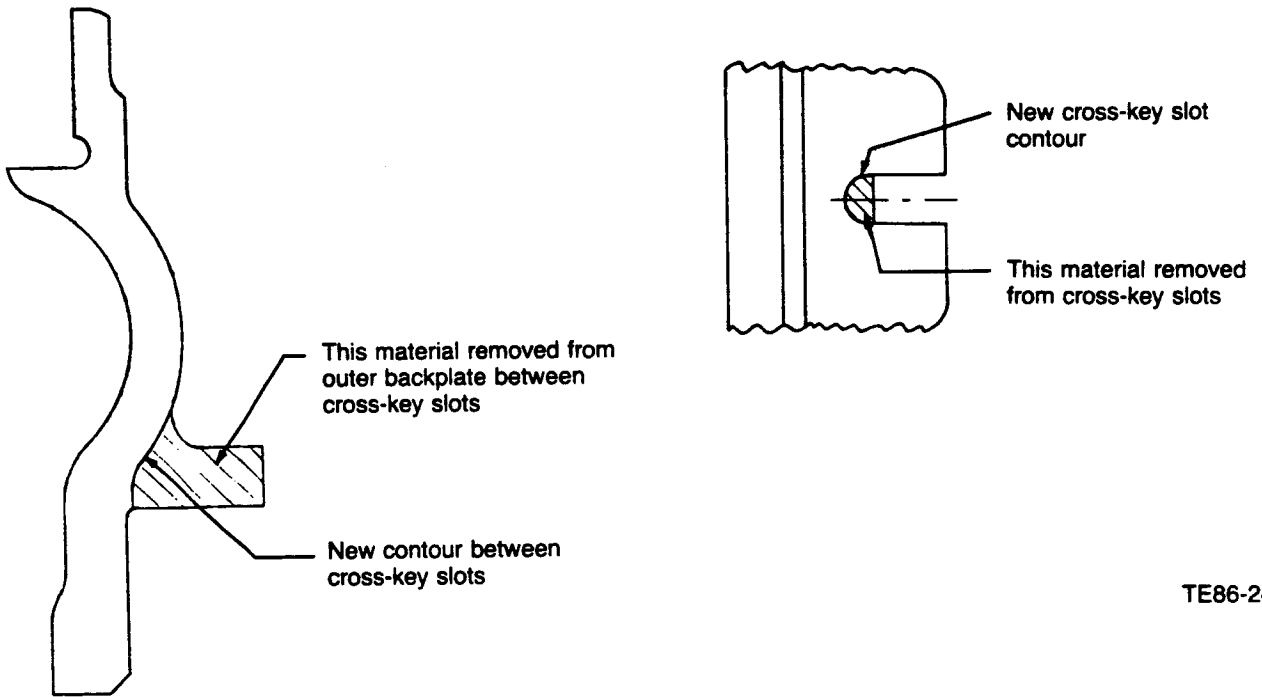
Figure 81. Origin of failure in α SiC gasifier turbine outer backplate.



Cross-key slot

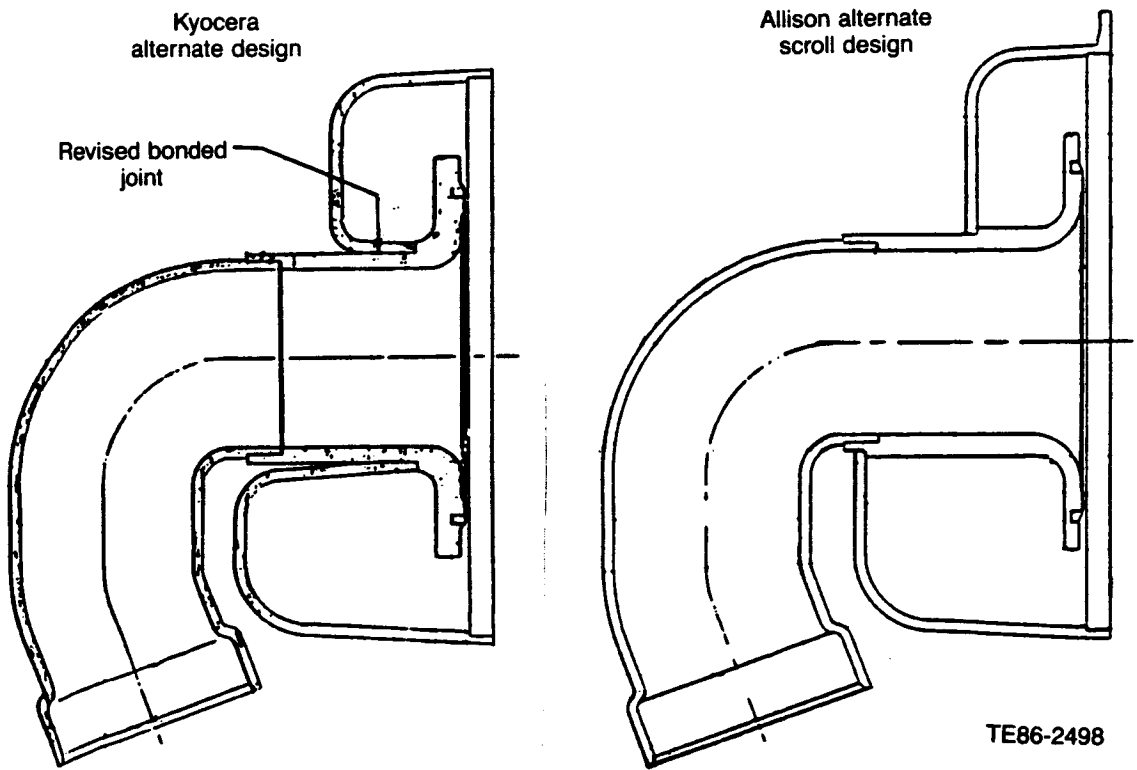
TE86-2829

Figure 80. Crack indications in α SiC gasifier turbine outer backplate after engine test.



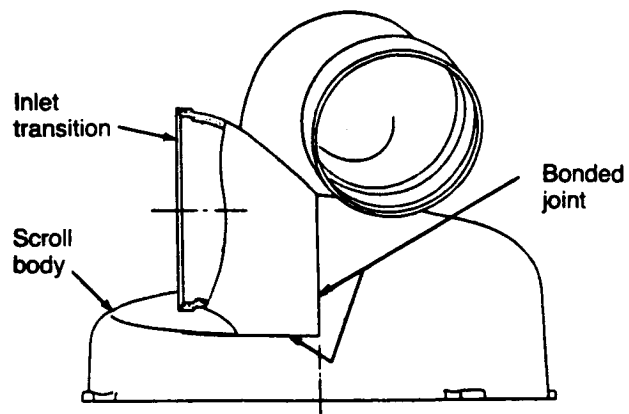
TE86-2497

Figure 82. Modification of gasifier turbine outer backplate to reduce local tensile hoop stress.

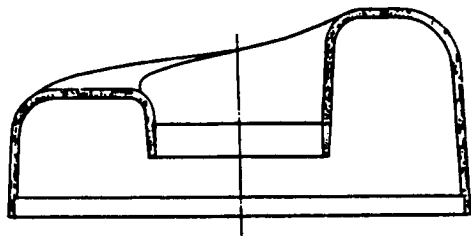


TE86-2498

Figure 83. Allison alternate gasifier turbine scroll design and Kyocera alternate scroll design.

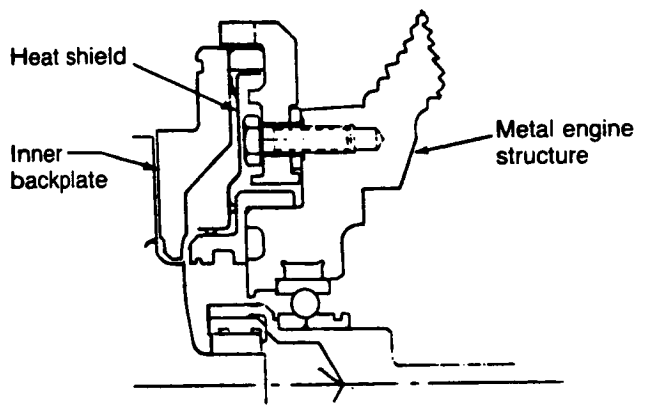


Scroll body casting cross section



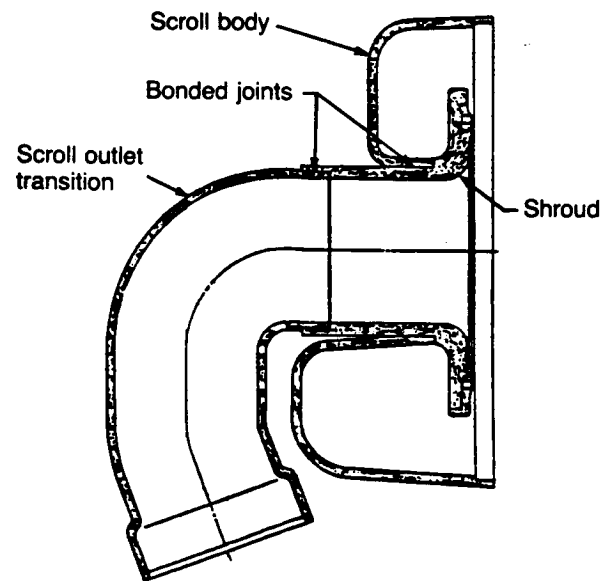
TE86-2499

Figure 84. Kyocera alternate design silicon nitride gasifier turbine scroll construction.



TE86-2501

Figure 86. Gasifier turbine heat shield installation.



TE86-2500

Figure 85. Kyocera alternate design silicon nitride gasifier turbine scroll assembly.

V. POWER TURBINE DEVELOPMENT

5.3 CERAMIC POWER TURBINE DESIGN

Power turbine ceramic design efforts during this reporting period involved the power turbine rotor and static components. The scope of work was similar to that performed on the gasifier turbine system as described in section 4.3.

5.3.1 Ceramic Power Turbine Rotor Design

Thickened Airfoil. The design of a thickened gasifier airfoil has been implemented (ref section 4.3.1) for potential improvement in impact resistance. Similar considerations led to a redesigned (resized) power turbine airfoil in which the thickness has been increased. The new airfoil design, as compared to the initial design, was thickened in the locations shown in Figure 87. Both the airfoil taper ratio and the size of the exducer throat controlling the flow rate remained unchanged. The resulting airfoil is applicable for power turbine rotors made either from silicon carbide or silicon nitride.

The procurement of silicon nitride power turbine rotors from Kyocera is discussed in section 9.3.3. The natural frequencies of the silicon nitride material thickened airfoil were calculated and the results are presented in the Campbell diagram in Figure 88. The airfoil design satisfies the general guideline that all natural frequencies be in excess of the fourth order engine (vane) excitation frequency.

Temperature contours, resulting stress gradients, and probability of survival calculations have been initiated for this rotor configuration made from silicon carbide material. Fabrication of the rotor in silicon nitride material (ref section 9.2.4) is also under consideration and the corresponding calculations will be performed for a silicon nitride rotor.

5.3.2 Ceramic Power Turbine Design - Static Components

During this reporting period, design activity efforts on the static ceramic power turbine components included the following:

Original inducer tip at 0.75 mm (0.030 in.) thick

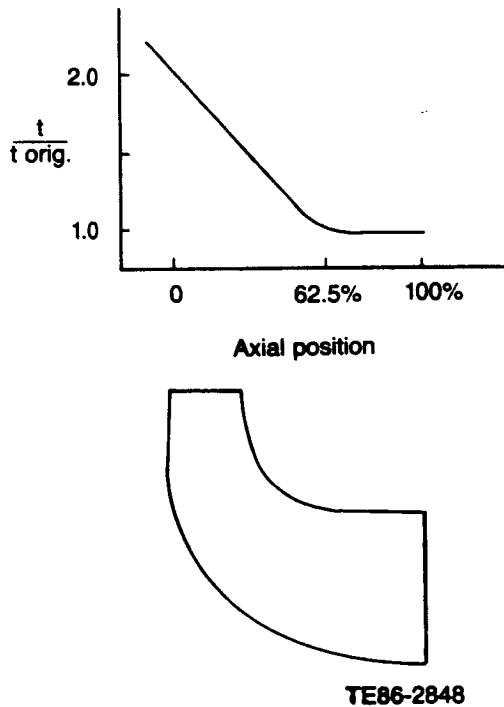


Figure 87. Redesigned (thicker) inducer region airfoil, ceramic power turbine rotor.

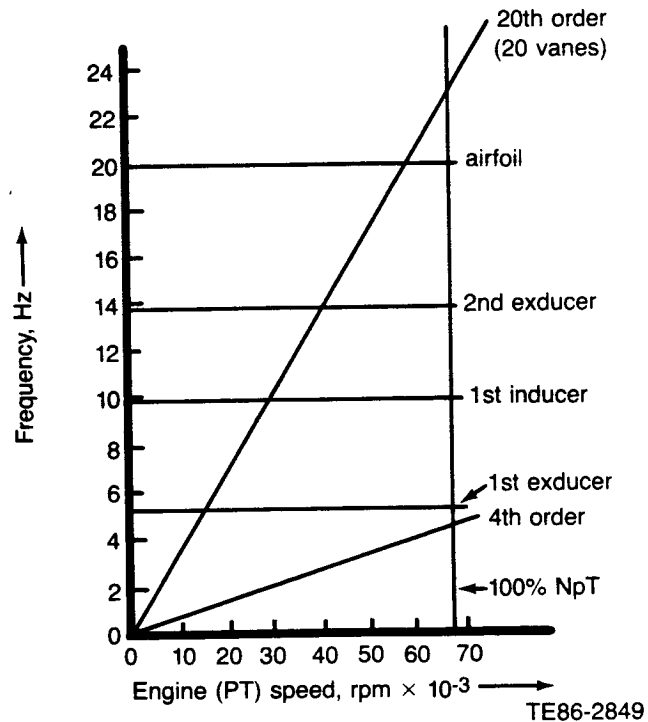


Figure 88. Campbell diagram, silicon nitride (SN 220M) material thickened airfoil.

Design

- scroll design update to reflect both gasifier turbine scroll design refinements and revised rotor to scroll clearance specifications
- design drawings finalized for silicon carbide and silicon nitride scroll/backplate assemblies
- design of power turbine heat shield to simplify installation on engine
- analysis of steady state and start-up transient operation of a silicon carbide turbine scroll assembly

Power Turbine Scroll Assembly Design. Detail drawings of the ceramic power turbine scroll and inner and outer backplates have been completed. The power turbine scroll design incorporates the current design features of the gasifier turbine scroll, which evolved through detailed finite element model (FEM) analysis directed toward improving the probability of survival (POS) of the gasifier turbine scroll. These changes include increased shroud and scroll wall thickness. The final design of the power turbine outer backplate also incorporates the revisions made to the gasifier turbine outer backplate (refer to section 4.3.3) to reduce thermal stresses in the nozzle vane/cross-key slot region of the part. The power turbine inner backplate design incorporates a modified shape to allow installation of an optional heat shield between the scroll/backplate assembly and the adjoining metal engine structure.

Drawings for α SiC power turbine static components have been released to Sohio for part fabrication. Tooling to produce scrolls and outer backplates has been procured.

Detail analysis of a silicon nitride gasifier turbine scroll assembly showed that silicon nitride is a viable alternative material for those components with a high calculated probability of survival. Based on the results of that analysis, detail drawings were prepared for silicon nitride power turbine components. These components are dimensionally interchangeable with like silicon carbide components. However, based on the results of the gasifier turbine analysis, use of a silicon nitride outer backplate with a silicon carbide scroll would not be acceptable because of the difference in thermal expansion rates of the two materials. A silicon nitride inner backplate may be used with an outer backplate made of either material. Silicon nitride vanes (already procured for this program) may also be used in either a silicon nitride scroll/outer backplate assembly or a silicon carbide assembly.

The vendor (Kyocera) quotation for the silicon nitride components contained a proposal for an alternate construction of the power turbine scroll/shroud assembly. Kyocera's proposal was similar to the proposal for their gasifier turbine scroll assembly de-

scribed in section 4.3.3. The proposed construction simplifies the scroll body casting and improves the probability of successful removal of the scroll body from the mold. In the power turbine scroll, the inlet transition is an integral part of the scroll body casting, and the shroud is a separate part that is bonded to the scroll body to complete the scroll assembly. A comparison of the silicon carbide scroll design and the alternate silicon nitride scroll design appears in Figure 89.

The inlet section of the power turbine scroll is an integral part of the scroll body casting in the silicon nitride design as presented in Figure 90. A typical cross section of the scroll body casting is also depicted in the same figure.

Power Turbine Heat Shield Design. A heat shield has been designed and parts fabricated for installation in the power turbine assembly. The heat shield is placed between the hot inner backplate and the metal engine structure to reduce radiant heat transfer to the metal engine structure. The reduced heat transfer results in cooler running bearings and less heat rejection to the oil. The heat shield is designed to be used with either ceramic or metal turbine scroll assembly components and may be optionally included in or omitted from the turbine assembly without impacting the dimensional stack up of the engine. The installation of the heat shield as it appears in the power turbine is shown in Figure 91.

Power Turbine Silicon Carbide Scroll Assembly Static Component Design Analysis. A two-dimensional (2-D) finite element thermal and stress analysis has been completed for the ceramic power turbine scroll, vanes, inner and outer backplates, and insulator/shim components. Calculations were made for steady-state and transient start-up operating conditions using the finite element model shown in Figure 92. The properties of the component materials used in the analysis were α SiC for all components except the zirconia insulator/shim.

Steady-State Operating Condition. Operating temperature, stress, deflection, and probability of survival were calculated for the α SiC static ceramic power turbine components operating in a steady-state manner at reference power-train design (RPD) conditions (gas turbine inlet temperature (TIT) = 1288°C (2350°F), power TIT = 1138°C (2080°F)). The POS for the four analyzed components are presented in Table XV. The POS of the outer backplate and the scroll, at steady-state operating conditions, is at or near the design reliability goal of POS = 0.999375. The inner backplate and insulator/shim POS are sufficiently high to be good candidates for experimental

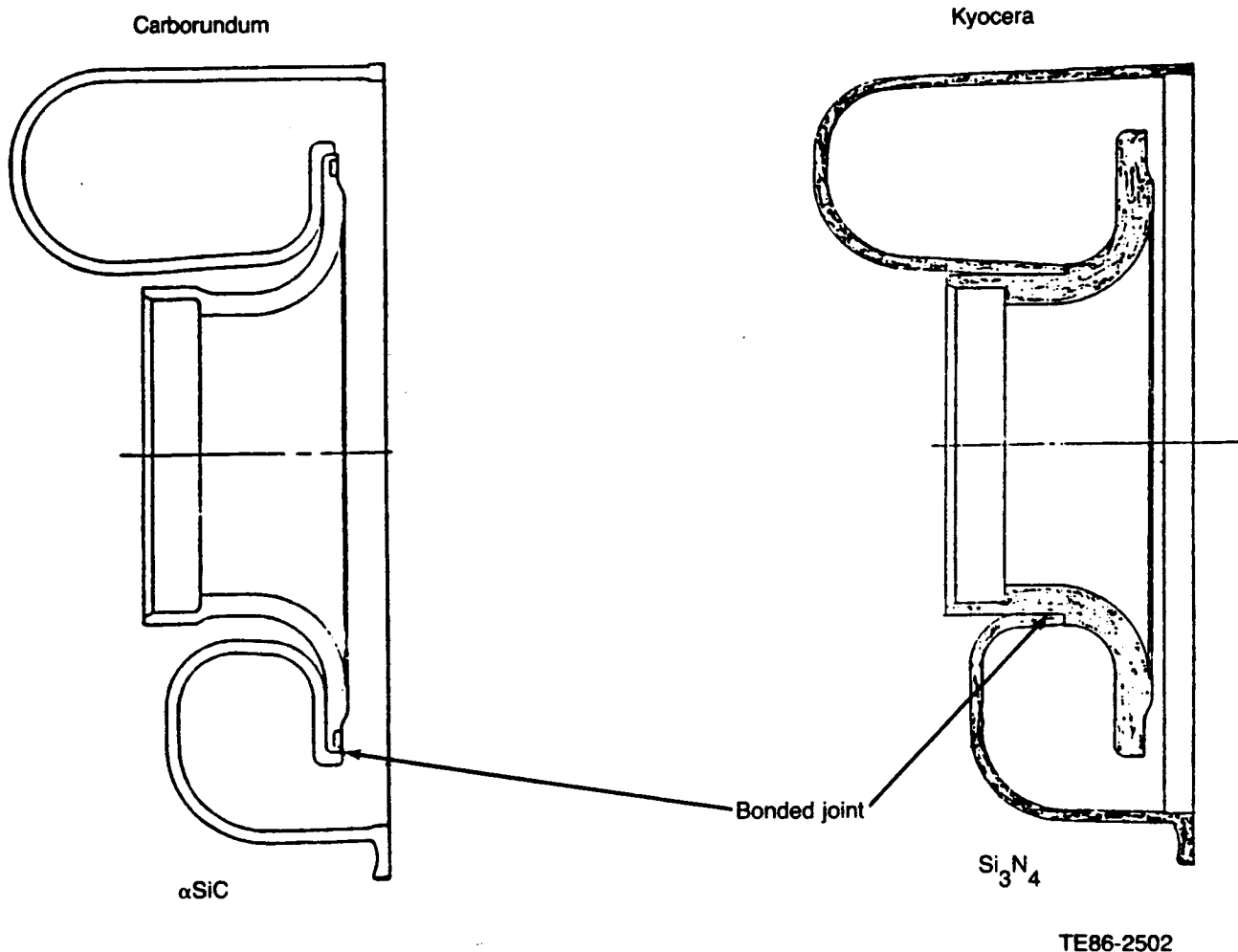


Figure 89. Comparison of original design SiC power turbine scroll and Kyocera alternate design Si₃N₄ power turbine scroll.

engine testing, but require further design refinement or improved material characteristics to meet reliability goals.

The results of operating temperature calculations of the components are shown in Figure 93. The maximum steady-state temperature occurs in the scroll at a location near the nozzle vane where the heat transfer coefficient is relatively high and the heat loss to ambient is at a minimum. A temperature drop in excess of 316°C (600°F) occurs across the ZrO₂ insulator/shim component.

The calculated steady-state operating principal stresses in the ceramic components are presented in Figure 94. The maximum principal stress in each component is tabulated in Table XV. The deflected shape

plot of the components operating at steady-state conditions is depicted in Figure 95. The deflections have been magnified to indicate how the components would deflect in operation.

Transient Start-Up Operating Condition. Operating temperature, stress, deflection, and POS were calculated for the static ceramic power turbine components during an engine start-up cycle. Calculations were made at 10 sec intervals up to 120 sec. The cycle simulates a cold (room temperature) engine start-up during which the gasifier turbine speed and temperature are increased linearly to 83% N1 and 1288°C (2350°F), respectively, during the first 20 sec and then held constant at those levels for the remainder of the

**ORIGINAL PAGE IS
OF POOR QUALITY**

period analyzed. The POS, as a function of time for the power turbine scroll, inner and outer backplates, and the insulator/shim, is presented in Figure 96. The POS of the scroll, inner backplate, and insulator/shim remain very high during the first 120 sec, while the POS of the outer backplate decreases to a minimum value at about 70 sec into the start-up and then increases to near unity as RPD steady-state conditions are approached. The reduced POS calculated at RPD steady-state condition for the inner backplate and insulator/shim is not experienced during the first 120 sec of the start-up cycle.

The temperature, principal stress, and deflected shape plots for the static ceramic power turbine components at the point of lowest outer backplate POS (approximately 70 sec into start-up) are presented in Figures 97, 98, and 99, respectively. At 70 sec into the start-up cycles the maximum principal stresses in the components are:

<u>Component</u>	<u>Maximum principal stress—mPa(lb/in.²)</u>
Scroll/vanes—(SiC)	89.57 (12,990)
Outer backplate—(SiC)	38.61 (5600)
Inner backplate—(SiC)	13.87 (2011)
Insulator/shim—(ZrO ₂)	59.01 (8558)

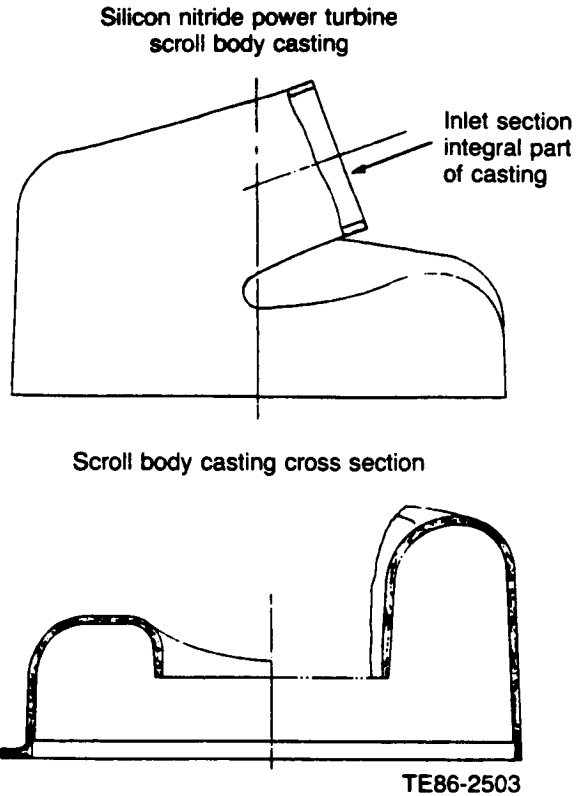


Figure 90. Kyocera alternate design silicon nitride power turbine scroll body casting.

Table XV.

Probability of survival and maximum principal stress for ceramic power turbine scroll assembly—steady-state RPD conditions.

<u>Component</u>	<u>Probability of survival</u>	<u>Maximum principal stress—mPa (lb/in.²)</u>
Scroll—SiC	0.9991900	80.26 (11,640)
Outer backplate—SiC	0.9999990	31.12 (4513)
Inner backplate—SiC	0.9958198	42.70 (6192)
Insulator/shim—ZrO ₂	0.9935034	94.25 (13,670)

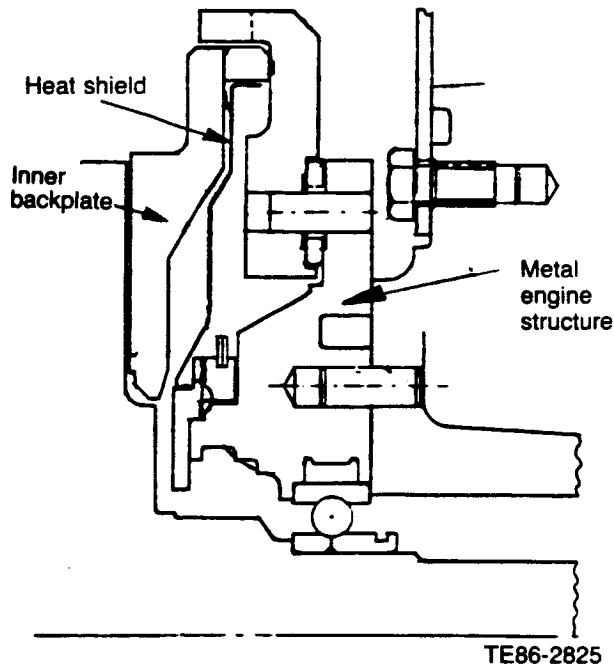
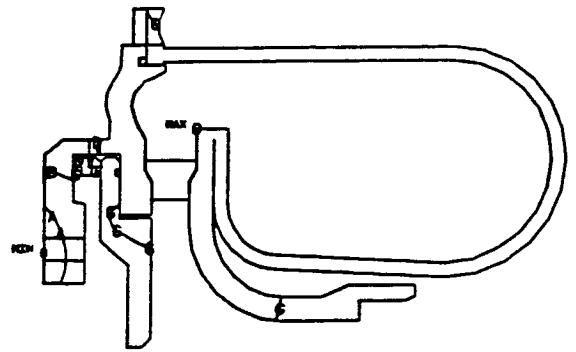


Figure 91. Power turbine heat shield installation.



LEGEND

A	600.00
B	800.00
C	1000.00
D	1200.00
E	1400.00
F	1600.00
G	1800.00
Max	1992.48
Max	537.53

TE86-2505

Figure 93. Steady-state (RPD condition) operating temperatures for SiC ceramics power turbine scroll assembly.

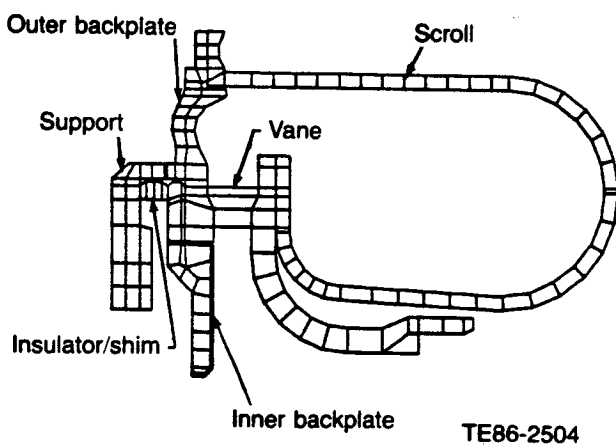
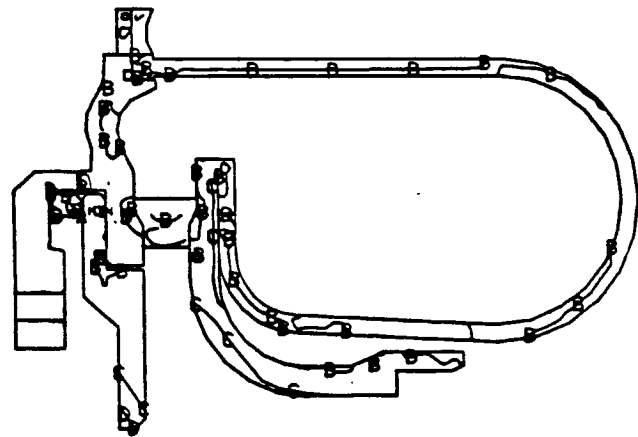


Figure 92. Power turbine scroll assembly finite element model.

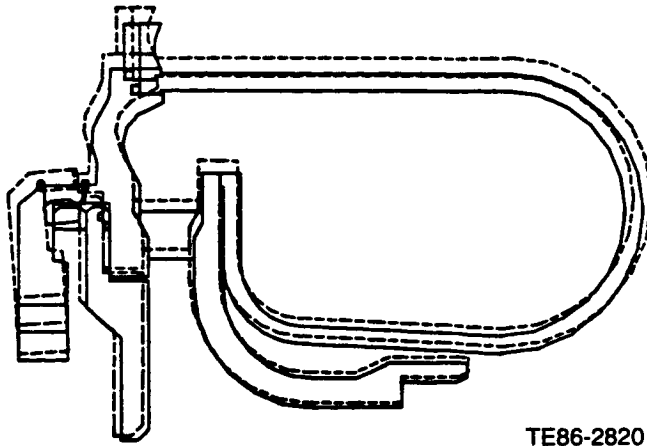


Legend

	MPa	lb/in ²
A	-48.26	-7000
B	0	0
C	48.26	7000
D	96.53	14,000
E	144.79	21,000
F	193.06	28,000
G	241.32	35,000
H	289.59	42,000

TE86-2819

Figure 94. Max principal stress in SiC ceramic power turbine scroll assembly—steady-state (RPD) conditions.



TE86-2820

Figure 95. Deflected shape plot for SiC ceramic power turbine scroll assembly operating at RPD conditions.

Calculated Probability of Survival
for
Static Ceramic Power Turbine Components
Transient: 83% N1, 1288°C (2350°F)
Gasifier Turbine TIT in 20 sec
Steady state: RPD point (1288°C (2350°F)) G.T. TIT

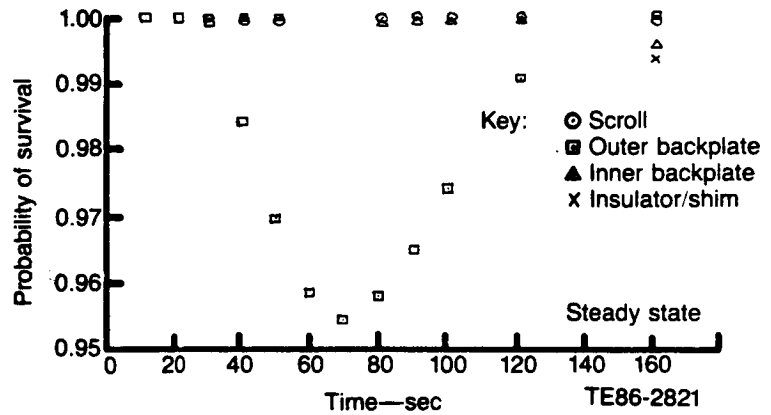
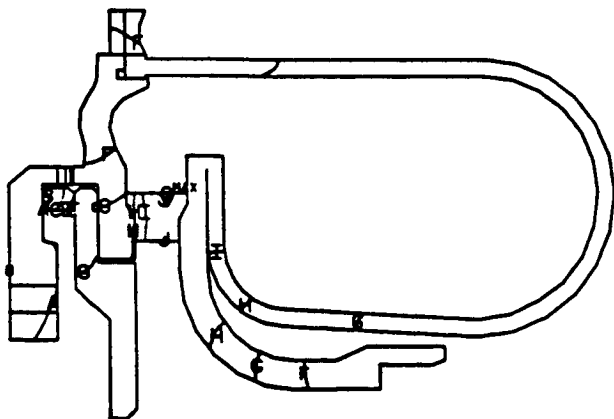


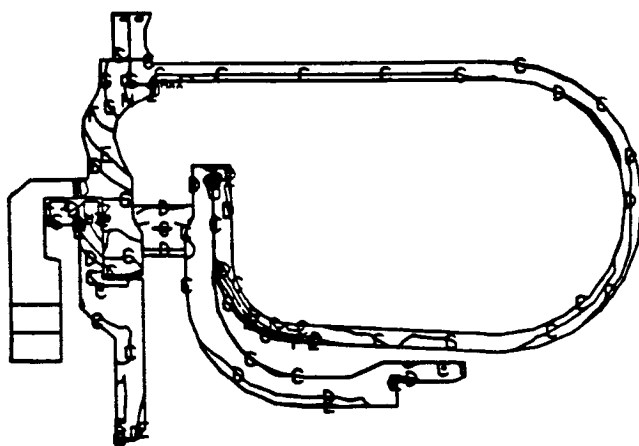
Figure 96. Probability of survival of SiC ceramic power turbine scroll assembly components as a function of time during start-up cycle.



Legend		
	°C	°F
A	800	316
B	700	371
C	800	427
D	900	482
E	1000	538
F	1100	593
G	1200	649
H	1300	704
I	1400	760
J	1500	816
Max	1525.05	829.47
Min	521.01	271.67

TE86-2822

Figure 97. SiC power turbine component temperatures at 70 sec into transient start-up cycle.



Legend

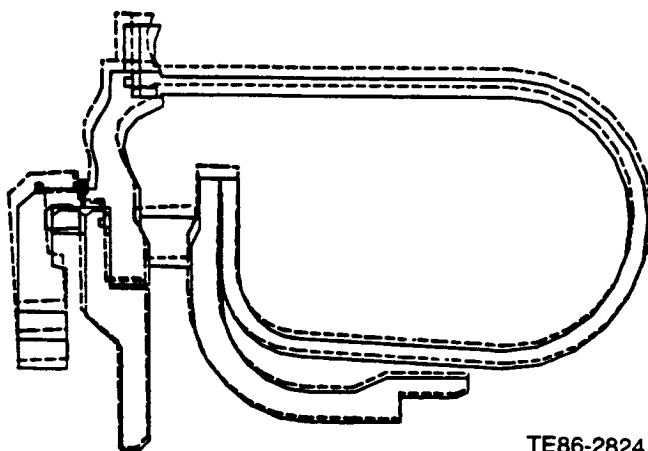
	MPa	lb/in. ²
A	-41.37	-6000
B	-20.68	-3000
C	0	0
D	20.68	3000
E	41.37	6000
F	62.05	9000
G	82.74	12,000
H	103.42	15,000
I	124.11	18,000
Max	126.25	18,310
Min	-43.99	-6380

TE86-2823

Figure 98. Max principal stress in SiC ceramic power turbine scroll assembly components 70 sec into transient start-up cycle.

The maximum temperature (829°C (1525°F)) at this point in the start-up cycle is at the leading edge of the nozzle vane. The temperature drop across the insulator/shim is approximately 204°C (400°F).

The deflected shape plot, Figure 99, indicates the same general shape as calculated for steady-state operation. Thermal growth at the 70 sec point is 57% to 70% of that at steady-state conditions, depending on the component.



TE86-2824

Figure 99. Deflected shape plot for SiC ceramic power turbine scroll assembly at 70 sec into transient start-up cycle.

VI. COMBUSTOR DEVELOPMENT

During this reporting period, combustion development efforts were primarily focused on the following items:

- combustor airflow distribution and liner pressure drop
- combustor proof testing
- alternate fuel (methanol) demonstration

In prior testing, rig measurements indicated that the pressure drop across the combustor was approximately 40% larger than the design condition. Consequently, tests during this reporting period were initiated to investigate this discrepancy. Engine development was also supported by qualifying combustion hardware through combustor proof testing. In addition, a rig demonstration test to evaluate the alternative fuel capability of the AGT 100 combustion system was completed with methanol used as the alternate fuel.

6.1 TEST FACILITY

As reported in the eighth AGT semiannual report, a combustor rig test section capable of handling the high temperatures of the RPD cycle has been in use. This facility, as modified in 1983, duplicates the environment expected in the engine—the general flow path, insulating features, combustor orientation, variable geometry control, and fuel systems—as closely as possible. A television camera, positioned to look through a periscope in the combustor exhaust, is connected to a television monitor to allow visual observation of the combustion tests. This arrangement is beneficial in analyzing the combustion phenomena during the continual development of the combustor. Several optical ports have been added to the rig (six for pyrometers and one for a camera) for viewing the combustor outer wall during hot firings. A large optical port allows an infrared camera to view the combustor body axially from planes just below that of the pilot to that of the combustor exit. Circumferentially, the view includes the two dilution holes across from the pilot. This method of observation has removed the requirement for thermally painting the combustor to determine potential ceramic skin hot spots caused by imperfections in the fuel spray pattern. The combustor rig is fitted with a preheater capable of providing inlet air temperatures up to 1024°C (1875°F) to permit investigation of engine problems that have occurred or may potentially occur during pilot, start, and main nozzle operation at such high inlet air temperatures.

6.2 TEST RESULTS

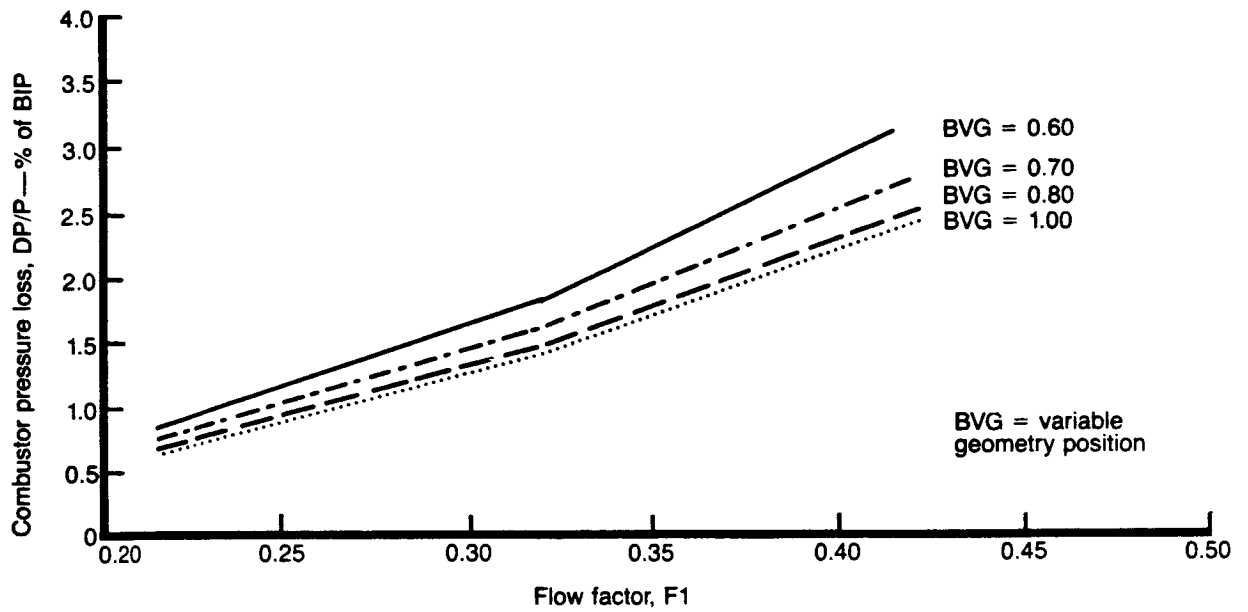
6.2.1 Combustor Liner Pressure Loss

Combustor development activity was initiated to resolve the difference between the design combustor liner pressure drop and the unexpectedly high pressure drop measurements acquired in 1984. The suspect measurements were obtained from nonreacting flow experiments in the burner rig (burner assembly BU16) to determine liner pressure drop as a function of flow factor and burner variable geometry (BVG) setting. It was concluded at that time that the measured $\Delta P/P$ liner loss was larger than the design specification. A 5% pressure loss at maximum power airflow rates with a BVG setting near 15.24 mm (0.6 in.) had been measured, nearly 1.7 times larger than expected. Even with the BVG set at the maximum setting (bypass holes fully open), the measured $\Delta P/P$ was still nearly 3.5%, or 1.4 times greater than the design specification.

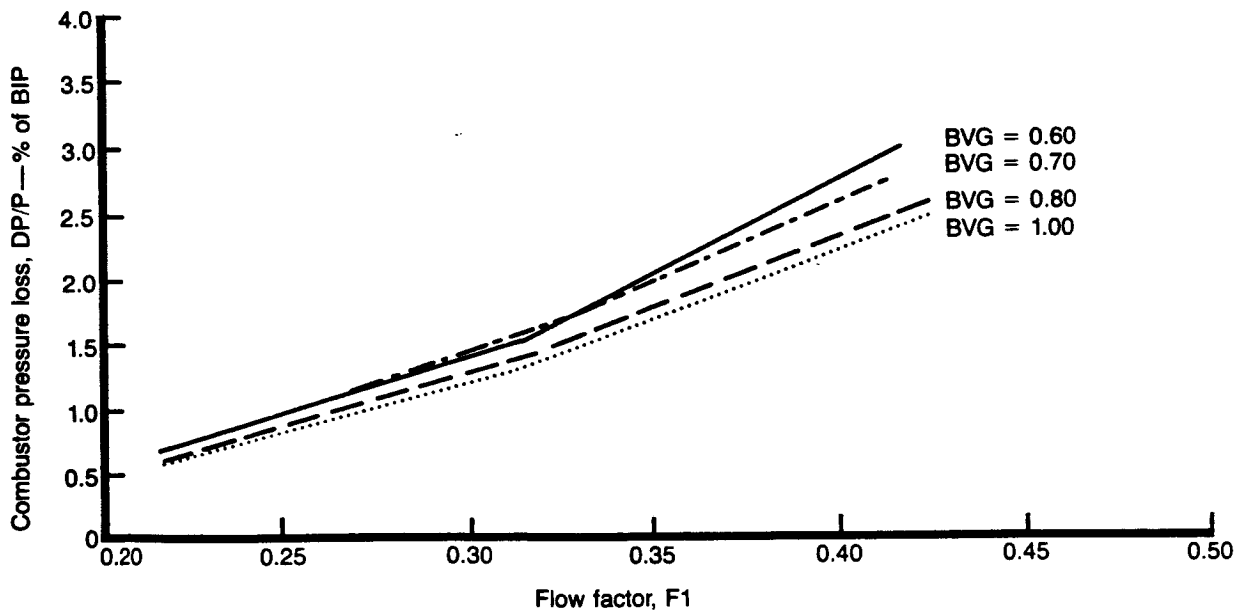
Nonreacting flow calibrations of combustor liner pressure drop versus flow rate as measured in the burner rig are essential to conduct scroll thermal shock rig tests. The inherent built-in leakage in the scroll rig requires an accurate calibration to determine the percentage of airflow into the scroll rig that actually enters the combustor when it is placed into the scroll rig. Calibration tests are conducted in the burner rig because it is leak-free.

The nonreacting flow calibrations were conducted at two inlet air temperatures, ambient and 537°C (1000°F). The relationship between combustor pressure drop, flow factor, and BVG setting do not change significantly with temperature as demonstrated in Figures 100 and 101.

Combustor rig burner assembly BU19 and BU20 refer to two different Asahi combustor bodies. Burner BU19 has small slots cut for the BOT thermocouples at the combustor exit plane while burner BU20 does not. Burner BU19 is dedicated to the scroll rig and often referred to as the scroll rig combustor. In all other aspects the burner assemblies are identical. Additionally, burner assembly BU20 is the same assembly previously referred to as BU16. Removal and reinstallation of the burner assemblies change their build numbers for purposes of identification. Thus, any difference in the comparison of liner pressure loss for burner assemblies BU16 and BU20 indicates that incorrect calibration data were obtained for one of the builds. Burner assembly BU19 calibration re-

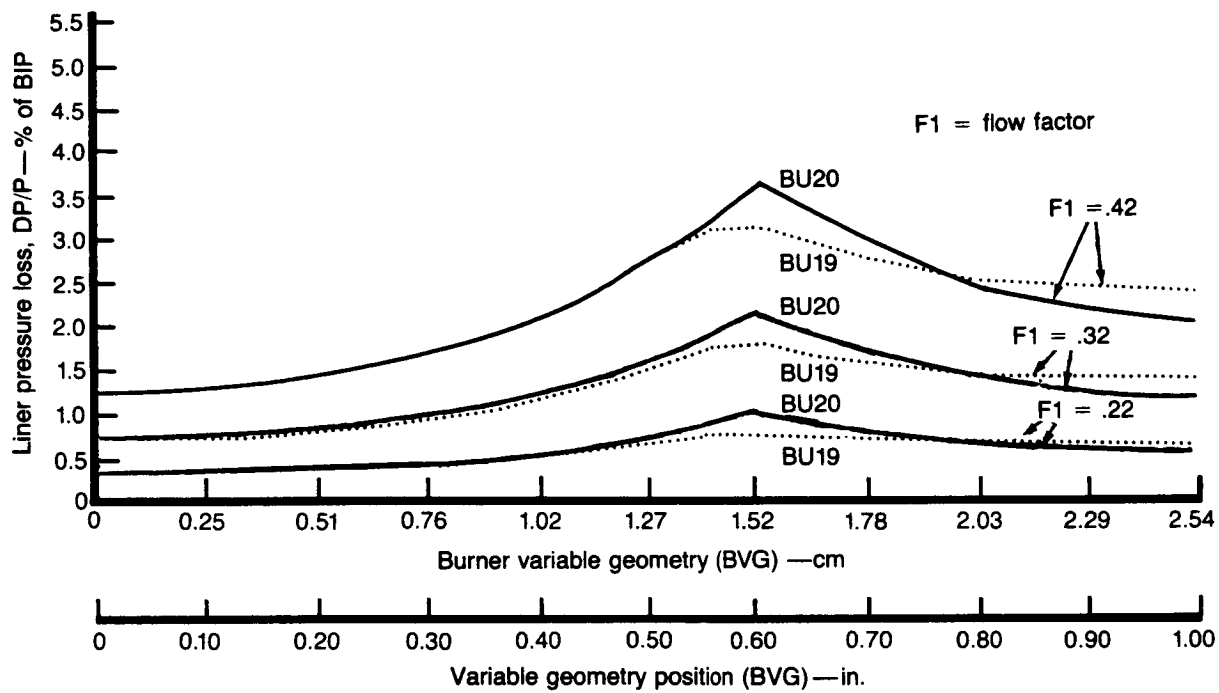


a. Ambient temperature data

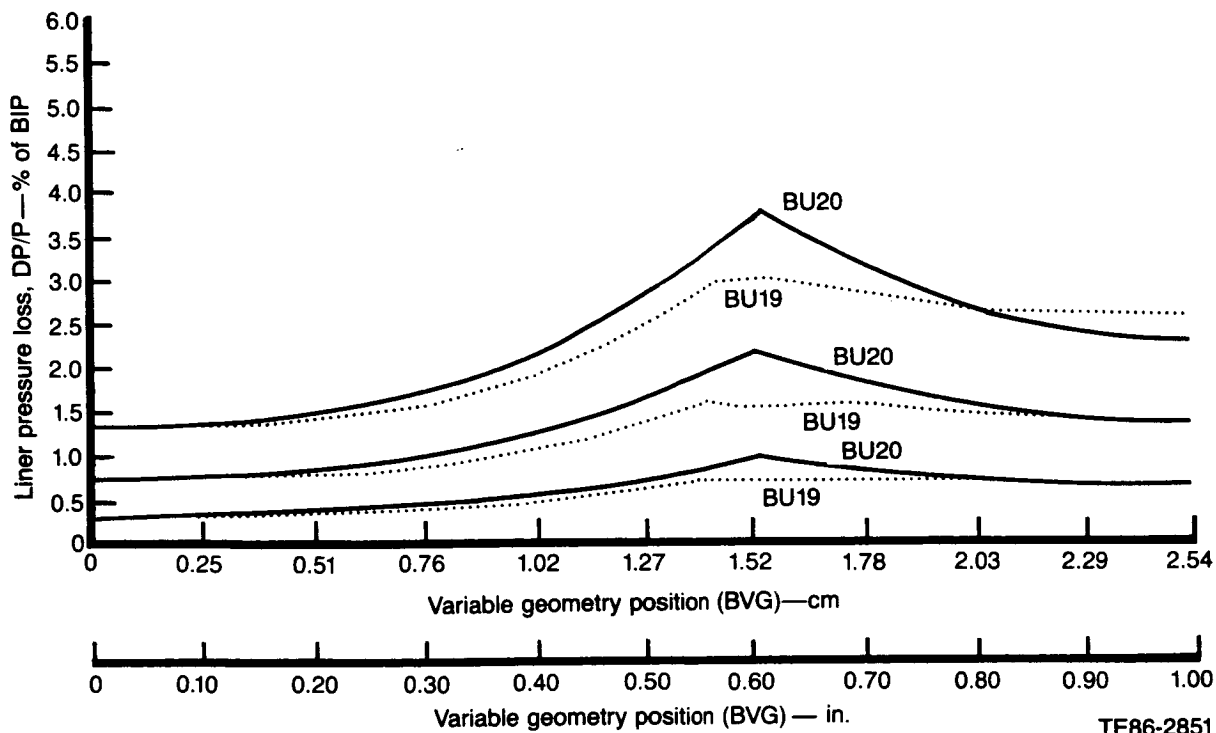


TE86-2850

Figure 100. AGT 100 combustor pressure loss calibration, Rig 54, BU19, Series A.



a. Comparison between BU19 and BU20, ambient inlet temperature data.



b. Comparison between BU19 and BU20, 338°C (1000°F) inlet temperature data

Figure 101. AGT 100 combustor pressure loss calibration.

sults are included to serve as a referee combustor liner to further indicate which set of data, BU16 or BU20, has the higher probability of being incorrect. Finally, it is important to note that no changes in the instrumentation or procedures to measure the liner pressure loss occurred between BU16, BU19, and BU20.

The ambient temperature data presented in Figure 100 for BU19 indicate that the maximum liner pressure drop was about 3% at a BVG setting of 15.24 mm (0.60 in.) and attained the design value of 2.5% at larger BVG settings where the combustor would normally operate under normal steady-state conditions. These measurements are in direct contrast to the larger pressure loss previously measured in the burner rig. As a result of these new measurements burner assembly BU16, now denoted BU20, was reflowed in the burner rig.

The data comparison between BU19 and BU20 as presented in Figure 101 indicates that the two liners have very similar but not identical pressure loss characteristics. It is not surprising that the scroll rig liner (BU19) pressure loss data are slightly lower. As previously stated, this is primarily due to the slots cut for the BOT thermocouples at the combustor exit plane and the fact that one of the slots is open (unfilled) due to an interference fit that occurred between the thermocouple designed for that slot and the gasifier scroll. The current measurements obtained in the burner rig for BU19 are compared to the pressure loss measurements for BU16 in Figure 102. The flow factor, F_1 , of 0.42 corresponds to maximum airflow rate at RPD conditions where the greatest deviation of measurements exists. At a BVG setting of 13.97 mm (0.55 in.), the deviation between the pressure drop results is over 60%. Because of the similarity of BU19 and 20 a direct comparison of BU16 and BU20 pressure loss data is not presented. An indirect comparison of BU20 and BU16 pressure loss data can be obtained by comparing the results presented for each in Figures 101 and 102. The current values for liner pressure loss are clearly lower, even though the same ceramic liner, radial swirler assembly, and centerbody/axial swirler assembly (BU16 and 20) were used. It can only be concluded that the 1984 cold flow test data, denoted BU16, are in error, most probably due to an instrumentation leak that was not detected.

As a result of these recent comparisons, liner pressure loss has been determined to be no larger than 3.75% and has approximately the design value of 2.5% at higher BVG settings. Further, the variation between liners and their different radial swirler and

centerbody/axial swirler configurations is not significant.

6.2.2 Combustor Proof Testing

Ceramic combustor hardware received from the various manufacturing vendors is assembled and tested under simulated engine conditions in the combustor rig before being installed in an engine build. The new combustor hardware is exposed to conditions similar to a typical engine lightoff and to full power operation. After testing, the combustors are carefully examined for damage and released to support AGT100 engine activity if no flaws are detected.

During this reporting period, two combustors successfully completed the proof test evaluation process. An Asahi combustor was subjected to the established proof test procedures that have proven to be a satisfactory evaluation of combustor integrity; also, a Sohio combustor was proof tested as part of the alternate fuel demonstration described in the next section. Limitations of the main fuel nozzle flow using methanol reduced the aerodynamic loading imposed upon the CBO combustor in the full power phase of the test. The test was, however, judged adequate because the temperature rise across the combustor simulated full power conditions and the burning time exceeded typical proof test requirements. In fact, the duration of the alternate fuel test was approximately triple the average proof test duration time.

6.2.3 Alternate Fuel Demonstration

The objective of this test was to demonstrate the alternate fuel capability of the AGT 100 combustion system. Traditionally, DF-2 and JP-5 have been used as fuels in the AGT 100 program. Methanol was selected as an alternate fuel for testing because of its relative low cost compared to DF-2, potential availability, and its low exhaust emission potential.

The AGT 100 combustion system consists of three individual fuel nozzles used during various engine operating regimes. The pilot nozzle acts as an initial ignition source at engine lightoff and as a sustainer source during main nozzle operation at low BIT and/or at operating conditions outside the lean-blowout limit. After ignition, the start nozzle is used to raise the combustor outlet temperature. Since the AGT 100 is a regenerative engine, the burner inlet temperature rises in unison. After the inlet temperature has risen sufficiently, the fuel flow transits from the start to the main nozzle that then sustains the engine operation. Methanol was successfully used as the primary fuel in all three of these fuel delivery systems.

The pilot torch was lit and a pilot fuel flow rate of 0.95 kg/s (2.1 lb/sec) produced an ignition source that ignited the start nozzle. Inlet temperature and

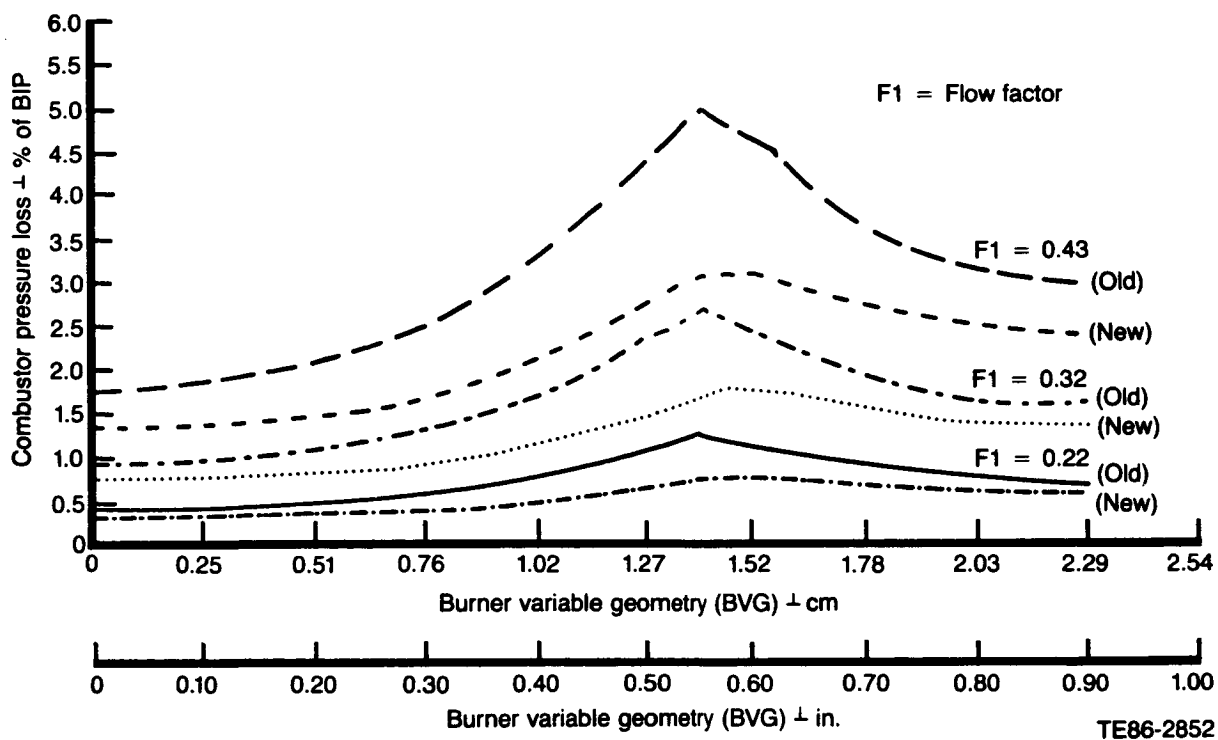


Figure 102. AGT 100 combustor pressure loss calibration comparison of BU16 (old) and BU19 (new) data.

pressure to the combustor were 315°C (600°F), and 0.18 kPa absolute (26 lb/in.² absolute) at ignition, respectively. The burner outlet temperature rose to 648°C (1200°F) with a corresponding start nozzle fuel flow of 58.5 kg/h (21.5 lb/hr). Optimal start nozzle combustion efficiency (98.4%) was achieved at a BVG setting of 5.08 mm (0.20 in.).

Methanol employment as the primary fuel for the main nozzle is flow rate limited with the existing hardware because the energy content per pound of methanol is roughly half that of DF-2 (heating value CH₃OH = 19.6 MJ/kg [8,580 Btu/lb], heating value DF-2 = 42.8 MJ/kg [18,400 Btu/lb]). Therefore, the quantity of fuel required to achieve a fixed temperature rise in the combustor using methanol is about twice the DF-2 flow rate. The main fuel nozzle was designed for DF-2 operation and does not have the capability to deliver twice that flow rate. Consequently, the RPD full-power engine airflow could not be flowed in the combustor rig and still achieve the desired high temperature rise across the burner. Thus, the alternate fuel demonstration test plan called for an airflow rate that corresponded to the maximum airflow rate of the current test-bed engine (approximately 0.26 kg/s [0.58 lbm/sec]).

The main nozzle test was conducted with the burner inlet temperature set at 815°C (1500°F) and a

420 kPa absolute (61 lb/in.² absolute) burner inlet pressure. Airflow was fixed at 0.26 kg/s (0.58 lb/sec). Methanol was introduced into the main nozzle to achieve a combustor fuel/air ratio of 0.012. With the BVG set to 12.7 mm (0.50 in.), chemical sampling revealed high hydrocarbon and CO emissions (UHC = 3.07 parts/million, CO = 635 parts/million) with relatively poor combustion efficiency (96.7%).

The emission data indicated that the optimum fuel/air mixture was not being introduced into the combustor. Therefore, the BVG was changed in 2.54 mm (0.10 in.) steps from 12.7 to 7.62 mm (0.50 to 0.30 in.). At 7.62 mm (0.30 in.) BVG position, emissions were dramatically reduced and combustion efficiency rose to 99.96% (UHC = 0.47 parts/million, CO = 6.57 parts/million). The outlet temperature from the combustor was recorded as 948°C (1738°F).

The burner outlet temperature was raised to 1038°C (1900°F) by increasing the fuel flow to achieve a 0.0197 fuel/air ratio. A flickering flame in the vicinity of the bypass holes was observed from the periscope viewing the combustor axially looking upstream from the combustor exit. The small flame appeared to originate at the stress relief crack in the combustor dome that extends radially from the bypass holes to the dome inner diameter. The flame is most likely a small diffusion flame that is stabilized in the local recircu-

lation region downstream of the crack and created by a locally rich fuel mixture. Corrective action was taken by moving the BVG so that more air was introduced into the upstream portion of the combustor. The small flame disappeared at a BVG setting of 12.7 mm (0.50 in.). This operation is also typical of DF-2 or JP-5 combustion.

Assessment of the combustor performance relied upon visual inspection and chemical sampling. Visual observation was possible because chemical reaction between methanol and air produces a translucent reaction zone, as shown in Figure 103. In terms of visual assessment of combustor performance, methanol is an ideal fuel.

The effects of combustor airflow distribution upon emissions and, hence, combustion efficiency, were examined by moving the BVG mechanism in 2.54 mm (0.10 in.) increments up to a BVG position of 20.32 mm (0.80 in.). The results of this survey are plotted in Figure 104 along with previous DF-2/JP-5 emission experience. The CO and NO_x emission levels from methanol are nearly an order of magnitude lower than those from DF-2 at similar burner inlet temperatures. Movement along an inlet temperature curve represents movement of the BVG mechanism. Optimal combustion efficiency for

methanol (99.97%) occurred at a BVG setting of 12.7 mm (0.50 in.), the lower point on the methanol emission curve of Figure 104.

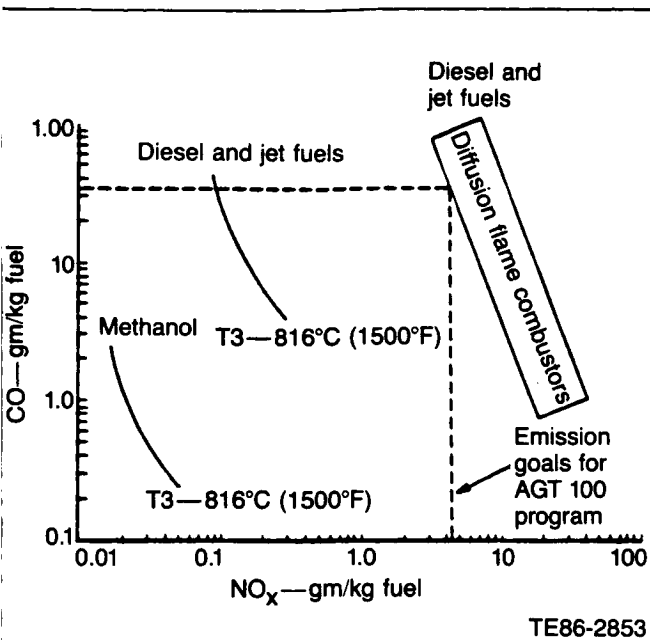
Main nozzle operation with methanol fuel required different optimal BVG settings than would be predicted from prior DF-2/JP-5 experience. This is not unexpected as the physical properties of methanol are quite different from the other hydrocarbon-based fuels. In fact, the atmospheric boiling point of methanol is near 66°C (150°F), at least half the normal boiling point of DF-2. The main nozzle vaporizes fuel distributed along a film surface placed in a prevaporization chamber located upstream of the primary reaction zone. A change in the physical properties of the fuel alters the evaporation rate at the film surface, and the standard operating procedures derived from DF-2/JP-5 testing need to be changed for methanol.

The methanol results are encouraging and suggest that the current main nozzle configuration is capable of handling fuels with a wide variation in physical properties through alteration of the burner variable geometry. Methanol combustor operation under both maximum airflow and temperature rise was not examined because of the current main nozzle tube size limitation. However, the successful results of this test imply that the combustor could be operated at full power conditions with hardware changes.



TE86-2854

Figure 103. AGT 100 methanol fuel combustion.



TE86-2853

Figure 104. Comparison of CO-NO_x emissions from methanol and diesel (jet) fuel combustion.

Overall, results of the alternate fuel test indicate that the AGT 100 combustion system is capable of methanol fuel operation. The start and main nozzles were ignited easily, and main nozzle operation was successful with no lean blowout or rich flashback problems. Chemical sampling revealed that main nozzle emissions with methanol fuel were an order of magnitude below DF-2 which, in turn, were about an order of magnitude below a typical diffusion flame combustor. Therefore, the potential for creating an ultra-low emission gas turbine burning prevaporized methanol, as in the AGT 100 system, is very encouraging.

VII. REGENERATOR DEVELOPMENT

Design and development of the regenerator disk and seals included the following activities during 1985:

- seals from new seal vendor evaluated in leaf seal rig test fixture
- seal rim preload tests conducted to evaluate patented feature to minimize seal distortion
- hot regenerator rig seal test of seals from new seal vendor
- characterization of the effects of permeability on radial and tangential strength of AS regenerator matrix material at 1100°C (2012°F)
- characterization of engine tested regenerator matrix material to determine effect of thermal cycling on radial strength
- strength as a function of thermal expansion requirements determined for advanced regenerator matrix materials for three engine operating conditions
- regenerator test rig repaired and recalibrated following test fixture failure

7.1 DESIGN AND MATERIAL DEVELOPMENT

7.1.1. Regenerator Seal Tests

Inboard Seals

Leaf Rig Tests. Three hot (in board) seals were tested for leaf leakage. These seals were the first produced by a new vendor and were of poor quality. The best of these three seals had leaf leakage of 0.013 kg/sec at 345 kPa-gage (0.028 lb/sec at 50 lb/in.²-gage). Previous seals have shown the following leakage rates:

- 0.013 kg/sec max at 345 kPa-gage (0.028 lb/sec max at 50 lb/in.²-gage)
- 0.009 kg/sec average at 345 kPa-gage (0.020 lb/sec average at 50 lb/in.²-gage)
- 0.006 kg/sec min at 345 kPa-gage (0.014 lb/sec min at 50 lb/in.²-gage)

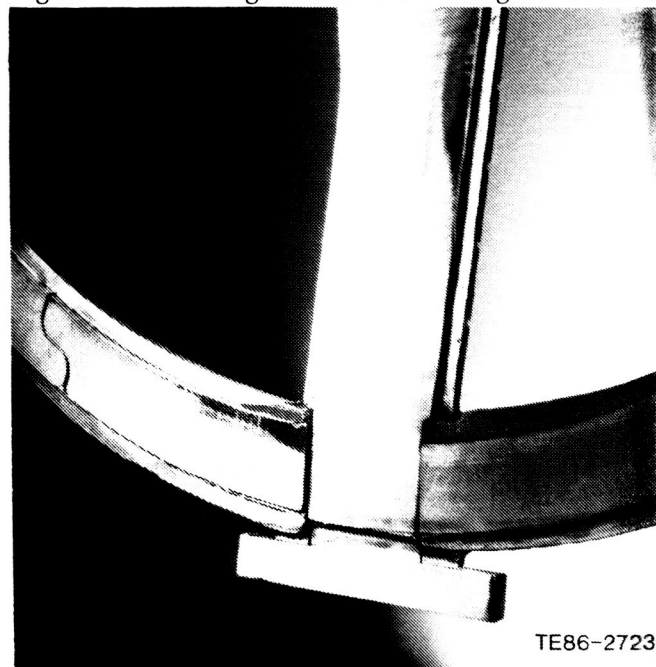
Sealing the platform-to-rim joint with wax produced 0.009 kg/sec (0.020 lb/sec) leakage. This demonstrated that most of the excess leakage was from a poor joint at that location. When 12.7 mm (1/2 in.) long rubber O-ring segments were installed beneath the leaf joints to act as helper springs, leakage was reduced to 0.008 kg/sec (0.017 lb/sec); however, metal helper springs inserted at the same locations, which were necessary for hot operation, could only produce 0.011 kg/sec (0.024 lb/sec) leakage. This failure of the metal helper springs to approach the leakage rate of

the rubber inserts demonstrates the need for better control of the metal load application.

Allison has completed a quality control program with the vendor on regenerator seals for the 404 Patriot engine that will provide improvement in future AGT 100 seals.

Seal Rim Preload Tests. Allison hot seal rim segments are preloaded by expanding them radially for joining with the crossarm. This patented feature counteracts thermal effects causing the rim segments to cone. These preloads are checked before hot operation and again afterward to confirm proper preload. Preloads on three short rim segments measured 13.6 to 14.5 kg (30 to 32 lb) and on three long rim segments measured 4.5 to 8.6 kg (10 to 19 lb). A recheck of rim preloads following several thermal cycles in the hot regenerator rig showed little change in preload. This showed that proper initial preloads have been established.

Hot Regenerator Rig Seal Tests. The best of the three new hot seals was tested briefly in the hot regenerator rig. It suffered disengagement between the short rim segment and the crossarm due to rounded corners at the step joint. This resulted in concentrated wear on the corner of the rim segment, as shown by Figure 105. The regenerator disk was grooved as a



TE86-2723

Figure 105. Regenerator seal showing displacement of rim segment and worn corner.

result. Keepers were installed on the three new seals to prevent this disengagement. After modification, the seal demonstrated 15% leakage at 100% speed and 14% at 55% speed. Future seals to be made by this vendor employing new quality controls are expected to provide 6% to 8% leakage.

Seals that had exhibited 33% leakage at 55% speed and 12% at 80% speed in the engine were shown to have 18% and 11% at similar conditions in the rig. The hot seal had a 7.6 mm (0.3 in.) bow in the crossarm and was believed to be not blowing down under the lower differential pressure conditions existing at low speed. Higher leakage in the engine was attributed to more adverse thermal gradients. An undistorted seal would be expected to produce 6% to 8% leakage in both rig and engine at all speeds.

7.1.2. Regenerator Disk

Characterization of Regenerator Matrix Strength.

The objective during the past year was to expand the data base for the wrapped 1100°C (2012°F) alumino-silicate (AS) matrix to include the radial modulus of rupture (MOR, Y_r), i.e., force per unit area. The vast majority of regenerator disk failures in the test rigs and engines occurred as circumferential cracks that involve tensile failure in the radial direction. Data from several sources show that the radial MOR is approximately one-third the tangential MOR. Work reported previously in this program has shown that the radial strength is dependent on the fracture plane wall thickness, the channel skew angle, and the cyclic thermal exposure (CTE) of the matrix.

Investigation during 1985 has shown that porosity of the matrix material also has an effect on the strength of the disk material. (This effect had been observed in engine disk tests where a low leak rate through the matrix walls is an acceptance test. The high leak rate disks showed a high rate of early failure). Comparison of the disk leak rate acceptance test data, which evaluates the tangential permeation rate, indicated that the leak rate data were about ten times larger than the radial permeation rate obtained in the laboratory for correlation with the tangential MOR. Accordingly, tangential permeation rates were measured to compare with the radial MOR values. It is recognized that the effect of the matrix structural geometry, which is quite different in the two directions, cannot be easily separated from the porosity/permeation effect.

Two disks were tested; disk 5 (GM16-04), which was exposed to an engine during the Ceramic Applications in Turbine Engines (CATE) program (1422 hours, 7800 cycles) and disk 7, a new untested disk. Samples from disk 5 were used to correlate the radial MOR (Y_r) with the effect of CTE (change in MOR due

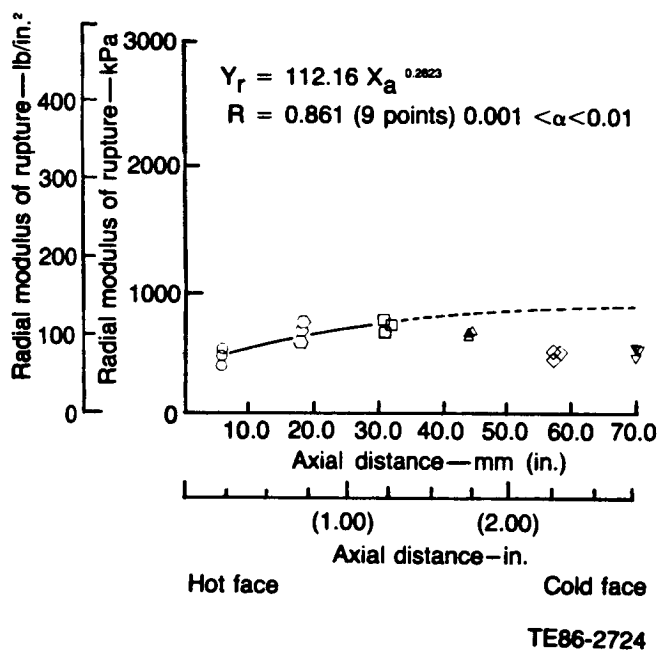


Figure 106. Power curve regression of radial modulus of rupture (MOR) on axial position.

to reduction of the amplitude of the temperature fluctuation with distance from the hot face). (See Figure 106). The key elements shown in the figure are the very low radial MOR, the reduced hot face strength due to CTE (engine cycles), and the drop off in strength from 4.5 cm (1.75 in.) to 7 cm (2.76 in.) due to channel skewness. The mean wall thickness of 0.0475 mm (1.875 mils) and lower than average skew angle of these test samples do not account for the low radial MOR values. A complete set of strength, wall thickness, skew angle, and porosity data in both tangential and radial directions was needed.

The second disk tested, disk 7, was selected from inventory and was in as-received condition. A sufficient number of samples to obtain a complete set of data comparing tangential and radial properties was obtained from disk 7. The results show the tangential MOR of disk 7 ($Y_t = 2.34$ MPa [341 lb/in.²]) to be very close to the mean strength (mean $Y_t = 2.32$ MPa [337 lb/in.²]) of the seven 1100°C (2012°F) AS disks tested during this program. The range of tangential MOR for the seven tested disks was 1.85 MPa (268 lb/in.²) to 2.77 MPa (402 lb/in.²). Thus the strength characteristics of disk 7 should be viewed as typical of the middle range of as-received wrapped 1100°C (2012°F) AS disks.

Disk 7, 1100°C (2012°F) aluminosilicate matrix as received, samples R-2-1 & RR2-2

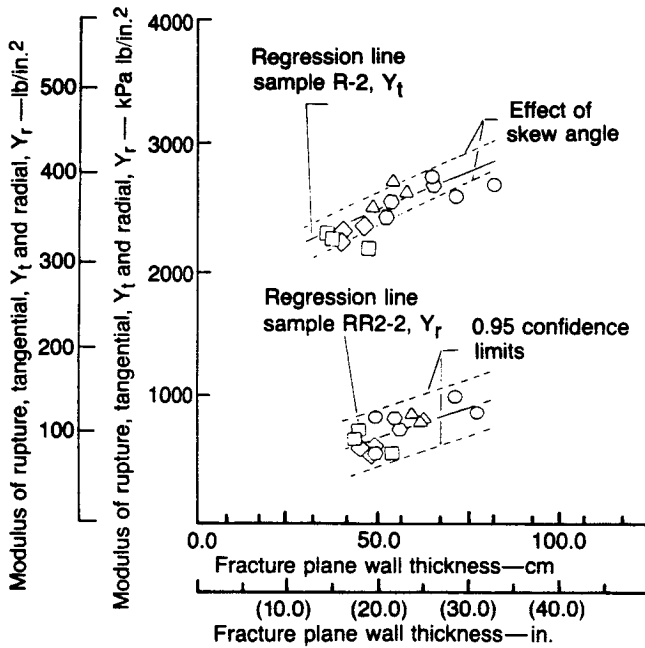
Multiple linear regression:

$$Y_t = 361.9 + 55.5(x_w - 1.99) + 3.50(x_s - 3.47)$$

$$\alpha_w \ll 0.001, \quad 0.001 < \alpha_s < 0.01$$

$$Y_r = 101.9 + 31.1(x_w - 2.08)$$

$$0.001 < \alpha_w < 0.01, \quad x_s \text{ not sign at } 0.10$$



TE86-2725

Figure 107. Comparison of tangential (Y_t) and radial (Y_r) modulus of rupture.

In Figure 107, a comparison of tangential and radial MOR properties is shown, which is typical of those run for disk 7. The plots show the difference in strength as a function of the wall thickness at a disk radius of approximately 25.4 cm (10.0 in.) to be about 1.79 MPa (260 lb/in.²). The relatively small effect of channel skew angle—obtained by multiple regression analysis—is shown by dashed bounds on either side of the tangential strength regression line. The variation in Y_t and Y_r due to wall thickness, over a very similar range of X_w is similar in trend. A similar plot for samples taken at a radius of 19.1 cm (7.52 in.) confirmed the data shown in Figure 107 and eliminated disk radius as a variable that must be considered in identifying the large difference in strength observed.

Two sets of gas permeation data were taken to compare the radial and tangential rates. One set of

data is for samples taken from the 25.4 cm (10.0 in.) radius and the other set from the 19.1 cm (7.52 in.) radius. Table XVI compares data at the two disk radii for radial and tangential permeation rates for a fixed ΔP of 138 kPa (20 lb/in.²).

The difference in permeation rates for the two axes is very large and in the direction that will produce the observed difference in strength. Further, the difference in permeation rates shown is not believed to be a function of wall thickness since the averages and ranges of wall thickness are quite comparable, as shown in Figure 107. As a consequence, it is believed that the permeability is caused by a corresponding difference in porosity, which produces a sharp reduction in strength in ceramic materials. Sufficient data are not available to relate MOR to permeability for this disk.

The process steps involved in fabricating the ceramic channels in the wrapped AS matrix disk are different for the separator walls (flat strips) and the sinusoidal (corrugated side walls) parts of the channels, and are considered to be a probable cause for the experimentally demonstrated difference in porosity.

This information will be of considerable practical importance in the near future when the extruded 1100°C (2012°F) AS matrix is made available by CGW. In the extruded matrix, the separator strips and side walls should be identical in processing and, having been formed under high pressure rather than solvent deposited, much lower in porosity than the wrapped matrix.

Allison has ordered extruded AS matrix samples from Corning for evaluation. The following are potential advantages for an extruded matrix:

- potentially less strength loss from temperature transients due to preferential grain alignment minimizing thermal stress caused by anisotropic expansion
- much greater strength due to improved geometry
- much greater strength due to less porosity due to compaction, grain alignment, and elimination of paper carrier burnout
- greater strength due to elimination of thin walls due to wicking in wrap process
- greater strength due to lower incidence of wall distortion
- ultimate lower cost especially when a one-piece extrusion is achieved
- higher effectiveness and lower pressure drop due to consistency in hole size

Overall, the conclusions reached from this work are as follows:

- Permeability and the correlate porosity are a factor

Table XVI.

Comparison of data for radial and tangential permeation rates.

Sample	25.4 cm (10 in.) radius		19.1 cm (7.52 in.) radius	
	radial	tangential	radial	tangential
Permeation rate—kg/sec mm ² /mm (lb/sec in. ² /in.)				
Mean X _p × 10 ⁵	0.00004 (0.0024)	0.0055 (0.3085)	0.00029 (0.0162)	0.00496 (0.2776)
Range X _{pmax} × 10 ⁵	0.0001 (0.0055)	0.0072 (0.4006)	0.00044 (0.0245)	0.0060 (0.3354)
X _{pmin} × 10 ⁵	0.00003 (0.0015)	0.0045 (0.2516)	0.0001 (0.0054)	0.00329 (0.1842)

of 17 or more times higher in the tangential direction than in the radial direction for wrapped AS matrix.

- Permeability in the tangential direction involves only corrugated walls.
- Permeability in the radial direction involves the same number of corrugated walls as in the tangential direction plus an equal number of flat walls.

Therefore, it can be concluded that corrugated walls are more permeable and weaker than flat walls. The effects of matrix geometry and permeability on strength have not been separated.

The laboratory tangential permeability data agree with figures calculated from leak rate acceptance checks and support rejection of disks with high leak rates for reasons of strength.

Regenerator Disk Stress Study. A regenerator disk stress study was done to predict required disk strength versus thermal expansion for future ceramic materials that will be required to withstand expected transient temperature peaks. Currently used AS material has adequate strength to withstand expected steady-state temperatures but cannot withstand an adequate number of transient temperature peaks and retain adequate strength. New candidate materials, which offer higher temperature capability, have higher thermal expansion that requires higher strength to resist resulting thermal stress. The objective of this study was to define required strength versus thermal expansion as a guide for material development. The effects of various engine operating conditions, nonlinear thermal expansion, and change in elastic modulus were also considered.

Figures 108 through 111 show maximum radial and tangential tensile and compressive stresses for constant coefficients of thermal expansion and for a variable coefficient representing a particular candi-

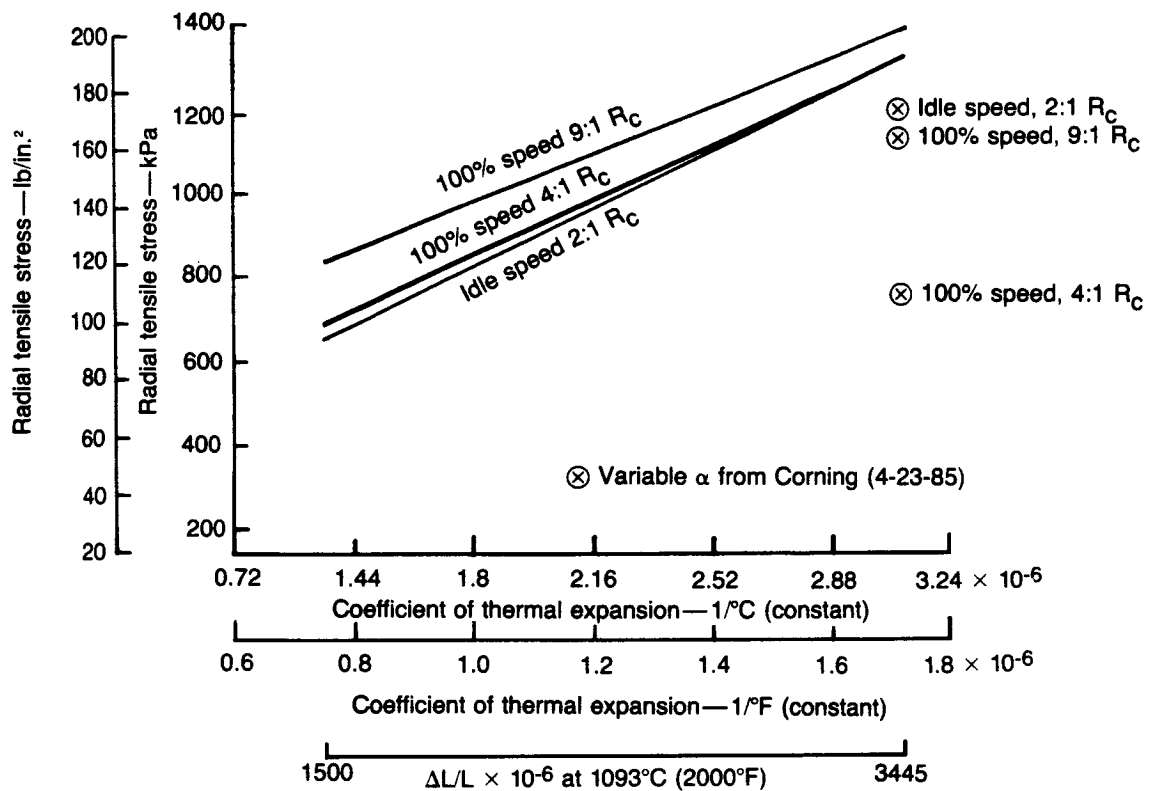
date material. The variable and constant expansion characteristics used in the study are shown in Figure 112. The stresses shown in Figures 108 through 111 are for the following engine conditions:

Power	Regenerator inlet temperature	Compression ratio
100%	788°C (1450°F)	9:1
100%	788°C (1450°F)	4:1
Idle	1093°C (2000°F)	2:1

With this range of conditions, estimates could be made of the strength required for specific conditions. The highest stress is 3.9 MPa (565 lb/in.²) tangential tension (Figure 110) produced at the idle, high temperature condition with either constant or variable coefficients of expansion. This stress is 99% thermal and only 1% pressure related. Allowing a factor of two for material variation, a new material with coefficient of expansion of 43.75 × 10⁻⁶ mm/mm—°C (1.7225 × 10⁻⁶ in./in.—°F) would be required to have a tangential tensile strength of 7.79 MPa (1130 lb/in.²). The predictions of strength for extruded material indicate this is an achievable goal. Stress at the idle condition was found to change in direct proportion to modulus of elasticity. Complete results of this study are contained in Allison TDR AD.0440-037.

7.2 RIG DEVELOPMENT TESTING

Extensive repairs have been made to the regenerator rig following a failure during testing. Rig inspection following failure of a ceramic flow straightener revealed burn through, cracking, and warpage of the inner liner and combustor, which required repair. The ceramic flow straightener had melted and collapsed. Debris from the straightener

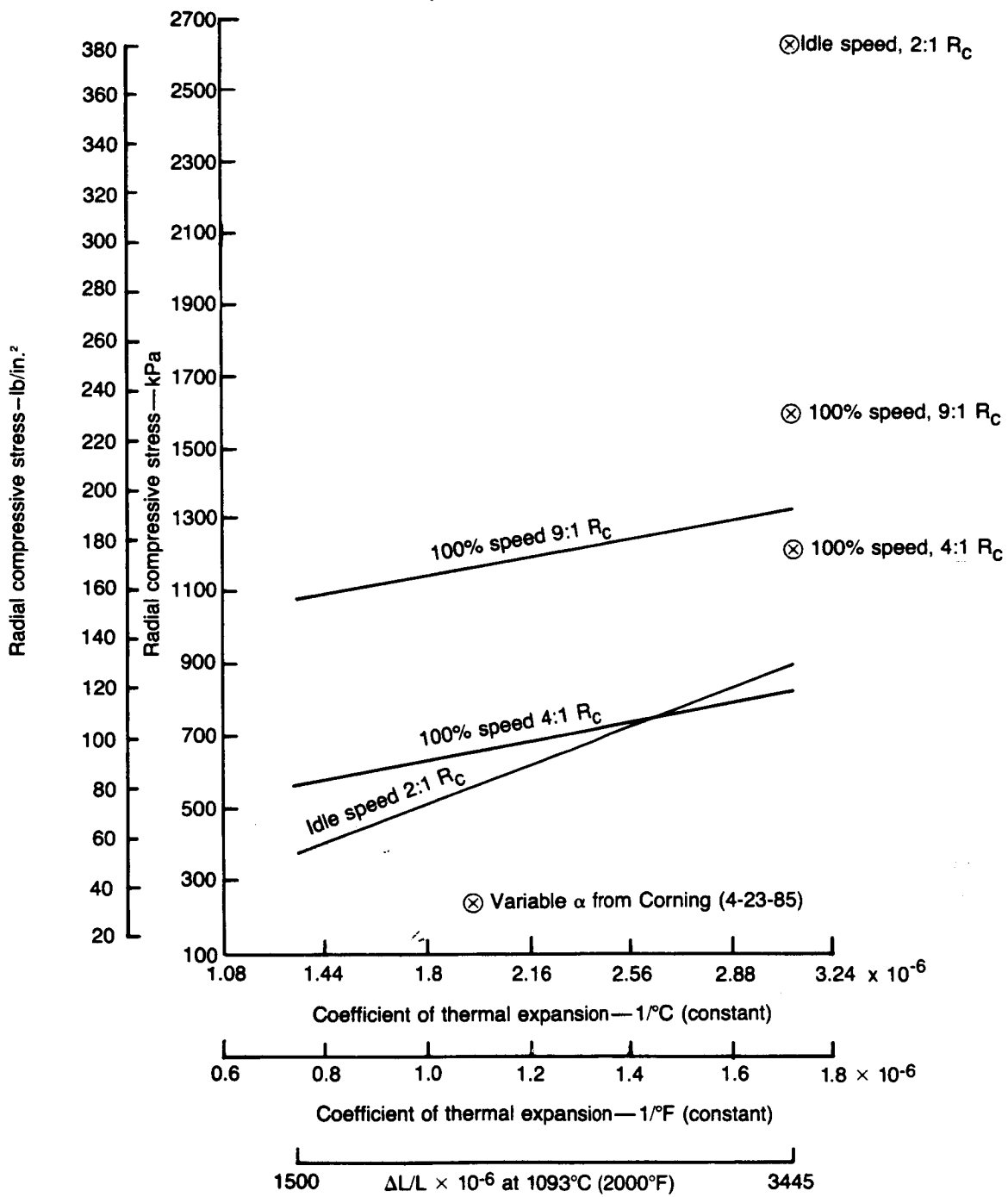


TE86-2718

Figure 108. Radial tensile stress versus coefficient of thermal expansion.

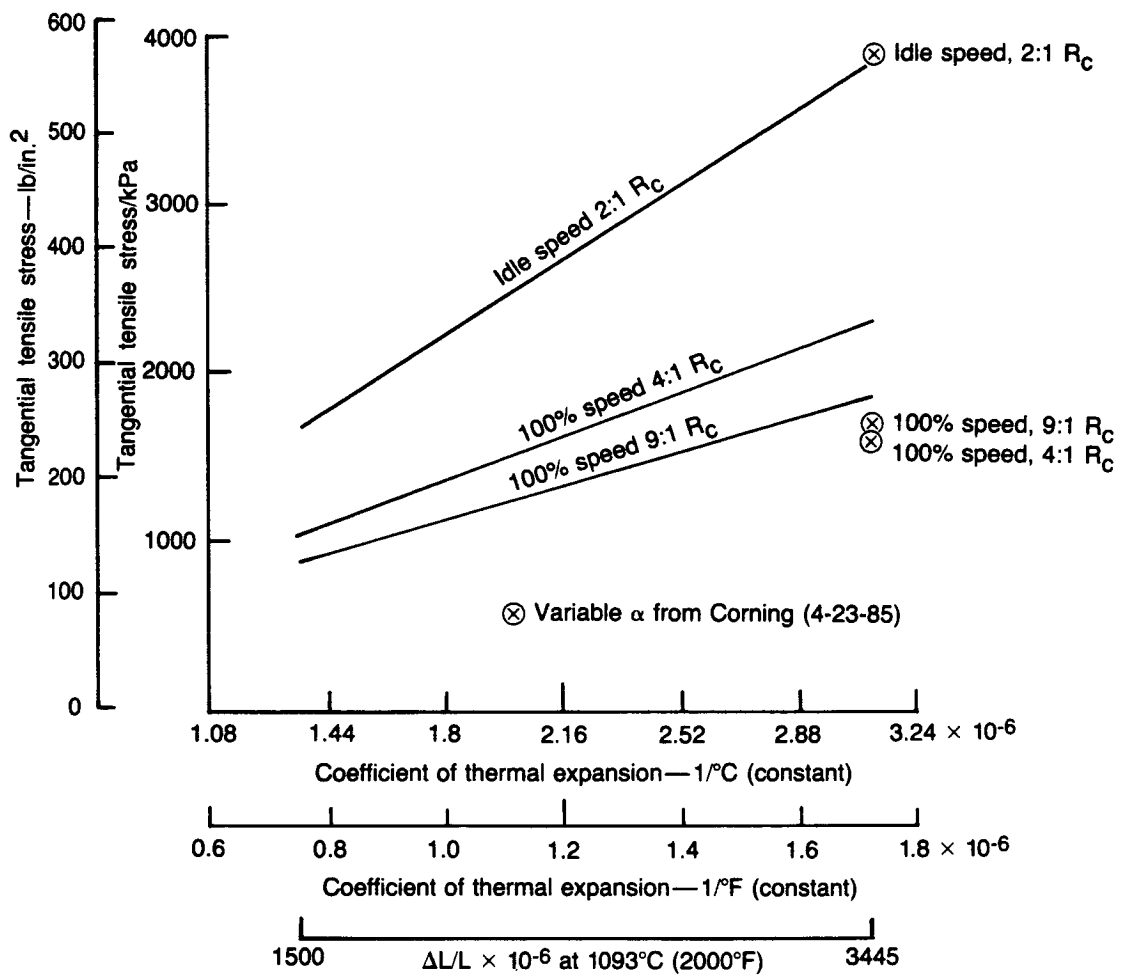
damaged the face of the regenerator test disk making it unsuitable for further testing. The failure was revealed by a 35% increase in on-line indicated seal leakage. All of the damage may have resulted from a malfunctioning pressure regulating valve that cut

airflow abruptly several times. It is planned to reduce maximum regenerator inlet temperature from 982 to 954°C (1800 to 1750°F) to improve durability and ease control. The rig is being leak checked and calibrated before resuming testing.



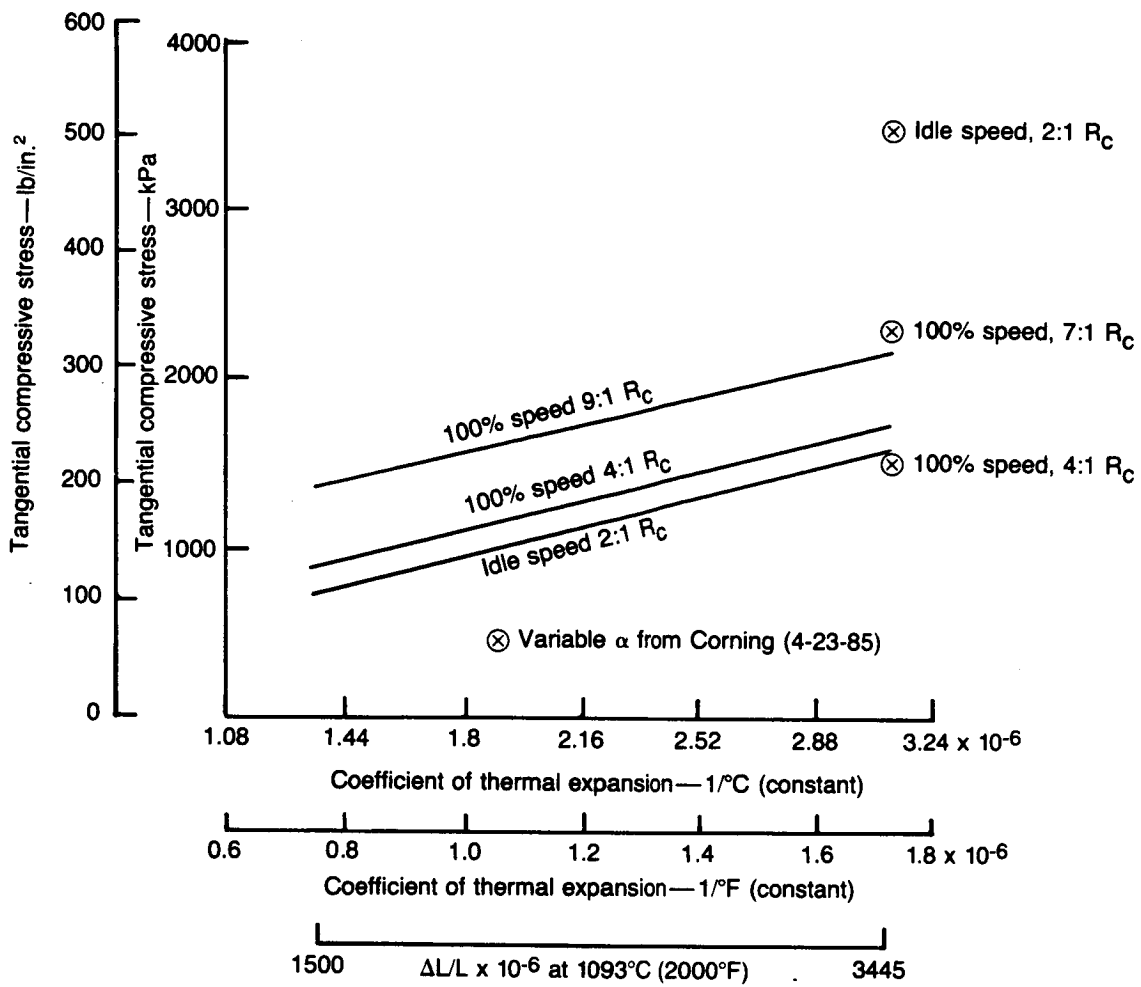
TE86-2719

Figure 109. Radial compressor stress versus coefficient of thermal expansion.



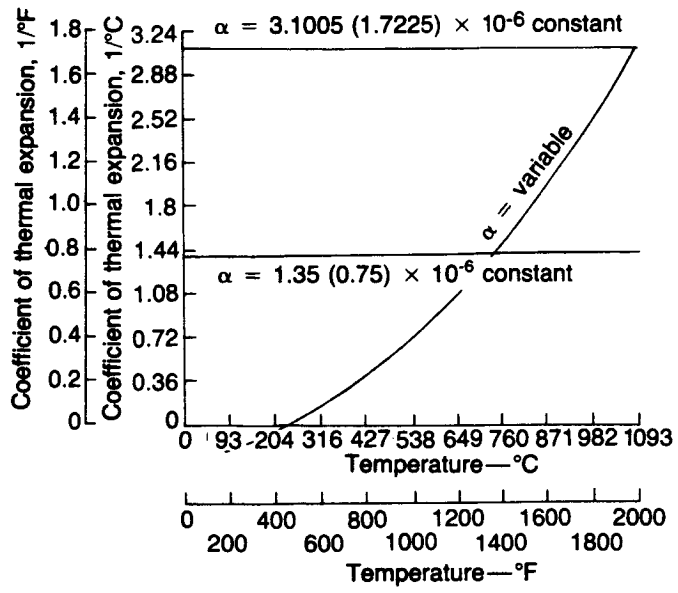
TE86-2720

Figure 110. Tangential tensile stress versus coefficient of thermal expansion.



TE86-2721

Figure 111. Tangential compression stress versus coefficient of thermal expansion.



TE86-2722

Figure 112. Coefficients of thermal expansion versus temperature.

VIII. SECONDARY SYSTEMS

Progress during 1985 has been made in the following areas:

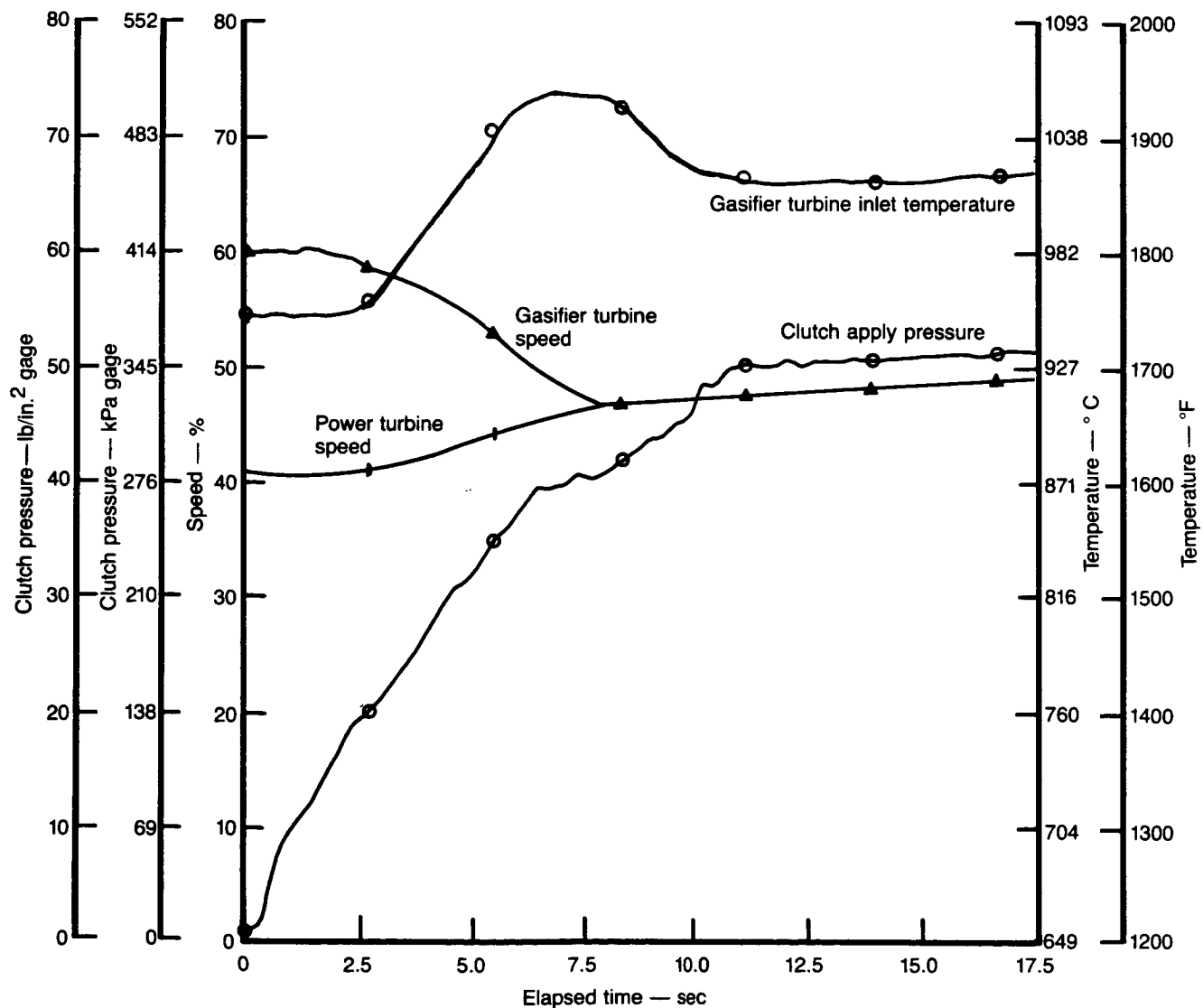
- power transfer clutch
- oil pump and regulating valve

8.1 GEARBOX

8.1.1 Power Transfer Clutch

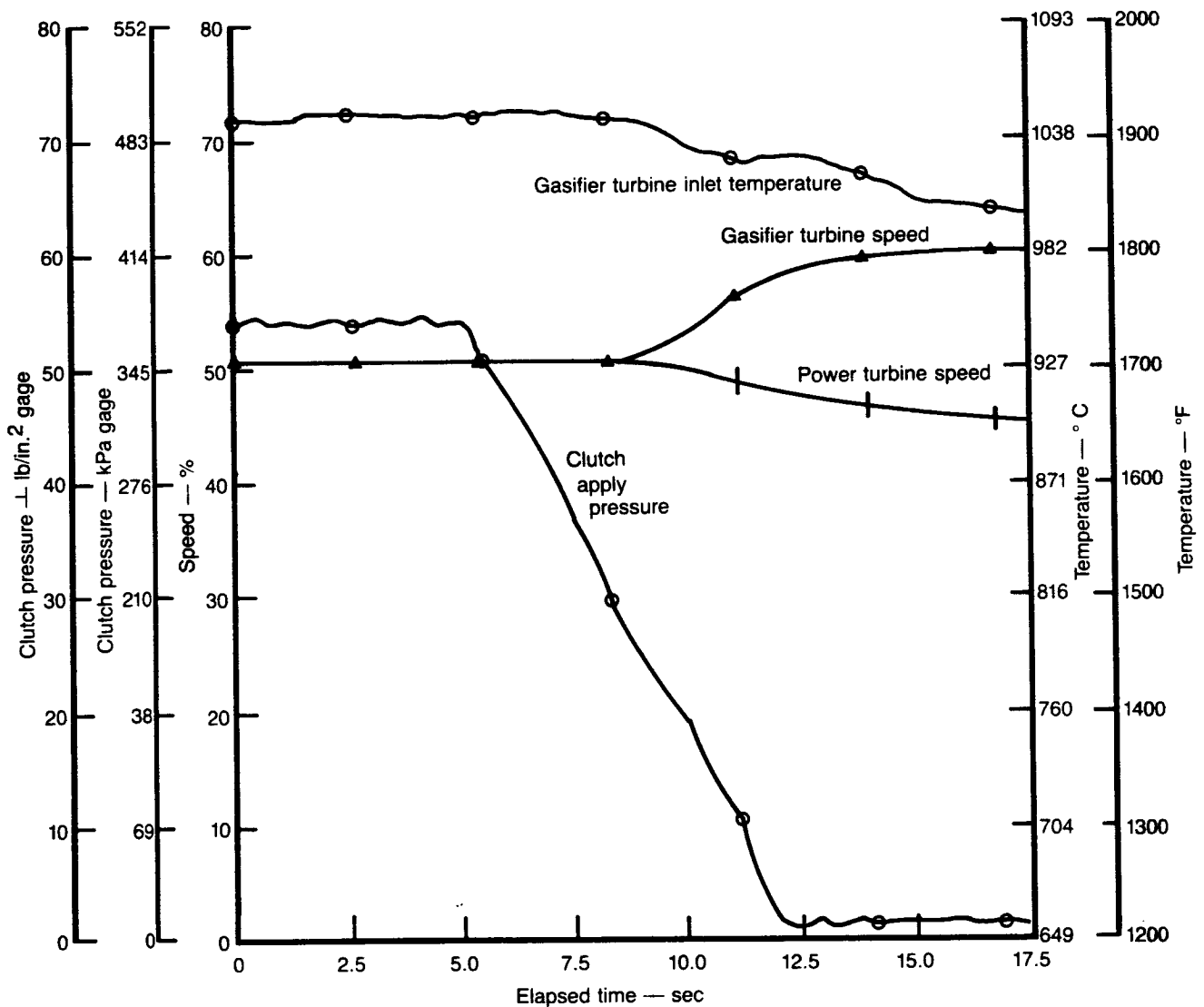
Limited engine clutch testing has continued during this reporting period. Clutch testing was

reinstated after installation of a redesigned engine oil pump that increased the supply pressure to the engine oil system. Testing of engine S/N 2 BU13 was performed during this period to evaluate control/engine response during clutch engagement and disengagement. Shaft speed differences between the two elements of the clutch were set prior to clutch activation; the shaft speed differences ranged from 3% to 20%. A typical engagement/disengagement cycle is presented in Figures 113 and 114. During this test the



TE86-2855

Figure 113. Speed, clutch pressure, and turbine inlet temperature as a function of time during power transfer clutch engagement.



TE86-2856

Figure 114. Speed, clutch pressure, and turbine inlet temperature as a function of time during power transfer clutch disengagement.

dynamometer was regulated to constant current, i.e., constant load. All testing was successful.

During the clutch testing the clutch was operated in the slipping mode for about 2.1 hr. This condition is the major mode of operation intended for the clutch in vehicular application. The test was performed to observe wear. Post-test teardown inspection revealed the clutch to be in excellent condition.

8.1.2 Oil Pump and Regulating Valve

Engine testing has been performed with an oil pump in which the pressure relief valve section was

redesigned to both prevent valve sticking and to deliver higher oil pressure. Test results indicate the oil pump modifications have been successful. No valve sticking has been encountered and system oil pressure has increased from 482 kPa (70 lb/in.²) to 689 kPa (100 lb/in.²).

8.2 BEARINGS AND SHAFT SEALS

8.2.2 Shaft (Carbon) Seals

The air-buffered, carbon, floating ring shaft seal behind the gasifier turbine continued to experience

oxidation failures. Data indicate that the air buffer pressure is less than that in the turbine backface allowing hot gas to enter the seal and replace the buffer air designed to protect it. Flow capacity of the present buffer air system has been determined to be inadequate to stop this hot gas backflow because of the large seal clearances that are being employed

during the shaft whip investigation. The air supply path is being reexamined to determine the potential to increase the flow capacity. Current carbon used in the seal is rated for 482°C (900°F). Carbon has been selected with 593°C (1100°F) rating and new seals with the more oxidation resistant carbon will be ordered.

IX. MATERIALS DEVELOPMENT

Materials development during this reporting period included effort on zircon thermal barrier material, silicon carbide components (gasifier and power turbine rotors and scroll assemblies), silicon nitride components (gasifier and power turbine rotors and scroll assemblies), and fiber-reinforced glass ceramics.

9.1 THERMAL BARRIER DEVELOPMENT

Material development for thermal barrier applications has concentrated on zircon. The effort has included property consistency studies, material qualification, process development, and advanced material development. During 1985, effort was directed primarily toward the last three items.

9.1.1 Material Qualification

Material qualification entails checking a new lot of spray-dried granules to see if it has the same character as previous lots. During 1985, 488 grams (1.08 lb) of a new batch (lot 4) were produced and qualified for thermal barrier application. The material is ZSA-100 zircon granules made at the AC Spark Plug Division of General Motors Corporation.

This material is considered to be the baseline or standard to which other advanced materials (or processes to produce zircon materials) are compared. A considerable study has been undertaken during past reporting periods to address the consistency (and characterize the variability) of this material.

Material qualification involves certain criteria; one of these is the thermal expansion characteristic of the material. It has been specified that the thermal expansion for the zircon material must lie between the upper and lower limits of the thermal expansion observed for sintered silicon carbide. As is evident in Figure 115, both lots 3 and 4 satisfy this criterion. Another criterion is strength. Material qualification requires that the mean modulus of rupture (MOR) of subsequent (or new) lots should not be less than the mean MOR of a previously qualified lot (lot 3 in this case) by more than one standard deviation, 24.1 MPa (3.499×10^3 lb/in.²) for this example. Strength data for lots 3 and 4 are listed in Table XVII.

The strength of lot 4 was within the specified limits; however, the material had surface inclusions high in zirconium and titanium oxide and its percent shrinkage did not fall within the limits presented in Figure 116. Nevertheless, the lot was sufficiently uni-

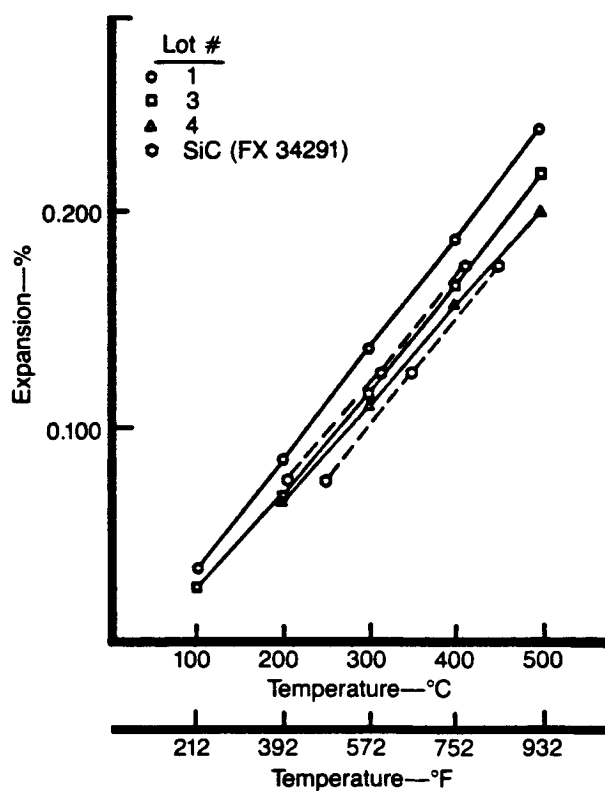
form to pass qualification requirements.

During 1986 more of this standard material will be prepared and checked for use in thermal barrier applications.

9.1.2 Process Development

Strength studies have been addressed to optimize MOR in zircon thermal barriers. If large voids on the order of 100 microns (shown in Figure 117) are present, the material is considered to be defective and material strength is greatly reduced. Such voids are usually attributed to entrapped air in the fired microstructure. High pressure processes have been developed to alleviate this problem.

It has also been observed that the spray-dried granules are frequently hollow or collapsed. Thus, an effort was initiated to reduce the frequency of this



TE86-2844

Figure 115. Thermal expansion of various zircon batches as compared to silicon carbide.

Table XVII.

Strength data for lots 3 and 4.

Lot	Mean MOR—MPa (lb/in. ²)	Standard deviation—MPa (lb/in. ²)	No. of bars
3	38.769 (267.27 x 10 ³)	3.499 (24.12 x 10 ³)	24
4	35.697 (246.09 x 10 ³)	4.593 (31.66 x 10 ³)	7

type of defect. A study was conducted to determine if lower water content in the spray slurry would improve the granule character. Granules were prepared from slurries with 67.15, 62.06, and 60.68% water and subsequently calcined. The granules were mounted and polished to permit examination of their interior.

Results of the study indicated that the lower water content contributed to a reduction of the frequency of collapsed and hollow granules (Figure 118). However, occasional large hollow voids (upper right corner of Figure 118C) were still present even in those

samples prepared with the lowest water content. Scanning electron microscope results also confirmed this result. Additional analysis is planned to resolve this problem.

9.1.3 Advanced Material Development

Research in advanced materials addresses improved strength, thermal expansion matching, and fabrication potential of new compositions. Results to date have indicated that zircon purity can affect reproducibility of thermal expansion. Both in-house and commercial sources to obtain high purity raw materials are being explored. Fully dense materials have been made from two different sources of raw material in an attempt to make a high purity fired final product. To date, the purity level has been increased, but a final product containing virtually pure zircon has not yet been obtained.

A fine grained zircon was obtained from M&T Chemicals, Rahway, NJ. A fired density of 4.216 g/cm³ (263.2 lb/ft³) was achieved; this is effectively the same

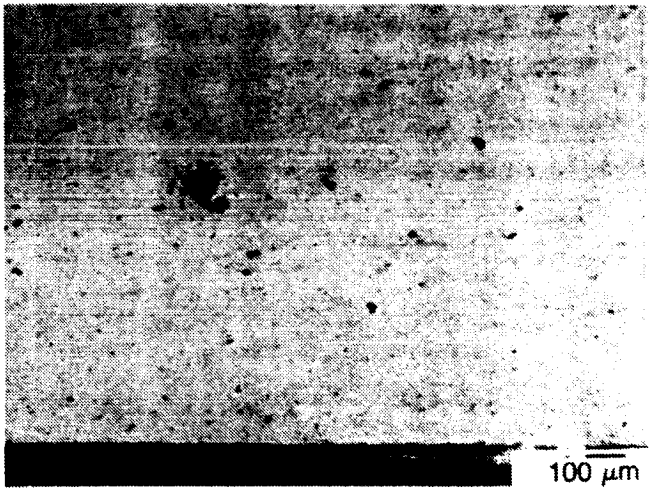
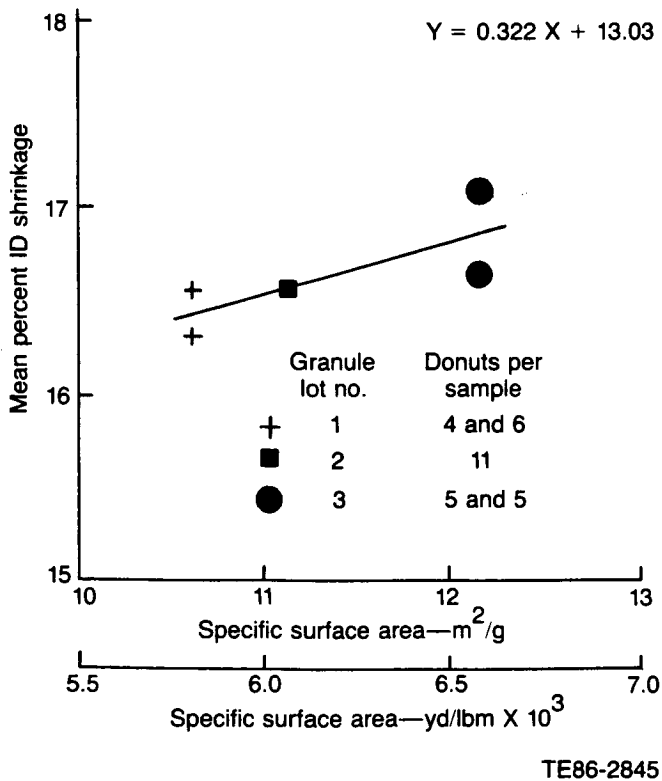


Figure 116. Shrinkage correlation with specific surface area.

Figure 117. Typical defect in fired microstructure.

as the present raw zircon material fired without added aluminum oxide. The M&T zircon does not appear to be an improvement over the present raw material.

Ceracryl (a General Motors trademark) zirconium oxide was added to the raw material in an in-house investigation to react in situ and produce pure, dense zircon. A maximum density of 4.467 g/cm^3 (278.9 lb/ft^3) was obtained, a yield which equates to 97% of the theoretical density for pure zircon. This is the highest purity ever obtained using an in situ reaction approach. Future MOR studies will indicate whether this material exhibits substantial property improvements over the present standard material.

9.2 SILICON CARBIDE COMPONENT DEVELOPMENT

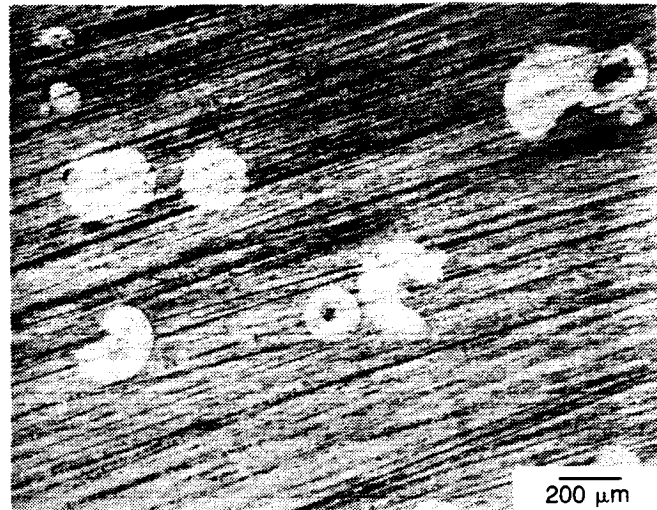
9.2.1 Gasifier Turbine Rotor

Process Development. The key features involved in the process development of αSiC material gasifier turbine rotors are summarized in Table XVIII. Particular emphasis was allocated to groups 8C and 8D that feature shaft end injection molding during this reporting period. Shaft end injection molding was successful in eliminating backface region molding flaws observed in prior processing. This resulted in a process yield (defined as green form to rotors suitable for spin proof test) of 52% as compared to only 11% for prior processing techniques. This substantially reduced the data scatter usually present from spin test results.

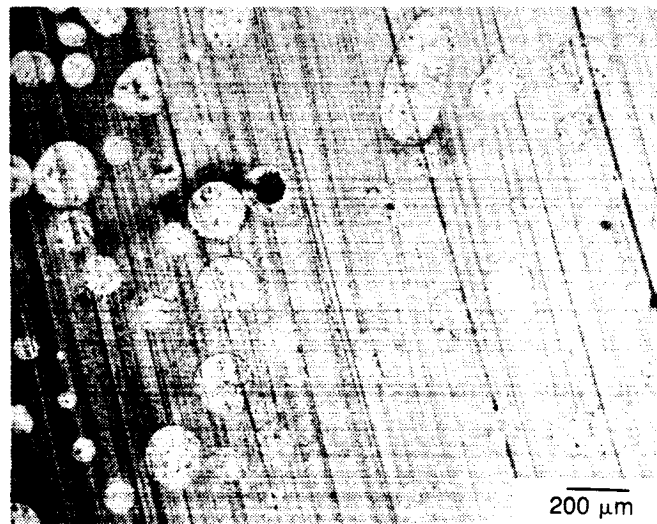
Evaluation Summary. The evaluation of 162 SiC rotors received during CY 1985 is summarized in Table XIX. The overall quality level (NDE) of the rotors is summarized as follows:

Quality level (surface)	Number
A	90
B	52
C	20
	162

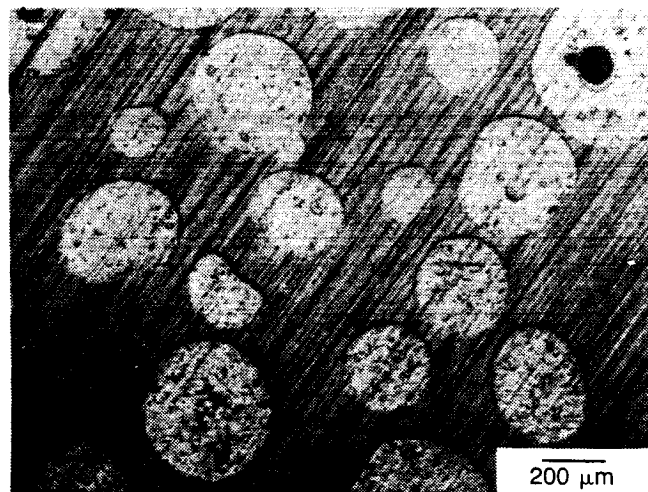
where A quality is free of visual or fluorescent penetrant inspection (FPI) indications, B quality rotors exhibit blendable indications, and C quality is rejected due to the presence of permanent (nonblendable) indications. Spin test and disposition of rotors number 105 through 162 (Table XIX) are pending at the date of this report.



A, 67.15%



B, 62.06%



C, 60.68%

TE86-2847

Figure 118. Granule interiors at three water contents.

Table XVIII.
Process development, gasifier turbines.

<u>P/N</u>	<u>No. molded</u>	<u>Sohio S/N</u>	<u>As-molded B or better</u>	<u>Sintered rotors Quantity/Date</u>		<u>Condition</u>
Time period—through 1984						
				<u>Actual</u>		
Group I	42	486 to 527	14	9	6/3/83	Reed + microprocessor
AA100395	90	528 to 617	21	20	6/8	Reed + microprocessor
(oval shaft)	110	618 to 727	33	29	7/18	Reed (65.09 mm [2.5625 in.] shot)
	16	728 to 743	0			Reed (66.68 mm [2.6250 in.] shot)
Group 2	138	744 to 881	16	12	7/29	SB-1, N-1 experimental
AA100932	15	882 to 896	7	6	8/5	SB-1, N-1 (15)
(round shaft)	20	897 to 916	5	4	8/22	SB-2, N-2 (20—same as 15)
	33	917 to 949	13	10	9/13	SB-2, N-2 experimental
	15	950 to 964	10	8	9/30	SB-2, N-2 (15)
	15	965 to 979	7			SB-3, N-1 experimental
	20	980 to 999	8	12	11/8	SB-3, N-1 (20)
Group 3A	100	1000 to 1099	17	9	11/21	SB-2, N-2 (100) without heat
	100	1100 to 1199	29	28		SB-2, N-2 (100) with heat
	76	1200 to 1275	0	0	1/19/84	Variable conditions
	100	1276 to 1375	27	27	1/25	SB-2, N-2 (100) with heat
Group 3B	100	1376 to 1575	64	20	4/27	SB-2, N-2 (100)
				20	5/18	with heat,
				19	6/8	invariant conditions
		233 received as of 6/30/84				
Group 4	125	1576 to 1700	8	8	8/31	Reed + microprocessor but with round shaft (see Group 1)
Group 5*	212	1701 to 1912	93	9	8/17	SB-2, N-2 with heat.
AA101151				13	8/27	Adjusted parameters but invariant from 1783 on.
(green body machining of backface, Baud curve)						Extra stock, backface, and shaft

Table XVIII (cont).

<u>P/N</u>	<u>No. molded</u>	<u>Sohio S/N</u>	<u>As-molded B or better</u>	<u>Sintered rotors Quantity/Date</u>		<u>Condition</u>
Group 6* AA101155	42	1913 to 1954	20	10	None delivered (experimental)	KX02 material, ECR tool (oversize), high polymer mix.
Group 7* AA100932	24	1955 to 1978	23	6	None delivered (experimental)	Experimental compound based on blade matrix High mold yield.
Group 8A* AA101156	60	1979 to 2038	49	12	None delivered (experimental)	Shaft end injection, extra stock base and shaft, invariant conditions.
Group 8B* AA101156	10	2039 to 2048	8	6	None delivered (experimental)	Shaft end injection, extra stock nose, invariant conditions.
263 received as of 31 December 1984						
Time period—1985						
Group 8C-1 AA101242	96	2049 to 2145	66	15	6/6 19 7/10 11 8/28	Shaft end injection, extra stock nose, base and shaft, invariant conditions, green machine Baud curve backface
Group 8D-1 AA101243	75	2146 to 2220	50	16	8/28 17 9/30	Shaft end injection, experimental mix, extra stock nose, base and shaft, three conditions, green machine Baud curve backface.
Group 8D-2 AA101243	52	2221 to 2272	48	5	2/26 12 3/4 10 3/29 6 4/2 4 6/6 4 7/10	Shaft end injection, experimental mix, extra stock nose, backface and shaft, green machine Baud curve backface, invariant conditions.
Group 8C-2 AA101242	78	2273 to 2350	32	6	4/2 21 4/26 2 6/6	Shaft end injection, extra stock nose, backface and shaft green machine Baud curve backface, four conditions.

Table XVIII (cont).

<u>P/N</u>	<u>No. molded</u>	<u>Sohio S/N</u>	<u>As-molded B or better</u>	<u>Sintered rotors Quantity/Date</u>	<u>Condition</u>
Group 5B AA101151	63	2351 to 2413	15	6/85	Extra stock base and shaft—replicate Group 5.
		162 received in 1985 425 received to date (12-31-1985)			

*Damaged compounder—metallic contamination of injection mold compound

Code:

Reed—Type of compounder

SB-1, -2, -3—Three sizes for the injection mold sprue busing

N-1, -2—Two sizes for the injection mold nozzle

Spin Test. A suspended item (proof and burst) Weibull treatment of the Group 8 spin tests is shown in Figure 119. The data are for 24 successful spin proof tests and 33 burst tests of the total group of 85 rotors suitable for spin. The balance (28) will be tested during the first quarter of 1986.

A cumulative probability of failure as a function of spin speed is presented in Figure 119. The successfully proofed rotors are flagged by an arrow pointing to the right (higher speed range). The data indicate an average burst speed of 115% N1 and a Weibull modulus (scatter) of 12. Calculations indicate that an average MOR bar strength in the 310 MPa (45×10^3 lb/in.²) to 345 MPa (50×10^3 lb/in.²) range corresponds to this average burst speed.

MOR Bar Strengths. The material strength calculated from spin burst speed data is generally substantiated by strength tests conducted on sample test bars sectioned from rotors serial number FX34408 and FX34412 (reference Table XIX). Results of the tests are summarized as follows:

MOR strength—MPa (lb/in.²)

<u>Rotor serial No.</u>	<u>Radial</u>	<u>Axial</u>
FX34408	383.4 (55.61×10^3)	338.13 (49.04×10^3)
FX34412	355.64 (51.58×10^3)	311.65 (45.20×10^3)

HIP Processed Rotors. Hot isostatic press (HIP) processing was investigated to determine its potential for producing rotors possessing high strength characteristics. NASA Lewis Research Center development

work indicates that a 20% strength increase can be achieved by HIPing sintered α SiC materials in test bar form.

A sample of nine, Group I, C quality rotors were HIP processed by NASA-Lewis. The objective of this study was to assess the potential microstructure/strength enhancement of fully sintered α SiC rotors. The assessment included sectioning, microstructure examination, MOR bars, and spin tests to burst. The rotors, identified by serial number, the HIP process, and status, are listed in Table XX.

The HIPed rotors exhibited an increase in density to 3.163 g/cm^3 (98.5% theoretical density) as compared to the original rotor density of 3.133 g/cm^3 (97.6% theoretical density). No observable differences in microstructure were detected. The observed spin burst speeds were similar to the non-HIPed group I results. This group was generally influenced by strength controlling surface flaws and the HIPed sample was likewise composed of C quality rotors with surface indications. HIPing is not effective in healing surface indications and it was concluded that this sample was not a definitive assessment of the potential of HIP processing.

A sample of 12 A and B surface quality Group 8 rotors were subsequently selected for another HIP process assessment. These are identified in Table XIX and at the date of this report are awaiting HIP at Lewis Research Center. It is anticipated that the rotors will be processed in March 1986.

Molding Trials, Thickened Airfoil Rotor. The gasifier airfoil was redesigned for increased thickness in the

Table XIX.

Inspection evaluation, gasifier turbines (1985 program).

No.	Shipment date	Group (1)	Part number	Serial number (2)	NDE		Spin (krpm) test	Disposition
					Quality level (3)	Dimen- sions (4)		
1	2-26	8D-2	AA101243	FX34405 (2221)	B		Proof at 96.8	Engine candidate (shaft machining)
2	2-26	8D-2	AA101243	FX34406 (2222)	B		2 blade fail- ures, 34.0 and 79.0	
3	2-26	8D-2	AA101243	FX34407 (2223)	B	-1.8%	Burst at 106.5	Broken airfoil
4	2-26	8D-2	AA101243	FX34408 (2225)	B		No	MOR bars
5	2-26	8D-2	AA101243	FX34409 (2226)	B		Burst at 101.6	Inducer airfoil release at 93.6
6	3-4	8D-2	AA101243	FX34410 (2227)	B		Burst at 93.0	
7	3-4	8D-2	AA101243	FX34411 (2228)	B		Proof at 96.3	Proof at 104.6
8	3-4	8D-2	AA101243	FX34412 (2229)	B		No	MOR bars
9	3-4	8D-2	AA101243	FX34413 (2230)	B		Burst at 79.3	Broken airfoil
10	3-4	8D-2	AA101243	FX34414 (2231)	B		Burst at 102.2	Inducer airfoil release at 79.3
11	3-4	8D-2	AA101243	FX34415 (2232)	B	-1.0%	Proof at 95.8	Engine candidate (shaft machining)
12	3-4	8D-2	AA101243	FX34416 (2241)	B		Proof at 95.2	Engine candidate (shaft machining)
13	3-4	8D-2	AA101243	FX34417 (2242)	B		Burst at 90	
14	3-4	8D-2	AA101243	FX34418 (2243)	B		Proof at 96.0	Engine candidate
15	3-4	8D-2	AA101243	FX34419 (2244)	B		Burst at 91.3	
16	3-4	8D-2	AA101243	FX34420 (2245)	B		Burst at 98.0	
17	3-4	8D-2	AA101243	FX34421 (2246)	B		Proof at 96.2	Burst at 100.7
18	3-29	8D-2	AA101243	FX34422 (2233)	A/C			Broken airfoil
19	3-29	8D-2	AA101243	FX34423 (2234)	C			Broken airfoil
20	3-29	8D-2	AA101243	FX34424 (2236)	B		Proof at 97.5	Burst at 114.2
21	3-29	8D-2	AA101243	FX34425 (2237)	A		Proof at 96.5	Burst at 98.5
22	3-29	8D-2	AA101243	FX34426 (2239)	B/C			Broken airfoil
23	3-29	8D-2	AA101243	FX34427 (2247)	C	0/-3.0%		Joining trial

Table XIX. (cont)

No.	Shipment date	Group (1)	Part number	Serial number (2)	NDE		Spin (krpm) test	Disposition
					Quality level (3)	Dimen- sions (4)		
24	3-29	8D-2	AA101243	FX34428 (2249)	C			Joining trial
25	3-29	8D-2	AA101243	FX34429 (2250)	C			Broken airfoil
26	3-29	8D-2	AA101243	FX34430 (2251)	A/C			Warped airfoil
27	3-29	8D-2	AA101243	FX34431 (2251)	A		Proof at 98.0	Burst at 101.3
28	4-2	8D-2	AA101243	FX34432 (2253)	B		Proof at 104.7	
29	4-2	8D-2	AA101243	FX34433 (2254)	A		Burst at 92.2	
30	4-2	8D-2	AA101243	FX34434 (2255)	C		Burst at 95.8	
31	4-2	8D-2	AA101243	FX34435 (2256)	A	-1.7%	Burst at 82.7	
32	4-2	8D-2	AA101243	FX34436 (2257)	A		Burst at 92.4	
33	4-2	8D-2	AA101243	FX34437 (2258)	C		Burst at 82.2	
34	4-2	8D-2	AA101242	FX34438 (2286)	B		Proof at 95.0	Proof at 102.5 HIP by Sohio
35	4-2	8C-2	AA101242	FX34439 (2292)	A		Burst at 92.0	
36	4-2	8C-2	AA101242	FX34440 (2293)	B	-1.5%	Burst at 88.8	
37	4-2	8C-2	AA101242	FX34441 (2295)	B		Burst at 85.6	
38	4-2	8C-2	AA101242	FX34442 (2297)	B		Proof at 95.0	Proof at 104.0
39	4-2	8C-2	AA101242	FX34443 (2300)	B		Burst at 89.9	
40	4-26	8C-2	AA101242	FX34444 (2312)	B		Proof at 96.5	Shaft broke after proof
41	4-26	8C-2	AA101242	FX34445 (2314)	B		Proof at 97.0	FOD test
42	4-26	8C-2	AA101242	FX34446 (2315)	C			Local void
43	4-26	8C-2	AA101242	FX34447 (2318)	B	-1.1%	Proof at 96.5	Proof at 103.5 HIP at Sohio
44	4-26	8C-2	AA101242	FX34448 (2322)	A/B		Proof at 92.0 and 105.4	Broken airfoil
45	4-26	8C-2	AA101242	FX34449 (2327)	B		Proof at 96.0	Engine candidate
46	4-26	8C-2	AA101242	FX34450 (2273)	B		Proof at 97.0	FOD test
47	4-26	8C-2	AA101242	FX34451 (2274)	B		Proof at 96.5	Burst at 99.2

Table XIX. (cont)

No.	Shipment date	Group (1)	Part number	Serial number (2)	NDE		Spin (krpm) test	Disposition
					Quality level (3)	Dimensions (4)		
48	4-26	8C-2	AA101242	FX34452 (2279)	B		Proof at 96.5 and 104.5	Engine candidate
49	4-26	8C-2	AA101242	FX34453 (2280)	B		Proof at 97.0	Engine candidate
50	4-26	8C-2	AA101242	FX34454 (2283)	A		Burst at 87.2	
51	4-26	8C-2	AA101242	FX34455 (2285)	C			Material sample
52	4-26	8C-2	AA101242	FX34456 (2330)	A/C			Broken airfoil
53	4-26	8C-2	AA101242	FX34457 (2331)	C			Material sample
54	4-26	8C-2	AA101242	FX34458 (2332)	A/B	-0/5%	Proof at 100.8	Burst at 101.5
55	4-26	8C-2	AA101242	FX34459 (2333)	B		Burst at 94.6	
56	4-26	8C-2	AA101242	FX34460 (2334)	B		Burst at 88.3	
57	4-26	8C-2	AA101242	FX34461 (2335)	A/B		Burst at 95.0	
58	4-26	8C-2	AA101242	FX34462 (2339)	B		Burst at 79.8	
59	4-26	8C-2	AA101242	FX34463 (2345)	A/B		Burst at 92.8	Warped blade
60	4-26	8C-2	AA101242	FX34464 (2346)	B		Burst at 78.0	
61	6-6	8C-2	AA101242	FX34465 (2348)	A			Broken blade HIP, LRC
62	6-6	8C-2	AA101242	FX34466 (2349)	A/B	-1.2%		Proof spin pending
63	6-6	8C-1	AA101242	FX34467 (2056)	C			Material sample
64	6-6	8C-1	AA101242	FX34468 (2057)	A/C			Warped blade HIP, LRC
65	6-6	8C-1	AA101242	FX34469 (2058)	A			Proof spin pending
66	6-6	8C-1	AA101242	FX34470 (2061)	B			HIP, LRC
67	6-6	8C-1	AA101242	FX34471 (2063)	B			Warped blade
68	6-6	8C-1	AA101242	FX34472 (2064)	A		Proof at 104.8	Engine candidate
69	6-6	8C-1	AA101242	FX34473 (2066)	A	-1.5%	Burst at 105.5	Proof spin pending
70	6-6	8C-1	AA101242	FX34474 (2067)	B			Warped blade HIP, LRC

Table XIX. (cont)

No.	Shipment date	Group (1)	Part number	Serial number (2)	NDE		Spin (krpm) test	Disposition
					Quality level (3)	Dimen- sions (4)		
71	6-6	8C-1	AA101242	FX34475 (2069)	A/C			
72	6-6	8C-1	AA101242	FX34476 (2071)	A		Proof at 105.5	Engine candidate
73	6-6	8C-1	AA101242	FX34477 (2102)	A/B			Proof spin pending
74	6-6	8C-1	AA101242	FX34478 (2103)	B			Proof spin pending, chipped blade
75	6-6	8C-1	AA101242	FX34479 (2104)	A			
76	6-6	8C-1	AA101242	FX34480 (2106)	B		Burst at 99.0	Proof spin pending
77	6-6	8C-1	AA101242	FX34481 (2108)	A			Warped blade HIP, LRC
78	6-6	8D-2	AA101243	FX34482 (2259)	B			Proof spin pending
79	6-6	8D-2	AA101243	FX34483 (2260)	A	+ 0.3%		Proof spin pending
80	6-6	8D-2	AA101243	FX34484 (2261)	A/C			3 broken blades
81	6-6	8D-2	AA101243	FX34485 (2262)	A/C			Broken blade HIP, LRC
82	7-10	8C-1	AA101242	FX34486 (2072)	A			Proof spin pending
83	7-10	8C-1	AA101242	FX34487 (2073)	A		Proof at 95.0	FOD Rig
84	7-10	8C-1	AA101242	FX34488 (2074)	A	0/+ 0.2%	Burst at 89.0	
85	7-10	8C-1	AA101242	FX34489 (2077)	A			HIP, LRC
86	7-10	8C-1	AA101242	FX34490 (2079)	B			HIP, LRC
87	7-10	8C-1	AA101242	FX34491 (2082)	A		Proof at 95.0	FOD Rig
88	7-10	8C-1	AA101242	FX34492 (2084)	A			HIP, LRC
89	7-10	8C-1	AA101242	FX34493 (2087)	C			Material sample
90	7-10	8C-1	AA101242	FX34494 (2089)	A/C			HIP, LRC
91	7-10	8C-1	AA101242	FX34495 (2091)	A	-0.8%		Proof spin pending
92	7-10	8C-1	AA101242	FX34496 (2092)	A			Proof spin pending
93	7-10	8C-1	AA101242	FX34497 (2096)	A			Proof spin pending
94	7-10	8C-1	AA101242	FX34498 (2097)	B		Burst at 94.8	

Table XIX. (cont)

No.	Shipment date	Group (1)	Part number	Serial number (2)	NDE		Spin (krpm) test	Disposition
					Quality level (3)	Dimensions (4)		
95	7-10	8C-1	AA101242	FX34499 (2101)	A			HIP, LRC
96	7-10	8D-2	AA101243	FX34500 (2263)	A			Proof spin pending
97	7-10	8D-2	AA101243	FX34501 (2264)	A			Proof spin pending
98	7-10	8D-2	AA101243	FX34502 (2269)	A	-1.0%		Proof spin pending
99	7-10	8D-2	AA101243	FX34503 (2270)	A			Proof spin pending
100	7-10	8C-1	AA101242	FX34504 (2121)	A		Proof at 95.0	FOD Rig
101	7-10	8C-1	AA101242	FX34505 (2123)	A		Proof at 103.6	HIP by Sohio
102	7-10	8C-1	AA101242	FX34506 (2124)	A			Proof spin pending
103	7-10	8C-1	AA101242	FX34507 (2125)	A	-1.3%	Proof at 95.0	FOD Rig
104	7-10	8C-1	AA101242	FX34508 (2126)	A			HIP, LRC
105	8-28	8C-1	AA101242	FX34509 (2128)	A/B			Distorted inducers
106	8-28	8C-1	AA101242	FX34510 (2129)	B/C			Broken inducer
107	8-28	8C-1	AA101242	FX34511 (2130)	A			Proof spin pending
108	8-28	8C-1	AA101242	FX34512 (2131)	B/C			Chipped inducer
109	8-28	8C-1	AA101242	FX34513 (2132)	C			Distorted inducers
110	8-28	8C-1	AA101242	FX34514 (2133)	C			HIP at Sohio
111	8-28	8C-1	AA101242	FX34515 (2134)	A			Proof spin pending
112	8-28	8C-1	AA101242	FX34516 (2136)	A			Proof spin pending
113	8-28	8C-1	AA101242	FX34517 (2142)	A/B			Chipped inducer
114	8-28	8C-1	AA101242	FX34518 (2143)	B			Proof spin pending
115	8-28	8C-1	AA101242	FX34519 (2144)	A			Proof spin pending
116	8-28	8D-1	AA101243	FX34520 (2154)	A			Proof spin pending
117	8-28	8D-1	AA101243	FX34521 (2159)	B/C			Chipped inducer
118	8-28	8D-1	AA101243	FX34522 (2160)	A/B			Chipped inducer

Table XIX. (cont)

No.	Shipment date	Group (1)	Part number	Serial number (2)	NDE		Spin (krpm) test	Disposition
					Quality level (3)	Dimensions (4)		
119	8-28	8D-1	AA101243	FX34523 (2162)	A/C		Broken inducer	
120	8-28	8D-1	AA101243	FX34524 (2164)	B/C		Broken airfoils	
121	8-28	8D-1	AA101243	FX34525 (2165)	A/B		Chipped inducer	
122	8-28	8D-1	AA101243	FX34526 (2166)	A/B		Chipped inducer	
123	8-28	8D-1	AA101243	FX34527 (2167)	A		Proof spin pending	
124	8-28	8D-1	AA101243	FX34528 (2168)	A/C		Chipped inducer	
125	8-28	8D-1	AA101243	FX34529 (2169)	A		Proof spin pending	
126	8-28	8D-1	AA101243	FX34530 (2171)	B		Proof spin pending	
127	8-28	8D-1	AA101243	FX34531 (2173)	A		Proof spin pending	
128	8-28	8D-1	AA101243	FX34532 (2175)	A		Proof spin pending	
129	8-28	8D-1	AA101243	FX34533 (2176)	A		Proof spin pending	
130	8-28	8D-1	AA101243	FX34534 (2177)	A/B		Chipped inducer	
131	8-28	8D-1	AA101243	FX34535 (2179)	A		Proof spin pending	
132	9-30	8D-1	AA101243	FX34536 (2180)	C		Distorted inducers	
133	9-30	8D-1	AA101243	FX34537 (2183)	A		Proof spin pending	
134	9-30	8D-1	AA101243	FX34538 (2186)	A		Proof spin pending	
135	9-30	8D-1	AA101243	FX34539 (2188)	B		Chipped inducer	
136	9-30	8D-1	AA101243	FX34540 (2191)	C		Chipped inducer	
137	9-30	8D-1	AA101243	FX34541 (2196)	A/C		Distorted inducers	
138	9-30	8D-1	AA101243	FX34542 (2199)	C		Material sample	
139	9-30	8D-1	AA101243	FX34543 (2203)	A/C		Broken inducer	
140	9-30	8D-1	AA101243	FX34544 (2204)	C		Material sample	
141	9-30	8D-1	AA101243	FX34545 (2205)	B		Proof spin pending	
142	9-30	8D-1	AA101243	FX34546 (2206)	A		Proof spin pending	

Table XIX. (cont)

No.	Shipment date	Group (1)	Part number	Serial number (2)	NDE		Spin (krpm) test	Disposition
					Quality level (3)	Dimensions (4)		
143	9-30	8D-1	AA101243	FX34547 (2207)	A/C		Broken inducer	
144	9-30	8D-1	AA101243	FX34548 (2208)	A		Proof spin pending	
145	9-30	8D-1	AA101243	FX34549 (2209)	B/C		Distorted inducers	
146	9-30	8D-1	AA101243	FX34550 (2210)	C		Chipped inducer	
147	9-30	8D-1	AA101243	FX34551 (2212)	B/C		Chipped inducer	
148	9-30	8D-1	AA101243	FX34552 (2213)	A		Proof spin pending	
149	11-4	8D-1	AA101243	FX34553 (2214)	A		Proof spin pending	
150	11-4	8D-1	AA101243	FX34554 (2215)	A/C		Broken exducer	
151	11-4	8D-1	AA101243	FX34555 (2220)	C		Material sample	
152	11-4	8D-2	AA101243	FX34556 (2271)	B		Proof spin pending	
153	11-4	8D-2	AA101243	FX34557 (2272)	B		Proof spin pending	
154	11-4	5B	AA101151	FX34558 (2375)	B		Proof spin pending	
155	11-4	5B	AA101151	FX34559 (2376)	B		Proof spin pending	
156	11-4	5B	AA101151	FX34560 (2377)	B		Proof spin pending	
157	11-4	5B	AA101151	FX34561 (2378)	C		Material sample	
158	11-4	5B	AA101151	FX34562 (2382)	B		Proof spin pending	
159	11-4	5B	AA101151	FX34563 (2390)	C		Material sample	
160	11-4	5B	AA101151	FX34564 (2407)	B		Proof spin pending	
161	11-4	5B	AA101151	FX34565 (2408)	B		Proof spin pending	
162	11-4	5B	AA101151	FX34566 (2409)	B		Proof spin pending	

(1) Prior groups per Table XVIII, 1984 Annual Report, EDR 12070

(2) Allison serial No. (Sohio serial No.)

(3) Quality level based on visual and FPI evaluation. Second rating (example A/C) refers to spin rating. Typically the C identifies a warped or broken airfoil.

(4) Exducer throat, nominal = 8.33 mm (0.328 in.)

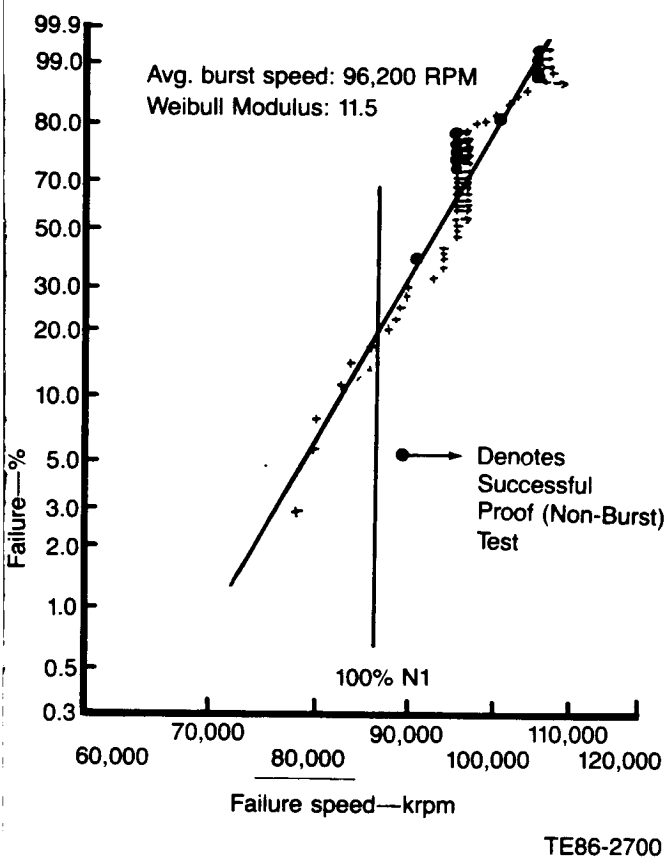


Figure 119. Cumulative probability of failure as a function of spin speed, Group 8 (1985) SiC gasifier rotors.

inducer region. The redesign was fully discussed in Section 4.3; the following describes the processing of this rotor.

Sohio modified the injection-molding tool with new inserts for the thicker airfoil (part number AA101326). The gasifier rotor tool with these inserts presented new molding problems. A total of 234 rotors were molded during December of which only 79 were selected for further processing; the mold yield was only 33.8%. The area between the blades was generally good and defects were largely on the base and nose. All 79 rotors were subsequently submitted for base contour machining (removing 0.254

mm [0.010 in.] on most of the rotors) and removal of the excess nose stock.

All 79 parts completed green machining and a total of 47 were submitted for binder removal. If subsequent processing is satisfactory, the first rotors should be shipped about mid-March 1986.

Engine Candidate Gasifier (SiC) Turbine Assemblies.

An example of a finished SiC rotor/metal shaft assembly is shown in Figure 120. The status of engine candidate gasifier turbine assemblies is summarized in Table XXI. Assembly number 10 (S/N FX34360) was engine (S/N 2, BU12) tested during August 1985. It experienced inducer airfoil failure similar to the test in November 1984. Two other assemblies are complete: Number 11 (S/N FX34357), which is scheduled to be installed in engine S/N 2, BU15 for a foreign object damage (FOD) free test, and number 13 (S/N FX34362), which is available for engine test.

9.2.2 Gasifier Turbine Scroll Assembly

Silicon carbide gasifier turbine scroll assembly development continued during the present reporting period and included the following major activities:

- two proof tests of a Sohio scroll assembly in thermal shock test rig—one to 898°C (1650°F) and one to 1051°C (1925°F)
- testing of Corning composite ceramic inner backplates in engine and static proof test rig
- two engine tests of the Sohio scroll assembly
 - one test completed at 926°C (1700°F)
 - one test begun at 1079°C (1975°F) and continuing at year's end
- analysis of fracture of outer backplate in 926°C (1700°F) engine test
- design modification and rework of outer backplates to reduce thermal stresses
- investigation of scroll braze joint oxidation
- preparation of second scroll assembly for testing
- silicon carbide gasifier turbine static components parts fabrication

These scroll assembly development activities are described in the following sections.

Table XX.
HIP process rotors (all processed at 137 MPa [20 x 10³ lb/in.²] in an Argon atmosphere).

<u>No.</u>	<u>S/N</u>		<u>Process</u>	<u>Status</u>
1	FX34134	2200°C (3992°F)	1 hr, carbon sand encapsulation	Microstructure
2	FX34137	2050°C (3722°F)	1 hr, carbon sand encapsulation	Spin burst at 86,000 rpm
3	FX34144	2200°C (3992°F)	3 hr	Microstructure
4	FX34151	2200°C (3992°F)	3 hr, carbon sand encapsulation	Spin burst at 98,300 rpm
5	FX34163	2200°C (3992°F)	3 hr, carbon sand encapsulation	Spin burst pending
6	FX34169	2050°C (3722°F)	1 hr	MOR bars
7	FX34181	2200°C (3992°F)	1 hr	MOR bars
8	FX34187	2050°C (3722°F)	1 hr, carbon sand encapsulation	Spin burst pending
9	FX34191	2200°C (3992°F)	1 hr, carbon sand encapsulation	MOR bars

Table XXI.
Status of engine candidate gasifier rotor assemblies.

<u>No.</u>	<u>Rotor S/N</u>	<u>Rotor only spin</u>	<u>Insulator installed</u>	<u>Joined to shaft</u>	<u>Machined</u>	<u>Inspected</u>	<u>Rotor-shaft spin</u>	<u>Installed in engine</u>	<u>Comments</u>
1	FX34305	X	X						The insulator and rotor shaft were damaged during finish grind of the o.d and length. (Joining of the insulator to the rotor shaft is the first step in the assembly buildup.) Stub shaft was not usable.
2	FX34311	X	X	X					Complete rotor/shaft assembly was successfully built. Rotor stub shaft fractured during routine handling at Allison.
3	FX34312	X	X	X					Complete rotor/shaft assembly was successfully built. Rotor stub shaft fractured during lathe setup for machining at Atlas. (Fracture was similar to FX34311.)
4	FX34307	X	X	X	X	X			Fractured during bearing assembly at Balco.
5	FX34286	X	X	X	X	X	X	X	Final spin test limited to 77,000 rpm due to equipment; operated in engine S/N 2 BU8. Inducer airfoil fracture. (November 1984)
6	FX34334	X	X	X	X	X			Failed at 52,500 rpm due to defective spin equipment.
7	FX34340	X	X						Two chipped airfoils at exducer section due to handling.
8	FX34346	X	X						Inducer airfoil broken in handling; not usable.

Table XXI. (cont)
1985 Group 8 processing

No.	Rotor S/N	Rotor only spin	Insulator installed	Joined to shaft	Machined	Inspected	Rotor-shaft spin	Installed in engine	Comments
9	FX34321	X	X						Proofed to 95,000 rpm; two airfoils broken in handling; not usable.
10	FX34360	X	X	X	X	X	X	X	Final spin test limited to 73,400 rpm due to equipment; operated in engine S/N 2, BU12. Inducer airfoil fracture. (August 1985)
11	FX34357	X	X	X	X	X	X	X	Assembly final spin to 50,000 rpm. Being installed in S/N 2, BU15, FOD free test.
12	FX34356	X	X						Not usable—2 broken exducer airfoils (handling).
13	FX34362	X	X	X	X	X	X	X	Rotor proofed to 95,000 rpm, shaft assembled and machined at Ahaus. Final spin test limited to 50,000 rpm (equipment) available for engine test.
14	FX34366	X	X	X	X	X	X		Proofed to 95,000 rpm. Not usable—broke two inducer airfoils during bal.
15	FX34369	X	X	X	X				Proofed to 95,000 rpm. Not usable—stub shaft fractured at Ahaus during machining.
16	FX34320	X							Proofed to 95,000 rpm. Not usable—one broken inducer airfoil.
17	FX34325	X							Proofed to 95,000 rpm. Not usable—one broken inducer airfoil.
18	FX34358	X							Proofed to 95,000 rpm. Not usable—damaged (chipped) rotor stub shaft.
19	FX34371	X							Proofed to 95,000 rpm; two induced blades released; not usable.
20	FX34405	X							Proofed to 96,500 rpm.
21	FX34411	X							Proofed to 104,600 rpm.
22	FX34415	X	X						Proofed to 95,800 rpm.
23	FX34416	X	X						Proofed to 95,200 rpm.
24	FX34418	X							Proofed to 96,000 rpm.
25	FX34432	X							Proofed to 104,700 rpm.
26	FX34438	X							Proofed to 102,500 rpm.
27	FX34442	X							Proofed to 104,000 rpm.
28	FX34445	X							Proofed to 97,000 rpm.
29	FX34447	X							Proofed to 103,500 rpm.
30	FX34448	X							Proofed to 105,400 rpm. Not usable, broken inducer (handling).
31	FX34449	X							Proofed to 96,000 rpm.
32	FX34450	X							Proofed to 97,000 rpm.
33	FX34452	X							Proofed to 104,500 rpm.
34	FX34453	X							Proofed to 97,000 rpm.
35	FX34472	X							Proofed to 104,800 rpm.
36	FX34476	X							Proofed to 105,500 rpm.

Notes:

X = completed

Items 4-8 had 3.5 deg backface and machined stub shaft.

Items 9-20 had Baud curved backface and machined stub shaft.

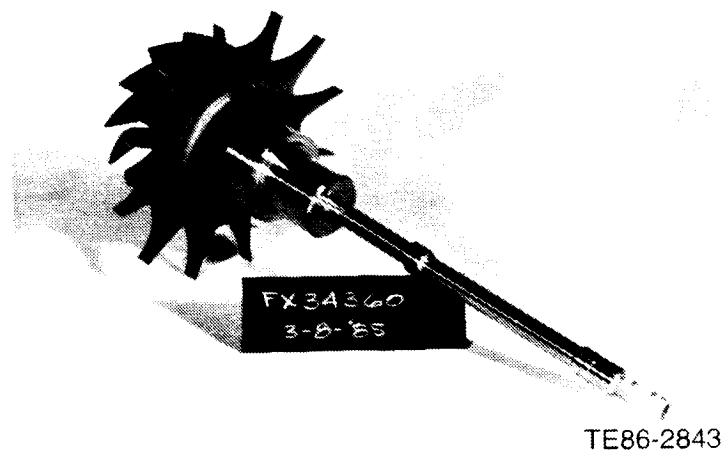


Figure 120. Rotor SiC/metal shaft attachment.

Gasifier Turbine. α SiC Scroll Assembly Developmental Testing.

Initial Thermal Shock Rig Testing to 898°C (1650°F). During the previous reporting period the first gasifier turbine α SiC scroll/backplate/vane assembly was successfully proof tested using the start nozzle fuel flow to 898°C (1650°F) (idle operating condition) in the thermal shock rig. A listing of the components incorporated in the scroll assembly is presented in Table XXII.

Engine Test to 926°C (1700°F). Following shock rig testing the scroll assembly was assembled into S/N 2 (BU9, BU10) engine, and tested to \sim 926°C (\sim 1700°F). The engine was operated through six start-up to idle test cycles, again employing the start nozzle as the fuel flow source. Total engine burning test time was 8 hr with 3 hr at 926°C (1700°F). Inspection of the ceramic scroll assembly components after test revealed the scroll, vanes, and inner backplate to be in good condition. The outer backplate had a fractured locating tang and a crack from the inside diameter of the part through a blade pocket and cross-key slot to a point about 75% of the way through the part toward its outside diameter. The investigation of this failure was described in Section 4.3.3 and the corrective redesign of this part is described in this section.

Thermal Shock Rig Test to 1051°C (1925°F). Following rework of another outer backplate, a second gasifier turbine ceramic scroll assembly was assembled for proof testing. This scroll assembly consisted

of the Sohio α SiC scroll and vanes previously rig proof and engine tested to approximately 898°C (1650°F), a new reworked outer backplate (P/N AA100623, S/N FX30562), and a new Corning BMAS-III composite ceramic inner backplate (P/N AA101353 S/N FX50502). This Corning inner backplate had a different fiber/matrix configuration than that previously engine tested. This scroll assembly was proof tested in the scroll thermal shock rig to 1051°C (1925°F) using the normal main nozzle steady-state operating condition procedure. The duration of the proof test was 1.6 hr with 0.24 hr at 1051°C (1925°F) and 1.35 hr at 898°C (1650°F) or above.

Following disassembly of the ceramic components at the conclusion of the rig proof test, the following observations were noted:

- The scroll, vanes, and outer backplate (all SiC) were intact, and FPI inspection revealed no cracks.
- A few vanes (three or four) had minor chipping at corners within the vane pocket region. No chipping or deterioration was observed in the gas path portion of the vanes.
- The inner and outer backplates were stuck together at the conclusion of the test. Light tapping was required to separate the backplates. The scroll and outer backplate were lightly stuck together. Only moderate hand force was required to separate them.
- A surface deposit was noted on the scroll assembly at the scroll-shroud braze joint, as shown in Figure 121.

*Table XXII.
Detail components in the first tested SiC gasifier turbine scroll assembly.*

<u>Part No.</u>	<u>Serial No.</u>	<u>Name</u>	<u>Vendor</u>	<u>Material</u>
AA 100626	FX30584	Scroll	Sohio	α SiC
AA 100623	FX30559	Outer backplate	Sohio	α SiC
AA 101218	18 parts	Vane	Sohio	α SiC
AA 101005	FX50503	Inner backplate	Corning	Composite SiC

The composite ceramic inner backplate delaminated at a point shown in Figure 122.

Disassembly of the scroll rig is discussed in the following paragraphs.

The scroll, vanes, and outer backplate are normally removed from the scroll proof test rig as a unit assembly while the inner backplate remains in the test fixture trapped behind a fixed test rig component that simulates the turbine rotor. After the 1051°C (1925°F) proof test, the complete scroll assembly could not be dislodged from the fixture by hand force. Consequently, the scroll was removed separately. Inspection revealed that the inner and outer backplates were stuck together at their o.d.-i.d. interface. Three light taps with a mallet broke the bond between the backplates allowing removal of the outer backplate from the test fixture.

Examination of the scroll body after testing revealed a thin glassy coating that appeared to have bled out of the scroll body-shroud braze joint. This substance was carried along the shroud surface through the vane row by gas flow during the test, as shown in Figure 121. A similar condition existed at other braze joints in the scroll body assembly. SEM analysis of the substance revealed it to be silicon, aluminum, and oxygen. Aluminum was an unexpected constituent in the deposit. An investigation was initiated to determine the source of the aluminum in the deposit.

Traces of the deposit entered some of the vane pockets in the scroll and outer backplate and caused light bonding of the vanes to adjoining parts. In addition, it is possible that some of the deposit material entered the clearance gap that exists between the inner and outer backplates during the proof test. When the parts cooled, the clearance gap decreased in size and the solidified coating may have caused the outer backplate to shrink tightly around the inner backplate, creating the difficulty in disassembly described previously.

Upon removal of the outer backplate, the inner backplate was determined to have separated into two pieces through delamination between flat layers of the composite material. The post-test condition of the inner backplate is shown in Figure 122. This inner backplate is of similar material but with different laminate configuration to an inner backplate successfully tested during several engine builds. The differences in laminate configuration is depicted in Figure 123. The stepped laminate configuration has demonstrated greater strength in static deflection tests and is now considered to be the preferred configuration for the inner backplate. No additional development of the flat laminate configuration is planned.

Engine Test to 1079°C (1975°F). The Sohio α SiC scroll/vane/backplate assembly that had been rig proof tested to 1051°C (1925°F) was assembled into S/N 2 BU14 engine along with the Corning composite ceramic inner backplate used in the first ceramic scroll engine test. The detail components of the scroll assembly used in this test are listed in Table XXIII. The main nozzle test was the second engine test for the scroll detail and vanes, the fifth engine test for the inner backplate, and the first engine test for the outer backplate. At the end of December 1985, two 1-hr thermal cycles had been completed with a total test time of about 3.4 hr. Additional testing will be accomplished in January 1986.

Analysis of Silicon Carbide Gasifier Turbine Outer Backplate Fracture in Engine Test. Examination of the α SiC gasifier turbine outer backplate at the completion of engine testing (S/N 2, BU10) revealed two separate failures. The first was a fracture of the locating tang from the main body of the part. The second was a crack running from the inside diameter of the backplate through a blade pocket and a cross-key locating slot and terminating near the outside diameter of the part. Except for the tang, the outer backplate re-

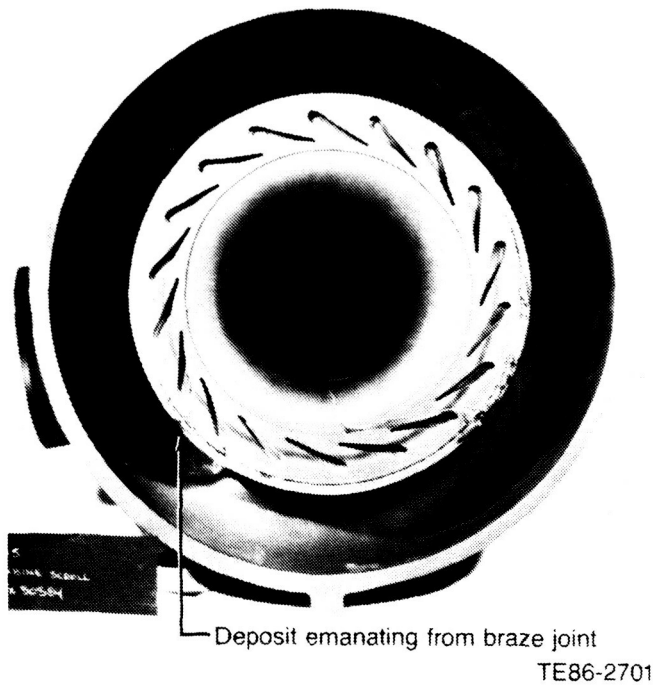


Figure 121. SiC scroll body following 1925°F proof test.

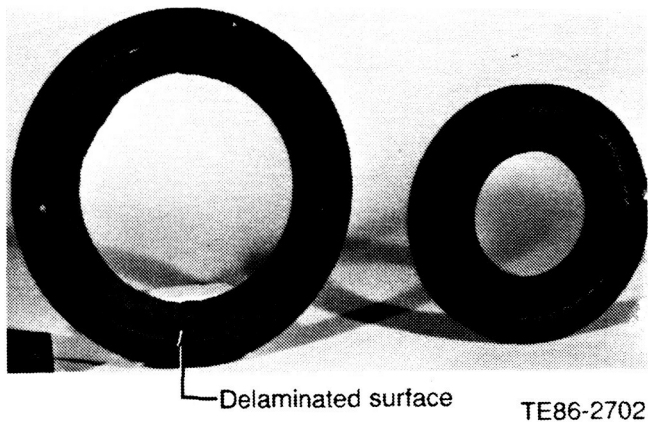


Figure 122. Corning composite ceramic inner backplate following 1925°F proof test.

mained in one piece. The failure of the outer backplate did not impair operation of the engine during the test.

The outer backplate had been proof tested to 898°C (1650°F) in the thermal shock rig without indication of cracks. During engine test the part was ex-

posed to six start-up-to-idle condition cycles. The temperature experienced in the engine test was similar to that of the proof test. An in-place inspection of the part after the first engine start cycle did not reveal the broken tang. The crack through the cross-key slot and vane pocket would not have been visible in that inspection. The failures were discovered after the outer backplate was removed from the engine following completion of the six start-up cycle test.

Metallurgical examination of the outer backplate showed the origin of the crack in the backplate to be in a corner of a cross-key slot as shown in Figures 124 and 125. The origin of the fracture of the tang from the backplate is shown in Figure 126. Contact marks on the fractured tang and the corresponding tang on the scroll body suggest that a tangential load was imposed on the tangs during engine test. The crack in the cross-key slot is on the loaded side of the slot when referenced to the loading indications on the tangs.

Investigation of the outer backplate failure revealed that the gasifier turbine scroll assembly that includes the outer backplate may have experienced an unintended load that contributed to the failure of the outer backplate. Engine operation with a ceramic gasifier turbine scroll assembly and a metal power turbine scroll assembly results in greater misalignment of the scroll connecting duct at operating temperature than would occur if the power turbine scroll was ceramic. The ceramic interturbine coupling could not, if situated in the worst case position in the scroll pockets, accommodate the misalignment caused by the thermal growth of the metal power turbine scroll.

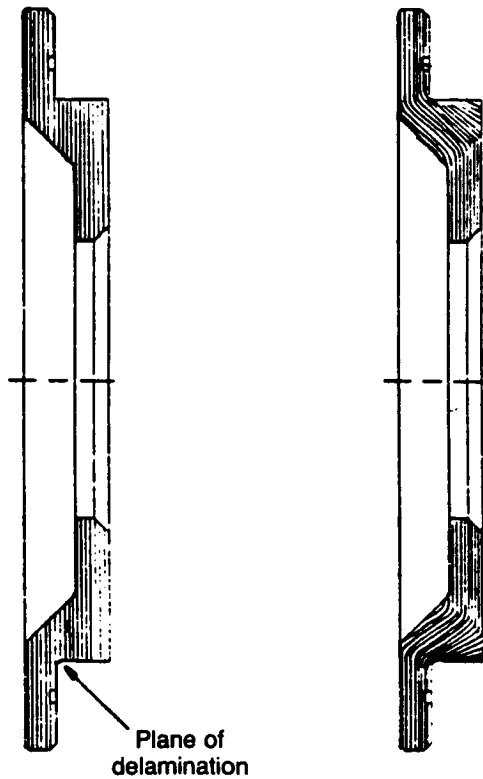
If this condition existed, a tangential load would have been imposed on the gasifier turbine scroll outlet elbow as shown in Figure 127. This tangential load would be transferred through the gasifier turbine scroll body to the mating locating tangs on the scroll and outer backplate and then through the outer backplate to the cross-key slots on the outer backplate that mate with the metal engine structure. Both outer backplate features (locating tang and one cross-key slot) that would have experienced such a load failed during the engine test. The order in which the failures occurred could not be determined from post-test evidence.

One theory is that the crack in the cross-key slot occurred first followed by the fracture of the locating tang. The supposition is that the slot in which the crack initiated may, because of dimensional tolerances, have been carrying more than an equal share of the load to locate the backplate/scroll assembly to the engine structure and to resist the tangential load from the spring loaded combustor body. In addition, the location of the cross-key slot in which the crack

Table XXIII.
Detail components of second engine tested ceramic gasifier turbine scroll
assembly (engine S/N 2 BU14).

<u>Part No.</u>	<u>Serial No.</u>	<u>Name</u>	<u>Vendor</u>	<u>Material</u>
AA 100626	FX30584	Scroll	Sohio	α SiC
AA 100623	FX30562	Outer backplate	Sohio	α SiC
AA 101218	18 parts	Vane	Sohio	α SiC
AA 101005	FX50503	Inner Backplate	Corning	BMAS/SiC Composite

initiated is nearest the scroll gas-path inlet (from the burner) and may be a region that experiences greater thermal shock/stress conditions than regions where the other five cross-key slots are located. After the crack in the backplate cross-key slot occurred, the load in the other five cross-key slots became more equalized and cracking in additional slots did not occur. Instead, the locating tang on the outer backplate (which prevents rotation of the scroll relative to the backplate) broke off, transferring the tangential locating function to the relatively loose fitting vanes. The vanes would have allowed enough rotation between the backplate and scroll to eliminate the tangential load on the cross-key slots caused by the thermal growth of the power turbine scroll. It should also be noted that only one tang on the outer backplate is used to locate the backplate tangentially to the scroll body.



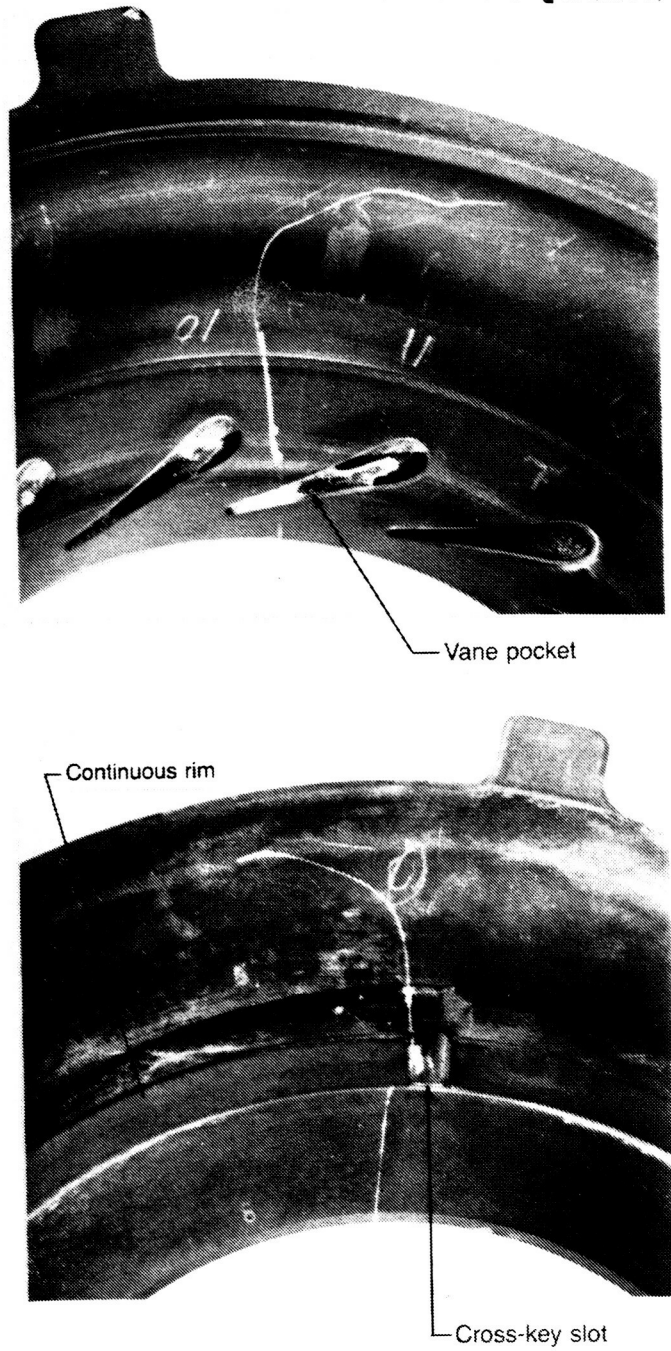
Flat laminate configuration Stepped laminate configuration
Failed in proof test Successfully engine tested

TE86-2703

Figure 123. Corning composite ceramic inner backplate laminate configurations.

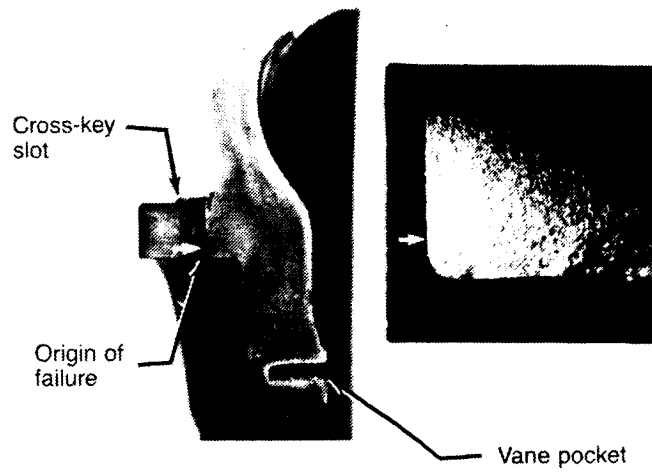
Part Modifications. To reduce the chance of outer backplate failure due to the loading described previously, two engine parts were modified. The interturbine coupling was modified by reducing the outside diameter between the seal ring grooves. This modification permits the coupling to accommodate up to 3 mm offset between the gasifier turbine scroll outlet elbow and the power turbine scroll inlet without transferring a lateral load from one scroll to the other. This amount of offset is 150% of that expected while operating at MOD I conditions with a ceramic gasifier turbine scroll and metal power turbine scroll. Additionally, two α SiC outer backplates were modified to remove the continuous circumferential rim that exists between the cross-key slots, leaving only six short segments in which the cross-key slots are located. This modification eliminates the tensile hoop stress that could exist in a continuous rim during engine operation. In addition, the stress concentration at

ORIGINAL PAGE IS
OF POOR QUALITY



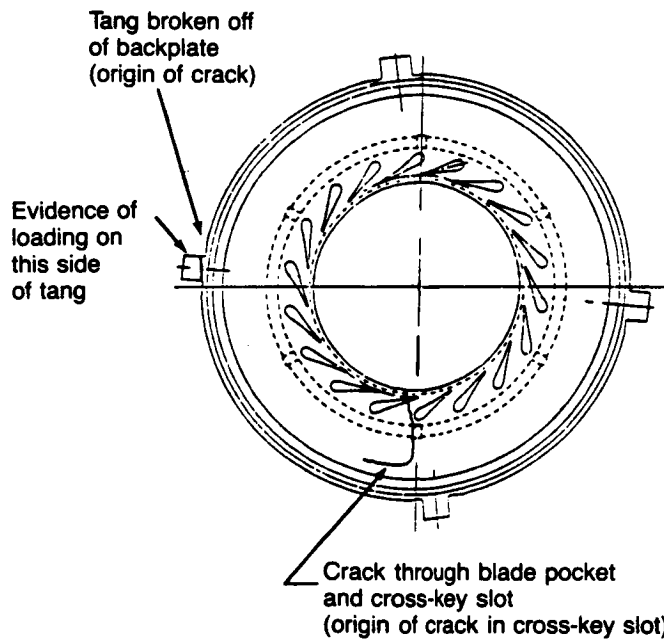
TE86-2829

Figure 124. Crack indications in α Sic gasifier turbine outer backplate.



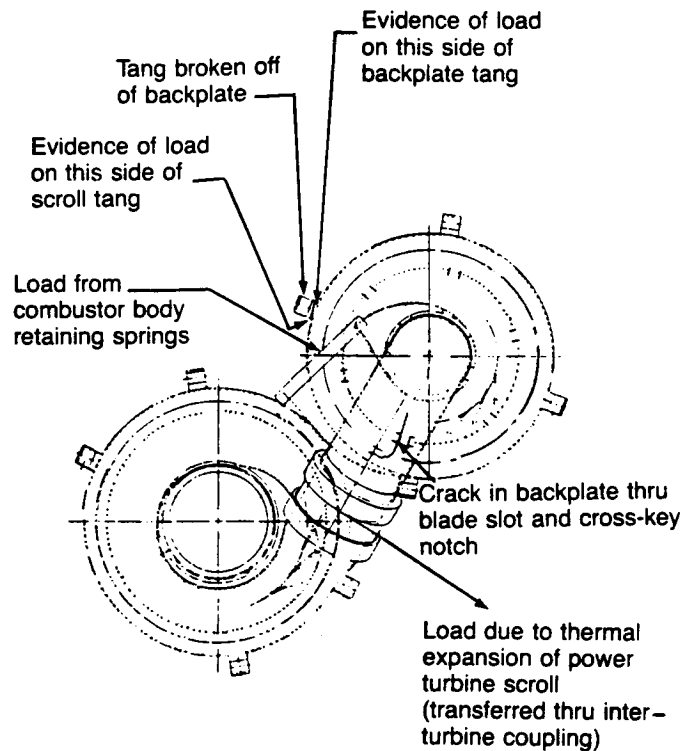
TE86-2840

Figure 125. Origin of failure in a SiC gasifier turbine outer backplate.



TE86-2706

Figure 126. Location of crack origins in gasifier turbine α SiC outer backplate.



TE86-2707

Figure 127. Loads imposed on gasifier turbine scroll assembly during engine test.

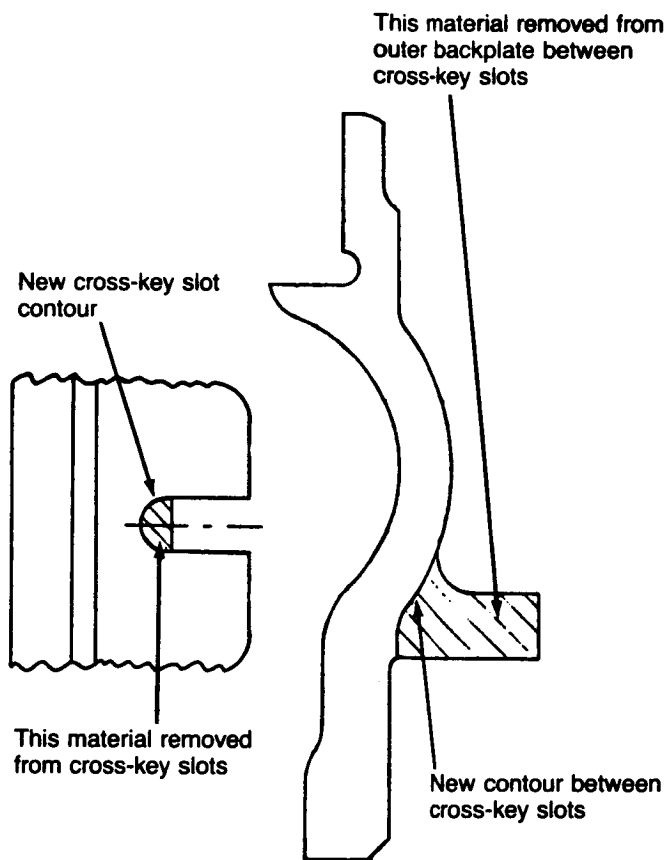
the bottom corners of the cross-key slots was reduced by increasing the depth of the slots and by adding a full radius contour at the bottom of the slots. These modifications are shown in Figure 128.

Scroll Braze Joint Oxidation Study. All of the scroll designs (Sohio, Norton, Kyocera) involve brazing of ceramic component parts. The first scroll tested (Sohio) has undergone a 898°C (1650°F) rig test, 926°C (1700°F) engine test, 1051°C (1925°F) rig test, and is currently undergoing 1070°C (1975°F) engine testing. Following the rig test, some of the nonbrazed parts of the assembly were stuck together and required light tapping to separate. Further, evidence of bleeding or running of some substance from braze regions was observed. The substance is a glassy layer and was found to contain silicon, aluminum, and oxygen. The source of the aluminum is not understood by Sohio as the braze material is molybdenum disilicide. Further, Sohio believes that the basic braze is good for much higher temperature levels (they are unable to debraze other units requiring modification). Other scrolls were exposed in an oven for 24 hr at 1287°C

(2350°F) in air. Those exhibiting no reaction were (1) Norton NC430 siliconized, (2) Sohio siliconized, and (3) a Sohio α SiC (also a first generation type). No conclusions have been made at this time. However, it is judged that the material is not from the basic braze and that scrolls exhibiting the glassy layer are structurally sound and acceptable for rig and engine test.

Second Gasifier Turbine Scroll Assembly Available for Proof Testing. A second gasifier turbine scroll/backplate assembly has been assembled for rig proof testing and subsequent engine testing. This assembly consists of the following components:

<u>Part name</u>	<u>Material</u>	<u>Vendor</u>
Scroll	α Silicon carbide	Sohio
Outer backplate	α Silicon carbide	Sohio
Vanes	Silicon nitride	GTE
Inner backplate	Silicon nitride	GTE



TE86-2708

Figure 128. Modification of gasifier turbine outer backplate.

This assembly differs from the first assembly that was engine tested in that the vanes are silicon nitride instead of silicon carbide and the inner backplate is silicon nitride instead of a composite BMAS ceramic matrix with silicon carbide filaments.

The second scroll assembly was installed in the scroll shock test fixture in December 1985 and is in the process of being proof tested to 1093°C (2000°F) at 100% N1 flow conditions.

Silicon Carbide Gasifier Turbine Static Component Parts Fabrication. Fabrication of silicon carbide gasifier turbine static components continued during 1985 with four vendors delivering parts. Parts procured included turbine scrolls, outer backplates, inner backplates, vanes, couplings, interturbine couplings, and exhaust couplings.

Sohio Engineered Materials. Sohio delivered the following gasifier turbine components in 1985:

<u>Component</u>	<u>Quantity</u>
Scrolls— α SiC	4
Scroll—siliconized SiC	1
Outer backplate— α SiC	4
Inner backplate— α SiC	4
Vanes— α SiC	54
Interturbine couplings— α SiC	6
Exhaust couplings (power turbine)— α SiC	6

The process used to bond the three details of the turbine scroll together underwent considerable development during 1985. Early scrolls were sinter bonded together with the joint filled with a silicon carbide paste. The most recent scrolls are presintered, machined in the bonded joint region and brazed together with a MoSi_2 braze material. Three

of the scrolls had dimensional deviations that could not be corrected in final machining. These scrolls were returned to Sohio for correction. Scrolls and outer backplates supplied by Sohio are supplied rough machined and are final machined at an outside vendor.

Norton Company. The Norton Company supplied gasifier turbine scrolls made of NC-430 siliconized silicon carbide. Ten scrolls were being processed during 1985. Five scrolls were shipped to Allison during 1985 and, except for vane pockets, came fully machined. The remaining five scrolls will be shipped in early 1986.

Pure Industries. Pure Industries supplied reaction bonded silicon carbide (PS-9242) interturbine couplings and power turbine exhaust couplings during 1985. This was a new material offered by Pure Industries. Previously, these components had been furnished in Purebide Refel PR8708 material. The material substitution was made because Pure Industries no longer supplies parts made of Purebide Refel, a reaction bonded silicon carbide.

Corning Glass Works. Corning fabricated gasifier turbine inner backplates of a composite material that incorporated silicon carbide (Nicalon) fiber reinforcement. BMAS, MAS, and LAS matrix materials were used with the SiC fibers in fabricating the inner backplates. Several composite (reinforcement) preform configurations were fabricated. The preferred (strongest) configuration was a stepped preform that allowed continuous (uncut) reinforcement in the inner backplate configuration.

9.2.3 Turbine Scroll Static Components Thermal Simulation Rig.

The turbine scroll static components thermal simulation rig (also known as the scroll thermal shock rig) is designed to produce AGT 100 engine combustor outlet conditions within an environment that duplicates the engine airflow paths, temperatures, and pressures. The rig was designed to provide a thermal simulator suitable for testing nonrotating ceramic components as a demonstration of their engine readiness.

The initial shakedown of the scroll thermal shock rig was performed using a metal scroll assembly, as described in the 1984 annual report (EDR 12070). This background work defined deficiencies in the rig hardware that were subsequently corrected, creating a scroll thermal shock rig capable of simulating engine operating condition.

Activity during 1985 revolved around testing the structural integrity of and, thus, qualifying the first

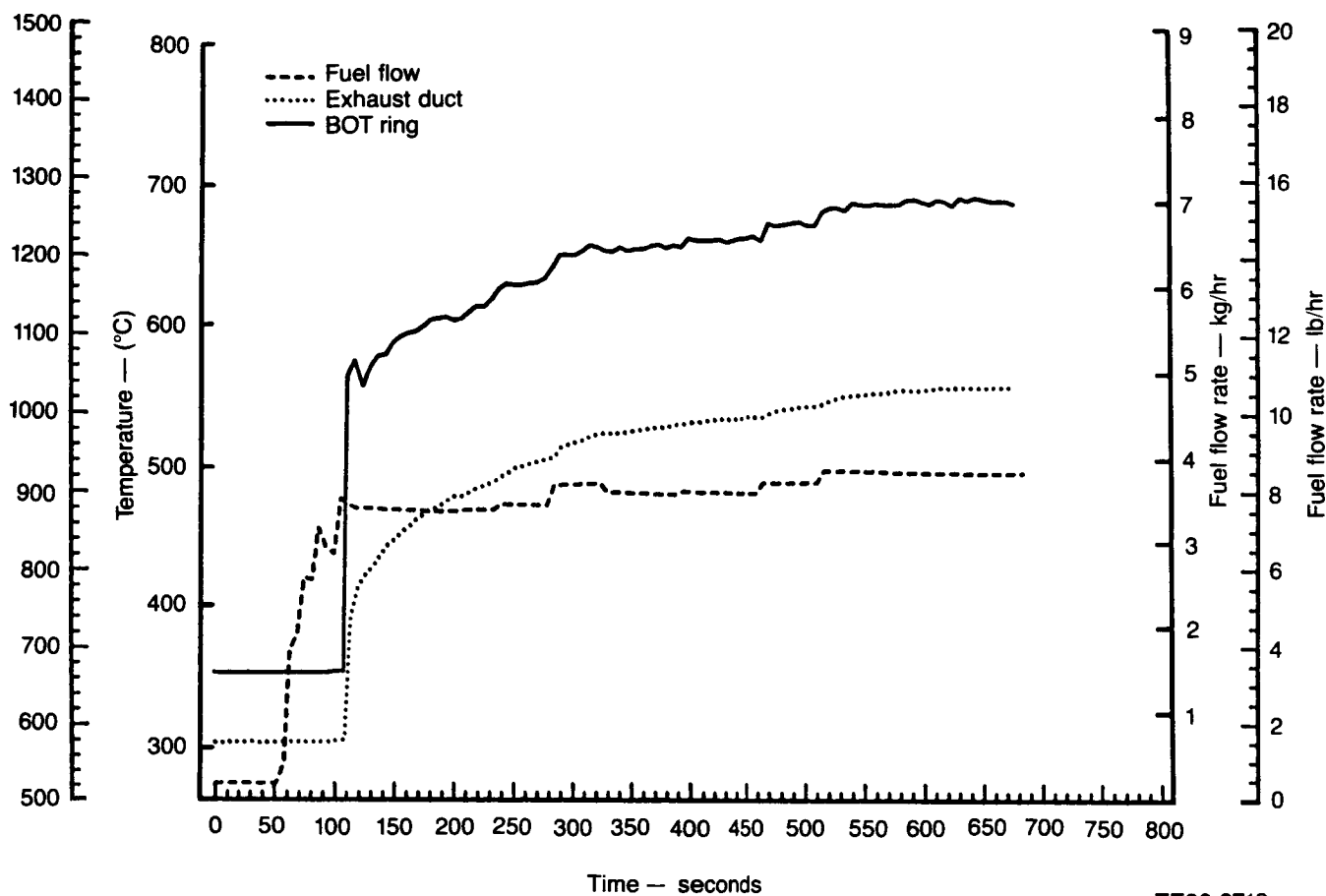
gasifier ceramic scroll for general engine use. A systematic, engine-verified approach was adopted that subjected the scroll assembly to a series of tests in which each successive rig test was followed by engine verification before imposing more demanding rig simulation conditions. The initial test of the ceramic scroll assembly subjected the hardware to rig simulated start nozzle operating conditions. After successful completion of this test phase, the scroll assembly was installed in an engine build and subjected to actual engine start conditions. The scroll assembly was then placed back into the scroll rig and tested at conditions simulating engine operation at 80% gasifier rotor speed. The material presented in this section reviews the scroll thermal shock rig data obtained during the start nozzle and 80% speed main nozzle simulations.

Start Nozzle Simulation (Scroll Rig BU4). The objective of this scroll rig test was to expose the SiC ceramic gasifier scroll hardware to a typical start sequence. For the purpose of simulation, the inlet air conditions to the combustor were set at 315°C (600°F), 179 kPa absolute (26 lb/in.² absolute) and 0.11 kg/s (0.25 lbm/sec).

Fuel was introduced into the start nozzle and the combustor ignited, raising the combustor exit temperature, i.e., gasifier scroll inlet temperature, to 565°C (1050°F), as shown in Figure 129. Fuel flow was gradually increased until the combustor exit temperature reached 693°C (1280°F) (Figure 130), and this temperature level was maintained for approximately 15 minutes. The data traces in Figure 130 show an abrupt drop in fuel flow with a subsequent rapid drop in combustor exit temperature. A random electrical failure of the fuel solenoid valve halted fuel flow to the combustor for approximately 15 sec and the combustor flamed-out with the result that the exit temperature fell dramatically. The operator applied a mechanical jolt to the solenoid and fuel resumed flowing to the start nozzle; the combustor relighted and the temperature recovered to 693°C (1280°F).

After the 693°C (1280°F) stabilization, the start nozzle fuel flow rate was gradually increased (Figure 131) until the combustor exit temperature reached 898°C (1650°F). Figure 132 shows the 15-minute stabilization at this operating condition. The fuel flow was then decreased gradually in two stages with stabilization again occurring at 676°C (1250°F) until the combustor reached a condition where lean blowout occurred.

Examination of the ceramic scroll assembly after rig teardown indicated that no damage was incurred by the ceramic parts. In fact, the actual test conditions were more severe than anticipated because very slow transients were planned to investigate the structural integrity of the ceramic scroll. However, as illustrated



TE86-2712

Figure 129. AGT 100 scroll test thermal shock rig: Rig 54, BU4 Series A, start nozzle operation.

in Figure 130, the ceramic scroll was subjected to a rapid thermal cycle. The temperature of the gas entering the scroll was cycled 226°C (440°F) from 693°C (1280°F) to 448°C (840°F) and back in a time period of 15 sec. The scroll assembly sustained no damage, implying that the SiC ceramic material is durable and tolerant to rapid thermal cycles.

Main Nozzle Simulation (Scroll Rig BU5). The scroll rig main nozzle test conditions were set such that the rig simulated a typical AGT 100 engine operating at 80% engine speed (80% gasifier rotor speed). The ceramic scroll hardware, with minor changes, installed into the rig for this main nozzle test was identical to the scroll hardware used in the previous rig and engine start nozzle investigations.

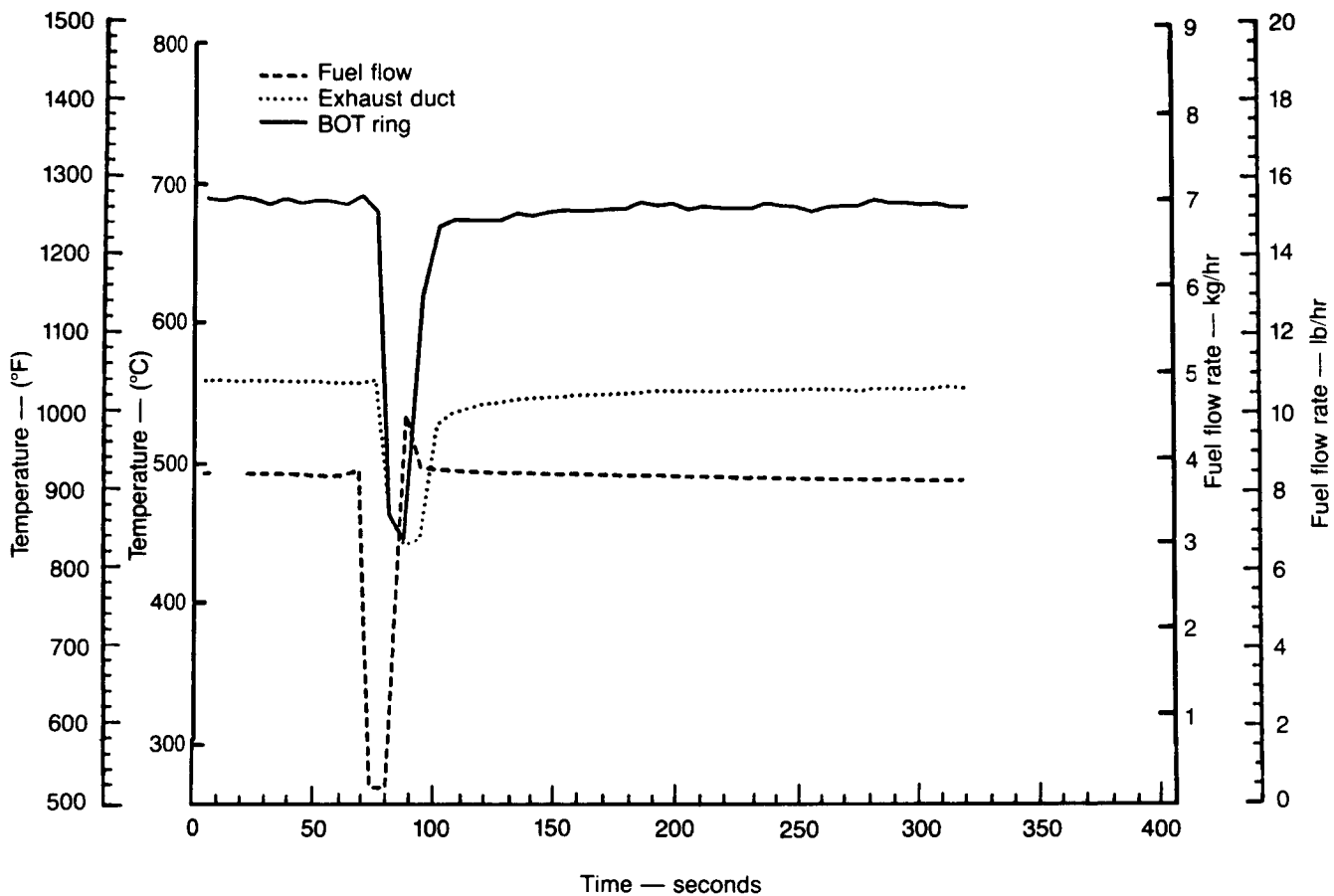
The scroll assembly within an engine operating at 80% speed typically is subjected to an airflow of 0/19 kg/s (0.42 lbm/sec) and a pressure of 275 kPa absolute (40 lb/in.² absolute) while the temperature of the gas leaving the combustor is around 1051°C

(1925°F). Figure 133 shows the combustor ignition and stabilization at 898°C (1650°F). After 15 minutes, the combustor outlet temperature was raised 135°C (275°) to 1051°C (1925°F). Stabilization at this condition is shown in Figure 134. The fuel flow rate delivered to the combustor was then reduced in two stages until combustor lean blowout occurred.

No damage to the SiC ceramic scroll components was evident during the teardown inspection of the scroll rig. Consequently, this scroll assembly was delivered to the engine to be tested at 80% power. Future scroll rig testing will be conducted at maximum engine airflow and temperature conditions.

9.2.4 Power Turbine Rotor

An initial sample of near power turbine size rotors was processed using the gasifier injection molding tool to mold green form bodies that were subsequently siliconized. The material was processed to KX02 (siliconized silicon carbide) standards in an inert atmosphere. The gasifier molding tool is approxi-



TE86-2713

Figure 130. AGT 100 scroll test thermal shock rig: Rig 54, BU4 Series A, start nozzle operation.

mately 20% oversize (for a 100% size sintered gasifier rotor) and thus produces a green form nearly the size of the power turbine rotor. Furthermore, no shrinkage occurs during siliconizing. Three siliconized (KX02 material) gasifier rotors were received during this reporting period, and the evaluation of these is summarized in Table XXIV.

X-ray examination indicated a uniform density through the rotor; that is, the silicon infusion was uniform. Although the inspection of surface quality appeared satisfactory, the spin burst test speeds were below expectations.

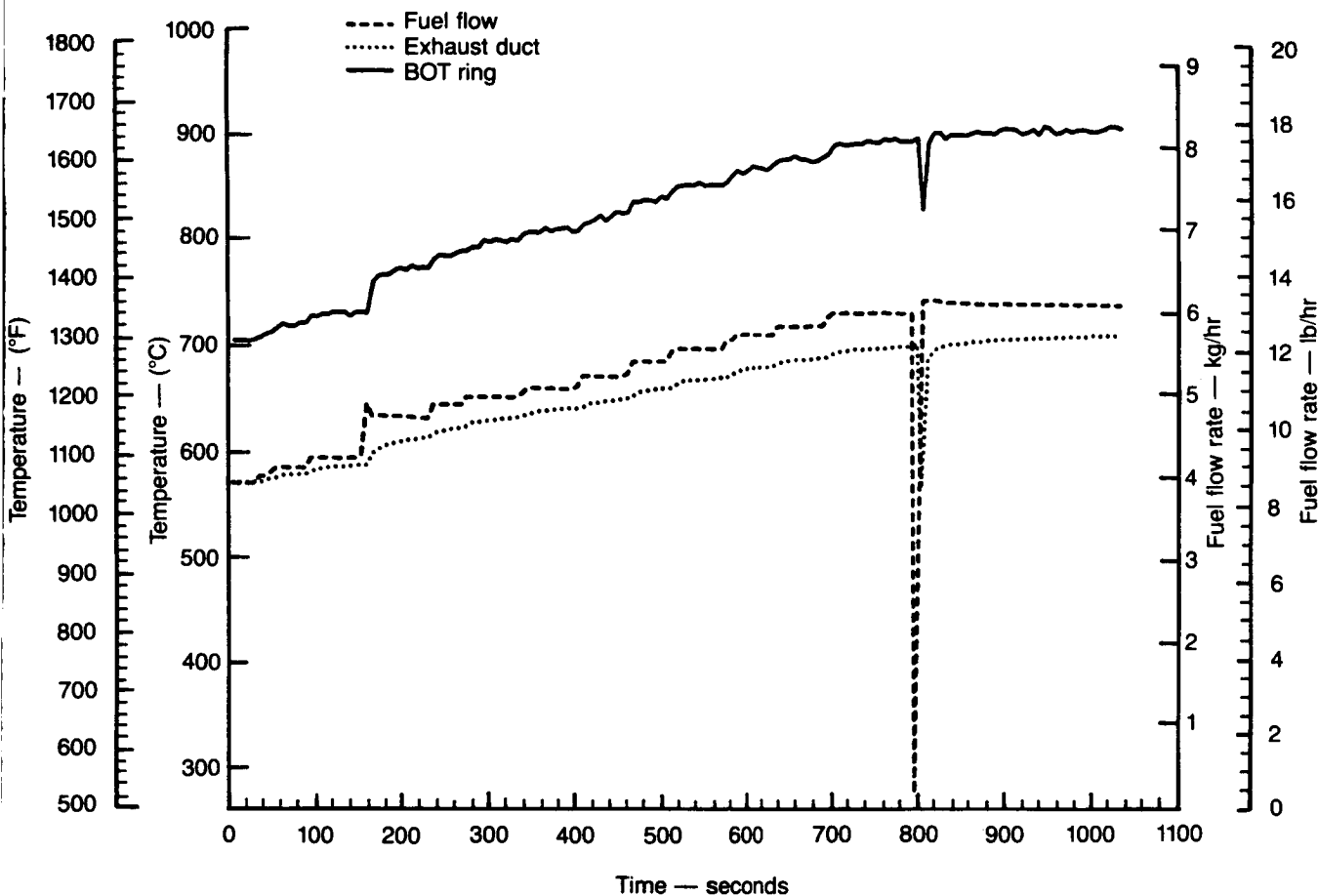
The spin test failure of rotor S/N FX28511 involved an airfoil release; the airfoil release occurred at the airfoil root at the rotor hub, and this in turn triggered the rotor burst. The second spin test failure of S/N FX28512 rotor was a more typical hub burst.

Subsequent processing of power turbine rotors used the power turbine metal rotor wax master die to mold a suitable green form for siliconizing. Sohio modified the aluminum wax master die for injection

molding and trials were conducted to produce test bars and rotors. The molding trials involved a range of SiC powder grit size and carbon level, which in turn addressed component strength and density after siliconizing. The molding trials are detailed in Table XXV.

The results of the siliconized rotor program are summarized as follows:

- test bars, mixes 1 through 6, were vacuum siliconized—density and strength were somewhat low, see Table XXV.
- sample rotors, mixes 1 through 6, were very fragile while mixes 7, 8, and 9, which were void of C, were less fragile; partial binder removal bake and bisque fire after bake were investigated as potential techniques to use if C is present in the mix; it was concluded that mixes free of C would be investigated in 1986
- sample rotors, mixes 1 through 6, were vacuum siliconized; the surface was extremely rough (not satisfactory) and the silicon was not uniformly infused



TE86-2714

Figure 131. AGT 100 scroll test thermal shock rig: Rig 54, BU4, start nozzle operation.

• sample rotors, Nos. 8-9, 8-11, and 1-11, were inert atmosphere siliconized; the density [silicon diffusion] was uniform and surface smoothness was satisfactory; two rotors, Nos. 1-11 and 8-11, were suitable for spin, neither exhibited fluorescent penetrant inspection (FPI) or visual indications. Results were as follows:

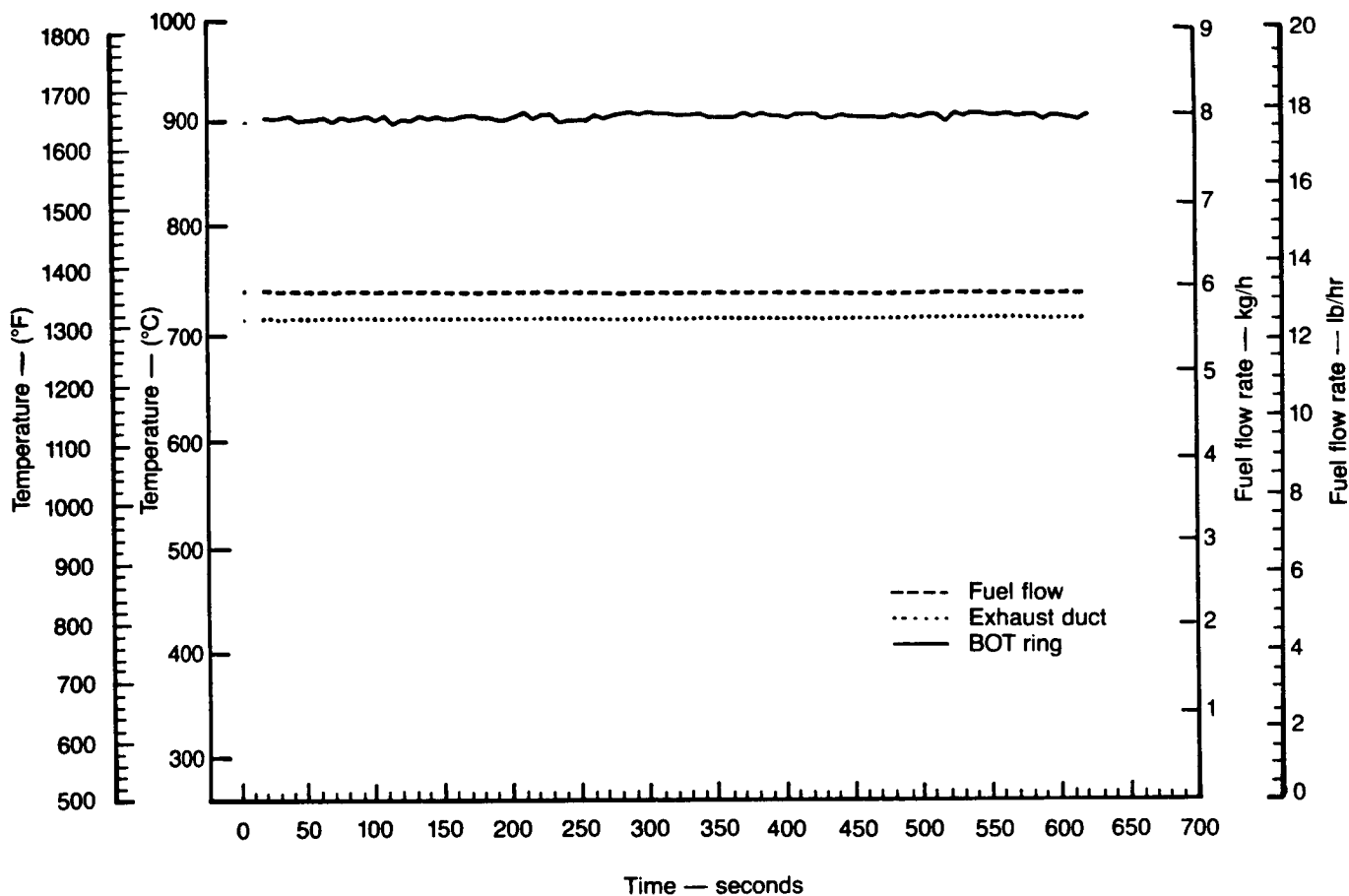
number 1-11, $p = 2.80 \text{ g/cm}^3$, burst at 54,800 rpm (80.6% N₂), see photo of burst, Figure 135

number 8-11, $p = 2.81 \text{ g/cm}^3$, burst at 48,100 rpm (70.7% N₂), see photo of burst, Figure 136

These burst speeds indicate substantial improvement compared to the initial sample of siliconized rotors, as shown in Table XXIV. Based on this favorable trend, Sohio has defined a process development pro-

gram for 1986 addressing further improvements in strength. The program will investigate time and temperature parameters associated with inert atmosphere siliconization. The objective is to identify a favorable combination of these parameters, which will produce a dense, fine grain, high strength structure. The 1986 process development plan for siliconized SiC material can be summarized as follows:

- powder—submicron and bimodal only, no carbon
- compound—identify the optimum level of binder considering viscosity for injection molding and porosity (after binder removal) for subsequent siliconization
- siliconization—inert atmosphere, identify optimum time/temperature parameters for component strength



TE86-2715

Figure 132. AGT 100 scroll test thermal shock rig: Rig 54, BU4, start nozzle operation.

Application of the redesigned, thicker inducer airfoil (see subsection 5.3.1) is also being considered for the siliconized silicon carbide power turbine rotor. It appears feasible to replace the airfoil inserts in the metal rotor wax master die with alternate inserts to form the thicker airfoil. Other considerations include cost, schedule, and process development. Following an evaluation of these considerations, a decision regarding airfoil replacement is planned for early 1986. A delivery goal of 40 acceptable quality siliconized SiC power turbine rotors has been scheduled for 1986.

9.2.5 Power Turbine Scroll Assembly Development

Development effort, during 1985, directed toward design and fabrication of a silicon carbide power turbine scroll/backplate assembly involved the completion of design drawings of the components, analysis

for steady-state and transient operating conditions, and the initiation of fabrication of the scroll and outer backplate at Sohio.

Tooling for the scroll and outer backplate has been procured and scroll body castings and pressed outer backplate details have been molded and sintered. Adjustments to the material mix have been made to obtain the desired shrinkage. The first outer backplates will be received at Allison in January 1986 in a rough machined state. After dimensional inspection to determine that details conforming to print can be machined from the rough parts, the outer backplates will be sent to a vendor for final machining. It is anticipated that fully machined outer backplates will be available for test in late May 1986.

Initial castings of the power turbine scroll indicated distress in the region where the inlet transition blends into the scroll body. A design modification of that portion of the scroll has been completed to in-

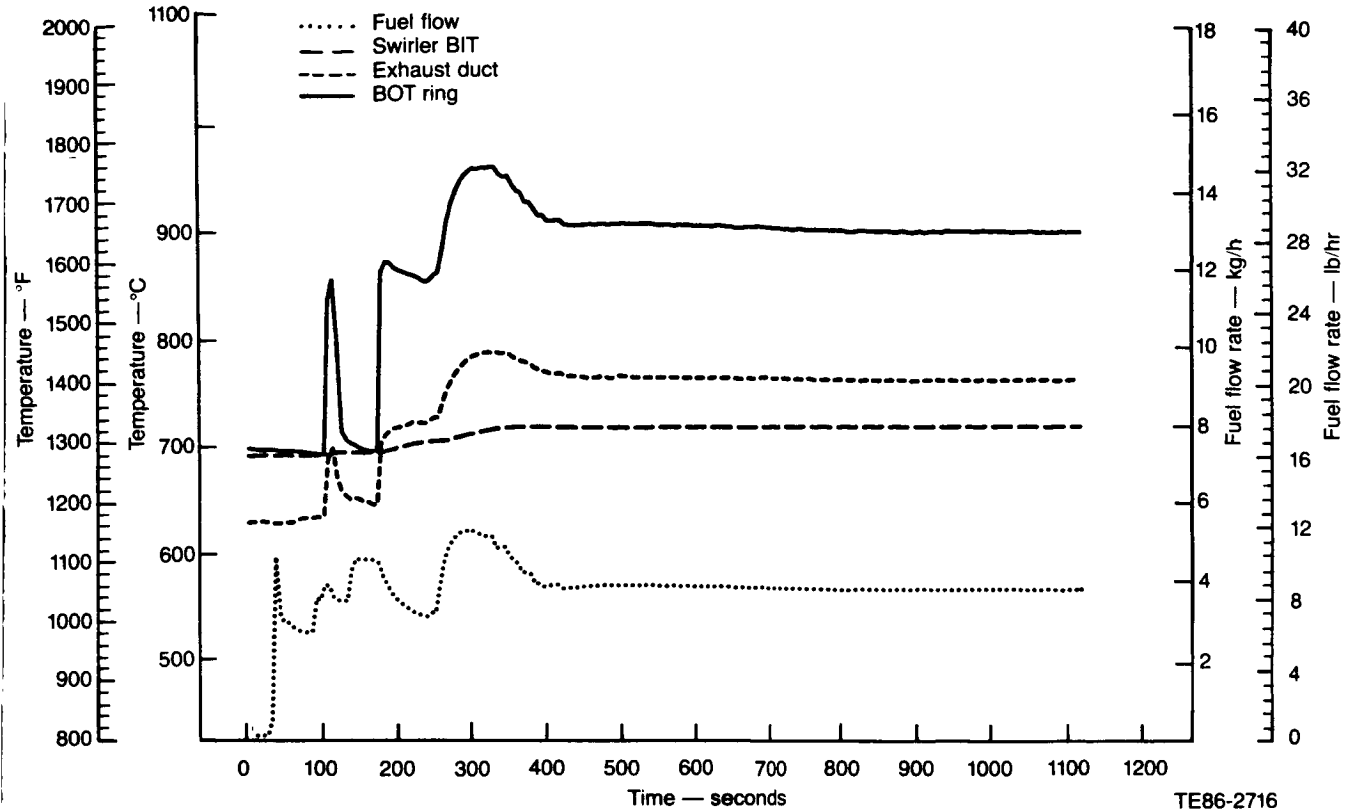


Figure 133. AGT 100 scroll test thermal shock rig: Rig 54, BU4 Series A, main nozzle operation.

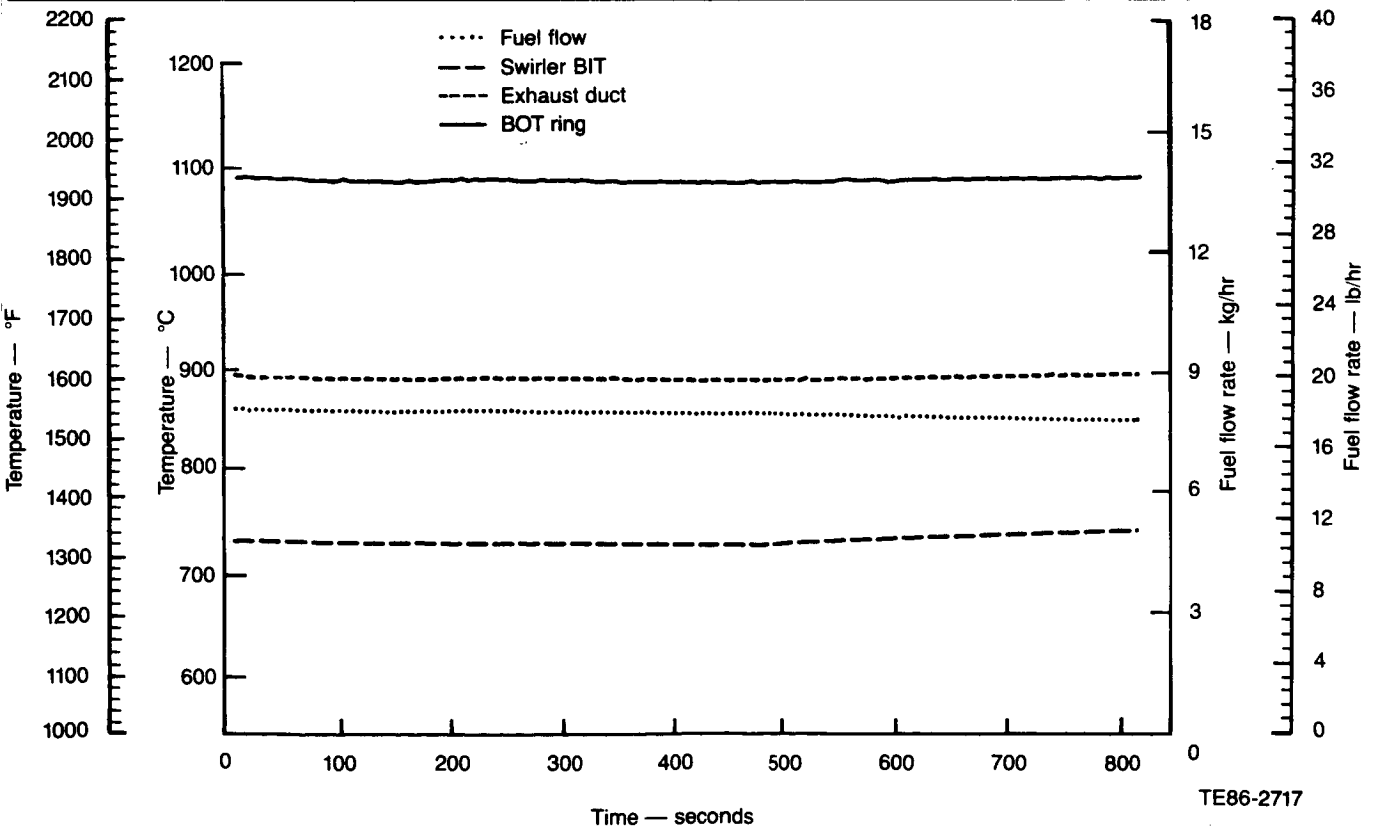


Figure 134. AGT 100 scroll test thermal shock rig: Rig 54, BU4 Series A, main nozzle operation.

Table XXIV.
Evaluation, siliconized (KX02) gasifier rotors.
(Oversize gasifier rotors—inert atmosphere siliconization)

<u>No.</u>	<u>Serial No.</u>	<u>Inspection</u>	<u>Disposition</u>
1	FX28510	Visual, FPI, and X-ray	Held for shaft joining trial
2	FX28511	were satisfactory	Spin burst at 43,300 rpm
3	FX28512	2.8/2.9 g/cm ³ (0.101/0.105 lb/in. ³) density	Spin burst at 30,000 rpm

Note: 100% design speed, power turbine = 68,000 rpm

Table XXV.
Siliconized rotor program.
(Power turbine)

<u>SiC grit</u>	<u>1000 μ</u>			<u>Submicron</u>			<u>Bimodal</u>		
Mix No.	7	1	2	8	3	4	9	5	6
Carbon level	1	2	3	1	2	3	1	2	3
Vacuum siliconized test bars (injection molded)									
Density—g/cm ³ (lb/in. ³)	2.81 (0.10)	2.75 (0.10)	2.76 (0.10)	2.85 (0.10)	2.78 (0.10)	2.88 (0.10)			
MOR—MPa (lb/in. ²)	411.69 (59.71 x 10 ³)						412.65 (59.85 x 10 ³)		

Note: Mixes 1-6 contain carbon (7, 8, & 9 are void of carbon)

crease the size of the fillet radius between the inlet transition and the scroll. This will permit better draining of the slip mold in this region and promote more uniform wall thickness in the casting. An additional design modification has been made to improve the braze joint configuration between the scroll body and the shroud. These design changes required modification to the model of the scroll body used to fabricate molds for the slip-cast part. Delivery of the first rough machine power turbine scroll/shroud assembly is scheduled for late April, 1986. Completion of a completely machined scroll assembly is projected to occur near the end of June 1986.

Silicon carbide power turbine vane parts have been procured and are available for test with the ceramic scroll and backplate assembly.

9.3 SILICON NITRIDE COMPONENT DEVELOPMENT

9.3.1 Gasifier Rotor

Kyocera Rotors. A ceramic technology development program conducted with Allison discretionary funds in parallel with this contractual effort has resulted in the delivery of 14 Si₃N₄ gasifier turbine rotors from Kyocera. The process development, tooling, and fabrication were funded in the referenced development program, while inspection, evaluation, attachment development, and engine testing were accomplished under AGT 100 contract funds. These rotors, configured for interference fit shaft attachment (AA101029) are shown in Figure 137, and are

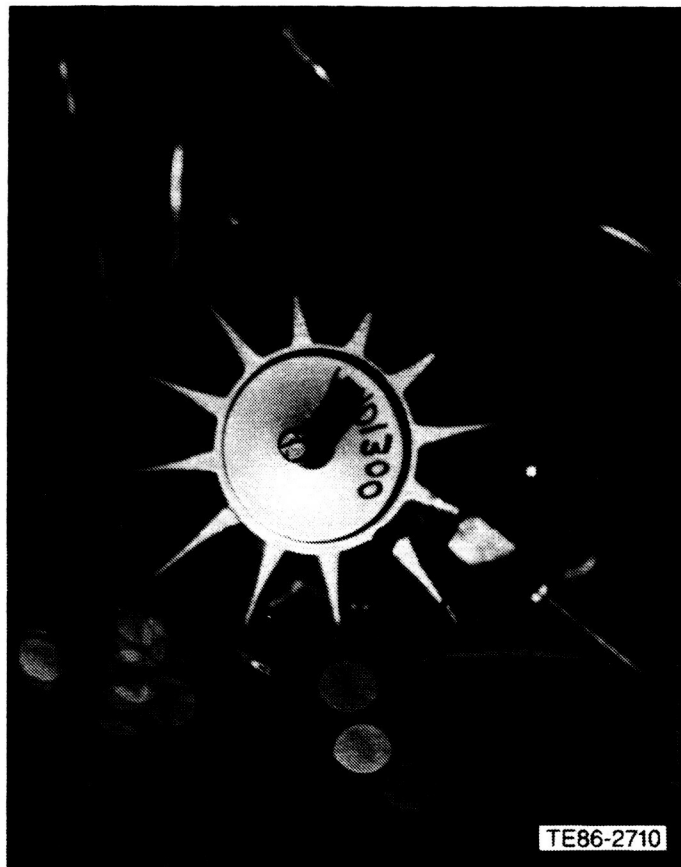


Figure 135. Initial failure, airfoil release at root (4:00 position) at 54,800 rpm, siliconized gasifier rotor, S/N 1-11.

fabricated of slip-cast SN220M sintered Si_3N_4 . Non-destructive inspection (visual and fluorescent penetrant) of these rotors revealed no objectionable indications. Dimensional evaluation indicated that all dimensions were within print tolerance with the exception of a minor closing of the exducer throat spacing observed in the first two rotors received (K-1 and K-2). This was corrected in subsequent rotors by the use of appropriate fixturing during the sintering process, and the remainder of the rotor met all structural and dimensional requirements. The overall disposition of the Kyocera SN220M sintered Si_3N_4 gasifier turbine rotors (AA101029) is summarized in Table XXVI. Each rotor (with the exception of K-2) was successfully proof spin tested to 100,000 rpm (116% design speed), Table XXVII.

Ten additional semifinished rotor assemblies were received from Kyocera during this reporting period. The assemblies consist of a Kyocera slip-cast SN220M sintered Si_3N_4 gasifier turbine rotor attached to an Inco 907 shaft by a Kyocera developed and applied braze operation. The rotors were proof spin

tested to 112,000 rpm (130% design speed) by Kyocera prior to shaft attachment.

One of the rotor/shaft assemblies (0004-8) fractured during airfoil machining. The rotor separated from the Inco 907 shaft at the front surface of the braze joint. Fractographic analysis of the Si_3N_4 rotor shaft revealed that the fracture initiated from two pre-existing surface cracks, identified in Figure 138 by the large black arrows. The two surface cracks were interpreted as having been present in the rotor shaft prior to the finish machining operation because both crack surfaces were observed to have a thin layer of an iron-nickel alloy. Further analysis revealed a nonuniform braze layer in the attachment, depicted in Figure 139, with no braze alloy present at the failure origins (direct ceramic/metal contact). An approximately 120 micron thick layer of braze was located opposite the origins.

The Kyocera brazed rotor shaft attachment underwent additional evaluation by selecting a second rotor assembly (0004-3) for flexural load testing. This rotor assembly failed at a bending moment of 22.6



Figure 136. Initial failure, airfoil release at root (2:00 position) at 48,100 rpm, siliconized gasifier rotor, S/N 8-11.

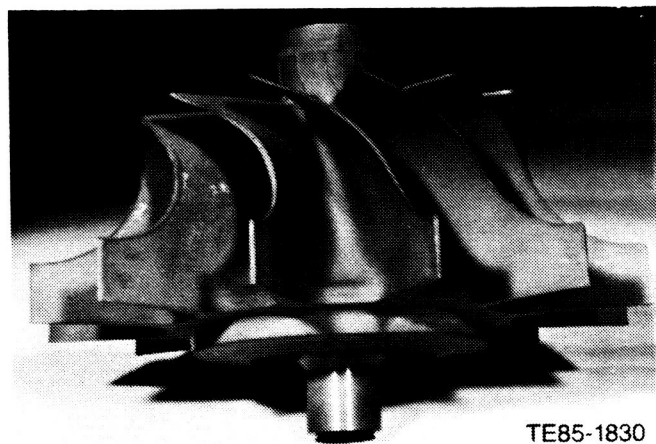


Figure 137. Kyocera slip-cast SN220M sintered Si_3N_4 gasifier turbine rotor.

Table XXVI.

Disposition Kyocera slip-cast SN220M gasifier turbine rotors.

Rotor serial No.	Spin test—rpm		Shaft assembly	Machined	Status
	Proof	Burst			
K-1	100,000				MOR bars
K-2					
0002-1	100,000		Yes		Engine test
0002-2	100,000	140,700		Yes	
0002-3	142,800				
0002-4	100,000	139,500			
0002-5	100,000	126,800			
0002-6	100,000		Yes	Yes	Spin test pending
0002-7	100,000		Yes	Yes	Airfoil frequency testing
0002-8	100,000		Yes	Active	
0002-9	100,000				
0002-10	100,000				
0003-1	138,000		Yes	Active	
0003-2	134,000				

Table XXVII.

Spin test results for Kyocera SN220M Si₃N₄ rotors.

Rotor No.	Spin speed—rpm
0002-2	140,700
0002-3	142,800*
0002-4	139,500
0002-5	126,800
0003-1	138,000*
0003-2	134,000*

*Rotor intact, test terminated at this speed due to facility limitations

ness, Figure 141, with no evidence of braze alloy adjacent to the fracture origin.

Kyocera is currently addressing modifications to the Si₃N₄/metal braze process to ensure improved positioning and more uniform braze coverage.

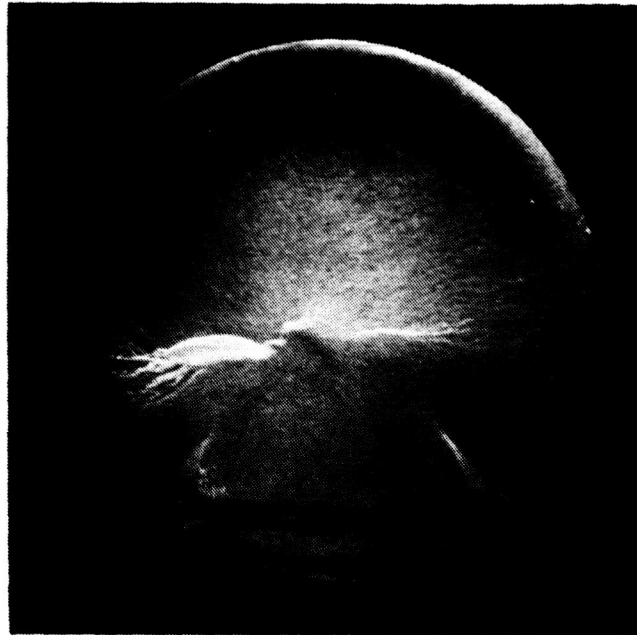
An additional order was placed with Kyocera for delivery of 10 gasifier turbine rotors fabricated of slip-cast SN250M sintered Si₃N₄ material. The SN250M Si₃N₄ features improved strength at elevated temperatures compared to the SN220M Si₃N₄. The material strength characteristics of the SN250 Si₃N₄ are summarized in Table XXVIII.

The rotors will be proof spin tested by Kyocera to 112,000 rpm (130% design speed) prior to shipment and will be configured for the Allison interference fit shaft attachment. Delivery of the rotors is anticipated in March 1986.

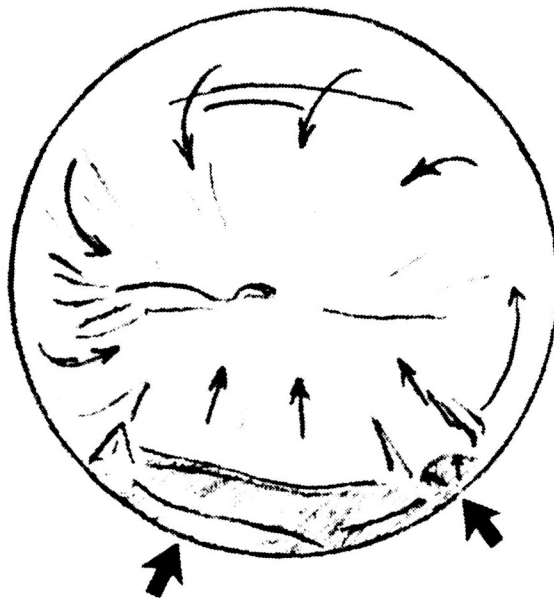
Ongoing material development activities at Kyocera have resulted in further strength improvements in advanced Si₃N₄ material. This material, identified as SN270, has demonstrated strengths of 689.48 MPa (100 x 10³ lb/in.²) at a temperature of 1400°C (2552°F). While this material is currently available in test bar form only, Kyocera is actively pursuing process development for fabrication of structural ceramic components.

As discussed, two techniques are being analyzed for joining the Si₃N₄ rotor to the metal (Inco 907) gasifier shaft, illustrated in Figure 142. Both

N·m (200 in.-lb), (36.56 MPa [5.3 x 10³ lb/in.²] stress). This compares to an average moment of 30.51 N·m (270 in.-lb), (111.74 MPa [16.2 x 10³ lb/in.²] stress) observed for fracture of the SiC rotor shaft assemblies and 35.36 N·m (313 in.-lb), (132.38 MPa [19.2 x 10³ lb/in.²] stress) measured for an interference-kit Kyocera Si₃N₄ rotor shaft assembly without failure. Fracture initiated from a large crescent-shaped surface flaw in the Si₃N₄ rotor shaft, Figure 140. This rotor assembly also had a nonuniform braze layer thick-



ORIGINAL PAGE IS
OF POOR QUALITY



TE86-2800

Figure 138. Fracture surface of Kyocera Si_3N_4 rotor brazed to Inco 907 shaft (0004-8). Origins are located at large black arrows.

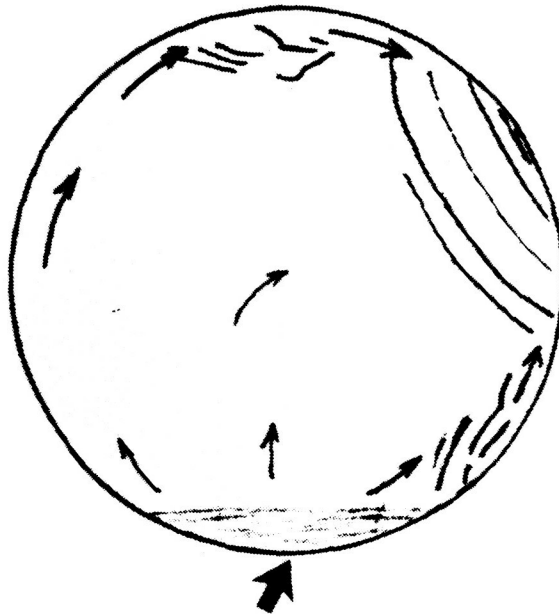
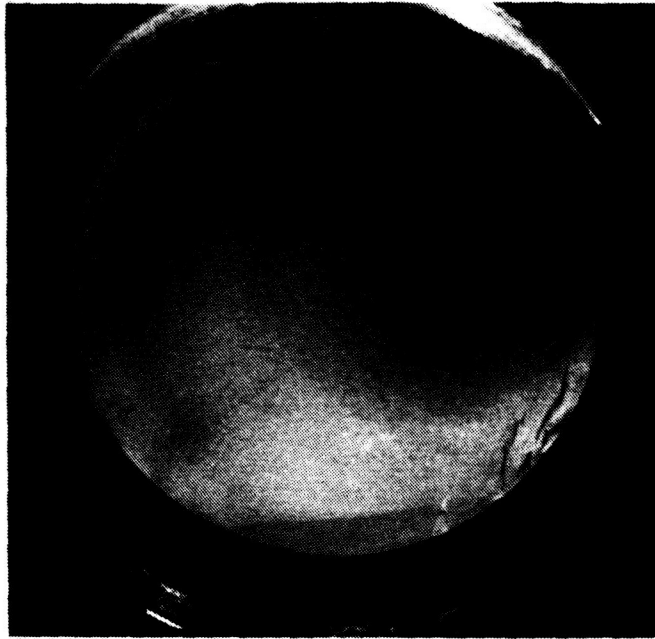
mechanisms utilize an air gap to reduce heat flux from the gasifier rotor into the compressor shaft. The difference in the techniques is in the method of joining the metal shaft to the ceramic rotor; configuration 1 (Figure 142) utilizes a braze joining while configuration 2 (Figure 142) employs an interference fit. Both mechanisms are being analytically evaluated to in-

clude the effects of rotor dynamics, heat transfer, and stress. The calculated rotor assembly modes and corresponding frequencies for configurations 1 and 2, respectively, are presented in Figures 143 and 144. The first three modes, which consist of the two rigid body modes (the two bearing mounts) and the first bending mode, are shown. All modes are outside the



TE86-2801

Figure 139. Cross section of Kyocera Si_3N_4 rotor 0004-8 showing nonuniform braze thickness. Note direct contact at fracture origin (bottom picture).



TE86-2802

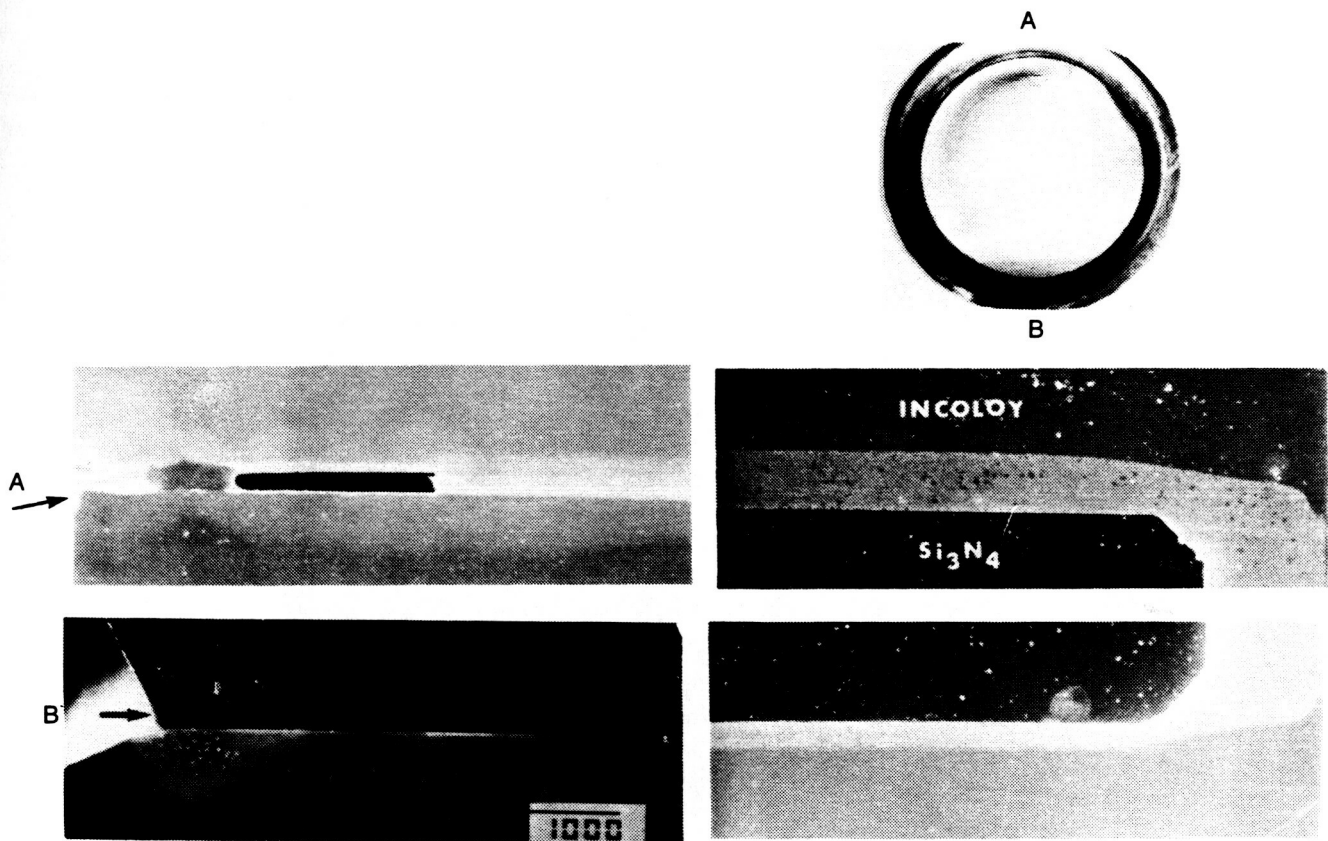
Figure 140. Fracture surface of Kyocera Si_3N_4 rotor 0004-3 broken in load test (36.54 MPa (5300 lb/in.²)). Origin is located at large black arrow.

engine operating speed range including the first bend mode, which is predicted to occur at 130% N1. This is considered a desirable and safe margin. This discussion and that in the next paragraph are similar to that in subsection 4.3.

The Si_3N_4 rotor and shaft attachment has been analyzed for stress, with the effort during this report-

ing period focused on the interference fit configuration. The calculated stresses for this configuration at the 100% speed, steady-state operation, and 1080°C (1976°F) TIT are shown in Figures 145 and 146. The predicted stresses are well within acceptable levels.

Kyocera's method to braze join the Si_3N_4 rotor and metal shaft, configuration 1, is based on their



TE86-2803

Figure 141. Cross section of Kyocera Si_3N_4 rotor 0004-3 showing nonuniform braze thickness. Note direct contact at fracture origin (B).

extensive turbocharger experience. This configuration also features an air gap between the rotor and shaft to reduce heat flux into the shaft. Thermal analysis performed at 100% speed and steady-state conditions at 1288°C (2350°F) TIT indicates the shaft temperature at the bearing location is 210°C (410°F) (Figure 147), approximately the same level as the SiC rotor system. The temperature distribution for the interference fit attachment, configuration 2, at 100% speed and 1080°C (1976°F) steady-state TIT is presented in Figure 148.

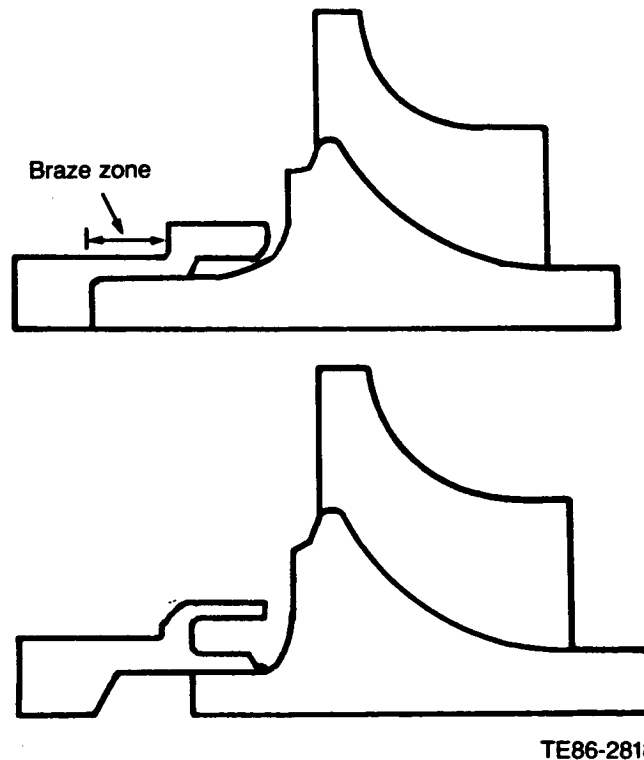
The airfoil natural frequencies were calculated for the finished machined Si_3N_4 rotor, and the results are presented in Figure 149. This figure, an interference diagram, compares the calculated frequencies with potential vane passage excitation sources over the entire rotor speed range. Potential response of the third and fourth modes can occur in the engine operating range. The calculated mode shapes for these modes are shown in Figure 150.

In preparation for engine testing, the rotor airfoil natural frequencies were also bench test measured. These data are also shown in Figure 149. A difference exists between the measured values of the first inducer and first exducer frequencies as compared to the calculated values of these frequencies; the measured values were determined to be at higher frequencies because the calculated frequencies were based on the print specified airfoil thickness of 0.76 mm (0.03 in.) while the actual thickness of the airfoils was 1.0 mm (0.039 in.). Both the inducer and exducer region of the gasifier airfoil successfully passed through potential airfoil natural frequency response/vane passage excitation regimes during numerous speed excursions of the rotor up to a maximum of 60,000 rpm during engine operation.

GTE Rotors. GTE apprised Allison of the development of an injection molding process for the fabrication of silicon nitride rotors. An order was placed for

Table XXVIII.
Strength characteristics of Kyocera SN250 Si_3N_4 .

Surface condition	MOR strength—MPa (lb/in. ²)		
	Room	1000°C (1832°F)	1150°C (2102°F)
Machined	751.53 (109×10^3)	496.42 (72×10^3)	558.48 (81×10^3)
As-fired	475.74 (69×10^3)	475.74 (69×10^3)	475.74 (69×10^3)



TE86-2818

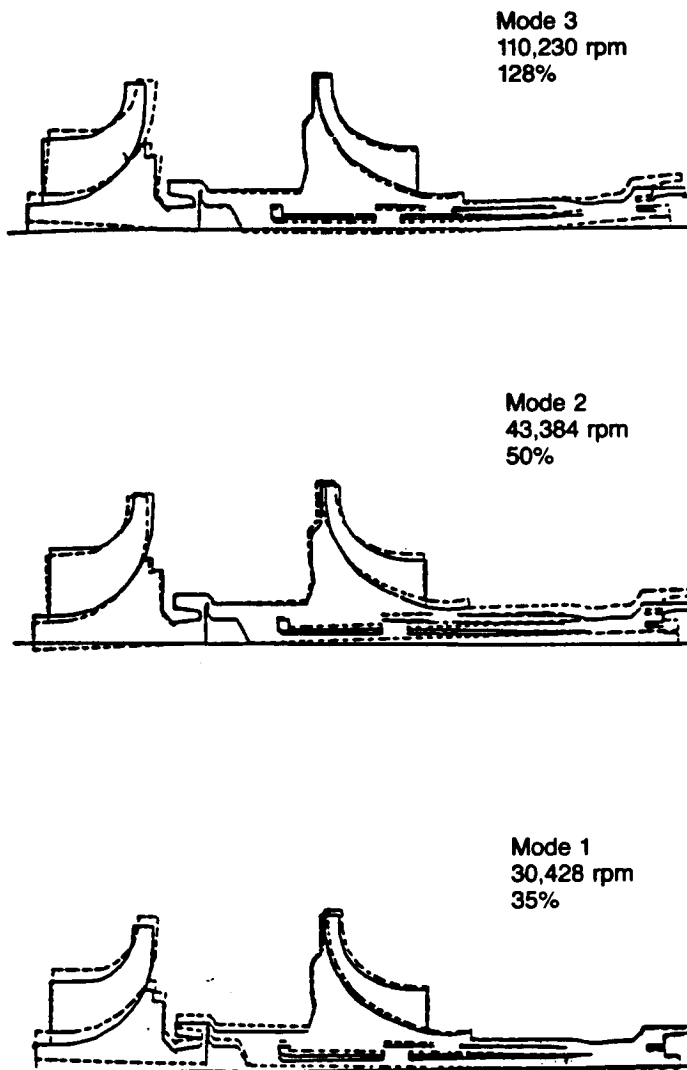
Figure 142. Si_3N_4 rotor shaft/compressor shaft joining schemes. (a) brazed joint (configuration 1), (b) interference fit joint (configuration 2).

10 gasifier rotors fabricated in the GTE PY-6 Si_3N_4 material by injection molding and HIP processing. The order also requires the proof spin testing of the rotors to 100,000 rpm (116% N1) by the vendor. The exducer region of the airfoil was shortened (see Figure 151) to render the airfoil radially pullable. This affected considerable savings in tooling costs for the relatively small order. Delivery of the rotors is projected by May 1986.

GTE Silicon Nitride Time Dependent Properties. During the current reporting period both dynamic and static fatigue were assessed for injection-molded AY6 sintered Si_3N_4 test bars from GTE Laboratories.

The object of this study is to determine some of the fundamental properties of ceramics, particularly injection-molded silicon nitride, to build a theoretical foundation permitting the development of better dynamic and static components for use in the engine. The study is highly theoretical in nature, reinforced by sophisticated experimental techniques. Allison has recently published the results of the study to date.* Interestingly, one of the conclusions is that it

*Khandelwal, P. K., Chang, J., and Heitman, P.W., "Slow Crack Growth in Sintered Silicon Nitride," *Fracture Mechanics of Ceramics*, Vol 8, Ed. by R. C. Bradt, et al, Plenum Publishing Corp, 1986.



TE86-2490

Figure 143. Calculated gasifier rotor assembly modes (configuration 1)—tiebolt stiffening load included.

may be possible to use the present GTE silicon nitride material, properly processed, up to 1000°C (1832°F) for 1000 hr at loadings between 206.84 to 275.79 MPa (30 to 40 x 10³ lb/in.²) static stress before material failure occurs.

9.3.2 Gasifier Turbine Scroll Assembly Development

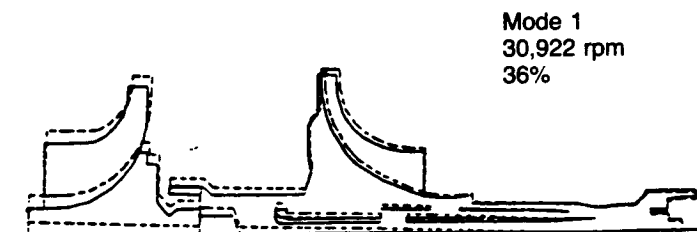
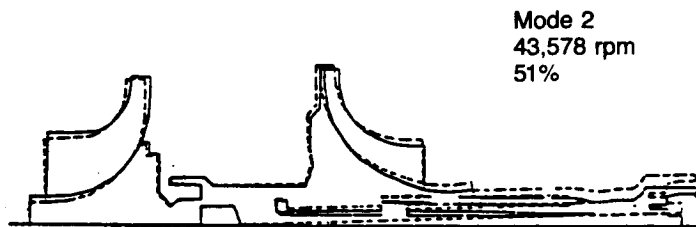
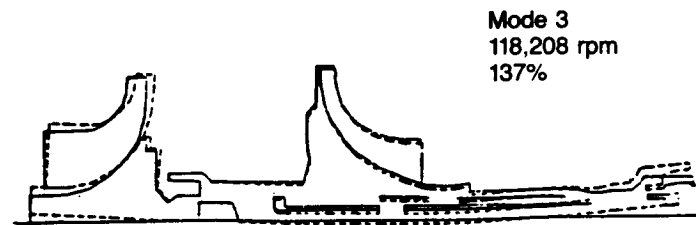
Development activity on the silicon nitride gasifier turbine static components during this reporting period included the following:

- vendor-proposed alternate design scroll body to simplify fabrication
- part fabrication initiated at vendor utilizing vendor alternate design concept

Calculated probability of survival for a silicon nitride gasifier turbine scroll/inner and outer backplate assembly is very favorable. Based on that result, purchase orders have been placed for silicon nitride scrolls, inner backplates, and outer backplates. Silicon nitride gasifier turbine vanes are already on hand. The silicon nitride gasifier turbine components will be supplied completely machined including nozzle vane pockets. Table XXIX details the quantity of components ordered and their scheduled delivery dates.

9.3.3 Power Turbine Rotor

The successful engine demonstration of a silicon nitride material gasifier rotor supported the decision



TE86-2489

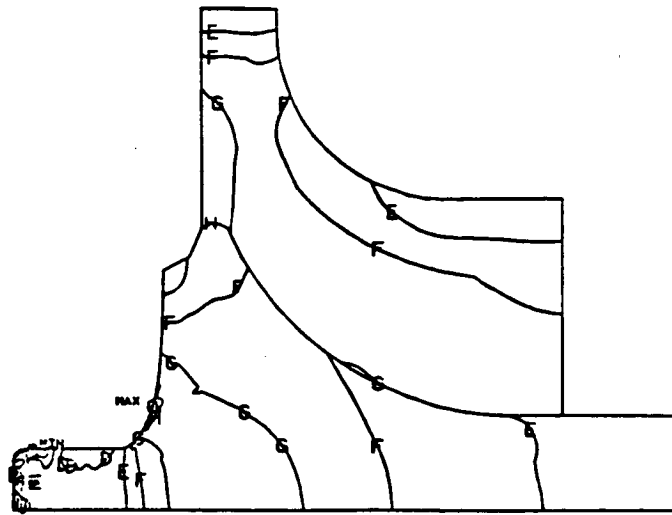
Figure 144. Calculated gasifier rotor assembly modes (configuration 2)—tiebolt stiffening load included.

to procure a power turbine rotor fabricated from the same material. An order was placed with Kyocera for 12 power turbine rotors made from the slip-cast SN220M material (same as used in the manufacture of the gasifier turbine). The order specifies vendor proof spin test to 130% NPT (88,500 rpm) and delivery of rotors suitable for interference fit joining to the power turbine shaft. Allison is supplying an oversize aluminum master die. Kyocera has specified a 114.5% master die size to accommodate subsequent shrinkage in the processing. The die features a redesigned (thicker) inducer airfoil in an effort to improve airfoil resistance to impact.

Table XXIX.
Summary of purchase orders issued for silicon nitride gasifier turbine static components.

Component	Quantity ordered	Scheduled delivery date	Vendor
Scroll	6	24 March 1986	Kyocera
Outer backplate	6	24 March 1986	Kyocera
Inner backplate	12	24 March 1986	Kyocera

Note: All components fully machined, ready for test



Legend

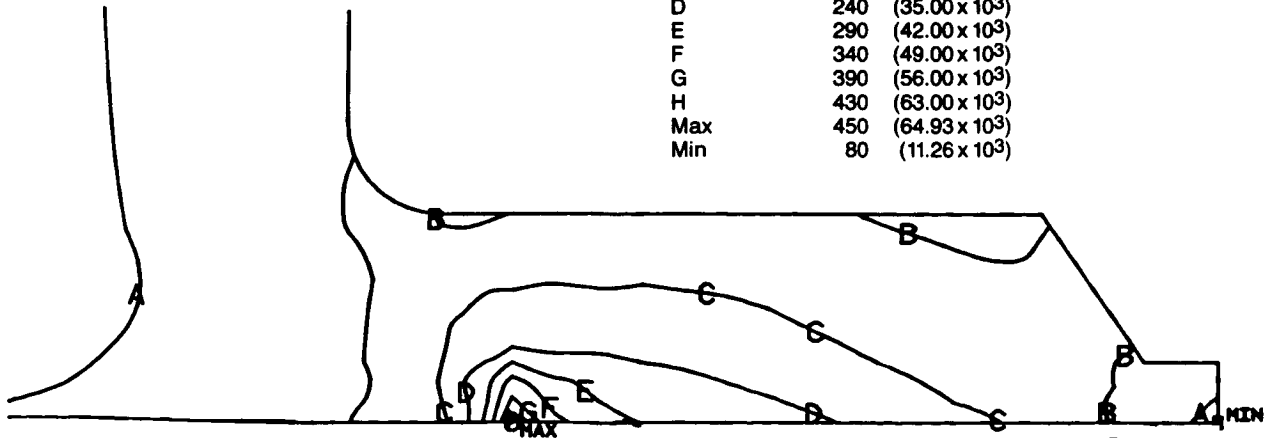
	MPa	(lb/in ²)
A	-100	(-15.00 x 10 ³)
B	-70	(-10.00 x 10 ³)
C	-30	(-5.00 x 10 ³)
D	0	(0 x 10 ³)
E	30	(5.00 x 10 ³)
F	70	(10.00 x 10 ³)
G	100	(15.00 x 10 ³)
H	140	(20.00 x 10 ³)
Max	160	(23.50 x 10 ³)
Min	110	(-16.05 x 10 ³)

TE86-2488

Figure 145. Contour plot of calculated maximum principal stress for interference fit (configuration 2), Si₃N₄ rotor at 100% speed and 1976°F turbine inlet temperature (TIT).

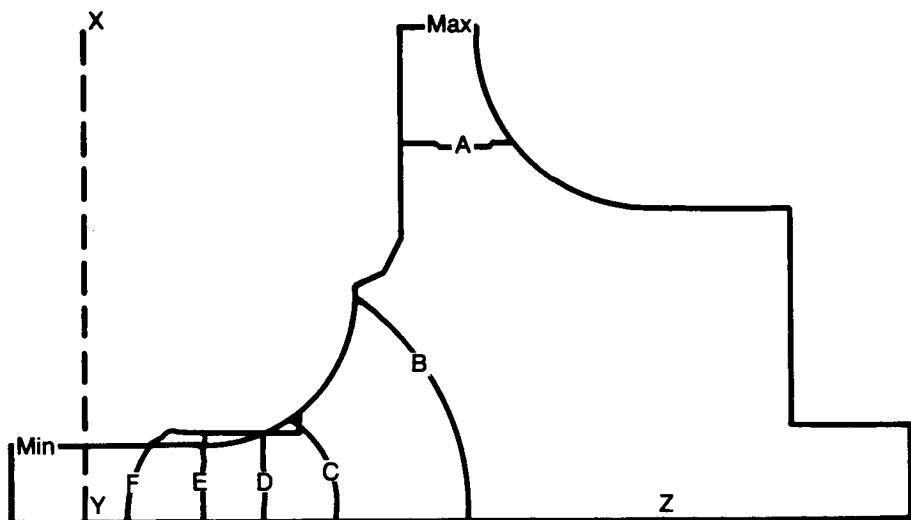
Legend

	MPa	(lb/in ²)
A	100	(14.00 x 10 ³)
B	140	(21.00 x 10 ³)
C	190	(28.00 x 10 ³)
D	240	(35.00 x 10 ³)
E	290	(42.00 x 10 ³)
F	340	(49.00 x 10 ³)
G	390	(56.00 x 10 ³)
H	430	(63.00 x 10 ³)
Max	450	(64.93 x 10 ³)
Min	80	(11.26 x 10 ³)

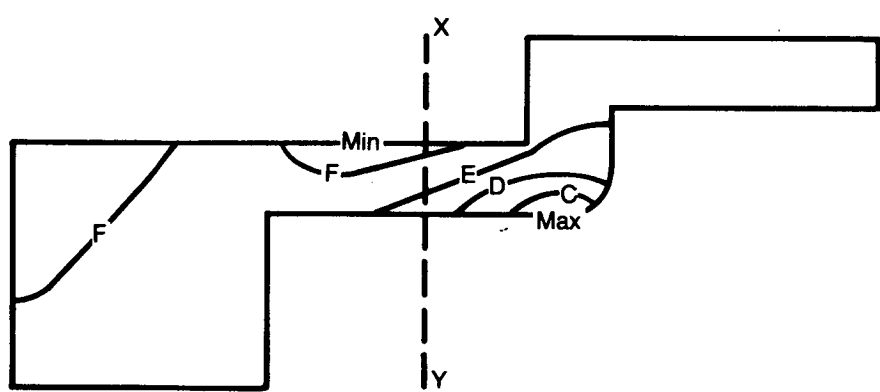


TE86-2487

Figure 146. Contour plot of equivalent stress, Inco 907 shaft at 100% speed and 1976°F turbine inlet temperature (TIT) for interference fit attachment.



Legend		
	°C	°F
A	1149	2100
B	982	1800
C	816	1500
D	649	1200
E	482	900
F	316	600
Max	1201	2194
Min	217	422



Legend		
	°C	°F
A	293	560
B	277	530
C	260	500
D	243	470
E	227	440
F	210	410
Max	299	570
Min	194	382

TE86-2804

Figure 147. Contour plot of calculated temperatures for the Kyocera braze joining of Si_3N_4 turbine and metal shaft (configuration 1) at 100% speed and 1288°C (2350°F) TIT.

At the date of this report, the drawing for the master die is being prepared. The die will be procured from Plumb Mold during the first quarter of 1986. Kyocera has estimated delivery of the rotors during the third quarter of 1986.

9.3.4 Power Turbine Scroll Assembly Development

Development activity on the silicon nitride power turbine static components during this reporting period included the following:

- completion of design drawings
 - vendor proposed alternate scroll design configuration
 - component fabrication initiated at vendor
- Purchase orders have been issued to procure silicon nitride power turbine scrolls (vendor alternate design), inner backplates, and outer backplates. Table XXX details the quantity of parts ordered and their expected delivery dates. The scroll and outer backplates will be supplied by Kyocera without vane pockets because they do not have the capability to

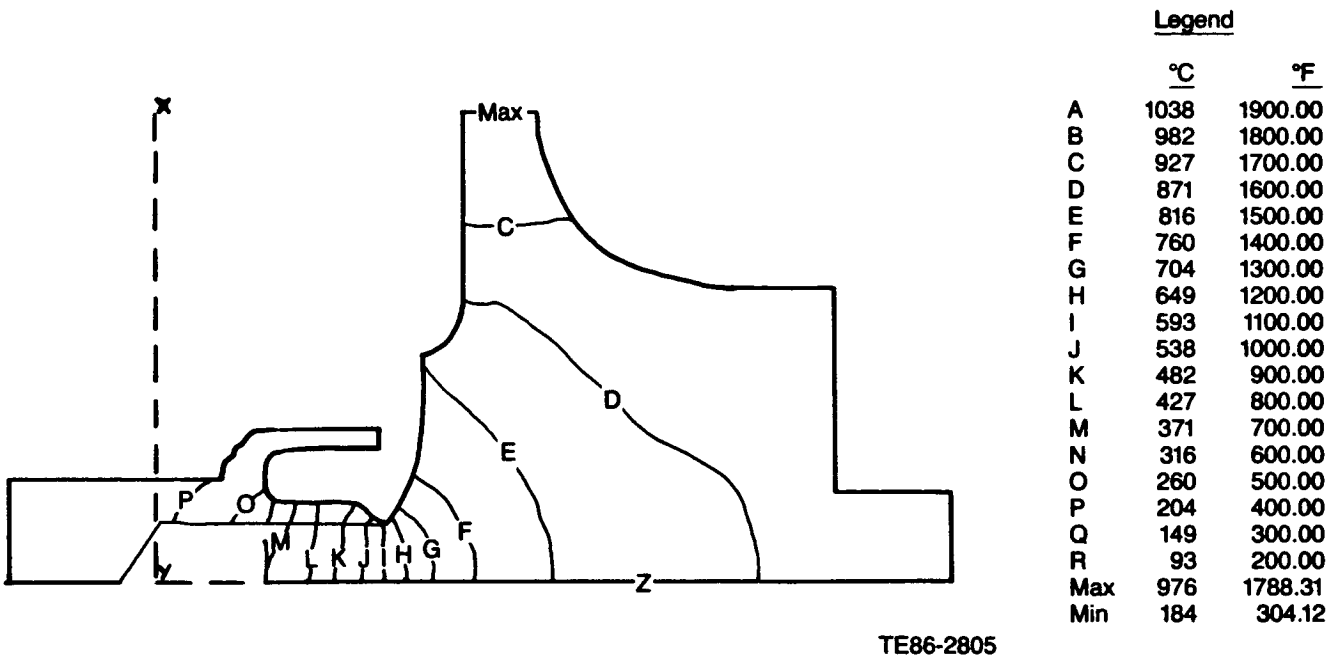


Figure 148. Thermal analysis of Si_3N_4 rotor and metal shaft at 1080°C (1976°F) TIT and 100% speed for the interference fit (configuration 2).

machine pockets (all at one time) in a component as large as the power turbine scroll or outer backplate. A domestic vendor will be selected to machine the vane pockets into the components. Silicon nitride power turbine vanes have previously been procured and are available for installation in a power turbine scroll assembly.

9.4 FIBER-REINFORCED GLASS CERAMICS

A total of six reinforced glass-ceramic composite gasifier turbine inner backplates were received from Corning Glass Works during this reporting period. These included four barium magnesium aluminosilicate (BMAS-III) and two magnesium aluminosilicate (MAS) whisker-reinforced parts.

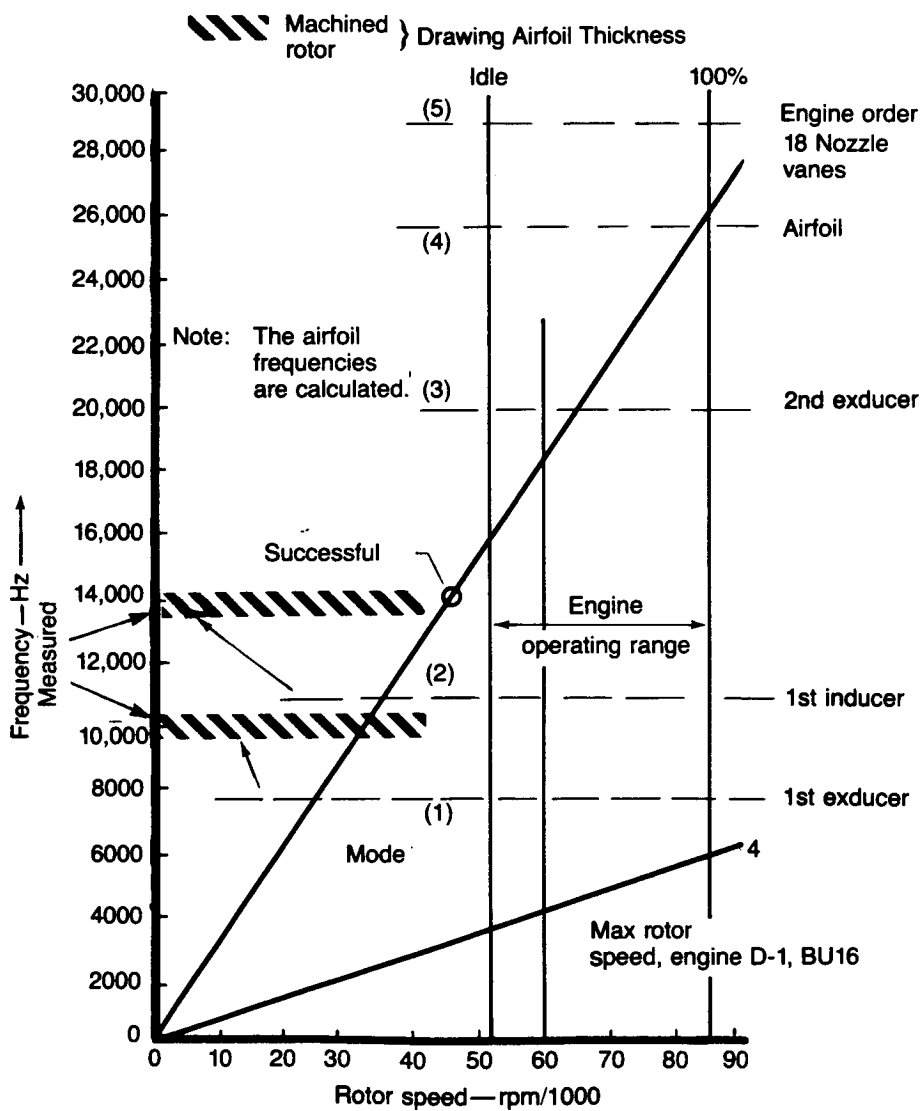
The BMAS-III inner backplates contain ceramic grade Nicalon SiC fibers from Nippon Carbon 30-40% by volume stacked in a 0-deg/±45-deg/90-deg orientation. The BMAS-III matrix is a glass-ceramic composition with higher temperature capability than the earlier lithium alumino-silicate (LAS) and BMAS-II matrices. Corning test data indicate a room temperature flexural strength of 1027.32 MPa (149×10^3 lb/in.²) for 0-deg/0-deg orientation BMAS-III test bars with a strength of 434.37 MPa (63×10^3 lb/in.²) measured at

1250°C (2282°F). Corning is also developing a matrix material with improved temperature resistance. Test material (0-deg/0-deg) of this new composition has demonstrated a strength of 372.32 MPa (54×10^3 lb/in.²) at a temperature of 1350°C (2462°F). The four BMAS-III backplates received were fabricated using a stepped preform. The stepped preform differs from the earlier flat preform backplates in that the stepped construction incorporates fibers at a 45-deg angle across the sharp corner to improve interlaminar shear properties. The differences in laminate configuration are shown in Figure 152.

A two-dimensional axisymmetric FEM model was employed to calculate deflections of the composite ceramic inner backplate under engine operating conditions. The analysis required an estimate to be made for the value of the elastic modulus of the material in the component. This estimate was based on vendor data. Static load tests were conducted on three different material/reinforcement configurations to obtain deflection as a function of load characteristics for the material configurations and to also verify the elastic modulus estimate used in the calculations. The results of these tests are presented in Figures 153 through 155. The LAS-III/flat preform configuration

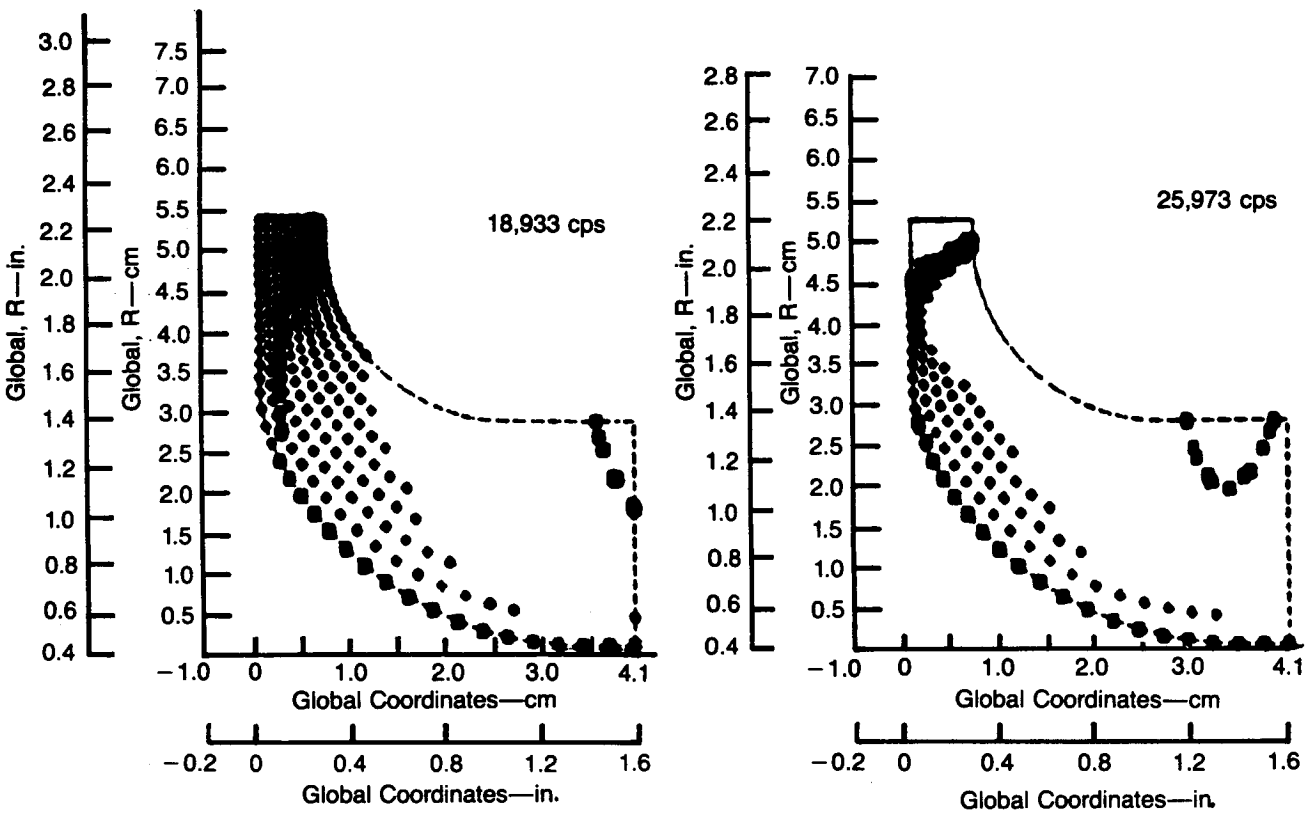
and the BMAS-III/flat preform configuration slope deflection dependency on load was greater than predicted as indicated in Figures 153 and 154, respectively. The slope of the deflection dependency on load for two samples of the BMAS-III/stepped preform configuration are very similar to the predicted value, Figure 155. These data show the BMAS-III/stepped preform configuration to be the stiffest of the three inner backplate configurations tested, and a sample of this configuration was selected for engine testing. A sample of a BMAS-III/flat preform composite ceramic inner backplate has been tested in the static thermal shock rig.

The remaining two backplates received from Corning were MAS matrices reinforced with approximately 25% SiC whiskers. This material has a flexural strength of 344.74 to 413.69 MPa ($50-60 \times 10^3$ lb/in.²) with a fracture toughness (K_{IC}) measured by single-edged notched beam (SENB) of 5.5 MPa m^{1/2}. The whisker reinforced backplates offer improved near-net-shape fabrication capability (sinter and/or HIP) compared with the fiber reinforced backplates (hot pressed) in addition to high surface hardness and erosion/wear resistance. These backplates have not as yet been rig or engine tested.



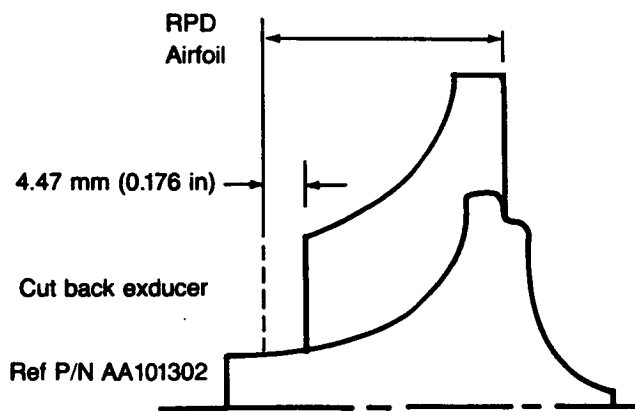
TE86-2806

Figure 149. Frequency-speed interference diagram gasifier turbine-silicon nitride (at speed and temperature), drawing airfoil thickness.



TE86-2486

Figure 150. Calculated mode shape, third and fourth mode, Si_3N_4 material rotor.



TE86-2485

Figure 151. GTE silicon nitride material (PY-6) gasifier rotor featuring radially pullable airfoils.

Table XXX.
Summary of purchase orders issued for silicon nitride power turbine static components.

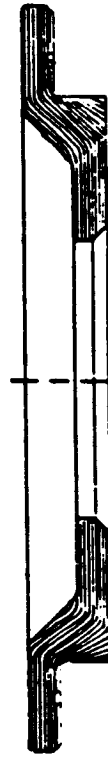
<u>Component</u>	<u>Quantity ordered</u>	<u>Expected delivery date</u>	<u>Vendor</u>
Scroll	6	15 June 1986* 1 Aug-15 Oct 1986**	Kyocera
Outer backplate	6	15 March 1986* 1 May-15 July 1986**	Kyocera
Inner backplate	12	15 March 1986	Kyocera

*Delivered without vane pockets

**With vane pockets machined by domestic vendor



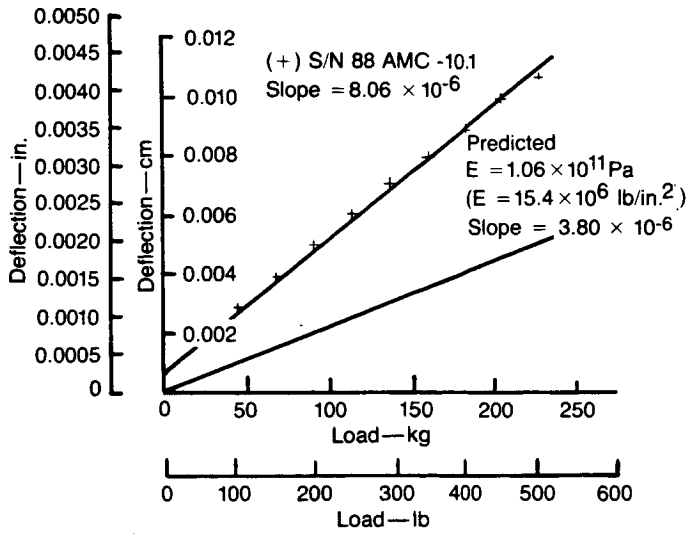
Flat laminate configuration



Stepped laminate configuration

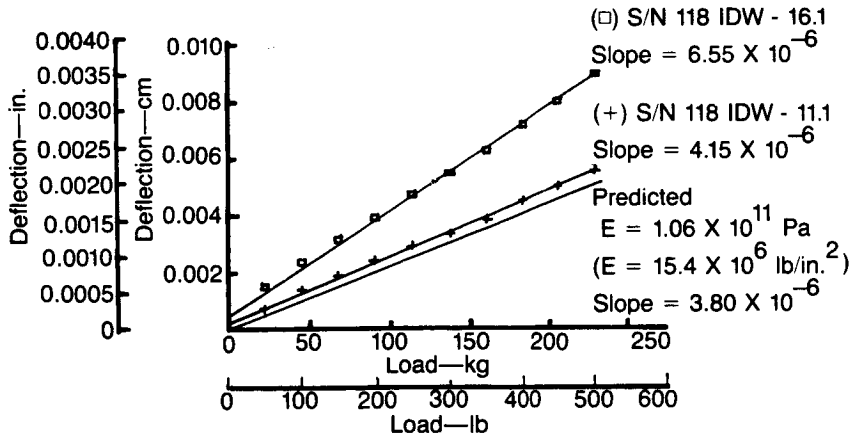
TE86-2703A

Figure 152. Corning ceramic composite gasifier turbine inner backplate laminate configurations.



TE86-2481

Figure 153. Linear deflection as a function of load, Corning LAS III—flat preform composite ceramic inner backplate.

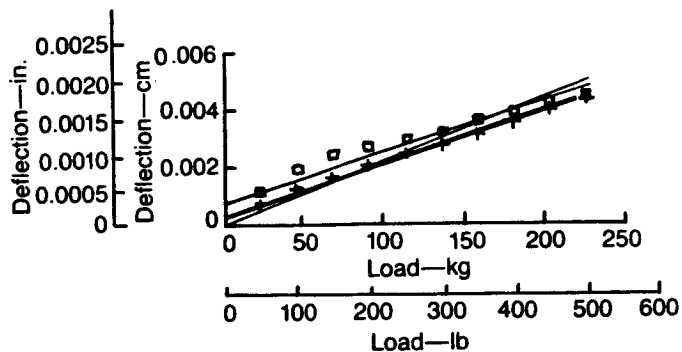


TE86-2480

Figure 154. Linear deflection as a function of load, Corning BMAS-III—flat preform composite ceramic inner backplate.

Predicted $E = 1.06 \times 10^{11}$ Pa
 ($E = 15.4 \times 10^6$ lb/in.²)
 Slope = 3.80×10^{-6}

(□) S/N 118 IDW - 14.1
 Slope = 3.07×10^{-6}
 (+) S/N 118 IDW - 19.1
 Slope = 3.17×10^{-6}



TE86-2479

Figure 155. Linear deflection as a function of load, Corning BMAS-III—stepped preform composite ceramic inner backplate.

X. CONTROLS DEVELOPMENT

10.2 SOFTWARE CHANGES TO SUPPORT ENGINE TESTING

Programming changes to support engine testing during this reporting period include:

- a new version of the electronic control unit software to permit engine operation with the pilotless combustor
- an improved version of the software required to permit engine operation with an electrical starter
- minor software improvements/adjustments to existing control systems

Pilotless Combustor Operation. A new version of the electronic control unit (ECU) software was written and tested to permit engine operation with the pilotless combustor. The original start sequence for the combustor employed a pilot nozzle through which fuel was introduced and ignited with a single electrical igniter. The pilot flame (torch) then ignited the start fuel introduced through the start nozzle.

In the pilotless combustor system start fuel is directly ignited with dual electrical igniters rather than with the pilot flame. This scheme simplifies the control system by eliminating the pilot and quickfill solenoids and the pilot nozzle temperature input. Light-off logic is also simplified in that one-stage, pilot nozzle light-off has been completely eliminated.

Other reductions in the software include elimination of the pilot nozzle flameout, pilot thermocouple failure, and pilot nozzle overtemperature logic. The ECU still energizes a single relay to turn on the ignition; however, in the absence of the pilot nozzle, dual exciters are paralleled from the ignition relay to activate the dual electrical start nozzle igniters. Pilotless combustor operation has been successfully demonstrated in the engine on the test stand and represents a sizeable reduction in both hardware and software in the ECU.

Electric Starter Operation. Software has been written and tested to permit engine operation with an electric rather than a hydraulic starter. The original engine start sequence used an electric starter and this new version of the software simply merges the original start logic with the improvements that have occurred during the engine development program. This version has not as yet been used on the test stand.

Other Engine Support. Minor software changes were also made during this reporting period to support normal engine testing. These include improvements to the software for the new fuel system, adjustments to the burner variable geometry schedule, and changes to improve operator control of the engine.

XII. SUPPORTIVE MANUFACTURING, COST, AND MARKETABILITY

12.1 MANUFACTURING FEASIBILITY

Pontiac Motor Division (PMD) has had integrated vehicle design and cost analysis responsibility throughout the program effort. Although the effort at Pontiac during this reporting period was curtailed because of the intense effort directed toward ceramic engine development, this annual report would not be complete without a brief summary of Pontiac's manufacturing feasibility studies to date.

Pontiac has successfully developed dies to manufacture (stamp) the engine sheet metal case. RPD design revisions proposed for the combustion case assembly included elimination of separate combustor support and mounting flange castings by including these formations in the sheet metal case (ref: Fifth Semiannual AGT Report, Section XII). An expansion forming die process was investigated for the formation of these areas during 1984.

The objectives of that program were as follows:

- to verify the manufacturing feasibility of the combustion case assembly incorporating design revisions as previously proposed and included in the manufacturing and cost analysis for the RPD engine
- to determine the feasibility of using an expansion forming die process to produce the combustion case assembly on a high-volume production basis
- to gain experience with the draw and forming characteristics of SAE 4130 steel
- to gain experience regarding the downstream machining requirements based on the outcome of actual parts fabrication

The expansion forming die process was only partially successful. During the die tryout program, the mounting flanges were successfully formed, but metal near the top surface of the combustor support area fractured before reaching the specified height. Various techniques tried during the die tryout program, including preforming the support area, did not alleviate the fracturing. The conclusions from this program were:

- The depth of draw in the combustor support area with the existing design and material specification exceeds the capability of the expansion forming process.
- The mounting flanges can be formed by using either an expansion forming or a conventional roll forming process.
- The expansion forming process can be used for sizing and qualifying the concentricity of the inside diameter of the case.

Pontiac recommended that the combustor support area should be formed by a conventional draw die process and initiated a program to verify this conclusion. Conventional draw die tooling was constructed but no experimental effort was performed during 1985 to verify formability of the case combustor support area. However, based on past experience, Pontiac is certain that the combustor support area could be formed by this more conventional process. Further, it is Pontiac's contention that their prior work is sufficient to verify the manufacturing feasibility of the engine sheet metal case and combustor support area incorporating all of the RPD design revisions to date.

APPENDIX. TERMS AND DEFINITIONS

AGT	advanced gas turbine	kPa	kilopascal
AGT 100	the AGT model being developed by Allison	kW	kilowatt
AREQ	equivalent area ratio	L	liter
AS	aluminum silicate	LAS	lithium aluminum silicate
BALCO	The Balancing Company, Inc.	lb	pound
BIP	burner inlet pressure	lbm	pound mass
BIT	burner inlet temperature	LBO	lean blowout
BOT	burner outlet temperature	m	meter
BU	buildup number	mA	milliampere
BVG	burner variable geometry	Metnet	a foamed metal later filled with a wear-face material
C	damping coefficient	MAS	magnesium aluminum silicate
C	degrees centigrade	mg	milligram
CATE	Ceramic Applications in Turbine Engines Program	mil	one thousandth of an inch
CBO	Carborundum Company	min	minutes
BDT	compressor discharge temperature	mm	millimeter
CGW	Corning Glass Works	MOR	modulus of rupture
cm	centimeter	MPa	megapascal
CO ₂	carbon dioxide	m _s	Weibull modulus based on surface characteristics
cpm	cycles per minute	m _v	Weibull modulus based on volume characteristics
CTE	coefficient of thermal expansion or cyclic thermal evaluation	mpg	miles per gallon
CY	calendar year	N	force (Newton) or speed of rotation (rpm)
DF-2	diesel fuel number 2	N ₁	gasifier speed of rotation
DOE	U.S. Department of Energy	N ₂	power turbine speed of rotation
E	Young's modulus	NASA	National Aeronautics and Space Administration
ECR	engine configuration rotor	NDE	nondestructive evaluation
ECU	electronic control unit	NGK	ceramics manufacturing company in Japan
EDR	Allison engineering report	O/B	outboard
EMI	electromagnetic inspection	o.d.	outside diameter
EMTL	Energy Materials Testing Laboratory	POS	probability of survival
EPA	experimental procurement authority	PMD	Pontiac Motor Division of General Motors
°F	degrees Fahrenheit	P _s	probability of survival based on surface characteristics
f/a	fuel-to-air ratio	P _t	total probability of survival
FEM	finite element model	P _v	probability of survival based on volume characteristics
FOD	foreign object damage	RBSiC	reaction-bonded silicon carbide
FPI	fluorescent penetrant inspection	ref	reference
ft	foot	RFB	rich flashback
GM	General Motors Corporation	RIT	rotor inlet temperature
GTE	General Telephone and Electronics Corporation	RPD	reference power-train design
h or hr	hour	rpm	revolutions per minute
HIP	hot isostatically pressed	RT	room temperature
hp	horsepower	RTV	room temperature vulcanizing
Hz	Hertz	s or sec	second
I/B	inboard	SAE 4130	moly steel containing 3.9% C and
i.d.	inside diameter		
IGV	inlet guide vane		
in.	inch		
kg	kilogram		
km	kilometer		

APPENDIX (cont)

SFD	5.1% Mg, along with P, S, Si, Cr, and Mo squeeze film damper
S/N	serial number
S/N 1	first experimental AGT 100 engine
S/N 2	second experimental AGT 100 engine
SiC	silicon carbide
Si ₃ N ₄	silicon nitride
SS	steady state
T/C	thermocouple
TD	teardown
TDR	Allison technical engineering report
T-I	Tri Industries Incorporated
TIT	turbine inlet temperature
TMOR	tangential modulus of rupture
TOT	turbine outlet temperature
v	volt
Y _r	radial modulus of rupture—regener- ator disk
Y _t	tangential modulus of rupture—regen- erator disk
2-D	two dimensional
3-D	three dimensional
Δ	difference between two measure- ments, e.g., temperature or pressure
η _R	regenerator effectiveness
μ	coefficient of friction
μm	micrometer (micron)
σ	stress
σ _o	Weibull characteristic strength
σ _{os}	Weibull characteristic strength— surface flaw strength distribution
σ _{ov}	Weibull characteristic strength— volume flaw strength distribution

1. Report No. NASA CR-179484		2. Government Accession No.		3. Recipient's Catalog No.	
4. Title and Subtitle ADVANCED GAS TURBINE (AGT) TECHNOLOGY PROJECT				5. Report Date September 1986	
				6. Performing Organization Code	
7. Author(s) Engineering Department, Allison Gas Turbine Division				8. Performing Organization Report No. EDR 12344	
9. Performing Organization Name and Address Allison Gas Turbine Division of General Motors Corporation P.O. Box 420 Indianapolis, IN 46206-0420				10. Work Unit No.	
				11. Contract or Grant No. DEN 3-168	
12. Sponsoring Agency Name and Address U.S. Department of Energy Office of Transportation Systems Washington, D.C. 20545				13. Type of Report and Period Covered Contractor Report January-December 1985	
				14. Sponsoring Agency Code DOE/NASA	
15. Supplementary Notes Annual report, prepared under Interagency Agreement DE-AI01-85CE50111. Project Manager P.T. Kerwin, Transportation Propulsion Division, NASA Lewis Research Center, Cleveland, OH 44135					
16. Abstract Engine testing, ceramic component fabrication and evaluation, component performance rig testing, and analytical studies comprised AGT 100 activities during the 1985 year. Ten experimental assemblies (builds) were evaluated using two engines. Accrued operating time was 120 hr of burning and 170 hr total, bringing cumulative total operating time to 395 hr, all devoid of major failures. Tests identified the regenerator seals as the primary working fluid leakage sources. Power transfer clutch operation was demonstrated in two builds. Build 16 of engine S/N 1 initiated Si ₃ N ₄ ceramic rotor testing, with this gasifier rotor running through year's end. An αSiC gasifier rotor engine test resulted in blade tip failures. Recurring case vibration and shaft whip have limited gasifier shaft speeds to 84%. Build 13 of engine S/N 2 gathered dynamic data indicating rotor unbalance as the vibration and whip source, and also verified the pilotless combustor igniter. An αSiC scroll assembly underwent six engine transient cycles, followed by scroll rig verification to 1066°C (1950°F), then running at 80% airflow and 1066°C in engine S/N 2 build 14. Ceramic components successfully engine tested now include the SiC scroll assembly, Si ₃ N ₄ turbine rotor, combustor assembly, regenerator disk, bulkhead, turbine vanes, piston rings, and couplings. Rig performance testing of a reduced surface friction compressor was completed. A compressor shroud design change to reduce heat recirculation back to the inlet was executed. A new compressor impeller design with target efficiency above 80% was initiated. Combustor activities included qualification of ceramic parts for engine use and alternate fuel testing (methanol). A new design was initiated to eliminate fuel tube coking on DF-2 at very high burner inlet temperatures. Regenerator activities included rig testing new inboard seals, a seal rim preload test of patented design features, and strength characterizations of matrix materials. Ceramic component activity continues to focus on the development of state-of-the-art material strength characteristics in full-scale engine hardware. Injection-molded sintered αSiC and slip-cast Si ₃ N ₄ gasifier turbine rotors were delivered from Sohio/Carborundum and Kyocera, respectively. SiC gasifier scrolls were supplied by Sohio (α and siliconized) and by Norton (siliconized). Power turbine scroll detail design drawings were released. Fiber reinforced glass-ceramic composite turbine (inner) backplates were fabricated by Corning Glass Works. The BMAS/III material performed well in engine testing. Backplates of MAS material have not been engine tested.					
17. Key Words (Suggested by Author(s)) Automotive gas turbine Alternate propulsion systems Ceramic components Vehicular propulsion Structural ceramics Improved fuel economy Engine configuration rotors			18. Distribution Statement		
19. Security Classif. (of this report) Unclassified		20. Security Classif. (of this page) Unclassified		21. No. of Pages	22. Price*